Universitat Autònoma de Barcelona

Doctoral Thesis

Measurement of the Muon Neutrino Charged Current Interactions and the Muon Neutrino Single Pion Cross Section on CH Using the T2K Near Detector

Author:
Raquel Castillo Fernández

Supervisor:
Dr. Federico Sánchez Nieto
Tutor:
Dr. Enrique Fernández Sánchez

A thesis submitted in fulfilment of the requirements for the degree of PhD on Physics

in the

Neutrino Group
Institut de Física d'Altes Energies (IFAE)

June 2015

"No es sabio el que sabe donde está el tesoro, sino el que trabaja y lo saca."

Francisco de Quevedo y Villegas

UNIVERSITAT AUTÒNOMA DE BARCELONA

Abstract

Facultat de Ciéncies
Institut de Física d'Altes Energies (IFAE)

PhD on Physics

Measurement of the Muon Neutrino Charged Current Interactions and the Muon Neutrino Single Pion Cross Section on CH Using the T2K Near Detector

by Raquel Castillo Fernández

The T2K experiment is a long baseline neutrino experiment which utilizes an almost pure muon neutrino beam. The main goal of the experiment is the measurement of the oscillation parameters of the muon neutrinos. In order to achieve this goal, T2K requires an accurate prediction of the interaction rates in the far detector, Super–KamiokaNDE. The near detector of T2K, ND280, measures the interaction rates and estimates the number of events at the far detector.

The muon neutrino charged current interactions in the near detector (ND280) are used to predict the rate at the far detector (Super–KamiokaNDE). To a better constrain of the cross section parameters, which are dominant in the analysis together with the flux uncertainty, we categorize the selected events in three different samples according to the number of pions in the final state. These categories allow for a better constrain of the oscillation signal channel (Charged Current Quasielastic) and the main oscillation background (Charged Current 1 Charged Pion).

Current and future neutrino experiments are limited by neutrino cross section uncertainties. The actual cross section models are in tension with the experimental data in some energy ranges. It is still critical to study neutrino–nucleus cross sections on all possible interaction channels. The muon neutrino charged current single pion production is one of the main channels in tension with the model. As a second contribution, we present the measurement of the Charged Current single positive pion production cross section using a model independent approach exploring the full capability of the ND280 detector to determine the kinematical distributions of the event. The improved knowledge of the interactions, and in concrete for the single pion channel, will allow the reduction of the the systematical uncertainties in the oscillation analysis.

Medida de las Interacciones de Neutrino Muónico de Corriente Cargada y Sección Eficaz de Producción de un Sólo Pión en Interacción de Neutrino Muónico de Corriente Cargada en CH usando el Detector Cercano de T2K

por Raquel Castillo Fernández

El experimento T2K es un experimento de neutrinos de largo recorrido que utiliza un haz casi puro the neutrinos muónicos. El objetivo principal del experimento es a medida de los parámetros de oscilación del neutrino muónicos. Para conseguir éste objetivo, T2K necesita una rigurosa predicción del índice de interacciones en el detector lejano, Super–KamiokaNDE. El detector cercano de T2K, ND280, calcula el índice de interacciones y estima el número de eventos en el detector lejano.

Las interacciones de neutrino muónico de corriente cargada en el detector cercano (ND280) son usadas para predecir el índice de eventos en el detector lejano (Super–KamiokaNDE). Para una mejor restricción de los parámetros de sección eficaz, los cuales dominan el análisis junto con las incertezas de la prediccion del flujo, categorizamos los eventos seleccionados en tres grupos de acuerdo con el número de piones en el estado final. Estas tres categorías permiten un mejor ajuste de la señal del canal de oscilación (Corriente Cargada Quasielástica) y el principal ruído en ocilaciones (Corriente Cargada de 1 Pión Cargado).

Actuales y futuros experimentos de neutrinos están limitados por las incertezas en las secciones eficaces de neutrinos. Los modelos actuales de sección eficaz están en tension con los datos experimentales en algunos rangos energéticos. Esto hace que sea critico estudiar secciones eficaces de neutrino–nucleo en todos los canales de interacción posibles. La producción the un solo pión en interacciones de neutrino muónico de corriente cargada es uno de los principales canales en tensión con los modelos. Como segunda contribución, presentamos el cálculo de producción the un solo pión en interacciones de neutrino muónico de corriente cargada usando un enfoque indepenediente del modelo explorando la capacidad total del detector ND280 para establecer las distribuciones cinemáticas del evento. La mejore del conocimiento de las interacciones, y en concreto del canal de producción de un sólo pión, permitirá la reducción de las incertidumbres sistemáticas en el análisis de oscilaciones.

Acknowledgements

First, I would like to thanks to Federico for the opportunity he gave me and all the disccussions we had during these four years. Each single discussion was important. I want to thanks as well Matteo and Ramon, previous and current IFAE's directors, thanks to take care of everybody!

I would like to thanks the people who provide me support during my first years of research, Michela and Mike, thanks for your patiente! Thanks a lot to my convener among all the analysis, Francesca, for the patiente and all the support.

I would like to thanks as well the rest of Cross Section Group conveners and specially to Kendall for her enthusiasm and motivation. Thanks to Martin, A.K.A "in potato", who was always providing support and very nice discussions during the cross section analysis. I would like to thanks specially to Alfons, who proposed to me to do the CC1π analysis during one of our jet–lag–discussions in that nice ryokan in Tokai. Thanks to the NIWG conveners and to the questioning sense of Kevin which make the analysis stronger. Thanks a lot to Michel and Sara which helped on the improvement of the work. And thanks to Stefania who read very carefully this thesis and make it easier to digest.

Haig d'agrair molt especialment a Xavier Vinyas qui em va donar la primera oportunitat de treballar en recerca. Moltes gracies per la motivació, pel carisma i per fer–me estimar la física nuclear.

I want to thanks to all the T2K collaborators for all the nice time in this great experiment. And specially I would like to thanks to Jiae, Leila, Javi, Callum, Matt, Thomas, Sasha, Panos, Teppei, Denis, Lorena, Anselmo, Melody, Tianlu and Minoo, thanks a lot for the very nice time!

Thanks to the IFAE people and especially to Gerard, Gianluca, Jöern, Iván and Emmanuelle. Welcome to the new neutrino's IFAE members, Alfonso, Bruno and John! And specially thanks to Alfonso, it was so funny to work with you.

Quiero agradecer a Irene, Sandrinha, Marta, Jose, Rafael, Miguel Angel, Roberto, Miguel, Roger y Carlos todos los buenos momentos en la UAB. Gracias por el gran sentido del humor. Me gustaría dedicar tambien esta tesis a Ana, nuestra mexicana loca y fuerte que siempre recordaremos.

Vull agrair tot el suport i sentit del humor a l'Anna, Fran, Agnese, Noa, Nuri y Ana. Moltíssimes grácies!!!

Pero sobretodo, quiero dar las las gracias a mi familia, mi madre, mi hermana Sara y Joaquín. Sin vosotros esto no hubiera sido posible.

Contents

List of Figures

List of Tables

A mi Madre

Chapter 1

Outline

This thesis describes the study of the muon neutrino (ν_μ) interactions on CH occurred at the near detector of the T2K experiment, the ND280. The T2K beam is predominantly composed by ν_μ, thus ND280 is used to constraint both flux and neutrino cross section parameters in order to provide an event rate prediction at the T2K far detector, Super–KamiokaNDE.

In Chapter 2 we present the basis of the neutrino–nucleus interactions, which is the basis of the analysis described. We focus on the neutrino charged current events, that are of main relevance for the oscillation analysis performed in T2K, and we focus on the quasi-elastic and the single pion production channels. The quasi-elastic channel is the signal used for oscillation analysis while the single pion production is one of the main backgrounds in T2K.

We describe the T2K experiment in Chapter 3. We present the two near detectors, the INGRID and the ND280. The off–axis near detector, ND280, is presented and the main components used in the analysis are described. We explain the basis of the particle identification performed at each sub–detector that is used later on the analysis.

Once the detectors are described, we explain the different detector uncertainties that affect the two analysis presented in the thesis, Chapter 4. We describe each uncertainty, the different control samples used to measure each systematic and finally we describe how it is performed the error propagation. One of the detector systematics measurements is fully described in Appendix B.

In Chapter 5 we detail the performance of the ν_μ charged current interactions selection. This analysis was officially presented in 2013 and was used to determine the neutrino event rates at the far detector. This result was also used to constraint some cross section uncertainties which are dominant for the oscillation analysis in T2K.

T2K presented the new constraints on the oscillation parameters and first results from a ν_e appearance channel in a ν_μ beam in 2013. From the results, we observed that one of the most relevant uncertainties in the oscillation measurement was the uncertainty on the cross section parameter of the ν_μ charged current single pion events ($CC1\pi^+$). With the aim to compare the T2K data against the model used and also to help to reduce the uncertainty in the prediction, we measure the $CC1\pi^+$ cross section on CH. The description of this analysis is detailed in Chapter 6.

Finally, in Chapter 7 we summarize the results and conclusions of the analysis presented.

Chapter 2

Neutrino Physics

Today we know that neutrinos are unique among all matter particles, they participate in only two of the four fundamental interactions. In addition to gravity, which is very weak and affects all particles, neutrinos can interact only through the weak nuclear force. Since neutrino interactions are free of interfering electromagnetic and strong contributions, neutrino–nucleus interactions can provide information about the structure of the nucleus. Moreover, due to the parity violating nature of the weak force, neutrino–nucleus interactions can explore on the vector and axial–vector character of these interactions.

In this introductory Chapter we describe the properties of neutrinos, specially in scattering on baryon targets. The theory of these interactions is introduced. The main topic of this document is discussed, a measurement of charged current π^+ production.

2.1 Historical Introduction

In the early 1900s, the emerging nuclear theory predicted that the electrons resulting from β–decay processes should have been emitted at an specific energy, due to energy conservation in a two body reaction.

The β-decay processes are a type of radioactive decays mediated by the weak force in which the proton (neutron) is transformed into a neutron (proton) inside the atomic nucleus and emits an electron or positron (β–particle).

Contrary to this prediction, in 1914, James Chadwick showed that electrons were emitted in a continuous spectrum. This result was in contradiction to the energy conservation law, as it appeared that energy was lost in the beta decay process.

In December 1930, motivated by the study of the nucleus composition that suggest the existence of a new neutral particle, Wolfgang Pauli tried to combine this problem with the problem of the continuous β spectrum. For the first time, Pauli proposed a new neutral particle with spin $\frac{1}{2}$ to preserve energy and angular momentum conservation in nuclear β–decay processes. He called the new particles *neutrons*. Two years later Chadwick discovered what we call now neutrons and he realized that these new discovered particles were too heavy to be consistent with Pauli's postulation in the β–decay.

Three years later, Enrico Fermi [6] included on his theory of the β–decay the neutral particle postulated by Pauli, calling it neutrino (ν) to distinguish from the neutron. He also presented some conclusions on the β spectrum. One of these conclusions was that, based on the β–decay tail shape, the neutrino mass was compatible with 0. Fermi explained the process as a neutron that decays into a proton, an electron and a neutrino. He assumed a point-like interaction, while today we know that the β–decay occurs with the exchange of the W boson, and in the current framework the Fermi theory is assumed to be the low energy limit of this process.

Despite of the success of Fermi's neutrino theory to explain the β–decay, part of the scientific community was not convinced on the validity of this theory since the neutrino was not yet observed.

In 1956, F. Reines and C. L. Cowan presented a direct detection of the neutrino [7]. The experiment, located near the fission reactor at the Savannah River Plant (South California), consisted on three scintillation counters and two target tanks, Figure 2.1. The scintillation counters were a tank filled with liquid scintillator and read by 110 photomultipliers each. The target was a water solution of $CdCl_2$. When a neutrino interacts with a proton in the target tank, a positron and a neutron are produced, eq. 2.1. The outcoming neutron is captured by an atom of cadmium in a time window of about 25μs. When the neutron capture occurs, a photon is emitted. To identify a neutrino interaction, they expected that they will get a coincidence signal of the positron and the neutron within a precise time window, energy window and in anti-coincidence with the third counter. As a result, they got the first clear direct detection of the neutrino, and they even measured a neutrino cross section of $6.3 \times 10^{44} cm^2 \pm 25\%$.

$$\overline{\nu_e} + p \rightarrow e^+ + n$$

During the 60's the muon neutrino was discovered at the Brookhaven AGS experiment[8] (Alternating Gradient Synchrotron). It was the first neutrino accelerator-based experiment. Neutrinos were produced from decayed pions coming from protons of 15 GeV

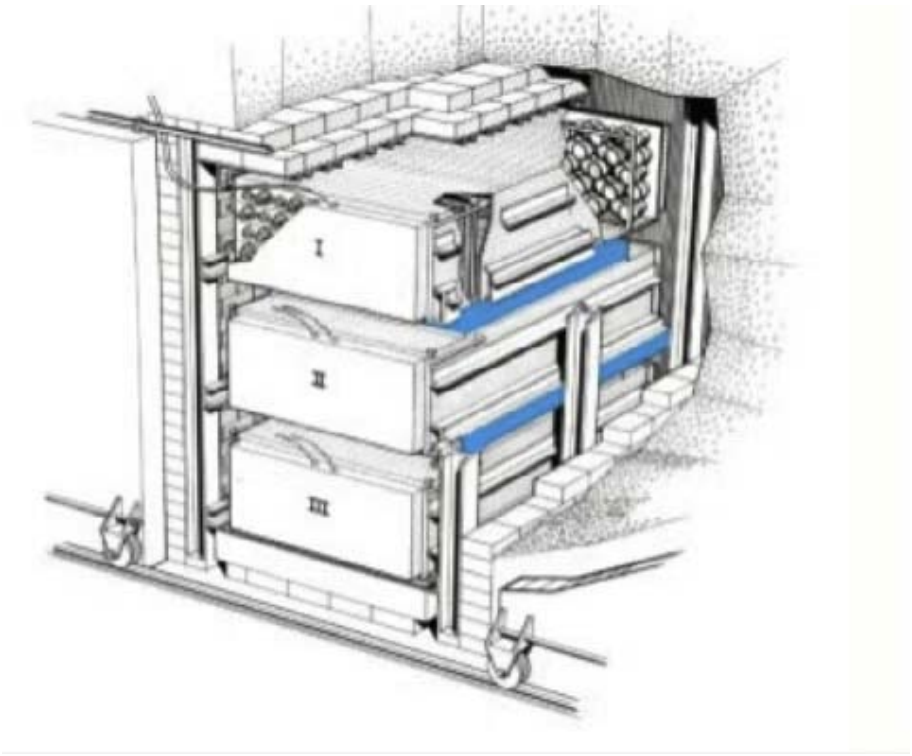

FIGURE 2.1: Concept picture of the Reines and Cowan detector. The big boxes I, II and III are the scintillation counters and the two small boxes A and B between the counters are the target tanks.

interacting with a beryllium target. The charged particles produced during the interaction were absorbed in 13.5 m iron shield and after the shield a spark chamber detector was placed. When the neutrino interacts the outgoing particles from the interaction flight through the chamber ionizing the gas on its path and producing sparks, due to the high voltage, showing this way the path of the particle. They observed 29 muons and only 6 electrons candidates that were compatible with background events. The experiment was thus probing that the process $\nu_\mu + N \rightarrow e^- + X$ is forbidden and that muon and electron neutrinos can be different particles.

At that time the study of nuclear reactions that produce the solar energy was in a very high stage, it was considered as an stable theory. This was explained with the CNO cycle, an exothermic chain of nuclear reactions that capture protons and produce helium, photons, positrons and neutrinos. To check the model a measurement of the solar neutrino flux was proposed and in 1968 Raymond Davis published the first measurement of the solar neutrino flux [9]. The detector was made of 520 tons of liquid C_2Cl_4 in a horizontal cylindrical tank located in 1480 m underground laboratory to reduce the cosmic ray background. The detection was based on the interaction $\nu + {}^{37}Cl \rightarrow e^- + {}^{37}Ar$. This argon isotope is radioactive, so one can measure the amount of argon by detecting its decay. The measurement shown a deficit in the number of neutrinos that the sun was

expected to emit. This was the starting point of the so–called *Solar Neutrino Problem*.

In the following year, Gribov and Pontecorvo published how $\nu_e \rightarrow \nu_\mu$ may oscillate and its relation with a decrease in the number of detectable solar neutrinos at the earth surface [10]. In their theory, an electron neutrino could spontaneously change into a muon neutrino and, since Davis'neutrino detector could not detect muon neutrinos, the deficit could be explained taking into account the electron neutrino disappearance. This new effect pointed to the need of new neutrino detectors to measure the solar neutrino deficit and oscillation. But one had to wait many years until the neutrino oscillation parameters were measured.

In 1975, the τ lepton was discovered at the SLAC National Accelerator Laboratory. Since then, theorist assumed that a third type of neutrino associated to this new charged lepton must exist within the standard model. Finally, the evidence of the three neutrino species was demonstrated by LEP experiments measuring the width of the Z boson [11]. The tau neutrino, ν_τ, was observed in 2001 by the DONUT experiment (which stands for Direct Observation of the Nu Tau) at Fermilab [12]. In DONUT, accelerated protons were used to produce ν_τ via decay of charmed mesons. After eliminating as many unwanted background particles as possible by a system of magnets and bulk matter (mostly iron and concrete), the beam passed through several sheets of nuclear emulsion. In very rare cases one of the neutrinos would interact in the detector, producing electrically charged particles which left visible tracks in the emulsion and could be electronically registered by a system of scintillators and drift chambers. The characteristic properties of tau neutrino interactions were that several tracks suddenly appeared without any leading up to them and that one of those tracks would show a *kink* after a few millimeters, indicating decay of a τ lepton.

The phenomenon of the neutrino oscillation is fundamental for the neutrino physics. As of today, this is the only evidence that neutrinos have masses different from zero and that the lepton flavor number is not preserved. A short description of the neutrino oscillation theory is shown in Appendix A.

However, current experiments working to provide precise measurements of the parameters associated to the neutrino oscillation phenomenon are strongly limited by systematical errors. These systematical errors are dominated by the neutrino flux prediction uncertainty and the uncertainties of the neutrino interaction model. We will focus on the second, the neutrino interactions.

2.2 Neutrino Interactions

Since neutrinos are assumed to have very small mass and they only have a weak nuclear charge [1], in the standard model framework, they only interact with matter via the weak interaction by exchanging a $W^{\pm}$ (charged current interaction) or a Z^0 (neutral current interaction) boson.

In this section we describe the neutrino-nucleon interaction, sub–Section 2.2.1, the most fundamental neutrino-hadron interaction. We present the neutrino charged current single pion production which one of the most important channels at the neutrino intermediate energy range scale ($\sim 1GeV$) and the main channel studied in this dissertation. It is also discussed the different models adopted in the different neutrino Monte Carlo generators, which are frequently used in neutrino experiments. Specially, we describe the NEUT Monte Carlo generator which is used in the T2K experiment.

2.2.1 Neutrino-Nucleon scattering

For most of the neutrino oscillation experiments, neutrinos are detected via neutrino-nucleus interactions. This is done by neutrino collision with a fixed target on which neutrino-nucleon interactions are predominant in the neutrino energy region of few GeV. In such energy range, a neutrino interacts with a nucleon in the nucleus (or the entire nucleus) via charged current (CC) and neutral current (NC).

The simpler nuclear model to describe the interaction with the nucleus is the so–called the "Fermi Gas" model on which it is assumed that the nucleons in the nucleus are moving in agreement with the nuclear potential. The outgoing nucleon, from the neutrino interaction with the nucleus, is supposed not to interact with the other nucleons but is affected by the Pauli bloking [2]. But this is just considering the nucleus media effect in a very basic level. More realistic approaches can be done by considering "short range correlation effects" with the inclusion of momenta distribution of the target nucleon and binding energies and also by adding "long range correlation effects" including the nucleon–nucleon forces.

To the neutrino–nucleus interaction formalism we have to add the interaction of the neutrino with the nucleon.

[1] The weak nuclear charge is the coupling constant of the $SU(2)_L$ symmetry

[2] The nucleons, since they are fermions, follow the Fermi–Dirac statistic which allow only two fermions (nucleons) per energy level. Then, any scattering which promote the nucleon to a new state which is already occupied by another fermion (nucleon) is not allowed.

In this section we describe the interaction of a neutrino with a bound nucleon, with special attention to the neutrino charged current single pion production. For now on we will focus on the charged current interactions. We describe the interactions at the energies we are interested in, i.e. neutrino energies below a few GeV that corresponds to the T2K energies.

In the charged current interactions with baryon targets, on which the baryon undergo a change in its electrical charge to accommodate the exchange of the charged $W^{\pm}$ boson; we call these interactions charged current quasi-elastic (CCQE).

In the case that in the interaction, not only alter the charge of the target baryon but also the $W^{\pm}$ transfers enough 4–momentum (Q^2) to excite the target into a low mass resonance state, the decay of the resonance typically produce a nucleon and a pion; we call these process charged current pion production ($CC\pi$).

In interactions where also the momentum transferred is so energetic to break the nucleon, tipically producing more than one pion in the final state, we call these processes charged current multi–pion or DIS (deep inelastic scattering), where the DIS usually refers to the non resonance production region. Usually the classification into multi-pion or DIS in the Monte Carlo generators depends on the momentum transfer and invariant mass values of the interaction. Each interaction type is described as follows.

2.2.1.1 Neutrino Charged Current Quasi-Elastic Interactions

The neutrino charged current quasi-elastic is the simplest charged current interaction in neutrino-nucleon scattering processes. In all charged current neutrino interactions, a charged lepton, of the same family of the incoming neutrino, is produced. In the quasi-elastic processes a single nucleon in the final state is produced as well 2.2.

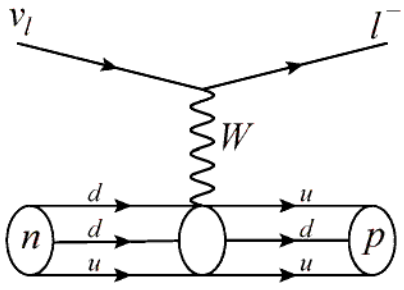

FIGURE 2.2: Feynman diagram of neutrino charged current quasi-elastic (CCQE) interaction.

Since a $W^{\pm}$ is exchanged the hadronic current must convert a neutron to a proton. For neutrino energies below $\sim$ 1.5 GeV charged current quasi-elastic (CCQE) interactions are

dominant [3] and is the preferred channel in several neutrino oscillation searches. This is the case for the T2K experiment. The far detector of T2K which is used to detect interactions from possible oscillated neutrinos, the Super–KamiokaNDE detector, is a Cerenkov water detector that allows a good lepton flavor association thanks to a good particle identification. To distinguish between hadron types becomes a bit more difficult in Super-KamiokaNDE. For this reason, CCQE-like events, in which only one lepton and one hadron can appear in the final state of the interaction, are well identified in Super-KamiokaNDE and used as main signal to perform oscillation studies. Neutrino energy can be well recosntructed in CCQE-like events.

One of the most common models used to evaluate the CCQE processes is the Llewellyn–Smith [**?**]. This model uses the vector and the axial-vector form factors of the nucleon. The axial-vector coupling constant, axial-vector mass M_A^{QE}, value is used to be set to be in good agreement with available neutrino experiments.

2.2.1.2 Neutrino Charged Current Single Pion production

When a neutrino interacts with enough energy with an atomic nucleon the hadronic current can be excited to a resonance state [3].

For the CCQE channel at these energies (from few Mev to few GeV) the main contamination comes from neutrino charged current single pion events ($CC1\pi^+$, in cases of $\bar{\nu}$ events it will be $CC1\pi^-$ events) 2.3. This makes that $CC1\pi^+$ cross section measurement is not only important by itself and for a better understanding of nuclear interaction properties, it is also important in order to reduce errors in neutrino oscillation measurements.

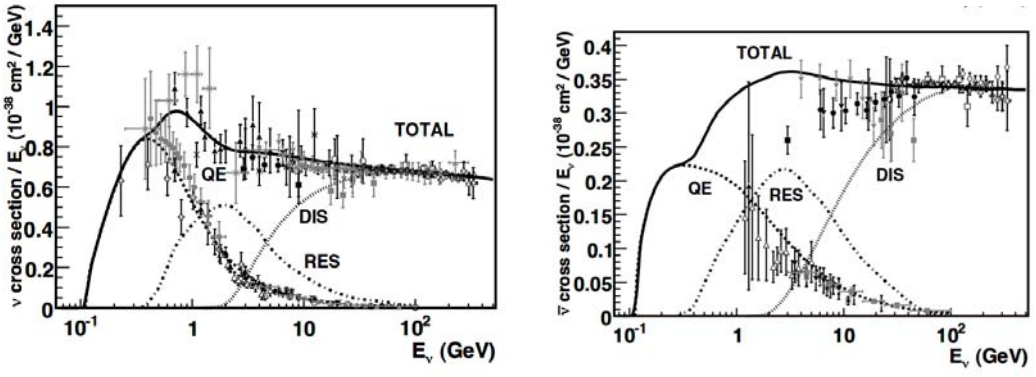

FIGURE 2.3: Total neutrino and anti-neutrino per nucleon CC cross sections (for an isoscalar target) divided by neutrino energy and plotted as a function of energy, from [3].

At low neutrino energies ($\sim$ 0.5-2 GeV), the generated resonance states are composed of isospin $\frac{1}{2}(N^*)$ and $\frac{3}{2}(\Delta)$ states. This Δ will typically decay into a nucleon and a pion.

Most of the Monte Carlo generators used in neutrino physics use the Rein and Sehgal model. The different Monte Carlo generators which use this model may differ in the range defined for the resonance contribution according to the invariant mass value and at higher values than this invarinat mass threshold defined is assumed the Bodek–Yang model for the DIS contribution.

Some other Monte Carlo generators use different models: MAID[13], Martini[14], Ghent[15] or Athar[16]. All these models provide different approaches to the single pion production which differs between each other and the Rein Sehgal on the different number of resonances taken into account, the inclusion or not of the quasielastic channel in the same scheme (Martini model), only consider the Δ and not the DIS contribution (for eaxmple, the Rein and Sehgal model add the DIS contribution).

The Rein-Sehgal Model of ν-induced Pion Production

The Rein-Sehgal (RS) model describes all ν and $\bar{\nu}$ induced pion production processes using an uniform framework [17], Figure 2.4.

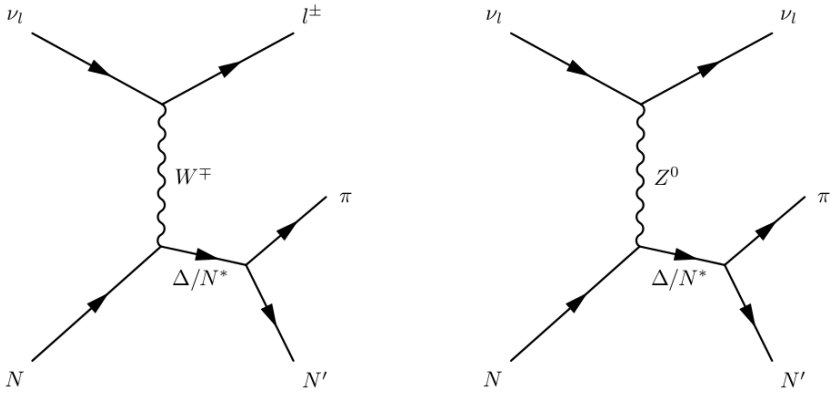

FIGURE 2.4: Neutrino CC and NC resonant Feynman's diagrams considered in the Rein and Sehgal model.

The interaction is splitted into:

$\nu + N \rightarrow l + N^*$
$N^* \rightarrow \pi + N'$

where N and N' are the nucleons and N^* is the baryon resonance. In this framework, all non-strange resonances below 2 GeV are combined, as well as the interference terms. In scattering off of free nucleons, there are seven possible resonant single pion reaction channels (seven each for ν and $\bar{\nu}$ scattering), three are charged current and four are neutral current. A total of 14 amplitudes of the different ν and $\bar{\nu}$ induced pion production

channels are produced. A small amount of isospin $\frac{1}{2}$ non-resonant background have been added incoherently in order to improve agreement with experimental data.

In case of the T2K experiment, the neutrino beam is mainly composed by ν_μ (when operatin in ν–mode, other wise the main component is $\bar{\nu_\mu}$, thus the total final hadronic states that are mediated by charged currents are:

$$\begin{array}{ll} \nu_\mu p \to \mu^- \Delta^{++} & \Delta^{++} \to p\pi^+ \\ \nu_\mu n \to \mu^- \Delta^{+} & \Delta^{+} \to p\pi^0,\ \Delta^{+} \to n\pi^+ \\ \bar{\nu_\mu} p \to \mu^+ \Delta^{0} & \Delta^{0} \to n\pi^0,\ \Delta^{0} \to p\pi^- \\ \bar{\nu_\mu} n \to \mu^+ \Delta^{-} & \Delta^{-} \to n\pi^- \end{array} \tag{2.1}$$

while the remaining 8 reaction channels, which are mediated by neutral current interactions, are:

$$\begin{array}{ll} \nu_\mu p \to \nu_\mu \Delta^{+} & \Delta^{+} \to p\pi^0,\ \Delta^{+} \to n\pi^+ \\ \nu_\mu n \to \nu_\mu \Delta^{0} & \Delta^{0} \to n\pi^0,\ \Delta^{0} \to p\pi^- \\ \bar{\nu_\mu} p \to \bar{\nu_\mu} \Delta^{+} & \Delta^{+} \to p\pi^0,\ \Delta^{0} \to n\pi^+ \\ \bar{\nu_\mu} n \to \bar{\nu_\mu} \Delta^{0} & \Delta^{0} \to n\pi^0,\ \Delta^{0} \to p\pi^- \end{array} \tag{2.2}$$

All these reaction amplitudes are expected to be dominant in the single pion interaction channel as long as the nucleon-pion invariant energy does not exceed $\sim 2GeV$ [17]. Above $\sim$ 2 GeV the formalism described in the model must be extended by including several interfering resonances which provide the single pion final state, due to simultaneus decay, at a fixed invariant energy.

We need to consider the sum of helicity amplitudes for all single resonances and the decay amplitude into the final state. We can write the invariant amplitude of the sum of helicity amplitudes as

$$T_{CC}(\nu N \to l N^*) = \frac{g^2 cos\theta_C}{8}[\bar{u_l}\gamma^\mu(1-\gamma^5)u_\nu]\left(\frac{g_{\mu\nu} - \frac{q_\mu q_\nu}{M_W^2}}{q^2 - M_W^2}\right)\langle N^*|J^\nu|N\rangle \tag{2.3}$$

$$T_{NC}(\nu N \to \nu N^*) = \frac{g^2 cos\theta_C}{8cos^2\theta_W}[\bar{u_l}\gamma^\mu(1-\gamma^5)u_\nu]\left(\frac{g_{\mu\nu} - \frac{q_\mu q_\nu}{M_Z^2}}{q^2 - M_Z^2}\right)\langle N^*|J^\nu|N\rangle \tag{2.4}$$

For the charged (CC) and neutral (NC) currents. With θ_W and θ_C are the weak mixing and Cabibbo angles respectively. The 4–momenta transfer of the interaction for W

(CC) and Z (NC) are given by $q = (E_q, \mathbf{q})$, with on-shell masses M_Z and M_W respectively. Since the Rein-Sehgal model is considering up to $|q^2| < 2GeV$ all terms that are proportional to $\frac{|q^2|}{M_{W,Z}}$ can be neglected. Since,

$$\frac{g^2}{8M_W^2} = \frac{G_F}{\sqrt{2}} \tag{2.5}$$

$$G = G_F cos\theta_C \sim G_F \tag{2.6}$$

$$\frac{M_W^2}{M_Z^2 cos^2\theta_W} \sim 1 \tag{2.7}$$

We can join equations 2.3, 2.4 in a single expression:

$$T(\nu N \to lN^*) = \frac{G}{\sqrt{2}}[\bar{u}_l \gamma^\mu (1-\gamma^5) u_\nu]\langle N^*|J_\nu|N\rangle \tag{2.8}$$

The leptonic current matrix element give us the polarization of the exchanged boson, $W^\pm$ or Z, in the interaction, and it can be expressed in terms of its right-handed, left-handed, and scalar components that are defined by the unit vectors:

$$e_L^\mu = \frac{1}{\sqrt{2}}(0, 1, -i, 0) \tag{2.9}$$

$$e_R^\mu = \frac{1}{\sqrt{2}}(0, -1, -i, 0) \tag{2.10}$$

$$e_0^\mu = (1, 0, 0, 0) \tag{2.11}$$

The leptonic matrix element is then calculated in the lepton Breit frame (LBF) [17] in which it is considered that the 3–momentum vectors of the leptons are anti-parallel along the z–axis. Then, neglecting the masses of the leptons, we obtain the leptonic current matrix as

$$\bar{u}_l \gamma^\mu (1-\gamma_5) u_\nu|_{LBF} = -2\sqrt{-2q^2 e_L^\mu} \tag{2.12}$$

For the remaining calculations is most convenient to adopt the frame of reference of the center of mass system of the outgoing hadrons (the resonance rest frame, RRF). In

this frame the nucleon, before the interaction, is traveling along the z–axis. This can be estimated using two Lorentz transformations. The first transformation connects the lepton Breit frame with the nucleon Breit frame (NBF) in which the incoming nucleon and outgoing resonance momenta are equal and opposite. Thus,

$$\bar{u_l}\gamma^\mu(1-\gamma_5)u_\nu|_{NBF} = -\sqrt{-2q^2}[(1-cosh\xi)e_R^\mu + 2sinh\xi e_0^\mu] \tag{2.13}$$

with

$$cosh\xi = \frac{(E_\nu^{lab} + E_l^{lab})}{|\mathbf{q}^{lab}|} \tag{2.14}$$

The second transformation is needed, along the z–axis to bring the resonance momentum to zero, to reach the RRF. Both e_L^μ and e_R^μ remain unaffected by this transformation and e_0^μ can be replaced with e_s^μ using the relation as follows

$$e_s^\mu = \frac{1}{\sqrt{-q^2}}(|\mathbf{q}^{RRF}|, 0, 0, E_q^{RRF}) \tag{2.15}$$

For simplification we define

$$u = \frac{E_\nu^{lab} + E_l^{lab} + |\mathbf{q}^{lab}|}{2E_\nu} \tag{2.16}$$

$$v = \frac{E_\nu^{lab} + E_l^{lab} - |\mathbf{q}^{lab}|}{2E_\nu} \tag{2.17}$$

$$Q^2 = -q^2 \tag{2.18}$$

Using these expressions we can write the leptonic matrix in the RRS framework as

$$\bar{u_l}\gamma^\mu(1-\gamma_5)u_\nu|_{RRF} = -2E_\nu^{lab}\sqrt{\frac{-2q^2}{|\mathbf{q}^{lab}|^2}}[ue_L^\mu - ve_R^\mu + \sqrt{2uv}e_s^\mu] \tag{2.19}$$

The energy dimension of the hadronic current, J_μ, is removed by factoring out the resonance mass,

$$F_\mu = \frac{J_\mu}{2M} \tag{2.20}$$

Components of the remaining portion of the current can be described using the same unit vectors as the lepton current,

$$\begin{aligned} F_+ = &\quad e_R^\mu F_\mu = \tfrac{-1}{\sqrt{2}}(F_x + iF_y) \\ F_- = &\quad e_L^\mu F_\mu = \tfrac{1}{\sqrt{2}}(F_x - iF_y) \\ F_0 = &\quad \sqrt{\tfrac{Q^2}{|\mathbf{q}^{RRF}|^2}} e_s^\mu F_\mu = F_t + \tfrac{E_q}{|\mathbf{q}^{RRF}|} F_z \end{aligned} \tag{2.21}$$

Combining the leptonic and hadronic currents we can derive the invariant amplitude as

$$T(\nu N \to lN^*) = -4GME[\sqrt{\frac{Q^2}{|\mathbf{q}|^2}}\langle N^*|uF_- - vF_+|N\rangle + \frac{m_N}{M}\sqrt{2uv}\langle N^*|F_0|N\rangle] \tag{2.22}$$

The invariant amplitude is then used to extract the differential cross section

$$\frac{\partial\sigma}{\partial Q^2 \partial E_q} = \frac{1}{64\pi m_N E_\nu^2} \sum_{spins} |T(\nu N \to lN^*)|^2 \frac{1}{2\pi} \cdot \frac{\Gamma}{(W-M)^2 + \Gamma^2/4} \tag{2.23}$$

the last factor is the Breit-Wigner function for a resonance of mass M, width Γ and observed mass W.

All resonances that contribute to the interaction process must be included in the calculation. The relevant resonances for each process are determined by the isospin conservation. The $CC\pi^+$ events can have two different final states: $(\mu^-, \pi^+, proton)$ and $(\mu^-, \pi^+, neutron)$, which depends on the target nucleon.

And the Clebsch-Gordan coefficients for each final state, $|I, I_3\rangle$, give

$$\begin{aligned} |\pi^+ p\rangle = &\quad |1,1\rangle \otimes |\tfrac{1}{2}, \tfrac{1}{2}\rangle = \quad |\tfrac{3}{2}, \tfrac{3}{2}\rangle \\ |\pi^+ n\rangle = &\quad |1,1\rangle \otimes |\tfrac{1}{2}, -\tfrac{1}{2}\rangle = \quad \sqrt{\tfrac{1}{3}}|\tfrac{3}{2}, \tfrac{1}{2}\rangle + \sqrt{\tfrac{2}{3}}|\tfrac{1}{2}, \tfrac{1}{2}\rangle \end{aligned} \tag{2.24}$$

Where states of isospin $\frac{3}{2}$ refers to the Δ resonances and the isospin $\frac{1}{2}$ states refers to the N resonances.

For the helicity amplitudes, from equation 2.22:

$$f_\pm = \langle N, j_z \pm 1|F_\pm|N^*, j_z\rangle \tag{2.25}$$

$$f_0 = \langle N, j_z|F_0|N^*, j_z\rangle \tag{2.26}$$

These coeficients are provided by the Feynman-Kislinger-Ravndal (FKR) relativistic quark model [18]. The FKR model represents hadrons as relativistic harmonic oscillators of their quark component. For baryons, the Hamiltonian is described by

$$\mathcal{H} = 3(p_a^2 + p_b^2 + p_c^2) + \frac{\Omega^2}{36}((u_a - u_b)^2 + (u_b - u_c)^2 + (u_c - u_a)^2) + C \tag{2.27}$$

where p_a and u_a correspond to the 4-momentum and 4-position of quark a. Using 3 parameters, the spacing of energy levels per unit angular momentum (Ω), the pseudo-scalar meson coupling to hadrons and a scaling factor as a function of energy, and in addition to the particle masses, 75 different transition amplitudes were calculated.

The FKR model is then extended to calculate pion production cross sections for all the nuclear resonances that are below 1.75 GeV[19]. This formulation makes use of separate vector and axial vector form factors. Being m_V and m_A the mass parameters respectively.

$$G^V(Q^2) = \left(1 + \frac{Q^2}{4m_N^2}\right)^{\frac{1}{2-n}} \left(\frac{1}{1 + Q^2/m_V^2}\right)^2 \tag{2.28}$$

$$G^A(Q^2) = \left(1 + \frac{Q^2}{4m_N^2}\right)^{\frac{1}{2-n}} \left(\frac{1}{1 + Q^2/m_A^2}\right)^2 \tag{2.29}$$

where n is the number of oscillator quanta in the final resonance. The vector mass, m_V, is measured by electron scattering experiments to be 0.84 GeV [20].

The only remaining uncertain quantitties in the determination of the $CC\pi^+$ cross section are the nucleon axial mass m_A (determines the strength of the interaction process) and the axial form factor, $C_5^A(0)$, which depends on Q^2, and they can only be measured in neutrino experiments.

Coherent $CC\pi^+$ Interactions

In addition to the resonant interactions, neutrinos can interact with the entire target nucleus coherently, Figure 2.5. Coherent processes can occur in both neutral and charged current interactions, always the target nucleus is unchanged.

$$NC \Rightarrow \nu + A \rightarrow \nu + \pi^0 + A$$
$$CC \Rightarrow \nu + A \rightarrow l^- + \pi^+ + A$$

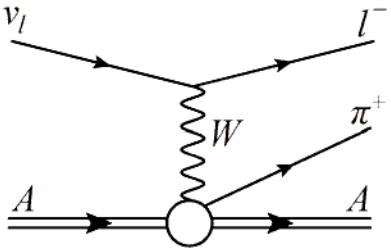

FIGURE 2.5: Neutrino CC Coherent pion Feynman's diagrams considered in the Rein and Sehgal model.

Coherent interactions are not well understood when compared to the analogous resonant processes. Several models exist that describe coherent pion production[21][22] [23], but the absolute cross sections predicted by these models can vary by an order of magnitude. In addition, both K2K and SciBooNE experiments have measured a deficit of coherent $CC\pi^+$ events, well below predicted levels [24][25], while similar deficits are not observed in neutral current coherent π^0 production[26]. More recent measurements, published by the $MINER\nu A$ experiment[27] found the kinematic of the outgoing pion in poor agreement with the expectation based on the neutrino event generators NEUT and GENIE. Latest results from T2K showed similar discrepancies in the coherent channel[28].

2.2.1.3 Nuclear Effects

The neutrino-nucleon interactions described above are developed when considering free nucleon. Neutrino scattering experiments are conducted in nuclear media. The properties of the free nucleon interactions described by the RS model are modified by taking into account the initial state and several nuclear effects (final state interaction effects, FSI): the nuclear binding, the particle motion and the screening of internal nucleons by particles on the surface of the nucleus. In addition to that, once an interaction occurs the outgoing final state particles should traverse the nuclear medium before they can be detected. The particles can interact with the nuclear medium, thus modifying the observed characteristics of the interaction. The final kinematics of the outgoing particles can as well be altered (i.e. loss of energy and direction altered when crossing the nuclear medium) and then the meaning of a measured cross section.

Pions are particularly susceptible to the effects of the nuclear medium, since they interact via the strong nuclear force. Charged pions can either be absorbed or converted into neutral pions via $n\pi^+ \rightarrow p\pi^0$. The nuclear medium can also influence whether a pion is even created. When a nucleon is excited into a $\Delta(1232)$ resonance, the Δ travels on the order of 1 fm before it decays, which is a significant fraction of the size of the nucleus. The Δ can then interact via $\Delta N \rightarrow NN$, which reduces the number of observed pions.

Multi-nucleon effects are also present in single pion production processes. It occurs when the $W^{\pm}$ that conducts the process interacts with more than one nucleon.

Finally, as the target nucleons are in a bound state, some energy is dissipated in liberating the interacting nucleon. Both Pauli blocking and nuclear binding have the effect of reducing the number of interactions at low Q^2.

Considering the above discussion, the validity of the Rein-Sehgal model predictions for neutrino interactions with bound nucleons is not clear. The FKR predictions for transitions to higher resonances are not obviously valid bound nucleons. Additionally, the modification to the masses and widths of the resonances due to the nuclear medium are not accounted for in the model.

2.2.1.4 When the Single Pion is Breaking Bad

Now we know that neutrino charged current single pion production it's a difficult channel to understand from a theoretical point of view. But we have to add the difficulties of the measurement in a real experiment. There is plenty of literature on $\nu - CCQE$ cross section measurements, as well as for CC inclusive measurements. In a minor number of papers we can find $CC\pi^+$ publications, accompanied by the brainteaser.

One of the most recent and famous publications has been the MiniBooNE $CC\pi^+$ cross section analysis [29]. This result was already in disagreement with the Monte Carlo generator used for the measurement (NUANCE) and is still not understood. This result has been used to constraint cross section parameters in the main Monte Carlo generator used in T2K, NEUT. Different theoreticians tried to fit MiniBooNE data with their models but surprisingly, in most of the cases, when adding final state interaction (FSI) effects disagreements increase.

The last publication on $CC1\pi^+$ is the one provided by the $MINER\nu$A experiment[30]. This last measurement also disagrees with respect to expected values from Monte Carlo generators (with the already provided fits to MiniBooNE data) and provides a very interesting differential measurement on pion angular variable.

There is a necessity on more data for $CC1\pi^+$ events and a more challenging analysis in order to understand better our models, the discrepancies and give some hint in order to improve the current modelization.

2.2.2 The neutrino Monte Carlo generator: NEUT

Different Monte Carlo generators are widely used in neutrino experiments. The neutrino interactions at T2K are simulated using the NEUT neutrino interaction generator [31]. NEUT is a program library that was originally developed to study interactions of the atmospheric neutrinos and estimate the detection efficiency of nucleon decay with the water Cerenkov detector KamiokaNDE. NEUT the neutrino energy range from several tens of MeV to hundreds of TeV. The NEUT release used in the analysis presented is NEUT 5.1.4.2, and is the one described in this Section. In NEUT, the relativistic Fermi gas model by Smith and Moniz [**?**] is used to calculate the cross section off nucleons in the nucleus.

The following neutrino interactions and models [3] are considered in NEUT:

1. *Charged/Neutral current (quasi-)elastic scattering.* ($\nu N \rightarrow lN'$)
   - Model based on the Llewellyn–Smith [**?**] model. M_A^{QE} is set to $1.2 GeV/c^2$.
2. *Charged/Neutral current single π production.* ($\nu N \rightarrow lN'\pi$)
   - Model based on the Rein and Sehgal's method. In total, 18 resonances below $2GeV$ are taken into account and the axial–vector (M_A^{RES}) is set to $1.2 GeV/c^2$. The pion–less Δ–decay is considered as well and 20% of the events do not have a pion in the final state.
3. *Charged/Neutral current single γ production.* ($\nu N \rightarrow lN'\gamma$)
4. *Charged/Neutral current single K production.* ($\nu N \rightarrow lN'K$)
5. *Charged/Neutral current single K production.* ($\nu N \rightarrow l\Lambda K$)
6. *Charged/Neutral current single η production.* ($\nu N \rightarrow lN'\eta$)
7. *Charged/Neutral current deep inelastic scattering.* ($\nu N \rightarrow lN'$hadrons)
8. *Charged/Neutral current coherent π production.* ($\nu^{16}O \rightarrow l\pi$X)
   - Model based on the Rein and Sehgal's method.

where N and N' are the nucleons (proton or neutron), l is the lepton, and X is the remaining nucleus.

[3] We only especify the CCQE and CC1Pion model used by NEUT which are of the most important for both analysis described in Chapters 5 and 6.

Interaction of pions, kaons, etas and nucleons in the target nucleus are simulated in NEUT using a cascade model with small differences for each kind of hadron.

Pion interaction is also simulated, considering inelastic scattering, charge exchange and absorption processes, as well as particle production for the high energy pions. The nucleon re–scattering in the nucleus is simulated with a similar cascade model as the one used for the pion interaction simulation. The processes considered are: elastic scattering and a single or two Δ production for the pion production. Probabilities of these FSI processes are extracted from existing data from other experiments.

2.2.2.1 Some other neutrino event Monte Carlo generator

There are several Monte Carlo generators used to simulate neutrino events. Here we just mention few of them and try to stress main differences respect to NEUT, for the CCQE and single pion production.

GENIE GENIE is very similar to NEUT. It uses the same modelling for CC(NC)(Q)E interactions, which only differs on the treatment of the nuclear effects. While NEUT only applies the Fermi Gas approaximation, GENIE uses a Bodek-Ritchie approach and adding some spectral function effect.

For the single pion production, GENIE uses the Rein and Sehgal model with 16 resonances, some parameters differs since most updated data is used in GENIE. As well, an hadronic formation zone effect is considered. The resonance region is establish to be below 1.7 GeV for the invariant mass.

The coherent pion production is based on the Rein and Sehgal model, while GENIE has more updated parameters with experimental data.

NuWro NuWro uses the same strategy as NEUT and GENIE, all of them use the Fermi Gas model implemented with a cascade model. Also for the CC(NC)(Q)E channel, NuWro relies on the Smith-moniz model, as NEUT and GENIE. The main difference is that NuWro has implemented an spectral function in order to prevent inconsistencies with data at low Q^2.

For the single pion production, NuWro only include the Δ resonance. The Δ form factors are extracted from ANL and BNL data. Some nuclear effects are also added.

GiBUU GiBUU is probably the most complete Monte Carlo neutrino event generator, but using the full potential of this Monte Carlo needs a huge amount of time.

GiBUU add corrections in the QE channel for the momentum and the density potential of the nucleons in the nucleus. Fermi motion is included in a local density aproximation. It is considered the full in–medium kinematics.

For the single pion production, GiBUU only include 13 resonances. The vector form factos use the MAID method of electron data. Fermi motion is included in a local density aproximation. FSI effects are included using several scattering data.

Some other neutrino interaction models There are more models as the "Martini" or "Nieves" models which are also compared by the different experiments. Some of these models are being added to the different neutrino Monte Carlo generators in order to provide more precise estimation of the neutrino interaction caracterization.

We do not enter into the details of models. The development of these models start mainly with the aim to simulate the so–called MEC (meson ex–change current) events and ssome other nuclear effects still not included by the main Monte Carlo generators.

Most of these models include some MEC channels as the "2p-2h" (two particles two holes) or also RPA (random phase approximation) corrections. this is the case of the "Martini" and "Nieves" models.

Currently, NEUT have implemented the "nieves" model for the "2p-2h" channel and incorporation of the RPA is being studied. At the level of the analysis presented in Chapters 5 and 6 these implementations were still not applied.

Chapter 3

T2K Long–Baseline Neutrino Oscillation Experiment

T2K (Tokai to Kamioka) is a Long–Baseline Neutrino Oscillation Experiment located in Japan [5]. The Japan Proton Accelerator Research Complex (J–PARC) produces a high intensity and pure ν_μ beam that is characterized in the near detector complex before it reachs the far detector Super–KamionaNDE (Super–Kamioka Neutrino Detection Experiment, Section 3.3) where the oscillated beam is measured.

The overview of the experimental setup is shown in Figure 3.1.

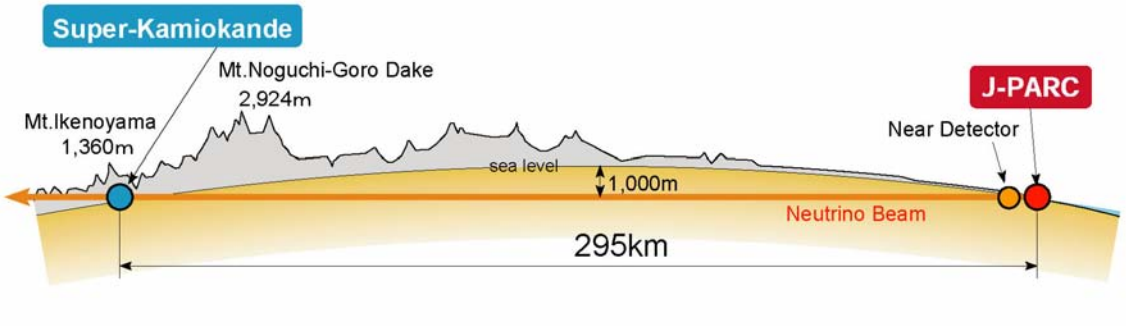

FIGURE 3.1: Schematical view of the T2K experiment in Japan. Neutrinos are produced in Tokai, detected at a near detector prior to the far detector, Super–KamiokaNDE in Kamioka.

The primary goal of T2K is the precision measurement of neutrino oscillations by:

1. The measurement of $sin^2\theta_{13}$ by searching for $\nu_\mu \rightarrow \nu_e$ appearance.
2. The precise measurements of $sin^2 2\theta_{23}$ and Δm^2_{23} searching for ν_μ disappearance.

3. New constraints on the θ_{23} octant, mass hierarchy and δ_{CP} degenerate parameter space.

4. Indirect confirmation of $\nu_\mu \rightarrow \nu_\tau$ oscillation though NC measurements.

The T2K experiment is the first neutrino experiment using an *off-axis* technique, whereby the Super–KamiokaNDE detector and one of the near detectors (ND280, Section 3.2.1) are both located $\sim 2.5^o$ off the neutrino beam axis. This modify the neutrino energy spectrum increasing the neutrino flux at the first oscillation maximum for the ν_μ disappearance and reducing the flux at high energies, resulting in a narrow band beam. This increases the number of CCQE–like signal events at Super–KamiokaNDE and also reduces the expected background events due to the high energy neutrinos. The T2K near detectors, INGRID and ND280, with main purpose of reducing systematic uncertainties on the T2K oscillation analysis, are used as well to measure neutrino cross sections in the intermediate energy region ($\sim 1GeV$) [32], [33], [34], [35].

In this Chapter we describe the different components of the T2K experiment setup. The proton accelerator and the neutrino beamline are decribed in Section 3.1, the on–axis near detector (INGRID) is briefly described in 3.2 . An overview of the off–axis near netector ND280 is described in Section 3.2.1 and finally the far detector Super–KamiokaNDE is described in Section 3.3.

3.1 The T2K Neutrino Beam

The T2K neutrino beam is produced at J–PARC (located in Tokai in the Ibaraki prefecture) from the collision of 30 GeV protons with a graphite fixed target. The resulting charged particles from the collision (pions and kaons) in the hadronic showers are focused by a set of magnetic horns and then they decay in flight, in a $\sim 96m$ Helium tunnel, to neutrinos and muons. These muons decay into neutrinos and electrons.

An schematic drawing of the neutrino production beam–line is shown in Figure 3.2.

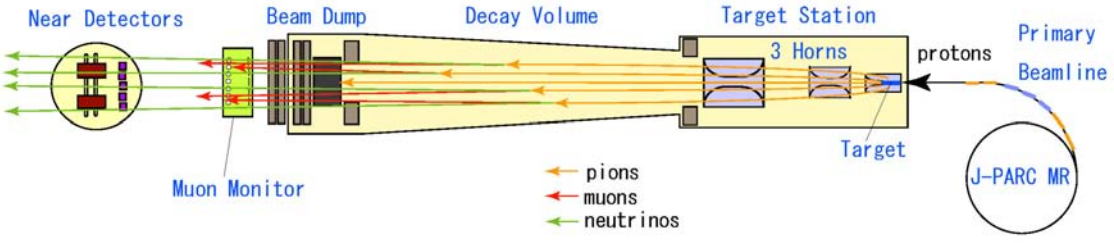

FIGURE 3.2: Schematical of the neutrino production beam–line. The neutrino beam is produced from the collision of 30 GeV protons.

A horn system focuses hadrons of a positive (or negative, depends on the beam mode used) charge reducing the contamination of $\bar{\nu}_\mu$ (ν_μ). A beam dump stops most of the resulting particles that are not neutrinos.

In Figure 3.3 an overview of J–PARC is shown, only the dedicated sections inside J–PARC to neutrino experiments are shown. We can distinguish three main parts: the proton beam accelerator complex, the primary neutrino beamline after proton extraction and the secondary neutrino beamline that includes the target station.

FIGURE 3.3: Overview of the part of J–PARC dedicated to neutrino experiments. Including the system of proton accelerators, the ν beamline and ND280.

3.1.1 The Proton Beam Accelerator Complex

The proton beam accelerator complex at J–PARC is composed by: a linear accelerator (LINAC), a rapid–cycling synchrotron (RCS) and a main ring (MR) synchroton.

In the LINAC, an H^- beam is accelerated up to 400 MeV [7] and is converted to an H^+ beam by charge–stripping foils at the RCS injection point. The beam is accelerated up to 3 GeV by the RCS with 25 Hz cycles. The proton beam, once injected into the MR, is accelerated up to 30 GeV. The MR can deliver a *spill* up to 8 *bunches* of protons [8]. There are two extraction points in the MR: slow extraction for the hadron beamline and fast extraction for the neutrino beamline. In the fast extraction, which is used by the neutrino facility, the 8 circulating proton bunches are extracted within a single turn by a set of 5 *kicker* magnets [9].

The time structure of the structed proton beam is key to discriminatating various backgrounds, including cosmic rays, in the various neutrino detectors. The MR machine parameters for the fast extraction are given in Table 3.1.

Circumference	1567 m
Beam power	$\sim$ 750 kW
Beam kinetic energy	30 GeV
Beam intensity	$\sim 3 \times 10^{14} p/spill$
Spill cycle	$\sim$ 0.5 Hz
Number of bunches	6 or 8/spill
RF Frequency	1.67-1.72 MHz
Spill width	$\sim 5\ \mu sec$

TABLE 3.1: Design parameters of the J-PARC main ring synchrotron [5].

3.1.1.1 Primary Neutrino Beamline

Once the protons are extracted from the main ring, they are directed into the primary beamline towards the near detectors and Super–KamiokaNDE (SK). In the primary beamline we can distinguish a preparation, arc and final focusing sections, as shown in Figure 3.4, it is also shown the monitor locations.

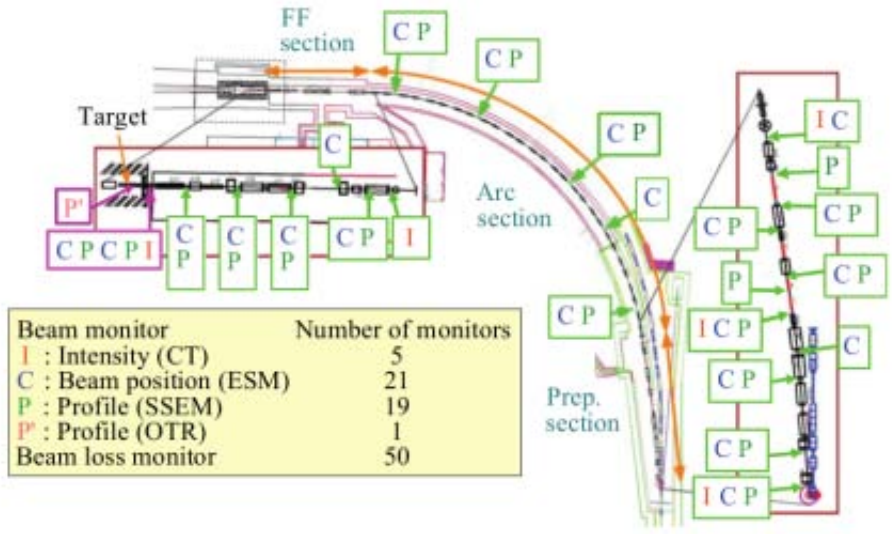

FIGURE 3.4: Overview of the primary neutrino beamline including location of the primary beamline monitors.

For the preparation and final focusing (FF) normal conducting magnets are used, while in the arc section superconducting magnets are used to guide and focus the proton beam.

[7] Currently at 181 MeV.
[8] The harmonic number of the MR is nine, and the number of bunches in the MR is eigth.
[9] *kicker* magnets are dipole magnets used to *kick* an incoming particle beam into a synchroton.

Several monitors all along the primary beamline provide information about the beam to optimize the magnet tuning. Such monitoring aim to minimize beam losses and to precisely control the final beam direction. Electrostatic Monitors (ESMS) measure the beam position while Segmented Secondary Emission Monitors (SSEMS) measure the whole beam profile at points along the beamline. Finally, current transformers (CTs) provide measurements of the number of protons in each bunch. The final uncertainty on the proton beam intensity is of 2.6% [1].

The information coming from all the beam monitors are then used to optimize the magnet currents and thus maximize the delivered protons–on–target (PoT). The monitoring allow also to precisely steer and control the beam profile at the target. That is important for target protection, as well as to ensure the beam stability of direction.

3.1.1.2 Secondary Neutrino Beamline

The protons collide with the neutrino production target in the secondary beamline where the resulting hadrons are focused and decay into neutrinos. The secondary beamline consists of a target station (TS), a decay volume, a beam dump and a muon monitor. A side view of the secondary neutrino beamline is shown in Figure 3.5.

The target station contains an helium vessel which houses the neutrino production target and magnetic horns to focus the hadrons produced by the proton–target collisions. The horns are protected from stray protons by an upstream collimator. Immediately upstream of the target, an Optical Transition Radiation (OTR) monitor provides the final measurement of the proton beam profile.

Protons from the primary beamline enter the TS through a titanium-alloy beam window separating the vacuum in the primary beamline from the helium vessel. The protons strike a $1.8 g/cm^3$ solid graphite target, 91.4 cm long (1.9 interaction lengths) and 2.6 cm in diameter. The target is encased by titanium and cooled by flowing helium gas.

The proton beam position[2] and direction at the target need to be measured with an accuracy of 1 mm and 0.5 mrad, respectively. A measurement of the beam size (of about 10% of resolution) near the target also facilitates target protection and minimization of

[1] Beam power is used to be reported as:

$$P[W] = n_p f_{rep}[Hz] E[J] \tag{3.1}$$

where n_p is the number of protons per spill, f_{rep} is the repetition rate or spill cycle as in Table 3.1 and E is the proton beam energy.

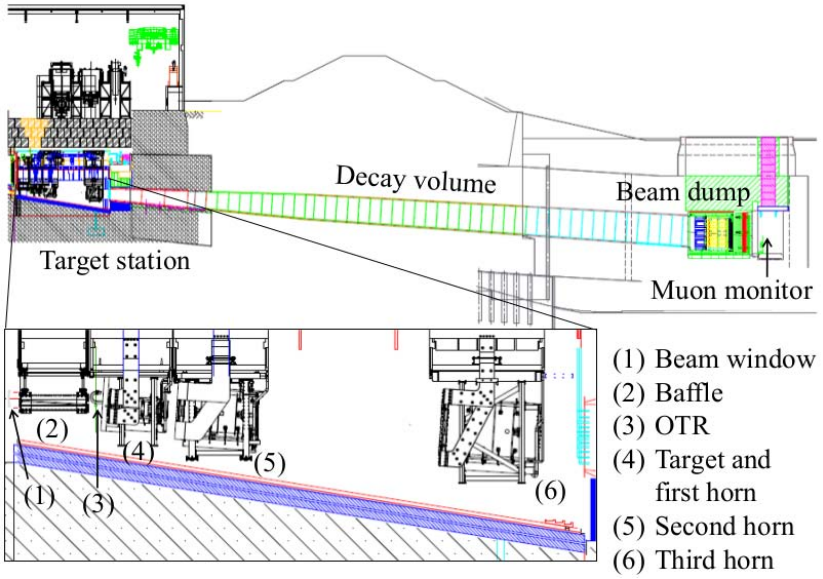

FIGURE 3.5: Side view of the secondary neutrino beamline. The proton beam travels from the left to the right and passes through the OTR monitor downstream of the collimator (baffle) before colliding with the target. The horns focus the resulting charged particles (mostly π and K), which decay in the decay volume to produce neutrinos. Any remaining hadrons and some muons are absorbed by the beam dump. Higher energy penetrating muons are measured by the muon monitor.

beam loss. The OTR has been instrumented to achieve this goal since it can work at high radiation zones.

The positively charged secondary particles, from proton interactions in the target, are collected and focused by three magnetic horns in order to maximize the resulting neutrino flux [36]. Each horn is made from aluminum inner and outer conductors, which are pulsed with 250 kA to provide a toroidal magnetic field in time with the proton beam arrival. The field can be reversed by reversing the applied current, and then focusing negative particles and obtaining a primarily anti-neutrino beam instead of a neutrino beam. The secondaries decay in a $\sim$ 100 m long decay volume, attached to the helium vessel downstream of the third horn. When the horn is run with an operation current of 320 kA, the maximum field is 2.1 T and the neutrino flux at Super–KamiokaNDE is increased by a factor of $\sim$ 16 (compared to horns at 0 kA) at the spectrum peak energy ($\sim$ 0.6 GeV).

A 75 ton (1.7 g/cm^3) graphite beam dump, 1.94 m wide, 3.174 m long, and 4.69 m high, is placed at the end of the decay volume. Iron plates with a thickness of 2.40 m are placed at the downstream side of the beam dump. The graphite and the iron plates are both used to stop muons and any remaining hadron coming from the the proton–target interaction with momentum below $\sim 5GeV/c$. More energetic muons

[2] A translation of the proton beam from the center of the target–horn axis results in a shift of the resulting neutrino beam direction.

are instead measured *bunch-by-bunch* with a muon monitor (MUMON) consisting of ionization chambers and silicon photodetectors to further measure the neutrino beam direction.

3.1.2 The *Off–Axis* Configuration

For any neutrino oscillation experiment is fundamental the reconstruction of the neutrino energy. In the T2K experiment, due to the optimal characteristics of Super–KamiokaNDE to reconstruct neutrino charged current quasi–elastic processes (Section 2.2.1), a narrow neutrino energy spectrum is required.

Before T2K, the neutrino beams used for studying the phenomenon of neutrino oscillation were working at a broad energy spectra of the beam. The neutrino energy spectrum and the magnitude of the flux depend on the angle of emission of the neutrino relative to the decaying pion beam. A detector can be placed off–axis to observe a pseudo–mono–energetic beam [37]. This can be derived from the kinematics of the 2–body decay of pions. The outgoing neutrino 4–momentum is given by:

$$p_\nu = (E_\nu, E_\nu sin\theta, 0, E_\nu cos\theta) \tag{3.2}$$

$$p_\nu = (\gamma E_\nu^{CM}(1 + \beta cos\theta^{CM}), E_\nu^{CM} sin\theta^{CM}, 0, \gamma E_\nu^{CM}(\beta + cos\theta^{CM})) \tag{3.3}$$

being E_ν the neutrino energy, θ the angle between the neutrino and the pion direction and the index CM is used to define the same variables but in the centre–of–mass frame. Equation 3.3 relates the CM frame to the laboratory frame (Equation 3.2) by a Lorentz boost with $\gamma = \frac{E_\pi}{m_\pi}$ and $\beta = v_\pi/c$, being E_π, m_π and v_π respectively the energy, mass and velocity of the pion. Taking the ratio of the second and the fourth component of the 4–momenta we found the angular relation following

$$tan\theta = \frac{E_\nu^{CM} sin\theta^{CM}}{\gamma E_\nu^{CM}(\beta + cos\theta^{CM})} \approx \frac{E_\nu^{CM} sin\theta^{CM}}{E_\nu} \tag{3.4}$$

on the last approximation we assume $\beta \approx 1$ for $E_\pi \gg m_\pi$. Since $|sin\theta^{CM}| < 1$, the maximum allowed angle for a given neutrino energy E_ν is:

$$tan\theta^{max} = \frac{E_\nu^{CM}}{E_\nu} = \frac{29.8\text{MeV}}{E_\nu} \tag{3.5}$$

with $E_\nu^{CM} = (m_\pi^2 - m_\mu^2)/2m_\pi = 29.8$ MeV. And the maximum neutrino energy for a given off–axis angle θ is:

$$E_\nu^{max} = \frac{29.8\text{MeV}}{tan\theta} \tag{3.6}$$

The dependency of the neutrino energy on the pion energy is then given by

$$E_\nu = \frac{(1 - m_\mu^2/m_\pi^2)/E_\pi}{1 + \gamma^2 tan\theta^2} \tag{3.7}$$

The relation described in Equation 3.7 is shown in Figure 3.6 (left), which shows the neutrino energy dependence on pion energy for on–axis and two different off–axis angles. The dotted lines show the maximum achievable neutrino energy as given by Equation3.7

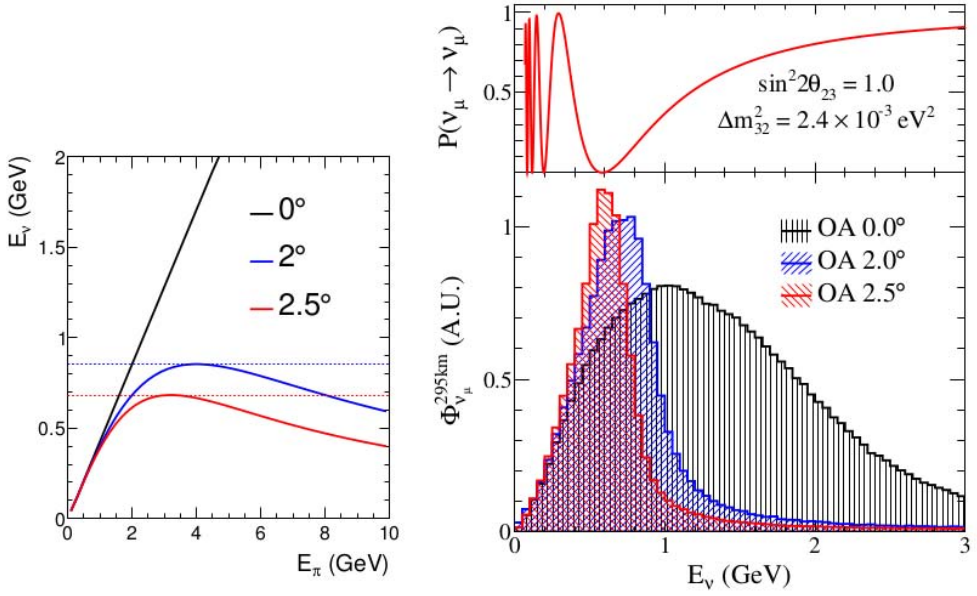

FIGURE 3.6: Left: Neutrino energy dependence on decaying pion energy for the three angles, one on–axis and two off–axis. Top right: ν_μ survival probability as a function of the neutrino energy with L = 295 km (T2K baseline). Bottom right: the T2K neutrino flux spectrum prediction for the three angles calculated [1].

As shown in Figure 3.6(bottom right), by going off–axis the high energy tail of the ν spectrum is strongly reduced, giving a energy spectrum narrow band, being the angular value of 2.5° the most narrowed on energy. For the T2K experiment, an off–axis angle of 2.5° was chosen such a way the peak of the neutrino energy spectrum coincides with the first ν_μ disappearance (and ν_e appearance) maximum (Figure 3.6, top right). That was motivated by the previous measurements of Δm_{32}^2 by SK[38] and K2K[39]. The supression of the high energy tail thanks to the off–axis strategy helps to reduce the contributions from neutral current interactions. Neutral current π^0 events are the main

source of background for the identification of ν_e events at Super-KamiokaNDE, then, one of most important backgrounds from ν_e appearance channel.

3.1.3 The Neutrino Beam Composition

When the protons hit the carbon target, charged pions and kaons are produced. Those hadrons decay to neutrinos according to the branching ratios given by Table 3.2. The 99.4% of the neutrino beam comes directly from secondaries or tertiary charged pions while the 5.4% comes from charged kaons. Neutrinos coming from neutral kaons are a negligible component. The neutrino flux is dominated at the peak by the pion component while the kaons form the high energy tail. We can see that ν_μ is the dominant component of the resulting beam (Figure 3.7).

Particle	Decay channel	Branching ration/%)
pi^+	$\rightarrow \mu^+\nu_\mu$	99.9877
	$\rightarrow e^+\nu_e$	1.23×10^{-4}
K^+	$\rightarrow \mu^+\nu_\mu$	63.55
	$\rightarrow \pi^0\mu^+\nu_\mu$	3.353
	$\rightarrow \pi^0 e^+\nu_e$	5.07
K^0_L	$\rightarrow \pi^-\mu^+\nu_\mu$	27.04
	$\rightarrow \pi^- e^+\nu_e$	40.55

TABLE 3.2: Branching ratios for the meson decays that yield neutrinos.

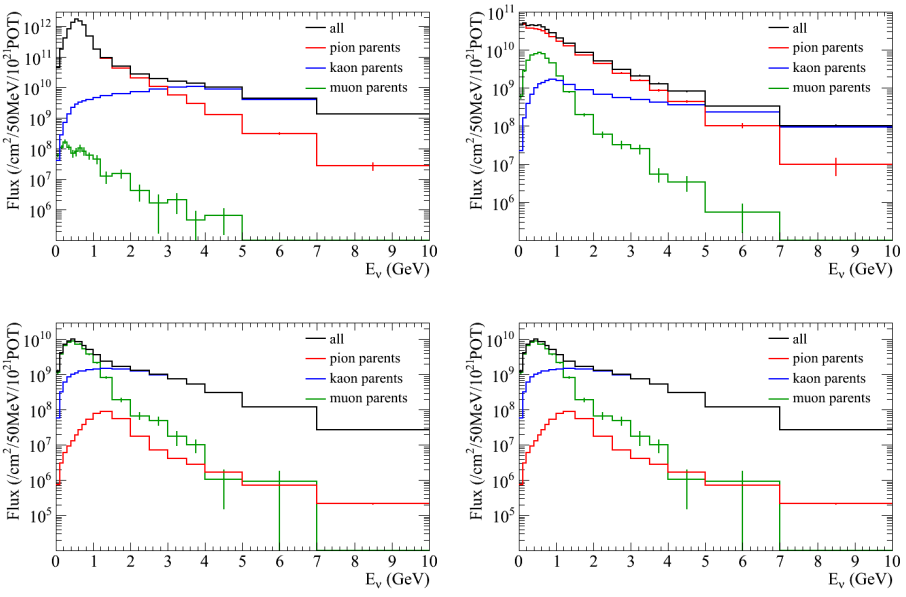

FIGURE 3.7: Neutrino parent prediction by flavor. Top Left: ν_μ parent. Top rigth: $\bar{\nu}_\mu$ parent. Bottom left: ν_e parent. Bottom right: $\bar{\nu}_e$ parent.

Nevertheless, the beam is not made of pure ν_μ since some negative mesons are not sufficiently defocused by the horns and they decay mainly in $\bar{\nu}_\mu$ according to the conjugated channels of Table 3.2. $\bar{\nu}_\mu$ are then the second component of the T2K neutrino flux, being of about the 6.2% of the total flux. Finally, a 1.1% of ν_e and a 0.1% of $\bar{\nu}_e$ are expected. Figure 3.8 shows the T2K beam expected flux, predictions are based on the NA61/SHINE3.1.3.2 π, K production measurements and T2K proton beam measurements.

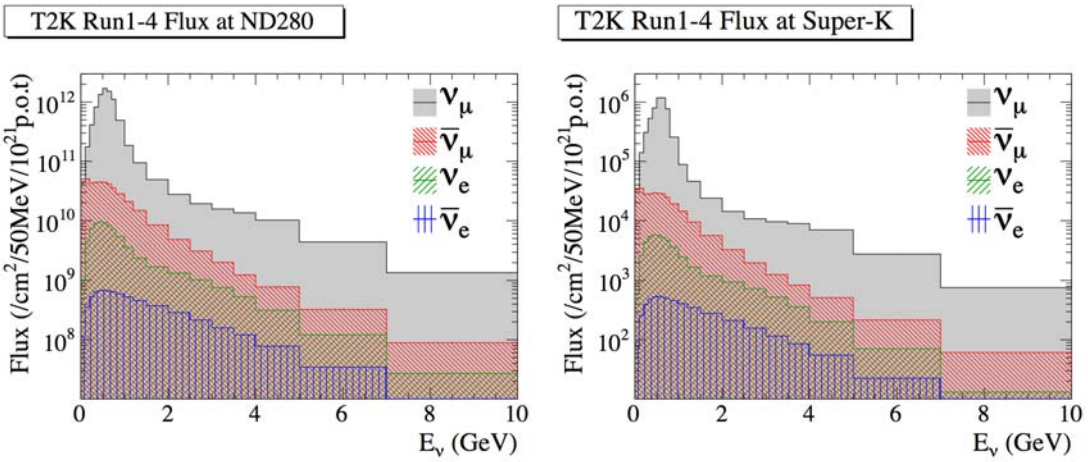

FIGURE 3.8: Neutrino flux distributions in neutrino energy predicted at ND280 (left) and SK (right). the colors show the contribution of each neutrino family.

3.1.3.1 The Neutrino Flux Prediction

The neutrino flux at INGRID, ND280 and SK is predicted by a Monte Carlo simulation based on experimental data. The full secondary beamline is simulated by the beam Monte Carlo developed by the T2K Collaboration. To simulate interactions inside the graphite target and the baffle FLUKA[40] is used. The kinematic information of the particles emitted from interaction with the target is transferred to the JNUBEAM program[41] which simulates the neutrino production from the hadron decays. JNUBEAM simulates propagation of the outgoing hadrons through the secondary beamline until the detectors, including hadron secondary interactions outside the target using the GEANT3/GCALOR software[42].

In neutrino experiments flux uncertainties are usually the dominant ones. This is mainly due to the limited knowledge we have on the hadron production at the working energies. As we have already seen (Figure 3.7) flux and energy are related to the neutrino hadronic parent (at each neutrino flavor). In order to reduce the flux errors the T2K collaboration use external data to constraint the hadron production. The FLUKA simulation is tuned by the results coming from the NA61/SHINE experiment. A small component of the

flux uncertainty (under 3%) comes from errors in the beam alignment. The size of this uncertainty is keep under control thanks to the INGRID monitoring.

The neutrino flux is also measured together with the neutrino cross section by ND280 using the ν_μ events (as it will be described in Chapter 5). This reduces the latter measurement error in the neutrino flux from 20% to about 10%.

3.1.3.2 The NA61/SHINE Experiment

The NA61/SHINE[43] (SPS Heavy Ion and Neutrino Experiment) is a multi–purpose facility to study hadron production in hadron–proton, hadron–nucleus and nucleus–nucleus collisions at the CERN Super Proton Synchrotron (SPS). It performs precise hadron production measurements at the same proton energy as T2K using a thin target and a replica of the T2K target to improve the knowledge of the initial neutrino beam flux. The layout of the NA61/SHINE detector is showed schematically in Figure 3.9.

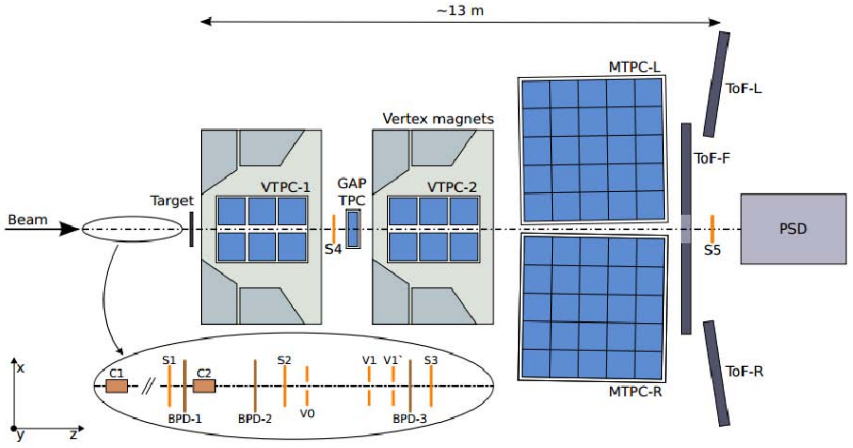

FIGURE 3.9: Schematic view of the NA61/SHINE detectors.

The phase–space of interest for T2K is fully covered by the NA61/SHINE experiment. It provides results for the pion[44],[45] and the kaon[46] interaction cross sections. Then, the T2K simulated flux is tuned according to this. Thanks to this external data the neutrino flux errors are reduced to $10\% - 15\%$ as we see in Figure 3.10. The largest contribution comes from the hadron production. The uncertainty on the ratio of the flux predictions at the far and near detectors is less than 2% around the peak.

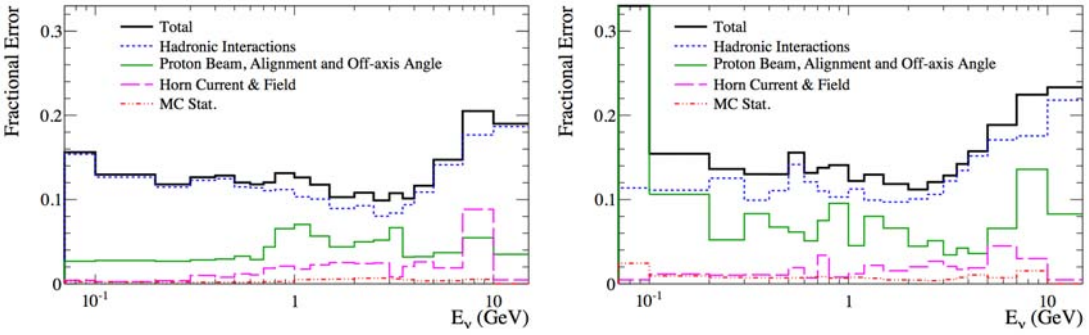

FIGURE 3.10: Neutrino flux uncertainty at ND280 as a function of the neutrino energy evaluated with the NA61 experiment and the T2K beam monitor, for ν_μ (left) and ν_e (right). The breakdown of the different error components is shown. Hadron production uncertainty is the dominant at both neutrino flavors.

3.2 The Near Detector Complex

The near detector complex is located at 280 meters from the hadron production target. The near detectors are used to measure the neutrino energy spectrum, flavor composition, and interaction rates of the un–oscillated beam. It is mainly used to predict the neutrino interactions at Super–KamiokaNDE. The complex is composed by two detectors:

- **the on–axis detector INGRID**. The INGRID detector consists of 14 identical modules, array of iron/scintillator detectors. These modules are arranged as a cross of two identical groups along the horizontal and vertical axis, and two additional separate modules located at off–axis directions outside the main cross. The detector samples the neutrino beam in a transverse section of 10 m $\times$ 10 m. The center of the INGRID cross, with two overlapping modules, corresponds to the neutrino beam center. INGRID is able to measures the on–axis neutrino beam profile and cross sections at the 280 m site. See Figure 3.12.

- **the off–axis detector ND280**. ND280 is a magnetized off–axis tracking detector. The off–axis detector elements are contained inside the refurbished UA1/NOMAD magnet. Following neutrino direction, the first element is a π^0 detector (P∅D) consisting of tracking planes of scintillating bars alternating with either water target/brass foil or lead foil. Downstream of the P∅D there is the tracker, composed by three Time Projection Chambers (TPCs) and two Fine Grained Detectors (FGDs) consisting of layers of finely segmented scintillating bars. The P∅D, TPCs, and FGDs are all surrounded by an electromagnetic calorimeter (ECal). The return yoke of the magnet is instrumented with scintillator to measure the ranges

of muons (Side Muon Range Detectors, SMRD) that exit the sides of the off–axis detector.

All detectors in the near detector complex use the same coordinate convention: z is parallel to the nominal neutrino beam axis, and x and y are horizontal and vertical respectively. These detectors are housed in a pit inside the ND280 hall (Figure 3.11). The pit has a diameter of 17.5 m and a depth of 37 m.

The ND280 off–axis detector, is located on the line between the average pion decay point and the far detector Super–KamiokaNDE, shifted by $\sim 2.5^{o}$ respect to the proton beam direction. The facility design can accommodate off–axis angles in the range of between 2.0 and 2.5^{o}.

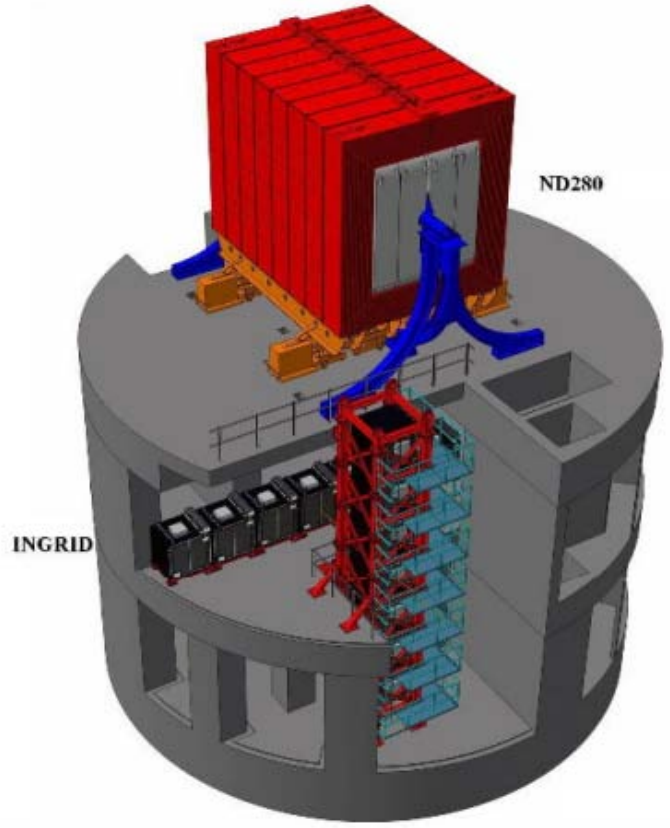

FIGURE 3.11: The near detector complex. The off–axis detector ND280 and the magnet are located on the upper level; horizontal INGRID modules are located on the level below; and the vertical INGRID modules span the bottom two levels. The magnet in this Figure is closed.

Following we describe the ND280 off–axis detector focusing on the detectors which are used in the analysis described in this thesis.

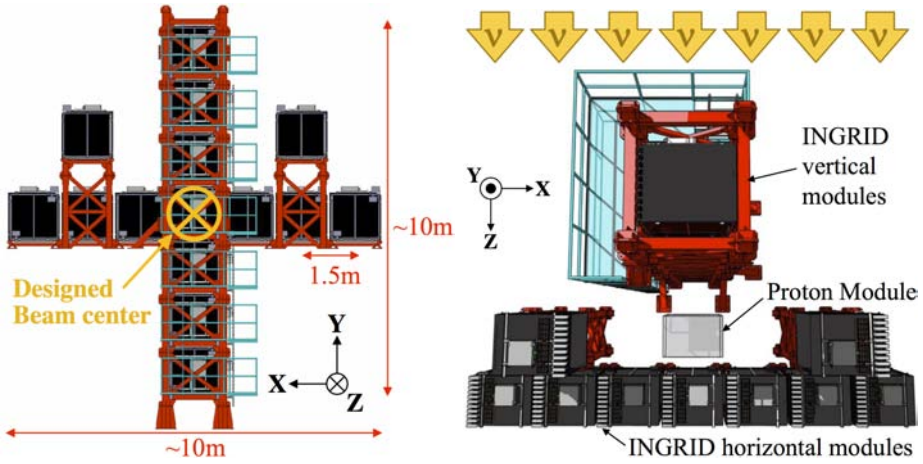

FIGURE 3.12: Schematical overview of INGRID on–axis detector. Front view (left) and upper view (right).

3.2.1 The Off–Axis Detector: ND280

The primary purpose of the ND280 detector is to characterise the neutrino beam prior to oscillation. It was built to fulfill several requirements:

- provide information to determine the expected ν spectra at SK detector,
- measure the ν_e contamination of the beam as a function of the neutrino energy,
- reconstruct neutral current single π^0 events to control the second most important background of the ν_e appearance channel at Super-KamiokaNDE (the first one is the ν_e contamination of the beam).

To achieve these goals the ND280 off–axis detector should have the capability to reconstruct neutrino exclusive event types: distinguish between events from different neutrino flavors, to measure contribution of CCQE–like events which are used to reconstruct the neutrino energy at SK (is the main channel used for oscillation analysis) and contribution of any other channel that can be used for the oscillation analysis improvement. The detector design of the detector has been chosen to fulfill these requirements. The ND280 overview is shown in Figure 3.13. It is composed by:

- the refurbished UA1/NOMAD magnet instrumented with scintillator to perform as a Side Muon Range Detector (SMRD);
- an Electromagnetic Calorimeter that surrounds the basket (Barrel ECal);
- the PØD, 3TPCs/2FGDs (also known as the *tracker* region) and the Downstream Electromagnetic Calorimeter (Downstream ECal), which are placed inside of a metal frame container, called *basket*.

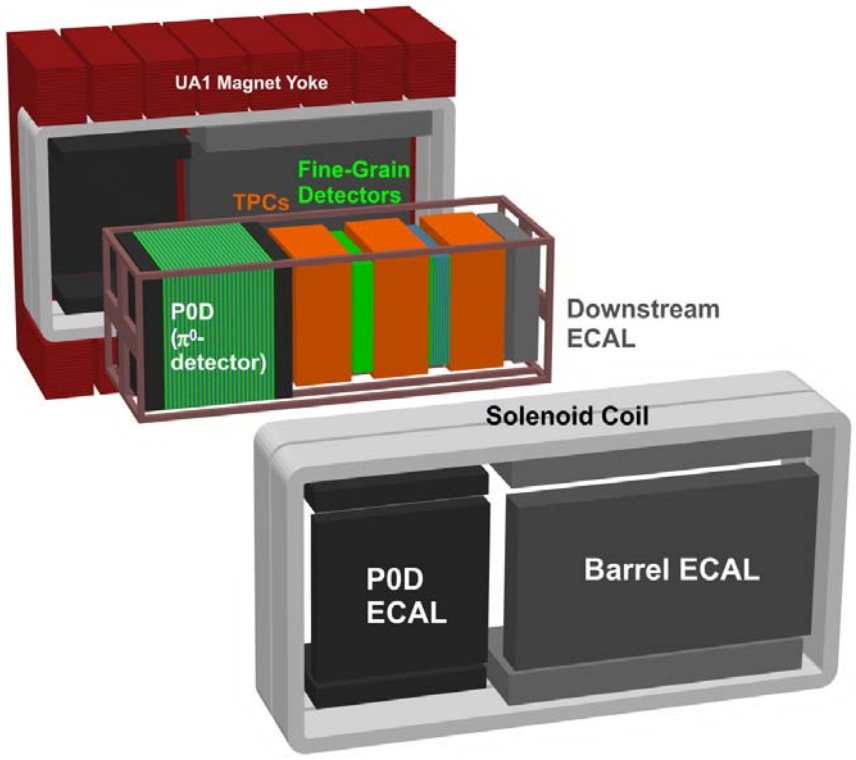

FIGURE 3.13: ND280 off-axis overview.

Figure 3.14 shows an event display of a ν_μ event, from data. Here the ν_μ candidate interacts in the first FGD. Particles produced in the interaction with the FGD material enters to the second TPC and some of these particles reach the second FGD on which they produce some showers.

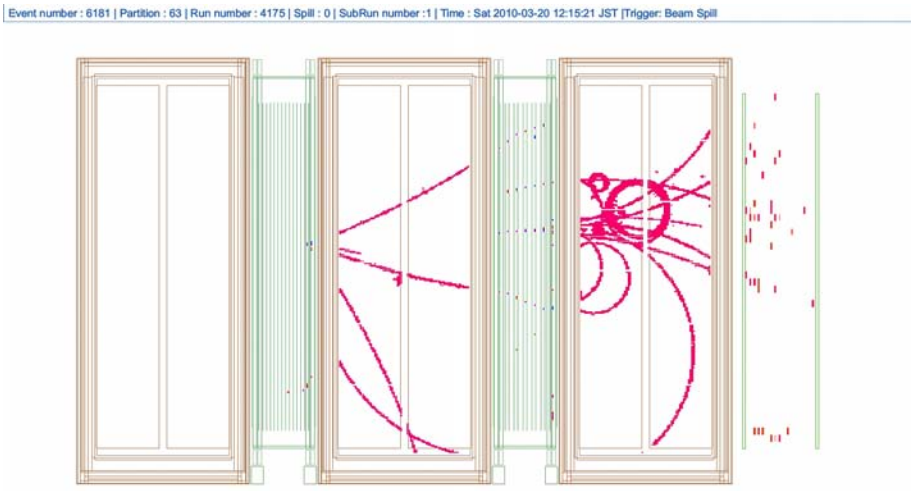

FIGURE 3.14: ν_μ data event display. The ν_μ candidate interacts in the first FGD. Particles produced in the interaction with the FGD material enters to the second TPC and some of these particles reach the second FGD on which they produce some showers. In this display only FGDs, TPCs and part of the ECal (the Dowstream) are shown.

The TPCs, FGDs and the ECal play a fundamental role in the analysis presented in this thesis.

3.2.2 The UA1/NOMAD magnet

The ND280 magnet is the magnet previously used at CERN for UA1[47] and NOMAD[48] experiments. The magnet was refurbished at CERN and shipped to J–PARC in 2008. It provides a dipole magnetic field of 0.2 T allowing to measure momenta with good resolution and determine the sign of charged particles produced by neutrino interactions.

It consists of water–cooled aluminum coils, which create the horizontally oriented dipole field and a flux return yoke. The dimensions of the inner volume of the magnet are $7.0m \times 3.5m \times 3.6m$. The external dimensions are $7.6m \times 5.6m \times 6.1m$ and the total weight of the yoke is 850 tons. The coils are made of aluminum bars with $5.45cm \times 5.45cm$ square cross sections, with a central 23 mm diameter bore for water to flow. The coils are composed of individual *pancakes* which are connected hydraulically in parallel and electrically in series.

The magnet consists of two mirror–symmetric halves. The two half yoke pieces consist each of eight *C-shaped* elements, made of 4.8 cm thick low–carbon steel plates, which stand on movable carriages. This allows to open allowing access to the detectors. Within the gaps of the magnet yokes the SMRD modules are inserted.

3.2.3 The Side Muon Range Detector (SMRD)

The SMRD performs the functions:

- to record muons escaping with high angles with respect to the beam direction and contributes to measure their momenta;
- it triggers on cosmic ray muons that enter the ND280 detector, thus external background contaminatation can be identified;
- it helps identify beam–related event interactions in the surrounding cavity walls and the iron of the magnet (sand muons).

The SMRD consists of a total of 440 scintillator modules, which are inserted in the air gaps between the thick steel plates which make up the UA1 magnet flux return yokes. Each yoke consists of 16 steel plates and hence has 15 air gaps in the radial direction. For every yoke, there are three layers of scintillator modules on the top and bottom. All

of the SMRD modules populate the innermost gaps so as to be able to detect particles escaping the inner detectors.

3.2.4 The Electromagnetic Calorimeter (ECal)

The ECal is a sampling electromagnetic calorimeter surrounding the inner detectors (PØD, TPCs and FGDs). It is mainly used to measure the energy and direction of photons, primarily from π^0 production. It also helps to distinguish electrons, muons and pions.

The calorimeter is composed by plastic scintillator bars as active material with lead absorber sheets between layers. The scintillator bars are made of doped 1% POP and 0.03% POPOP polystyrene with a TiO_2 reflective coating and a 1 mm in diameter WLS fiber inserted in a central hole, they have a $4cm \times 1cm$ cross section and vary in length depending on the module they belong to. The calorimeter is composed by 13 independent modules of three different types:

1. six Barrel-ECal modules (Br-ECal) surround the tracker volume on its four sides parallel to the z (beam) axis;
2. one downstream module (Ds-ECal) covers the downstream exit of the tracker volume;
3. and six PØD-ECal modules surround the PØD detector volume on its four sides parallel to the z axis.

The Ds-ECal is located inside the basket carrying the inner sub-detectors of the off–axis detector. The other 12 ECal modules are mounted inside the UA1 magnet. The Ds-ECal consists of 34 layers with 1.75 mm thick lead sheets corresponding to 10.6 ${X_0}^4$ ($\sim 1{\lambda_I}^5$).

Limited by available space inside the UA1 magnet and structural considerations, the 6 Barrel-ECal modules surround the tracker. Each module is formed of 31 layers corresponding to 9.7 X_0.

The PØD-ECal has a reduced granularity in comparison with the others ECal modules and is made of six scintillator planes containing 2.34 m long bars always oriented in z-direction interleaved by 4 mm lead sheets.

[4]The X_0 is the radiation length which is defined as the distance after which an electron has only $1/e$ of its initial energy remaining, where e is the Eule's number.

[5]The λ_I is the interaction length, defined as the mean free path of a particle before undergoing and interaction that is neither elastic nor quasi-elastic (diffractive) in a given medium.

The Br-ECal and PØD-ECal modules were constructed in 2009-10 and were installed in ND280 only in July- October 2010. The T2K first data run lacks on these detectors.

The ECal particle identification The general principle of an electromagnetic calorimeter is to reconstruct the energy of the particles. Most of the particles entering the calorimeter can initiate a particle shower and the energy deposited by these particles can be measured. The ECal is able to provide particle identification (PID) by:

- Distinguish showering particles, such as electrons, from non–showering particles, such as muons.
- Identify charged pions which behave like minimum ionising particles (MIPs) from hadronic interactions in the ECal.
- Identify low energy photons from neutral pion decay.

Muons pass through the material as minimum ionizing particles (MIP) and hence, they can be reconstructed as tracks. On the other hand, electrons and photons cross an ECal module releasing most of their energy, thus they are reconstructed as electromagnetic showers. Pions and protons can create shower or be reconstructed as tracks since their hadronic nature makes them to have a big probability for interact with the calorimeter material.

Thanks to the deposited energy of the particles in the ECal, for each ECal reconstructed object some observables can be built and help to the PID. The observables we use to distinguish between tracks and showers in the ECal are:

- the *MipEM*, which is negative for MIP–like and positive for shower–like clusters as it is illustrated in Figure 3.15. It uses information of the hits in the cluster.
- the total energy deposited (*EMEnergy*).

3.2.5 The π^0 detector (PØD)

The primary goal of the PØD is to measure NC π^0 production ($\nu + N \rightarrow \nu_\mu + N + \pi^0 + X$) on a water target ($H_2O$) with the same neutrino beam flux as reaches the Super-KamiokaNDE detector. Measure interactions on water allows for constraint systematics in oscillation analysis due to different target (since SK uses water target).

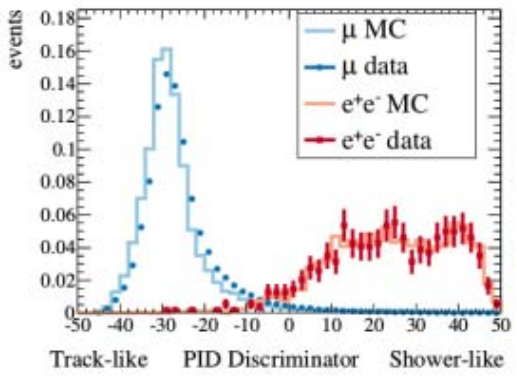

FIGURE 3.15: ECal discriminating variable (MipEM) distribution for muons and electrons particle guns for Monte Carlo (lines) and through-going muons and photon conversions for data (dots). MipEM is used to ditinguish between shower-like cluster (MipEM<0) and MIP-like (MipEM>0).

The PØD is made of four sections (so called Super-PØDules): the *upstream ECal* followed by the *upstream water target*, the *central water target* and the *central ECal*, as shown in Figure3.16. The combination of 134 2.2 m long vertical and 126 2.34 m long horizontal triangular scintillator bars form a PØD module, or PØDule. Seven PØDules alternate with 0.4 mm thick lead sheets in the case of the two ECal sections, and for the two water target sections 13 PØDules are interleaved with 28 mm thick water bag layers followed by a 1.5 mm thick brass sheet. Thanks to the upstream and central ECal the containment of electromagnetic showers from photon conversion is improved and provides a veto region before and after the water target to reject particles entering from outside the PØD.

FIGURE 3.16: Schematic view of the PØD. The beam is coming from the left and going right. Insets show details of the water target super-PØDule and central ECal layers.

3.2.6 The Time Projection Chambers (TPCs)

The 3 TPCs perform three key functions in the near detector:

- precise 3–D tracking: the charged particles are very well tracked as they cross the light gaseous material. Since the speed of the electrons is constant and depends on the gas composition, a measurement of the arrival time of the electrons allows a three-dimensional reconstruction.
- momentum and charge measurement: thanks to the magnetic field inside the basket, the particles are curved with a radius that is proportional to the momentum of the track. The measurement of the radius allows to measure the momentum and retrieve information about the charge;
- particle identification: electrons coming from the ionization of the gas produced by the charged particles that cross the gas are collected on the TPC readout system, the Micro Mesh Gaseous detectors (MicroMegas). The measurement of both the deposited energy and the momentum of the particle provides a powerful tool for its identification.

Each of the three TPCs has outer dimension $2.3m \times 2.4m \times 1.0m$ and consists of an inner box filled with an argon-based drift gas ($Ar : CF_4 : iC_4H_{10}$, $95 : 3 : 2$). Such mixing has been chosen for its high speed, low diffusion, and good performance with MicroMegas chambers. The inner box is contained in an outer box that holds CO_2 as insulating gas. The inner box has a lower presure respect tot he outer one.

The TPCs are separated into two sides by a central cathode. The voltage on the cathode is set in order to have an uniform electric field in the active drift volume of the TPC, aligned with the magnetic field provided by the UA1 magnet. A simplified drawing of the TPC design is shown in Figure 3.17.

The MicroMegas can detect the particles by amplifying the charges created by the ionisation in the gas volume. They provide a high gain, fast signal and good resolution [49]. The MicroMegas have dimension $7.0mm \times 9.8mm$ (vertical $\times$ horizontal) pad segmentation (48 rows $\times$ 36 columns). The signal produced by the charge amplification at the anode pads combined with the arrival time, allows the 3D imaging of charged particle trajectories within the TPC. Two vertical columns of six $342mm \times 359mm$ MicroMegas modules form a readout plane for a total of 72 MicroMegas modules. Each TPC has 2 readout planes of 12 MicroMegas, giving 24 MicroMegas per each TPC. The MicroMegas columns are slightly offset in the vertical direction such that the inactive regions between the modules in a single readout plane are not aligned (Figure 3.18). The MicroMeagas

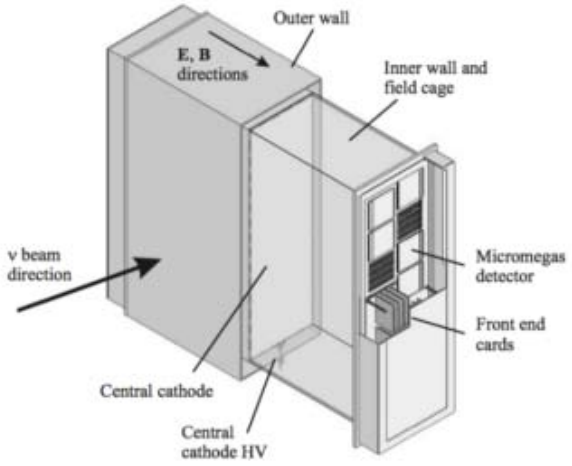

FIGURE 3.17: Simplified cut-away drawing showing the main aspects of the TPC design.

amplify the deposited charge applying an strong electric field of $\sim 40kV/cm$ in a thin region of about $100\mu m$. A mesh separes the drift region from the amplification region and provides this high potential. When the drifting electron cross the mesh, they are accelerated triggering a shower (formed by avalanche process) that is detected by the read out pads in the MicroMegas.

To calibrate the TPCs, a calibration system is used to diffuse light of a 266 nm laser and illuminate small alluminum discs which are glued to the central cathode surface. The emerging photo-electrons provide a control sample which is used to precisely determine the electron drift velocity and to measure distortions due to any inhomogenity or misalignement of the electric and magnetic fields.

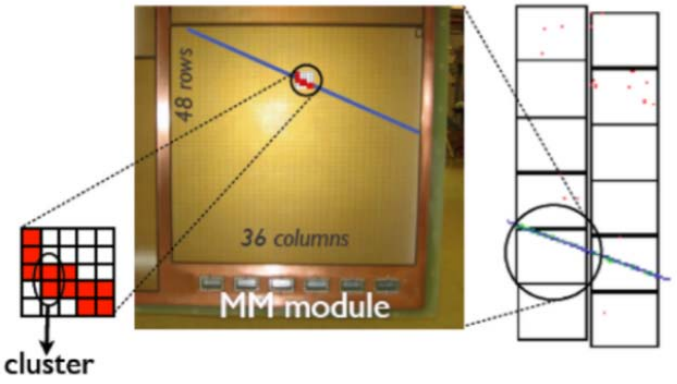

FIGURE 3.18: Track reconstruction in a MicroMegas detector.

The neutrino energy estimation for the CCQE–like events (dominant interaction channel in T2K) is limited at about the 10% level due to the Fermi motion of the struck nucleons. Thus, the TPC goal is to achieve a resolution in the momentum of $\delta p_\perp/p_\perp < 0.1 p_\perp$ [GeV], where $p_\perp$ is the component of the momentum perpendicular to magnetic field

direction. This requirement is fulfilled and the precision on the measured momentum is $\sim$ 10% for tracks of momentum $\sim$ 1 GeV, momentum of the the most part of the particles reconstructed in the TPCs from a neutrino interaction in ND280.

The TPC particle identification The particle identification (PID) in the TPC is based on the combination of precise measurements of the momentum and the ionization energy. The ionization energy depends on the relativistic $\beta\gamma$ factor through the well known Bethe-Bloch formula[2]. The function as computed for muons on copper is shown on Figure 3.19.

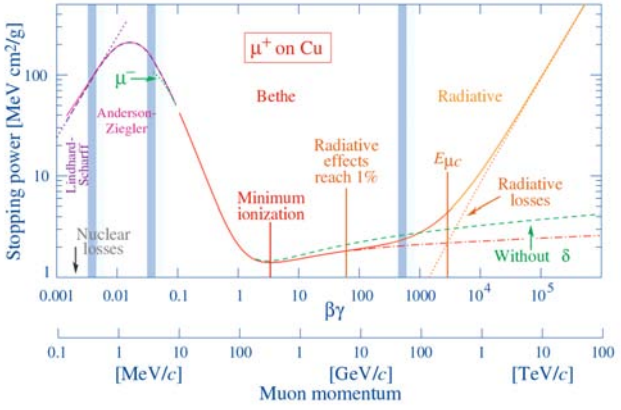

FIGURE 3.19: Stopping power ($< -dE/dx >$) for positive muons in copper as a function of $\beta\gamma = p/Mc$ over nine orders of magnitude in momentum (12 orders of magnitude in kinetic energy). Solid curves indicate the total stopping power. From the Particle Data Group [2].

A simplified expression to stress the relation with respect to $\beta\gamma$ is

$$-\frac{dE}{dx} \propto \beta\gamma = \frac{p}{m} \tag{3.8}$$

where p and m are respectively the momentum and the mass at rest of the particle. For the identification of the particles we measure and compare the momentum and the expected energy loss at that momentum for each particle type hypothesis with the measured one. We can see for the TPC the dependency of the ionization as a function of the momentum for different particle type hypothesis in Figure 3.20.

The deposited energy of the electrons in $1atm$ of Argon gas is very different for that of the for muons over the momentum range of interest. Only at very low momentum, $\sim 100-200$ MeV we will have more difficulties for their separation. Then to distinguish electrons from muons the requirement in the ionization resolution needs to be better than 10%. We may have to be carefull for the pion–muon identification to avoid ν_μ charged current mis–identification because of neutral current with pions in the final state.

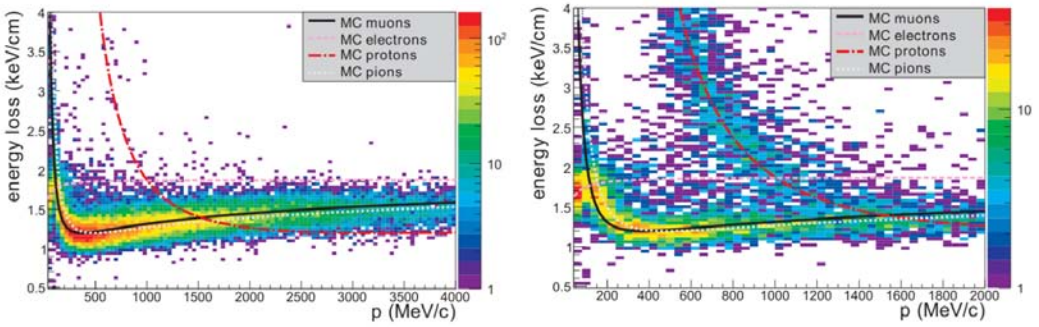

FIGURE 3.20: Energy loss calculated using the truncated mean method C_T (see later) versus the momentum of the negative (left) or positive (right) particle measured by the TPC. The different curves represent the prediction for different hypothesis and the colored histograms correspond to the data.

For the rest of particles we also have a good separation. For protons, we see that generally the shape of the energy loss distribution provides a very good discrimination, only possible contamination from positrons at $\sim 900 - 1100$ must be taken into account and for positive pions at from 1300 MeV and above.

The resolution on the deposited energy is computed by using the mean value of the charge deposited by the particle crossing the gas. As the ionization is affected by long tails (Landau tails) the resolution improves substantially if we reduce those tails. To reduce these tails we use the so–called *truncated mean method*. The method is optimized and the truncated mean of the energy loss, C_T, is defined as the mean of the 70% of the MicroMegas clusters with less charge.

To discriminate among the different particle types we define the pulls, δ_α, for each particle hypothesis, $\alpha = e, \mu, proton$,... as follows:

$$\delta_\alpha = \frac{C_T^{measured} - C_T^\alpha}{\sigma^\alpha} \tag{3.9}$$

where $C_T^{measured}$ is the measured C_T and C_T^α and σ^α are the predicted C_T and its deviation for the α hypothesis. For the muon and electron hypothesis, which are of main interest for the ν_μ and ν_e separation in ND280, the distribution of the pulls are shown in Figure 3.21. We observe that we can distinguish between muons and electrons by using these distributions. The C_T resolution is about 7.8% for the minimum ionizing particles. This allows muons to be distinguished from electrons in the TPCs being the muon misidentification probability bellow 1% for any momentum range [50].

In Figure 3.22 we show the pull distributions for the pion (left plot) and proton (right plot) hypothesis. We show the distributions only for the most energetic particle of the event without any reuirement than to pass the TPC quality reconstruction checks.

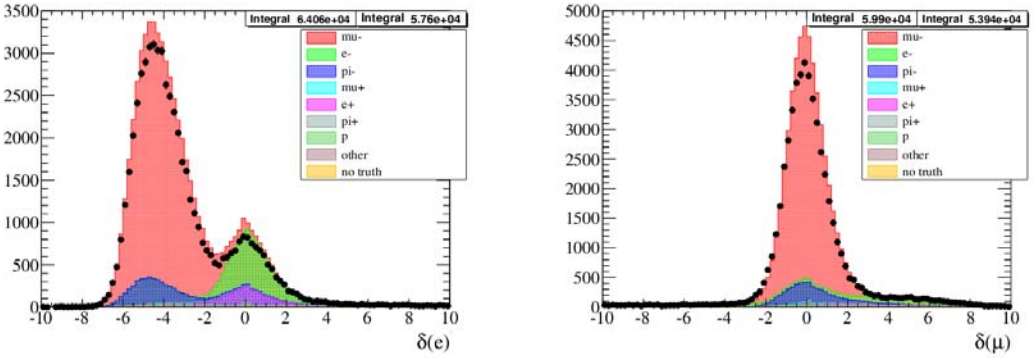

FIGURE 3.21: Pulls, δ_α for the electron (left) and muon (right) hypothesis for Monte Carlo (color) and data (dots) using the total data for the run periods 1+2+3+4 that corresponds to $5.9 \cdot 10^{20}$ proton on target.

Then, due to the properties of the neutrino beam in T2K, most part of the events will be CCQE and the most energetic one should be the muon particle. Nevertheless, these plots can provide a good test on how the pull distributions are working. As we can see in the pull pion distribution (left plot), the true pion component is centered at zero but the dominant particle type is the muon. This is due that pions and muons have similar behaviour in the TPC and muon is more abundant than pions in T2K. The biggest contribution comes from CCQE processes where the pion, if no consider nuclear effects, is not present. Nuclear effects can lead to a pion in the final state. For the distribution for the proton pull hypothesis (right plot), we see how the proton contribution is well centered at zero and the muon contribution is not centered at any specific value.

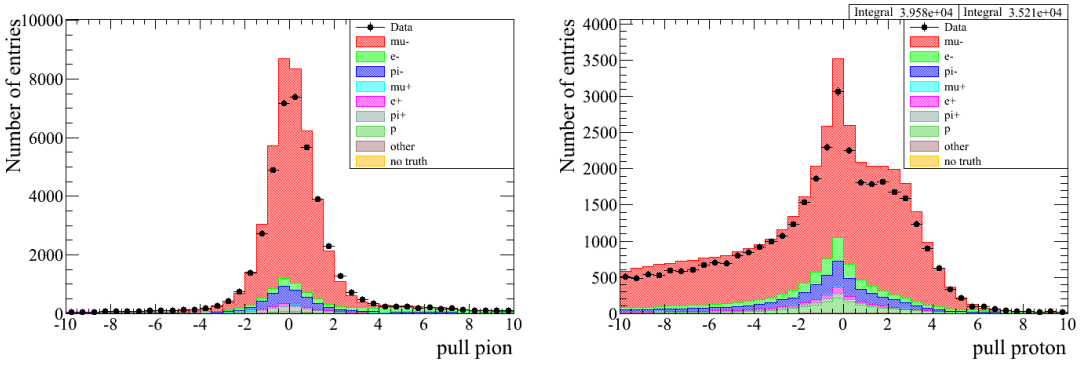

FIGURE 3.22: Pulls, δ_α for the pion (left) and proton (right) hypothesis for Monte Carlo (color) and data (dots) using the total data for the run periods 1+2+3+4 that corresponds to $5.9 \cdot 10^{20}$ proton on target.

3.2.7 The Fine Grain Detectors (FGDs)

Two FGDs interleave the three TPCs. The purpose of those detectors is to provide target mass for neutrino interactions and to track the particles leaving the vertex. The

combination of the FGDs and the TPCs allows a precise track reconstruction of the charged particles.

Each FGD has outer dimensions of $2300mm \times 2400mm \times 365mm$ [11] and provides 1.1 tons of target material.

The FGDs are constructed from $9.61mm \times 9.61mm \times 1864.3mm$ bars of extruded polystyrene scintillator, which are oriented perpendicular to the beam direction in either the x or y direction.

However, the two FGDs are different. The first FGD (FGD1) consists of 5760 scintillator bars, arranged into 30 layers of 192 bars each. The bars are orthogonally oriented in successive planes and each pair of orthogonal layers builds an XY module. The second FGD is made of seven XY modules interleaved with 2.5 cm thick water layers at sub-atmospheric pressure[6], for a total of 2688 active scintillator bars and 15 cm total thickness of water. Each scintillator bar has a reflective coating containing TiO_2 and a WLS (WaveLength-Shifting) fiber.

For the analysis presented in this thesis we use the FGD1 as target for the neutrino interactions. Then, we define a fiducial volume in the FGD1 in order to reduce contamination of events with vertex out of the FGD. The FGD1 fiducial volume (FV) cut dimensions are $|x| < 874.51$ mm, $|y-55| < 874.51$ mm, and $136.875 < Z < 446.955$ mm. The x and y cuts are chosen to match the outer boundaries of the central 182 scintillator bars in the x and y layers. So 5 bars on either end of each layer are excluded from the fiducial volume. The 55 mm offset in the y cut reflects the fact that the XY modules are displaced 55 mm upwards relative to the centre of the ND280 coordinate system. The upstream z cut places the fiducial volume just after the first XY module, but includes the remaining 14 XY modules.

Thanks to the design of the FGD1 and FGD2, one scintillator–based and the second one scintillator–water, we can produce comparisons of neutrino cross sections on carbon and water, complementary to the PØD cross section.

3.2.7.1 The FGD PID

The FGD can be used for particle identification of short tracks that doesn't exit the FGD. To identify these short tracks we measure and compare the expected energy loss for each particle type hypothesis with the measured one. And similarly to the TPC we

[11] $width \times height \times depth$ in beam direction.

[6] The lower pressure with respect to the surrounding volume is a safety measure to avoid the water spilling over the electronics in a case of a leak.

construct the pull distributions for each particle hypothesis. We can see in Figure 3.23 pull distribution for the pion hypothesis for both FGDs, for tracks contained in one of the FGDs (FGD–Only). In this case, the pull is not centered at zero due to reconstruction limitations in the FGDs. The main problem when reconstructing these tracks is that we found that some of the times we reconstruct a single track with two different tracks and then two different particles. This is mainly due because of the difficulties to reconstruct very short tracks. Then, when computing the pull distributions we observe peaks not centered at zero as it was expected.

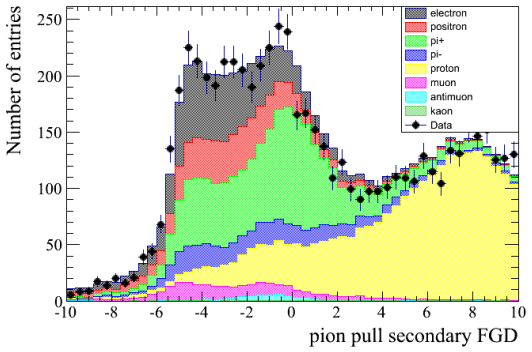

FIGURE 3.23: Pion pull distribution of the FGD-only tracks.

3.3 The far detector: SuperKamiaokaNDE

The world's largest water Cerenkov detector, Super-KamiokaNDE [51] (SK), is the far detector in the T2K experiment. It is located in the Kamioka Observatory and has been successfully taken data since 1996. The detector was previously used as a far detector for the K2K experiment [52]. SK is a 50,000 tons detector located at a depth of 1,000 m (2,700 meters water equivalent) in the Kamioka mine in Japan. During its four major running periods (SK I to SK IV) Super-KamiokaNDE contributed to the search of neutrino oscillations with results concerning atmospheric, solar and accelerator-produced neutrinos [53][54][55][51][56]. Setting measurements of proton lifetime has been performed at SK giving the world best limit [57][58][59].

The principle of a neutrino Cerenkov detector is the following:

- a neutrino interacts with a nuclei in the water producing a lepton,
- the lepton travels faster than light in the water, then a shock light wave is produced and the particle emits light in a direction θ with respect to the lepton direction such that

$$cos\theta = 1/\beta n \tag{3.10}$$

where β is the speed of the lepton in units of c and n the refraction coefficient of the medium (water in this case). This is called the Cerenkov effect [60].

- the light forms a cone whose axis is collinear with the path of the lepton. It arrives to the innner detector (ID) walls where photomultipliers (PMTs) detectors collect its light detecting a light ring.

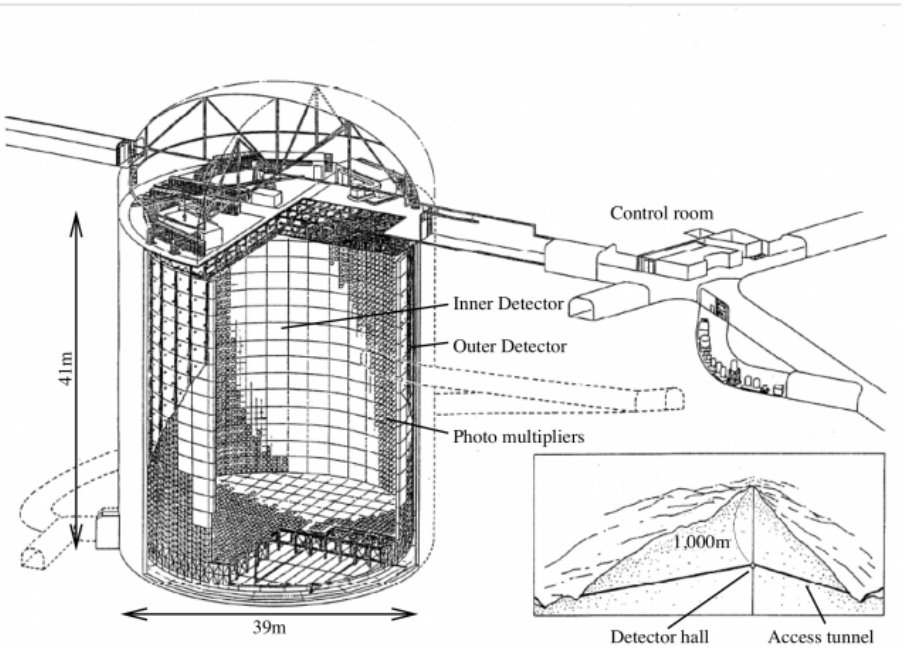

FIGURE 3.24: Schematic view of the Super-KamiokNDE detector. The detector is mainly comprised of two segments, the inner and the outer detectors. The boundary between the two segments is defined by a cylindrical scaffold used to mount photomultiplier tubes and optically separate the segments.

An schematic view of the detector is shown in Figure 3.24.

The cylindrical detector cavity is 41 m in height and 39 m in diameter. SK consists of two major volumes, an inner and an outer detector which are separated by a cylindrical stainless steel structure. The inner detector (ID) is a cylindrical volume 33.8 m in diameter and 36.2 m in height which houses along its inner walls 11,129 PMTs of 50 cm diameter. Enclosing the ID is the outer detector (OD) which is a cylindrical volume about 2 m thick radially and on the axis at both ends. The OD contains along its inner walls 1,885 outward-facing PMTs of 20 cm diameter. The role of the OD is to identify entering(exiting) particles to(from) the ID.

The primary strategy to measure the flavor composition of the T2K neutrino beam at SK, and thereby observe the oscillation of ν_μ to either ν_e (or ν_τ if any), is to count

charged current quasi-elastic (CCQE) interactions for muon and electron neutrinos. The typical signature of which are leptons on the final state with their respective flavour (CC interaction), and no hadrons except for a posible proton. SK has a very good performance to identify leptons. On the other side, to identify hadrons becames more challenging and the detector is not optimized to distinguish between charged hadrons.

Many features of the out-coming lepton can be measured: the position and time of the interaction or the energy and direction of the lepton. The particle is performed by looking at the characteristics of the rings. The idea is that the muon, which is a heavy lepton and diffident to change its momentum when travelling in a medium, travels very straight. On the other hand, electrons are lighter and easily scatter on the water producing electromagnetic showers. This results in a very sharp reconstructed Cerenkov ring for the muons and a fuzzy ring for the electrons as can be appreciated in Figure 3.25

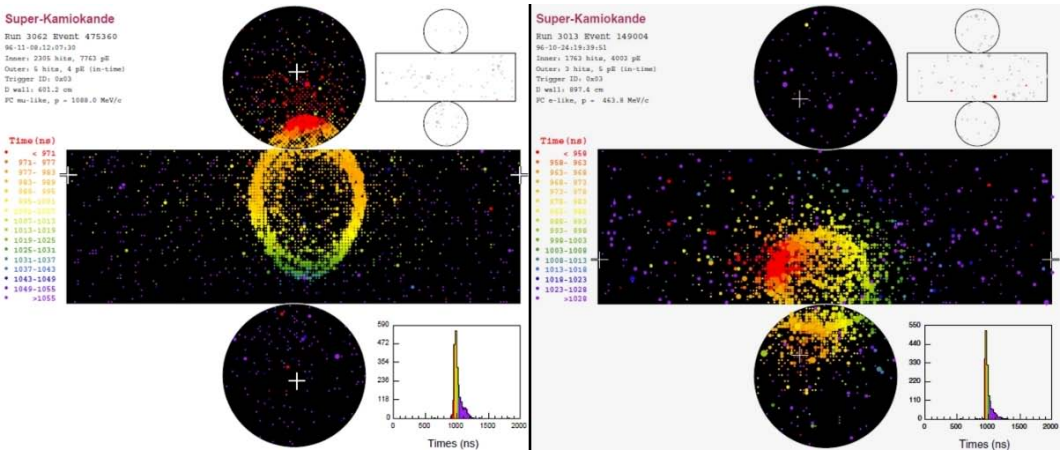

FIGURE 3.25: Super-KamiokaNDE event display. Cerenkov light ring reconstructed at SK. The left plot corresponds to a muon-like event and the rigth plot to an electron-like event.

In addition, SK can also disentangle between electrons and π^0. The π^0 decays immediately in two photons that leaves electron/positron pair and then two Cerenkov rings instead of only one as for the ν_e CC inclusive interaction. However, the reconstruction of both rings is very hard in the case that photons are emitted almost collinear (the two rings overlap) or if one of the photons is very low energetic (the ring is very small then can be indistinguishable).

Chapter 4

Detector Systematical Uncertainties and Propagation

In this Chapter we summarize the detector systematical errors that are needed in the two analysis presented in this thesis. In both analysis we use the FGD1 and TPCs detectors to identify muons and pions, as we will see in Chapters **??** 6, as well as for some kinematical reconstructed observables. In Chapter 6, the $CC1\pi^+$ cross section measurement, we include a neutral pion identification using the Barrel and Downstream ECal detectors. Thus, all detector systematics except of one, the ECal shower reconstruction efficiency, are common for both analysis. The propagation of the systematics is also described.

In Appendix B, an example of detector systematic measurement is shown, the ECal shower reconstruction efficiency. This systematic has been computed explicitly for this analysis. Concerning the other detector systematics, we just give a brief description and the control samples used.

4.1 ND280 Detector Systematics

This Section summarizes the ND280 systematics relevant for the analysis. An overview is given in Figure 4.1. Each systematic is measured by comparing data and Monte Carlo values using independent control samples. Except for the out of FGD1 fiducial volume on which we only use Monte Carlo estimation. The complete list of systematics is presented in Table 4.1. This table also present the approach followed to propagate such systematics. Each systematical detector is propagated into the selected sample event by event using a probability density function approach. In Table 4.1 is shown in

the first column the systematic source, the type of model used for the propagation on the second column, which will depend on the type of systematic, and at last column it shows the probability density function approach used.

Systematic error	Implementation model	Probability Density Function
B Field distortion	Reconstructed observable variation	Flat
TPC tracking efficiency	Efficiency like systematics	Gauss
TPC–FGD matching efficiency	Efficiency like systematics	Gauss
TPC charge confusion	Efficiency like systematics	Gauss
TPC momentum scale	Reconstructed observable variation	Gauss
TPC momentum resolution	Reconstructed observable variation	Gauss
TPC quality cut	Efficiency like systematics	Gauss
Michel electron efficiency	Efficiency like systematics	Gauss
FGD mass	Normalisation systematics	Gauss
OOFV Systematic	Efficiency like systematics	Gauss
Pile–up	Normalisation systematics	Gauss
Sand muon systematic	Efficiency like systematics	Gauss
TPC PID	Reconstructed observable variation	Gauss
FGD PID	Reconstructed observable variation	Gauss
FGD tracking efficiency	Efficiency like systematics	Gauss
Pion secondary interactions	Efficiency like systematics	Gauss
Übermerging	Efficiency like systematics	Gauss
ECal shower reconstruction	Efficiency like systematics	Gauss

TABLE 4.1: Systematic error propagation model for each of the systematic errors considered for the analysis presented in this thesis (Chapters 5 6). They are focus on FGD1-TPC-ECal particle track reconstruction, specially for muons and pions. Except for the ECal shower reconstruction, all detector errors showed here are used in Chapter 5.

In following sub–Section we briefly describe each uncertainties for each detector systematic and the main idea of the performance used. Except for the ECal shower reconstruction which is fully described in Appendix B.

4.1.1 TPC Particle ID

The TPC PID systematic [61] measures the error associated to the particle identification in the TPC, which is based upon the pull estimation for each particle hypothesis (see 3.2.6). It is computed from the difference between data and MC for different samples of interest in the analysis, i.e muons and pions. For the muon measurement, a control sample of sand muons [1] is used. Pions have an energy loss similar to the muons and systematics for them are considered the same as those computed for muons. The TPC particle ID systematic for protons has been computed since that might affect the pion selection which is of interest. Thus, for the proton case a high purity proton sample is selected based on the most energetic positive track with vertex in FGD1 fiducial volume.

[1] Sand muons refers to muons coming from events originating from neutrino interactions outside the ND280 detector.

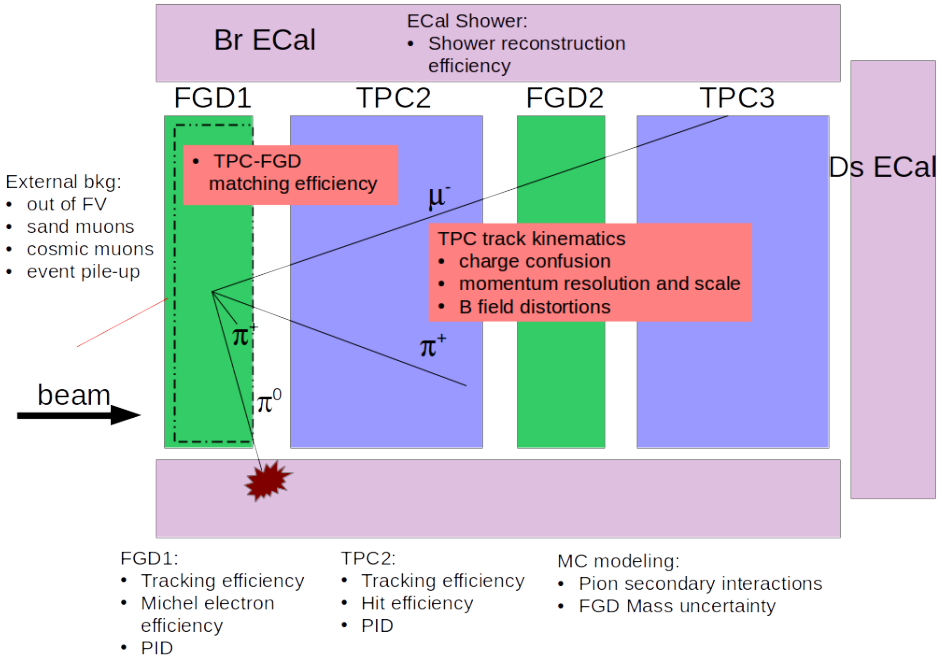

FIGURE 4.1: Sketch of the sub–detectors relevant for the analysis with the corresponding associated systematic components.

A small effect is also expected due to the systematics for the electrons, to compute it, a γ control sample have been used. This γ sample is selected by requiring pair of electron/positron where both start in the FGD1 enter TPC2.

4.1.2 TPC cluster efficiency

A cluster in the TPC is defined as a collection of contiguous pads with charge above a threshold (hit). Depending on the track angle a cluster will have several hits in the same column (for horizontal tracks) or in the same row (for vertical tracks). Given the beam direction (nearly horizontal), tracks are reconstructed mainly by clusters with hits in the same column. The TPC cluster efficiency is defined as the probability to find a reconstructed cluster at a given column where the particle should have produced one [61]. The systematic is computed by the different efficiency in data and MC. The control sample uses muons selected as the higher momentum negative track in the event and starting in the FGD1 fiducial volume which reach TPC2 [2].

[2]The sample is similar to the ν_μ CC inclusive sample presented in Chapter 5.

4.1.3 TPC single and double track–finding efficiency

The TPC track–finding efficiency describes the efficiency with which the TPCs successfully reconstruct the tracks of particles crossing them [61] [62]. Since the behaviour of the reconstruction could be different when reconstructing one single track or two close tracks overlapping, the track–finding efficiency is evaluated separately for these two cases. Then, the difference data/MC such in efficiency is taken for the systematic.

For the single track–finding efficiency, a muon control sample is used. These muons are selected to pass trought the upstream and downstream detectors around a TPC, to select events in which a single muon crossed the tested TPC.

The track–finding efficiency for two close tracks use a basic selection to find events with two tracks in a TPC that have a topology similar to neutrino interactions [3], this is done to reduce δ–rays.

4.1.4 TPC momentum resolution

The systematic is obtained by the difference in resolution between data and MC [61]. We use a muon control sample by requiring only one negative track in the event and selected as muon candidate using the pull distributions of the TPC PID. The muon candidate must start in the FGD1 FV. This muon candidate have to cross at least two TPCs to allow to compute the difference between the momentum reconstructed using the two TPC segments of the same global track. For the resolution measurement the inverse of the transverse momentum to the magnetic field is used, $1/p_t$. The distribution of its difference between TPC1 and TPC2 can be interpolated by a Gaussian on which their standard deviation is related to the intrinsic resolutions of the TPCs involved.

4.1.5 TPC charge confusion

The charge mis–identification systematic consider the uncertainty on assigning a charge value to a recosntructed track in the TPC. The calculation is done using a statistical approach [61]. The charge mis–identification systematic is extracted by comparing the reconstructed charges in the different TPCs and then comparing the reconsturcted charge provided by each single TPC or the global reconstruction which uses the different detectors information. The control sample used is composed mainly by straight muons crossing the three TPCs. In addition, a MC truth study was used to cross–check the

[3] These tracks should start from the same vertex and coming from the interaction of a missing particle.

statistical approach. The final systematic error is given by the difference of the charge mis–identification between data and MC.

4.1.6 Track "Übermerging"

The "Übermerging" systematic error take into account the limitation in the current TPC reconstruction that leads to the merging of two TPC segments from two different particles. This systematic is only related to the tCP reconstruction. As a result of this false merging, the track multiplicity may be wrong and the track momentum and particle identification from the merged track may be wrong as well.

The estimation of the systematic is done by pre–selecting the events before any selection in the analysis. The merged tracks are checked to see if they correspond to two segments that should not have been merged because they overlap in z direction. This procedure found no übermerged tracks in data and few in MC. The events are then passed through a reconstruction where the false merging is corrected. The difference between the corrected and wrong reconstruction is considered as a systematic error[61].

4.1.7 TPC field distortions

In the TPCs, due to imperfections in the magnetic and electric fields, the path of the drifted electrons in the gas can be distorted respect to the direction of the field lines. The impact of inhomogenaties in the TPCs is perform using a Monte Carlo study. A first measurement on the "field correction" is done. This field correction is a calculation of the magnetic field inside the basket exists. Then, a second measurement to account for additional distorsions of the magnetic and electric field in the TPCs is performed using the results from a laser flashing the central cathod of the TPCs. With this second measurement we obtain an additional correction, the "the field distortion". For the real data the field correction alone is used. The size of the distortion correction is considered to define the systematic error for the field distortion effect. In both measurements, data/MC differences are used to obtain the systematic [61].

4.1.8 TPC Momentum Scale

The momentum scale error is obtained from the B–field measurement [61]. Deflections in the plane transverse to the drift direction distort the image of the track at the readout plane. This distortion of the track shape leads to a bias in the reconstructed momentum of the track. The inhomogeneities in the electric and magnetic fields must be calibrated.

This is done by using MC studies of th effect of different magnetic field (one homogeneus and other MC not homogeneus).

4.1.9 FGD-only track efficiency

The FGD–only track efficiency is the efficiency to reconstruct a track from hits in the FGD1 using only the stand–alone reconstruction in that FGD. To measure the systematic[61], a control samples of stopping protons in FGD1 is used. such sample consider protons that pass trougth TPC1 and do not leave the FGD1. This way from the TPC1 we can retrieve the information about the direction and the moemntum of the track. This systematics reconstruction efficiency has been computed from the ratio of the data efficiencies over the Monte Carlo efficiencies. Being the efficiency the number of successful tracks in the control sample divided by the number of good candidates in that control sample. The final systematic is provided by momentum and direction of the track.

4.1.10 FGD-only track PID

Similar to the TPC PID, to estimate the FGD PID systematics we use information from the deposited energy along a track. The FGD PID systematic [61] uses a control sample of stopping non-interacting particles (we select them at low momentum). The estimation is based on the measurement of the energy deposited along the track. This quantity is then compared to the expected energy deposit for a particle with a momentum in a given range in the FGD and particle type. To do this, control samples of protons and muons stopping in the FGD1 and crossing TPC1 are selected. The pions are not selected as it is difficult to select stopping pions non-interacting in the FGD. The muon sample is then used to model the pion identification in the FGD. To estimate the systematic, the probability of particle mis–identification in data and MC is calculated for each given particle hypothesis.

4.1.11 FGD Hybrid IsoRecon Efficiency

This analysis [61] was designed to examine the FGD FGD–Only track reconstruction efficiency in the presence of at least one long muon track and an additional, optional long proton track. Since these FGD–Only tracks are used by the analysis presented in this thesis.

It is called hybrid because it involves different information from different sources. Here it is used the combination of hit information from individual, single–particle particle gun

events into beam CCQE vertices selected from data and Monte Carlo. It is generated four hybrid samples, namely CCQE data and MC events each of which are separately proton–hybridized and pion–hybridized. The data/MC ratio efficiency of the FGD–Only reconstruction is used to evaluate the size of the systematic for each sample.

4.1.12 FGD Mass Uncertainty

This systematic takes into account the uncertainty in the FGD1 mass. It count the mass for each component of the FGD1 and take into account each error. The analysis concluded that the uncertainty on the total FGD XY module mass was 0.67% [63].

4.1.13 Michel Electron efficiency

This systematic uncertainty measures the Michel electron detection efficiency [61]. Michel electrons are electrons that come from the decayed pions into muons. We identify these electrons from delayed particles respecto the primary ones (the ones coming from the neutrino interaction). The FGD–triggered cosmic data was used to estimate the differences in the Michel electron detection efficiency between the data and the Monte Carlo simulation.

4.1.14 TPC-FGD matching

This systematic includes two kinds of uncertainties [61]:

1. *Basic TPC–FGD tracking efficiency*: efficiency for a TPC track is to be matched to any FGD hit.
2. *Good TPC–FGD tracking efficiency*: efficiency for a TPC track is matched to be to most/all FGD hits.

For both efficiencies we apply a data/MC comparison to estimate the for the final systematic.

For the *basic matching efficiency* a control sample of through–going muons is used. These muons are required to be long tracks in the first two TPCs. The assumption is that if there are tracks in the TPCs, it was probably a long track that also crossed FGD1; by checking for the presence of a second TCP-FGD1 reconstructed track the TPC-FGD matching efficiency can be calculated.

For the *good TPC–FGD tracking efficiency* we need more requirements. The matching failures are checked first using the same set of through-going muons that were used in the basic matching. An additional check is then done by looking how far into FGD1 the second TPC track was matched (for the matched hits) is added. A different sample that probes the rate of matching failures for tracks that come at high angle from the FGD to the TPC is also used. This high angle sample is composed of FGD-triggered cosmic-ray events, where no reconstructed track in first or last TPC is required. This ensures that a high angle track enters from upstream FGD to the second TPC.

4.1.15 Out of Fiducial Volume events

The method for assigning systematics to the out of fiducial volume events (OOFV) relies on the MC[61]. It is computed a quantity which takes into account the different reasons, and their percentage, as to why the event wasn't rejected. For each reason an uncertainty is assigned and then all the different reasons are joined into a single quantity taking into account their percentage and uncertainty assigned.

4.1.16 Event pile up

The possible event pile–up is estimated using a sand muons sample [61]. Since sand muons are not included in the standard NEUT simulation, the Monte Carlo does not include the effect of events that are rejected due to coincidence with a sand muon and a correction must be made. An specific Monte Carlo is built to generate events that enters the ND280 forum outside. Then the data and the sand muons MC are used to estimate a this correction which is applied to reduce the weight of MC events.

4.1.17 Cosmic ray background

The cosmic rays background has been studied using a dedicated cosmic muon Monte Carlo simulation[61]. To compare the rates of cosmic events in MC and data, a number of runs taken with the beam trigger when the neutrino beam was off ("empty spill" data), is used. The rate of such events in data is found to be 1.13-1.41 times higher than in the simulation. The data/MC difference is taken as systematic.

4.1.18 Sand muon backgrounds

The analysis concerning the events originating from neutrino interactions outside the ND280 detector is performed using a dedicated Monte Carlo simulation[61]. Among the

particles produced by the neutrinos in the pit walls and surrounding sand, those which entered the magnet are simulated and reconstructed in the same way as in standard Monte Carlo. The size of sand MC sample corresponds to $2.6 \cdot 10^{20}$ PoT. The rates of sand interactions in data and sand simulation are compared using the tracks entering through the upstream wall of the P0D. The data/MC discrepancy is about 10% and it is included as a systematic uncertainty to the predicted numbers of sand events after the analysis selection.

4.1.19 Pion secondary interactions

A "pion secondary interaction" is an interaction that a pion undergoes outside of the nucleus from which it was produced. These processes are modelled in Geant4, however the model has been found to differ significantly from the available external data (mainly considering MiniBooNE data). In addition, related to the measurements of the external data the uncertainty in the external data needs to be taken into account.

This systematic is computed by taking into account two types of weigths [61]:

1. One weight to consider Monte Carlo disagreement with respect to the pion secondary interaction data (a correction weight).
2. One weight to consider variations based on the uncertainty in the data, for systematic calculations (a variation weight).

These weigths are is applied considering each pion momentum and charge (done for positive and negative pions).

4.2 Systematic Error Propagation

A framework have been developed for the systematical error propagation which is based on several models depending on the nature of the systematic error. In all cases, the Monte Carlo sample is modified or *re-weighed* and the full sample selection then re–applied on the newly modified observables.

We use four different methods for the systematical propagation:

- Efficiency–like. To take into account the efficiencies on the reconstructed variables with respect to the true associated ones in the Monte Carlo.

- Reconstructed observable variation. to take into account the possible different resolution or biases in the observables between the data and the Monte Carlo.
- Normalization systematic error. For systematics associated to the total event normalization.
- Nominal Monte Carlo. For systematic that can alter the central value of the Monte Carlo prediction.

The propagation model applied to each of the systematic errors is shown in Table 4.1 and described in the following sub–Sections. We do apply this procedure for the propagation of the detector uncertainties in both analysis presented in this thesis, the ν_μ CC inclusive and the the $CC1\pi^+$ cross section.

4.2.1 Efficiency–like systematics

The systematic propagation interface searches for the Monte Carlo true object associated to the reconstructed track, also in Monte Carlo. If the event is properly reconstructed, it is weighted according to:

$$Weight = \frac{(\epsilon + \delta\Delta\epsilon)}{(\epsilon)}$$

But, when the reconstruction variable differs from the original (like for example in a wrong charge association to a particle track) or the object was not found in the reconstruction, the event is weighted according to its inefficiency:

$$Weight = \frac{(1. - \epsilon - \delta\Delta\epsilon)}{(1. - \epsilon)}$$

where ϵ is the true efficiency of the association (true–reco), $\Delta\epsilon$ is the systematical error in the efficiency and δ the toy random variable that follows the corresponding probability density function, normally a normal distribution.

The way the efficiency–like is computed in the systematic error studies is based on studies comparing the data and the Monte Carlo prediction using control samples. Sometimes the efficiency of the control sample doesn't correspond to the one of the analysis on which we need to apply this systematic. For this reason, we applied a correction on the efficiency obtained by control samples. To do this, we obtain the efficiency in our analysis (ν_μ CC inclusive analysis) using only Monte Carlo and the resulting efficiency is:

$$\epsilon_{final} = \frac{\epsilon_{\text{control sample, data}}}{\epsilon_{\text{control sample, MC}}} \times \epsilon_{\text{analysis, MC}} \tag{4.1}$$

The efficiency type systematics do not require repeating the selection, the error propagation takes place uniquely through the event weights.

4.2.2 Reconstructed observable variation

This systematic propagation model is applied to the particle identification and momentum reconstruction variables. Those observables might show different resolution in data and Monte Carlo or a small bias. The systematic propagation interface smears the observables before running the event selection on the new observables.

This type of systematic error propagation is performed in different ways depending on the properties of the error. They can be grouped in four classes:

1. When the true observable is known (i.e. the momentum), the interface re-scales the difference of the reconstructed observable with respect to the true one:

   $$Obs^{new}_{reco} = Obs_{true} + (Obs^{old}_{reco} - Obs^{true})\frac{\sigma_{new}}{\sigma_{old}}$$

   where

   $$\sigma_{new} = \sqrt{\sigma^2_{old} + \delta^2 \Delta\sigma^2}$$

   and σ_{old} is the nominal observable dispersion in Monte Carlo, $\Delta\sigma$ is the systematic error associated and δ is a random variable following the corresponding probability density function (normally a normal distribution). The momentum resolution error is treated this way.

2. To correct the observable for a specific particle, for example the ionization for one type of particle, it is identified the true particle associated to the track and applied the corresponding correction, normally a bias smeared with a normally distributed random variable:

   $$Obs^{new}_{reco} = Obs^{old}_{reco} + \delta \Delta Obs_{reco}$$

   where δ is the random variable, and ΔObs_{reco} is the bias to apply to the observable. This propagation is applied to the TPC and FGD ionization systematics.

3. When there is a simple observable scale, like the momentum scale due to the B field calibration, it is corrected the value with an scale factor that varies according to the expected error:

$$Obs^{new}_{reco} = Obs^{old}_{reco}(1. + \delta\Delta Scale)$$

where δ is the random variable, and $\Delta Scale$ is the error on the scale to propagate.

4. When there are 2 possible values, like in the case of the residual TPC B field distortions, the observable is computed by weighting the two results with a random variable following a flat distribution between 0 and 1:

$$Obs^{new}_{reco} = Obs^{nominal}_{reco} + (Obs^{alternate}_{reco} - Obs^{nominal}_{reco})\delta$$

where δ is the random variable, $Obs^{nominal}_{reco}$ is the nominal observable and $Obs^{alternate}_{reco}$ the alternate result with other reconstruction criteria.

4.2.3 Normalization systematics errors

These are systematic errors associated to the total event normalization. The pile–up systematic error or the FGD mass systematics are good examples of this type. For this case the event is re–weighed according to the variation suggested by the systematic error studies.

$$Weight = (1. + \Delta Nom\delta)$$

where $\Delta Norm$ is the error in the normalization and δ a random variable to propagate the variations.

This systematic error is propagated to all the events in the case of the pile–up errors. Some times this is propagated to a sub–sample of events, events from the FGD for the FGD mass uncertainty and events from outside the fiducial volume for the out of fiducial volume errors.

An special case of this type of systematic is the pion re–interaction uncertainty. For this systematic, the event is re–weighed with the product of the weights of all the pions in the event. The weight per pion is computed following the history of the pion interactions before reaching the TPC and associating a weight error depending on the type of interaction.

4.2.4 Nominal Monte Carlo

Some of the systematic error propagation can alter the central value of the Monte Carlo prediction. This is clear for the cases where the probability density function is a flat distribution between 0 and 1. To compute the nominal Monte Carlo, the variation is set to 0 for the normal distributions and to 0.5 for the flat distributions.

Chapter 5

The ν_μ Charged Current Inclusive Analysis

A critical factor in improving neutrino oscillation measurements is the control of the systematic uncertainties, especially as more powerful neutrino sources are available and the statistical uncertainty is thus reduced. Because much remains uncertain in the modeling of neutrino sources and cross sections, most of modern neutrino oscillation experiments use two detectors to constrain their systematic uncertainty by measuring the flavor content of the source close to the source, before neutrinos have had time to oscillate. At this purpose, the T2K experiment use ND280 to constraint the flux and cross section uncertainties.

In this chapter we describe the ν_μ CC inclusive event selection adopted in ND280 since 2013. We explain which are the differences with respect to the previous ν_μ CC inclusive analysis and which are the advantages and the impact of the results obtained with this new approach.

5.1 Previous ν_μ Charged Current Inclusive Selection

The first ND280 data analysis to extract the muon neutrino beam properties was done using a CCQE and CCnQE analysis technique. This starts by selecting all the charged current (CC) interactions occurring in the FGD1 detector. In each event, the highest momentum negative track is the muon candidate. This CC interaction sample is subsequently split into a charged current quasi-elastic (CCQE) sample, and a charged current non quasi-elastic (CCnQE) sample for interactions in which at least one pion was produced.

Events in the CCQE sample have only one TPC-FGD track and no Michel electrons in the upstream FGD, originating from the decay of a pion stopped in FGD producing a muon, and then an electron. The Michel electrons are identified using the time information in FGD.

The results obtained by this analysis use only the data from 2010, 2011 and 2012. Momentum–angle spectra were produced for the CCQE and CCnQE samples. The main physics application of these results was to estimate beam and neutrino interaction properties with a maximum likelihood fit of the ND280 data along with the beam flux prediction and external cross section data as constraints.

The results of the fit and the high correlation between the ND280 and SK fluxes provide a significant reduction of the beam and cross section systematic uncertainties in the SK neutrino interaction rate prediction. The CCQE and CCnQE samples were split in the ND280 analysis to allow the CCQE sample to constrain the spectral shape, the flux and cross section parameters, while the CCnQE sample constrains backgrounds and cross section parameters. The momentum projection of the CCQE and CCnQE spectra prior to the fit, Figure 5.1, show a good agreement between data and MC.

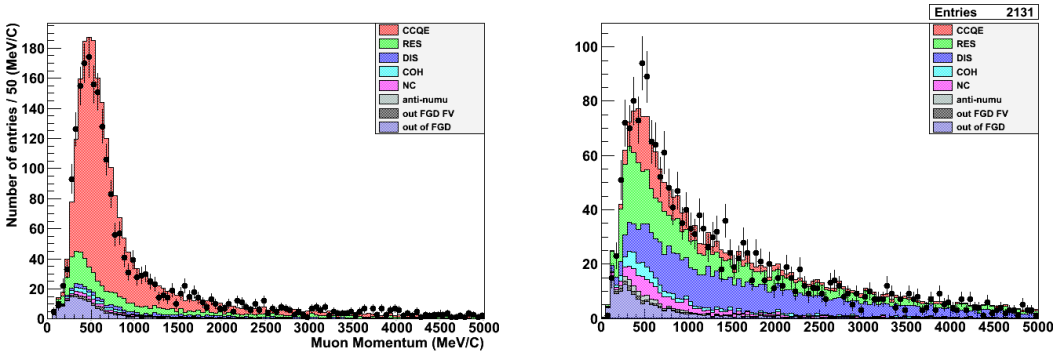

FIGURE 5.1: Momentum distribution of muon from selected CCQE interactions for data and simulation (left). Momentum distribution of muons from selected CCnQE interactions for data and simulation (right).

Nevertheless, contrary to what was expected the cross section parameter errors using this sample selection strategy remains the same also when doubling the data used in the measurement. This was confirmed when comparing results on the cross section parameters and their errors from 2010 and 2011 to the data from 2010 to 2012. This can be seen in Table 5.1. On this table, we can see the cross setion parameter errors after the constraint with ND280 data. Second column shows the values and their errors from the data obtained in 2010 and 2011 and the proton on target (PoT) used, on third column we show values for 2012 and on last column we show results for the total of the two sets, from 2010 to 2012. By comparing second and last columns errors on the parameters, we realize that by doubling the statistic the errors remains almost the same.

Cross section error	2010-2011 ($9.510^{19} PoT$)	2012 ($1.5610^{20} PoT$)	2010-2012 ($2.5110^{20} PoT$)
M_A^{QE} (GeV)	1.21 ± 0.20	1.32 ± 0.23	1.33 ± 0.20
M_A^{Res} (GeV)	1.15 ± 0.10	1.18 ± 0.10	1.15 ± 0.10
CCQE Norm (< 1.5 GeV)	0.95 ± 0.09	0.97 ± 0.09	0.95 ± 0.09
CC1π Norm (< 2.5 GeV)	1.61 ± 0.30	1.44 ± 0.29	1.61 ± 0.29
NC1π^0	1.19 ± 0.40	0.19 ± 0.40	1.19 ± 0.40

TABLE 5.1: Cross section parameter errors using the *old muon neutrino CC inclusive selection*. They are showed using data obtained from 2010 to 2011 on the second column, from 2012 for third column and on last column it's showed using data from 2010 to 2011. Errors on each cross section parameter is shown. Proton on target (PoT) used is also shown.

5.2 New Strategy for the ν_μ Charged Current Inclusive Selection

With the result of the previous strategy, it was realized that it was needed to perform a better constraint for the different interaction channels in order to reduce the uncertainties related to the cross section parameters. This goal motivated the current approach where a separate CC1π^+ sample is created with the aim of improving the determination of the M_A^{Res} parameter.

In this new approach, the CC inclusive sample is divided into three samples: CCQE-like, CC1π^+-like and CC-Other.

The CCQE-like sample consists of events without any pion (CC0π), the CC1π^+-like sample consists of events with one, and only one, positive pion, and the CC-Other contains all the other categories (a negative or neutral pion, or more than one positive pion). For the categorization of the Monte Carlo an event "topology" scheme is used. This approach is based on looking at the true particle types that emerge from the nucleus after the interaction happens. These categories are more consistent with what is detected.

The sample separation provides a basic cross section constraint on the CCQE and CC1π^+ samples as a function of the muon momentum and angle.

This analysis uses as its starting point the "global" ND280 reconstruction that combines reconstruction information from multiple detectors. In practice, only the reconstruction information from the FGDs and TPCs plays a primary role in this event selection. Only interactions in the FGD1 are included in this analysis. For simplicity and due to the stage of the reconstruction at the different detectors, we only look for interactions in FGD1 and use information from the tracks reaching the TPC.

As it was done for the previous ν_μ CC analysis, we provide the measured interaction rates, along with the Monte Carlo predictions and the detector systematics. The oscillation analysis working group then constructs a joint likelihood fit that includes the neutrino flux covariances from the beam group flux predictions, cross section uncertainties, and the ND280 spectrum analysis, ie this analysis.

5.2.1 RUN Data and Monte Carlo Sets

All data and Monte Carlo reconstructed events used are based on the ND280 reconstruction production for year 2013 which is called Prod5.

The data set for this analysis includes the data collected by ND280 between January 2010 and May 2013. Only data collected that passed the beam and quality check is used in the analysis ($\sim 90\%$ of the total data collected).

The Monte Carlo data sets are divided into the different run periods: Run 1, Run 2, Run 3 and Run 4 to take into account the possible different beam and detector conditions of the four run periods. In order to do a proper data–Monte Carlo comparison, we need to take into account the further possible different beam and detector conditions per each Run. Moreover, there is a dedicated MC sample ("sand muons") with the events coming from the interactions of the muon neutrino beam with the sand surrounding the detector. This is different from the standard Monte Carlo sample that includes only events interacting in the ND280 detector. The sum of the events coming from the interactions with the sand and with the detector should correspond to our observation. The two different MC samples are summed, according to the different PoTs, in the analysis.

We summarize the PoT in Table 6.1 for data and Monte Carlo. The comparisons data–Monte Carlo are performed using MC samples correctly normalized according to the PoT to the different periods.

5.2.2 Topology Categorization

We measure the contribution of each true interaction type in the selected samples using the Monte Carlo information. We define as *topology* the set of particles we have when they leave the nucleus after the Final State Interaction inside the target nucleus (after FSI). This approach give us a sample of what we can reconstruct with our detectors. The different true categories are classified according to the different topologies and are defined similarly to the selection ones:

Sample	Data PoT	MC PoT	Sand PoT
Run 1	$1.66891 \cdot 10^{19}$	$9.985 \cdot 10^{20}$	$9.49 \cdot 10^{20}$
Run 2	$7.83776 \cdot 10^{19}$	$2.133 \cdot 10^{21}$	$1.898 \cdot 10^{21}$
Run 3b	$2.14598 \cdot 10^{19}$	$3.0 \cdot 10^{20}$	$9.49 \cdot 10^{20}$
Run 3c	$1.34821 \cdot 10^{20}$	$1.5 \cdot 10^{21}$	$9.49 \cdot 10^{20}$
Run 4	$3.38734 \cdot 10^{20}$	$4.6135 \cdot 10^{21}$	$1.898 \cdot 10^{21}$
Total	$5.90082 \cdot 10^{20}$	$9.545 \cdot 10^{21}$	$6.643 \cdot 10^{21}$

TABLE 5.2: Number of PoT for each data set. The PoT in data corresponds to the collected data after beam and quality criteria checks, the PoT in MC corresponds to the used MC sample. The third and fourth columns correspond to the MC events coming from the interaction of the beam with the detector and the sand surrounding the detector, respectively.

1. *CC0π*, that is "CCQE": is defined as events with a true negative muon and without any (charged or neutral) pion in the final state.

2. *CC1π$^+$*: is defined as events with a true negative muon and one positive pion, and no negative or neutral pions in the final state.

3. *CC-Other*: corresponds to the rest of the *CC* events that are not in the previous two samples. This means events with a negative muon and at least one neutral or negative pion, or with more than one positive pion are included. Also events with less common particles (kaon or eta) are included. This sample constitutes basically the DIS sample, since the presence of a negative pion is a good signature of DIS, as it will be shown later in this Chapter.

4. *Background*: is composed of the anti-neutrino and the neutral current events.

5. *External*: corresponds to events on which the interaction vertex is outside the FGD1 fiducial volume defined. These events can be in the FGD1, but not in the fiducial volume or coming from outside the FGD.

5.2.3 General Particle Identification Criteria

In this analysis, the muons and pions are identified using the TPC and the FGD detectors and different PID requirements are applied in each detector. The TPC is used to reconstruct muons, charged pions, electrons and positrons. The electrons and positrons are used to identify the neutral pions. All particles that are not the muon candidate, main particle in the event, are called *secondaries*.

The FGD is used to reconstruct short track positive pions. The main reason for this is that the muon has been already identified (in the TPC) and positive pions are more abundant than negative ones, and no charge identification is possible in the FGDs. No

electrons/positrons are identified, thus no neutral pions are reconstructed in this analysis using the FGD PID. We use two different methods to identify pions in the FGD1: i) the Michel electron tagging sub–Section 5.2.3.2 and ii) the FGD PID sub–Section 5.2.3.3, that identifies pions when there is a track without segments in the TPC (FGD-Only tracks).

5.2.3.1 TPC PID

The TPC PID has been described in sub–Section 3.2.6. To improve the particle discrimination which can be achieved using the simple pull variable, we build two different methods to identify particles in the TPC. The first method is used to identify muons as primary particles in the event [1] and the second method is used to identify all other primary particles in the event once the muon has been already selected. Note that the TPC particle selection has been build in order to describe ν_μ charged current events, for this reason, we start by the muon selection.

Before to apply the PID criteria, all the TPC selected tracks have to accomplish the *quality and Fiducial cut*. This cut is performed in order to achieve a minimum condition of the track that ensures the quality of the reconstruction. To accomplish the *quality and Fiducial cut*:

- the TPC track must start inside the FGD1's fiducial volume (FV), see 3.2.7, and has more than 18 TPC clusters. The vertex is generally based on where the fitted 3D track intercepts the vertical plane of the upstream-most matched FGD hit. The requirement that the track has more than 18 clusters in the TPC rejects short tracks for which the reconstruction and the particle identification is less reliable.

Muon PID The first method described is a simple likelihood function which combines the different particle hypothesis for the pull distributions. We define a new variable, L_i, where i is the particle type we want to check and it is defined as:

$$L_i = \frac{e^{-\delta_i^2}}{\Sigma_l e^{-\delta_l^2}} \tag{5.1}$$

and l= muon, pion, proton and electron. Given the estimated momentum of the track, the discriminator function is calculated for the muon, pion, and proton hypotheses. We define this discriminator function for the MIP particles, L_{MIP}, as

[1] We refer to primary particles to those coming from the neutrino interaction.

$$L_{MIP} = \frac{L_\mu + L_\pi}{1 - L_p} \tag{5.2}$$

We can see in Figure 5.2 the L_{MIP} distribution. This function can be used to distinguish MIP particles, in addition with the charge and momentum information. This method is used in sub–Section 5.2.4 to identify muons.

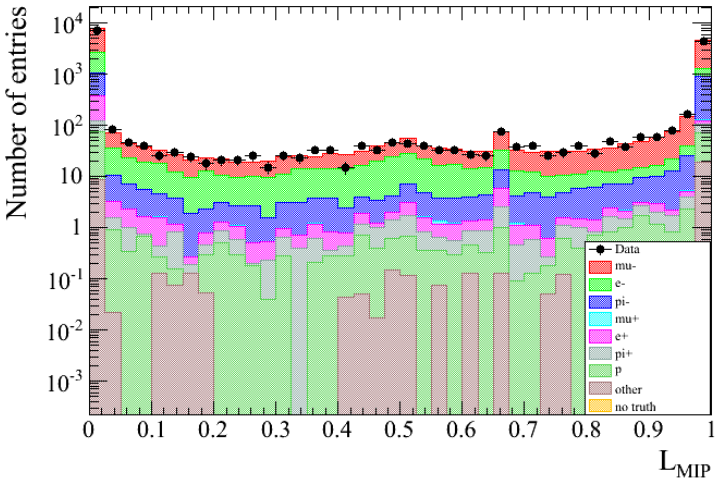

FIGURE 5.2: L_{MIP} distribution for Monte Carlo (color) and data (dots) using the total data for the run periods 1+2+3+4 that corresponds to $5.9 \cdot 10^{20}$ proton on target.

We know that electrons should concentrate at lower energies, then we look into different strategies in order to combine the momentum information of the track and the L_{MIP} information. Two cuts are then applied, by defining L_{MIP} and requiring:

$$L_{MIP} = \frac{L_\mu + L_\pi}{1 - L_p} > 0.8 \qquad \text{if } p < 500 \text{ MeV/c} \tag{5.3}$$

$$L_\mu > 0.05 \tag{5.4}$$

The first of this cut rejects electrons. The cut is only applied for $p < 500$ MeV/c, since at low momentum electrons are more abundant and we need the MIP condition to remove possible ν_e contamination. The second cut removes protons and pions. Note that the PID cuts are applied after the Monte Carlo PID resolution has been smeared to have the same pull width in the data–this is a ∼5% difference in width before the correction.

In Figure 5.3 it is shown momentum of the muon candidate once selected in the TPC following this prescription. We see that muon contribution is quite high also considering that we didn't add any extra cut.

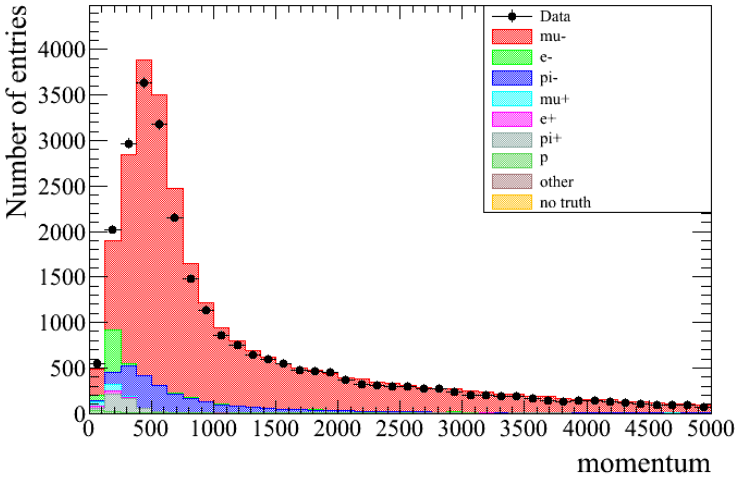

FIGURE 5.3: Momentum of the TPC selected as muon candidate following the TPC PID conditions. For Monte Carlo (color) and data (dots) using the total data for the run periods 1+2+3+4 that corresponds to $5.9 \cdot 10^{20}$ proton on target.

Pion and electron PID The other method developed to identify particles is based upon the previous likelihood method explained. We use this information provided by the L_i distributions to check which is the "most probable particle" for each TPC track. Once the muon candidate has been already selected abundances of each particle type should change. Then, the method is based on computing the probability that the track is consistent with a given particle hypothesis, and then attributing the particle type according to the highest probability.

The most probable particle method starts by separating negative from positive particles in the TPC. For the positive case three different types (or particle hypothesis) are considered: positive pion, positron or proton. In the negative case two types (since the muon is already selected): negative pion and electron are considered.

A "probability of the particle" for each particle type is computed using the L_i criteria.

To check which type is the most probable particle type, the ratio of each L_i and the sum of all the L_i of all the particle types is computed:

$$P_i = \frac{L_i}{\Sigma_l L_l} \tag{5.5}$$

where i = *particle checked* and l = *positive pion, positron or proton* in the positive case and l = *negative pion or electron* in the negative case.

Then, in case of a positive particle, it is tagged with the type that has the highest probability. If the most probable case is to be a positron, but the momentum is bigger

than 900 MeV we tag the particle as a proton, otherwise, as a positron. This requirement on the momentum is explained by Figure 3.20 on which we observe the difficutlties on distinguish protons from positrons.

In the case of a negative particle, if the probability to be a pion is > 0.8 it is tagged as a negative pion, if not, it is an electron. This is shown in Figure 5.4. The plot shows the distribution for the probability to be a pion, the blue line corresponds to the case when the true particle is a negative pion and the red line corresponds to the case where the true particle type is an electron.

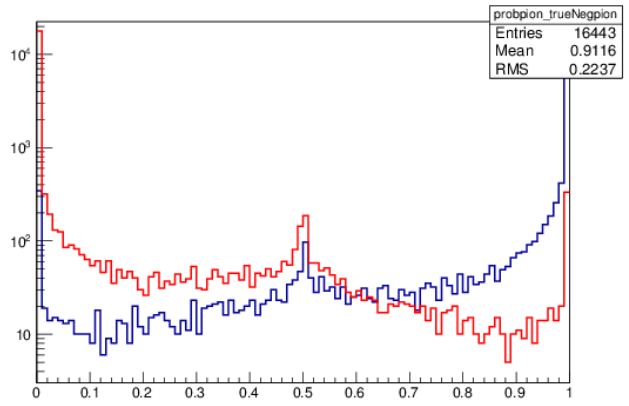

FIGURE 5.4: Distribution of the probability of being a pion in the TPC. The blue line correspond to the cases when the true particle type is a negative pion and the red line corresponds to cases where the true particle type is an electron.

The momentum distribution of the selected positive and negative pions and electrons/-positrons in the TPC, once the muon has been already selected, are shown in Figure 5.5. We can observe a general good particle identification for these secondary tracks. As expected, in the negative pion tracks contamination comes mainly from muons. This is due to the fact that muons and pions have a similar behavior with respect the dE/dx distributions, as already seen from Figure 3.20. These events can be events on which the muon candidate is not a real muon but a pion and then we have the muon as secondary track in the event. For the positive pion, we observe that the main contamination comes from protons. This is also expected from Figure 3.20 since the muon contamination is reduced by applying the positive charge requirement and there are very few positive muons coming from $\bar{\nu_\mu}$ events. This proton contamination is done in the momentum region where the pion and proton has more problems to be distinguished, according to Figure 3.20. For the electrons, contamination comes from negative pions. And for positrons we observe a sharp cut, this cut on momentum has been already explained and it is applied to reject protons. Main contamination in positrons is due to positive pions.

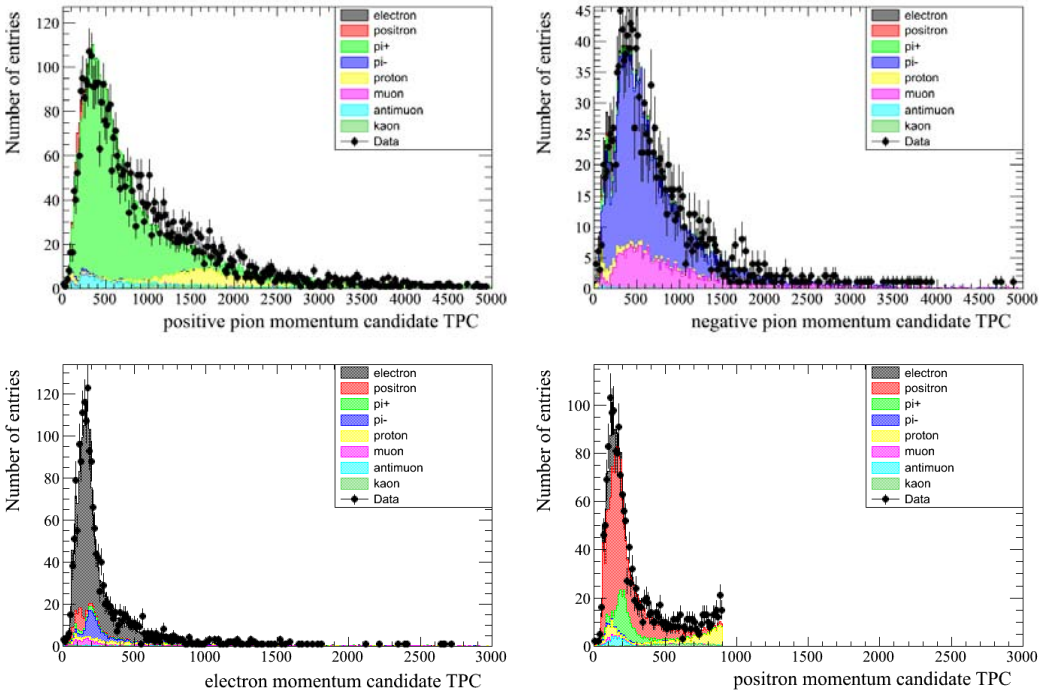

FIGURE 5.5: Upper row, from left to right, distribution of the momentum (units are in MeV) of positive pions, negative pions and (bottom row, from left to right) electrons and positrons reconstructed in the TPC using the TPC probability criteria, once the muon has been already selected.

5.2.3.2 Michel Electron tagging

The identification of the Michel electrons is done by looking for time-delayed FGD hit clusters with respect to the beam bunch window, with a total charge deposit of at least 200 photoelectrons. A full description of this requirements is explained in [64]. Every Michel electron is tagged as a positive pion.

If an event has Michel electrons there is no need to look for more pions reconstructed using the FGD PID. This is because if a pion is identified using the Michel electron and also using the FGD–Only they most probably refer to the same track, and the short pion track has been reconstructed using FGD–Only and then it decays into the Michel electron.

5.2.3.3 FGD PID

The FGD PID is used to identify positive pions reconstructed as FGD-Only tracks [2]. For this analysis the FGD PID only is applied in cases where there are no Michel electrons and we reconstruct a maximum of one, and only one, pion track using the FGD PID

[2]Tracks with segment only in one of the FGDs.

criteria. This is done in order to eliminate the possibility of having broken tracks that can be reconstructed as two pions when there is only one. This PID in the FGD1 is build using the dE/dx information and calculating the pull distributions at each particle hypothesis, see 3.2.7.1.

The true particle type accordingly to the pion pull distribution in the FGD for FGD–Only tracks is shown in Figure 3.23. Notice that in this plot all tracks that are FGD-Only defined are included, for FGD1 and FGD2. They are also some of these FGD–Only tracks that are broken tracks [3]. The inclusion of these broken tracks can explain why the pull of the pion seems not clearly centered at zero, since these broken tracks can produce a bias of the reconstructed dE/dx with respect to the expected one (the expected one is not assuming a broken track, just a pion in the FGD).

To identify positive pions in the event the following requirements on the FGD-only track were applied:

1. The track must start in FGD1.
2. Must be fully contained in the FGD1 in a fiducial volume which is different to the one used for the TPC tracks. The fiducial volume used for FGD–Only is defined as: $-887. < |x| < 888.$ mm, $-834. < |y| < 942.$ mm, and $1 < Z < 28$ plane units. This fiducial volume is adopted according to reconstruction FGD expert recomendations, the main purpose is to reduce the number of broken tracks.
3. The cosine of the angle, with respect to the Z direction (along the ND280) must be $>$ 0.3 (or $<$ -0.3 in case of negative cosine). This condition is applied to be consistent with the systematics studies which still not cover that region [4]. Figure 5.6 shows the tracks that fulfill these conditions explained here and once the muon has been already selected in the TPC. It is possible to see that the pion pull, when the true particle is a positive pion, is centered at zero. Any dispersion of this distribution, for example the peak of protons or the second peak of pions, can be explained by the mentioned broken tracks. A broken track can start outside the FGD fiducial volume, but be reconstructed as fully contained particle. To limit such contamination when FGD-only tracks are used to reconstruct the pion, the maximum number of FGD-Only tracks allowed is one.
4. The pion pull must be $>$ -2. and $<$ 2.5.

[3] Broken tracks are tracks that due to reconstruction failure are reconstructed as two different tracks.
[4] This systematic is studied using interactions of a replica of the FGD1 detector and some angles were still not covered in the systematic studies for this measurement.

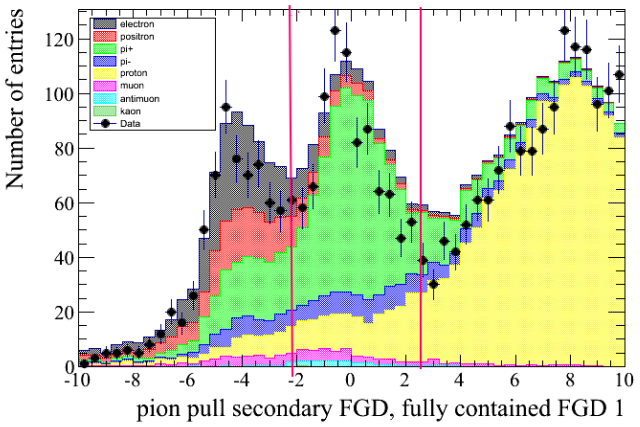

FIGURE 5.6: Pion pull distribution of the FGD-only tracks once the muon has been already selected in the TPC, without apply specific cuts to identify pions.

The result of all the conditions is a clean sample of positive pions (sample selected with the red lines) as seen in Figure 5.6, which shows the pull pion distribution for the selected tracks.

5.2.4 Event Selection Cuts

In order to get the cleanest sample of CC signal events, a series of cuts designed to select the inclusive CC ν_μ interactions in the FGD1 were applied. Then a set of cuts were applied to separate this sample into CC0π-like, CC1π^+-like and CC-Other-like events. A flowchart is shown in Figure 5.7, where "ME" referes to Michel electron. The inclusive CC selection criteria are:

1. *Data quality flag.* The full spill must pass the ND280 data quality criteria [5].

2. *Bunching.* The tracks are grouped together in bunches according to their times. Neutrino interactions in two different bunches but within the same beam spill are treated as two different events, eliminating accidental pile-up of events. We analyze only events associated to the beam trigger, i.e. compatible with one of the 8 [6] bunches of the beam spill. We accept events within 4σ ($\sigma = 15ns$) from the center of each bunch. In this way, the background coming from the cosmic neutrinos is largely reduced, assuming flat cosmic rate.

3. *Total Multiplicity cut.* In every event there has to be at least one reconstructed track in the TPC.

[5] There are several criteria that are used by the different detectors to assess the quality of the data, starting from the hardware status of the detector and also some reconstructed variables. In ND280, only if all the detectors pass the data quality established in each detector, then the data can be considered good for analysis.

[6] They were only 6 bunches for Run I

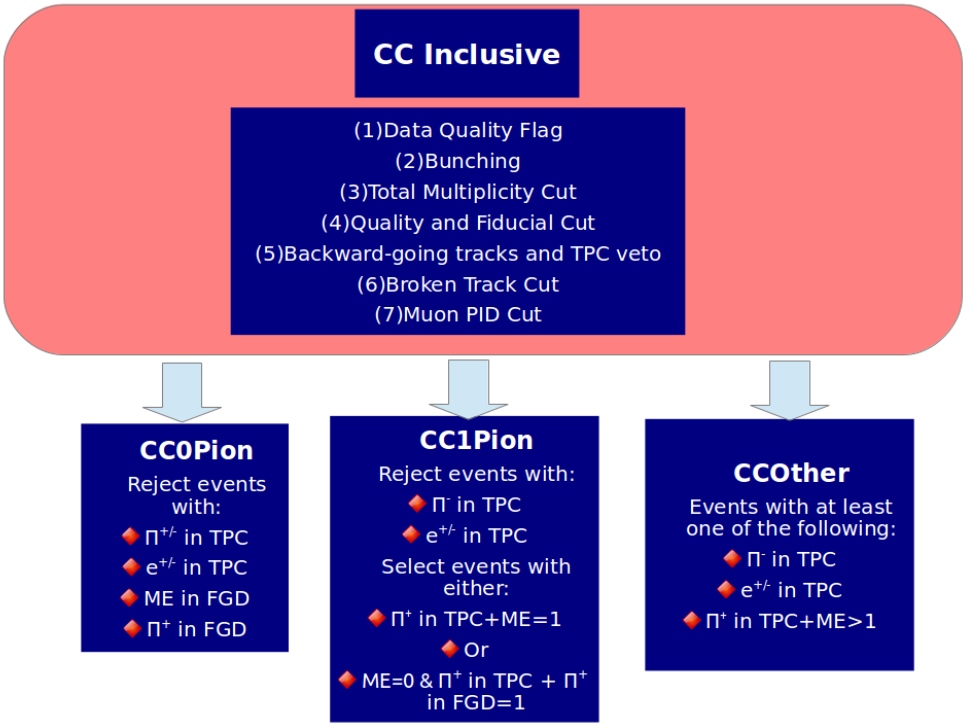

FIGURE 5.7: Selection flowchart. First a CC-inclusive sample is selected, then it is split into three different samples: CC0π-like, CC1π^+-like and CC-Other. The corresponding selection cuts are shown in each box.

4. *Quality and Fiducial cut.* In every event there has to be at least one track with FGD and TPC components that starts inside the FGD1's fiducial volume (FV), see 3.2.7. The TPC track has to accomplish the *quality and Fiducial cut* already defined for all TPC tracks in sub–Section 5.2.3.1.

5. *Backwards-going tracks and TPC1 veto.* The goal of these cuts is to remove mis–reconstructed events entering the FGD1 fiducial volume from the upstream edge of the detector. This is only applied in events on which we have more than one track.

   The start position of the second highest–momentum track (if any) with a TPC segment must be less than 150 mm upstream from the higuest momentum negative track's starting position. If it is less, the event is rejected on the grounds that there is a track in the event that probably entered the detector from the P0D or magnet region. This cut was needed since at this reconstruction stage we don't have timing information from the different detectors which may help to distinguish backward–going events from events coming from any other detector than the FGD1, for example coming from the P0D, see Figure 5.8. Then we consider only events on which the highest momentum negative track is forward–going.

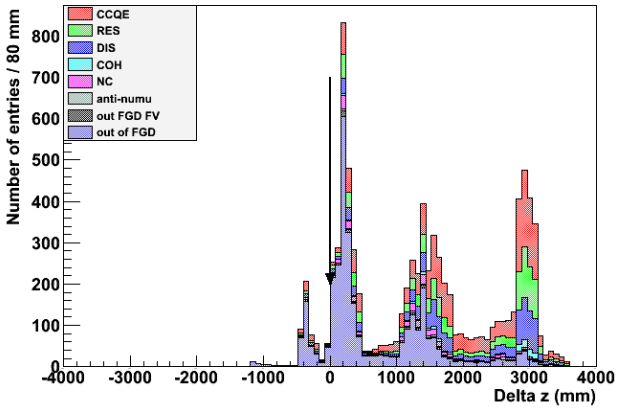

FIGURE 5.8: Distribution of the TPC Veto Δ_z observable (start position of the second higuest–momentum track minus hte start position of the higuest momentum negative track) before the cut is applied.

6. *Broken Track cut.* This cut is applied in order to reject the external background that comes from the last two layers of FGD1. This external background is produced mainly by tracks entering the FGD from the upstream side and with their vertex outside the FGD fiducial volume being reconstructed as two different tracks, see Figure 5.9. In most the cases the second part of this broken track is reconstructed as the highest energetic track of the event and then selecting out of FGD1 fiducial volume in the CC sample. Events with the highest momentum negative track's z start position is more than 425 mm away from the FGD1 upstream edge and there is at least one "FGD-only" track with its vertex out the FGD fiducial volume, are rejected. The "FGD-only" tracks are defined as tracks starting and not exiting the FGD. By applying this cut we reduce the out of FGD1 fiducial volume in the sample a $\sim 2\%$ and the sample is reduced by a $\sim 1\%$.

7. *Muon PID cut.* The highest momentum track that is compatible with the muon hypothesis from the TPC identification (see 5.2.3.1) is selected as "muon candidate".

Events that pass these seven cut steps are selected as ν_μ CC events.

5.2.4.1 Classification into CC0Pion, CC1Pion and CCOther samples

Once the CC inclusive sample is selected, conditions up to 7, we split the sample into the CC0π, CC1π^+ and CCOthers sub–samples. This is done thanks to the identification of all the other particles, not the muon, in the event. All the secondary tracks are required to be in the same time bunch as the muon candidate.

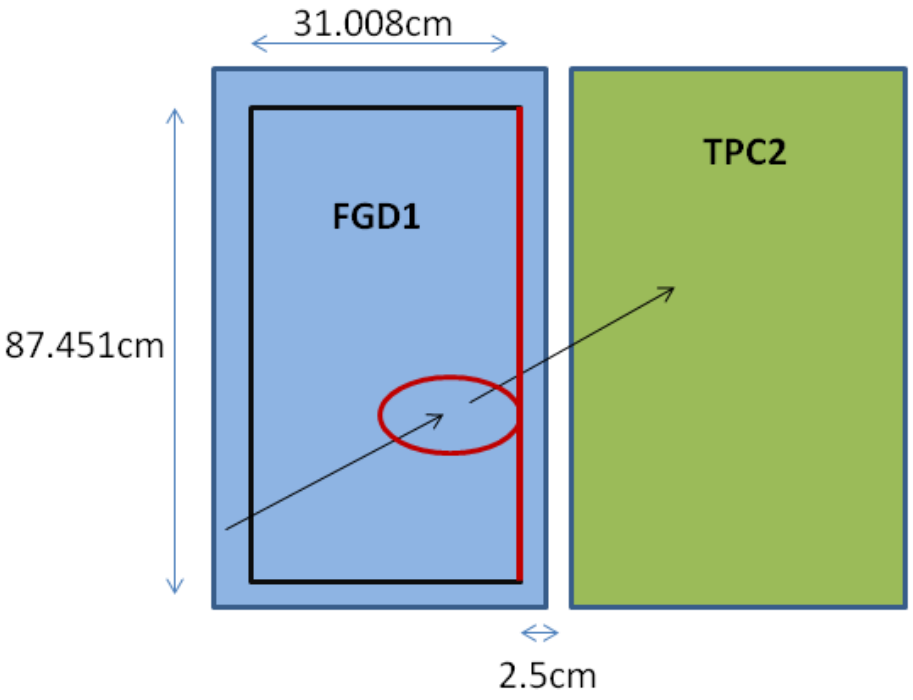

FIGURE 5.9: Example of a broken track. The long track is reconstructed as two different tracks in the FGD1 and TPC2.

We identify pions and electrons, positive or negative in the TPC according to criteria explained in sub–Section 5.2.3.1. Figure 5.10 shows the number of each type of particle tagged in the selected secondary tracks in the CC sample with TPC PID. It is shown with respect the true topology of the event according to the MC. In the plots inset of each distribution it is shown the same distributions with the unidentified particles (those in the zero bin) excluded. We can see for the plot showing the number of positive pions that in the first bin, when excluding the zero bin, we have a composition of $CC1\pi^+$ and CCOther, while from the second bin and bigger ones it is dominated by CCOther, the CC0π contribution is always negligible. This means that our positive pion tagging is working well. Contamination of CCOther events in the bin with one positive pion can be explained by the presence of other particles not showed in this plot (i.e. negative pions, electron/positrons, or ME/FGD pions).

For the plot showing the number of negative pions we see a clear CCOther dominat contribution, also in the bin with one negative pion. In this case, the negative pion tag is working fine as well. And for the electron/positron plot we also observe a dominant CCOther contribution. For the bin with only one electron/positron we also observe a dominant contribution of the CCOther cathegory what it is what is intented. In this case the tagging is also working well but not as well as for the pion tagging since here

we observe some contribution of $CC1\pi^+$ and $CC0\pi$. These can be caused by several reasons, it can be due to the tagging itself which can be not so good as in the pion case or it can be also due to secondary interactions of primary positive pion that interacts with the detector, very close to the vertex and for this reason we reconstruct the track as coming from the muon vertex, and we observe an electron/positron that comes from a this secondary interaction. We will discuss more these kind of effects on Section 5.4.

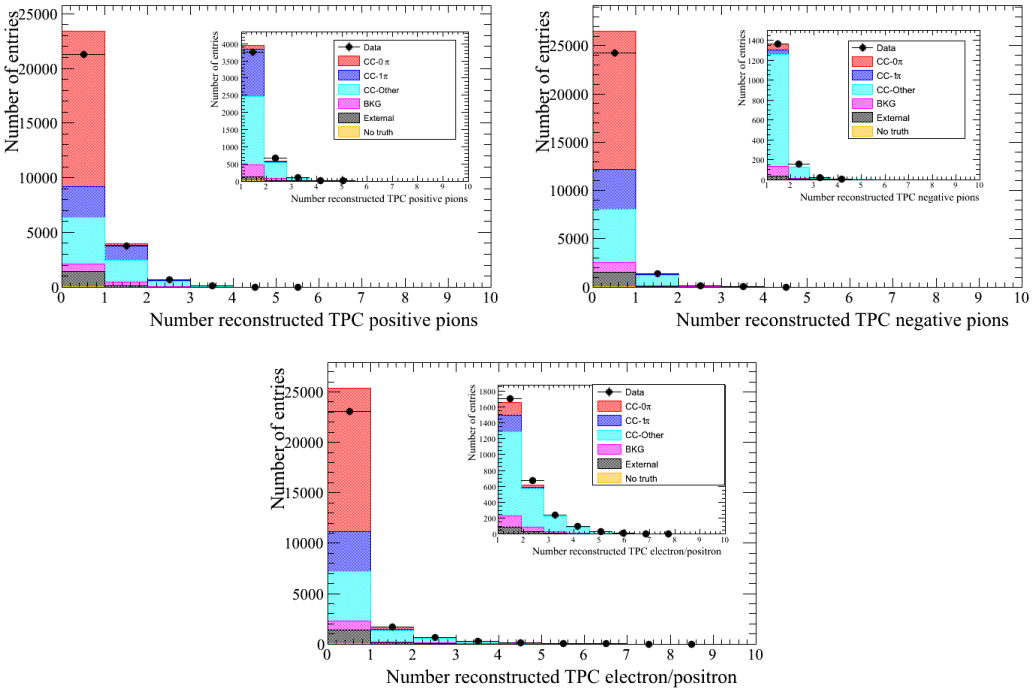

FIGURE 5.10: Up–left, distribution of the number of (from left to right) positive pions, negative pions (up–right) and electrons plus positrons (bottom). For the CC sample, reconstructed in the TPC using the TPC probability criteria. The plots inset of each distribution show the same distributions with the unidentified particles (those in the zero bin) excluded.

The reason for showing together the number of reconstructed electrons and positrons is because they are both signature of a neutral pion because neutral pions has a very short lifetime and they mainly decay via electromagnetic force into two photons.

Selection of positive pions using the Michel electron criteria is explained in sub–Section 5.2.3.2, while the FGD–Only pion tracks are explained in sub–Section 6.3.2.

In Figure 5.11 the top plot shows the distribution of the number of Michel electrons in the case where there is no secondary TPC track, according to the topology type. Events having only one Michel electron can be identified as $CC1\pi^+$ events. Events with more than one Michel electron the main contribution is CCOthers.

The distribution of the number of selected Michel electrons, for the CC sample is shown in Figure 5.12.

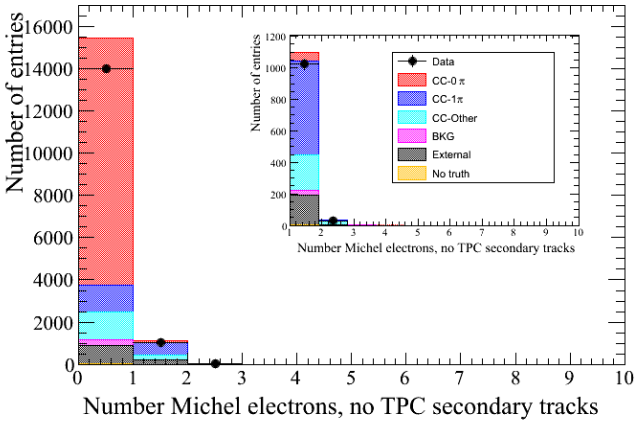

FIGURE 5.11: Distribution of the number of Michel electrons per event when there are no secondary tracks in the TPC.

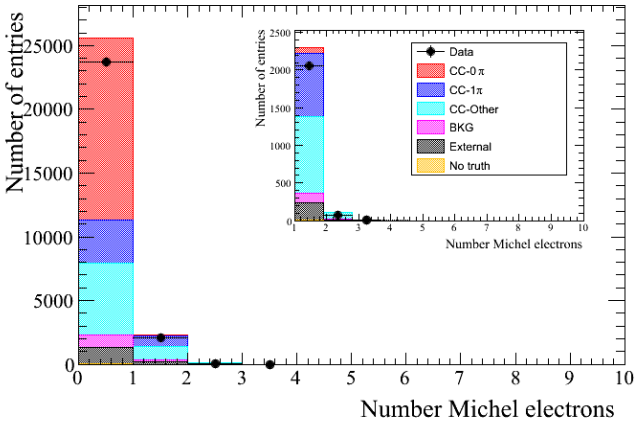

FIGURE 5.12: Distribution of the number of Michel electrons split accordingly to the true topology type, for the CC sample.

For the FGD–Only pions, Figure 6.5 shows the distribution of the number of selected positive pions using the FGD-only tracks criteria.

We see that when we select at least one FGD–Only pion we have a composition which is mainly CC1π^+ and CCOthers, while the CC0π contribution is very small.

According to the distributions showed here, we identify the CC0π, CC1π^+ and CCOthers sub–samples applying the conditions presented in Figure 5.7.

5.3 Details on the CC–Inclusive and the subsequent CC0π, CC1π^+ and CCOthers Samples

In this Section we present the resulting sample from the ν_μ CC inclusive selection and the subsequent sub–samples. We detail the composition of each sample and the agreement

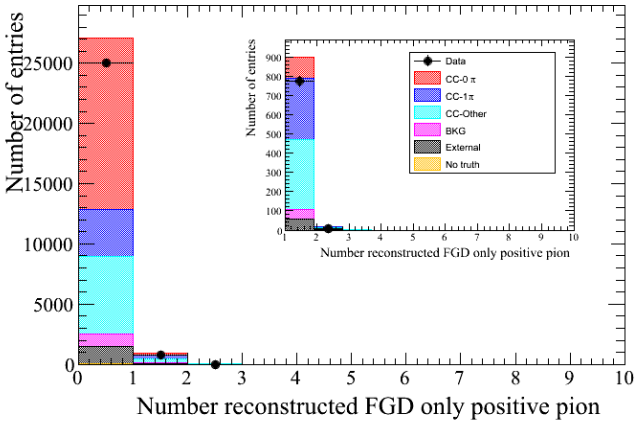

FIGURE 5.13: Distribution of the number of positive pions reconstructed using the FGD PID criteria for FGD-only tracks, according to the true topology type.

data–MC along the momentum and angular distributions of the muon candidate.

5.3.1 Selection Composition and Efficiency

Here we describe the composition and efficiencies of the selected inclusive CC ν_μ sample and the CC0π, CC1π^+ and CC-Other sub–samples. Results are shown for all the four run periods, the data/MC re–weighting has been done period–by–period and then put together.

Table 5.3 shows the composition of the CC sample depending on the true particle type of the highest momentum negative track. The muon purity is ∼90% and the main remaining background is due to the indistinguishable π^- contamination. This pion contamination is expected from the dE/dx behaviour of both muon and pion particles in the TPC (3.20) which is used to perform the muon identification. The purity of a cathegory type X is defined as:

$$Purity_X(\%) = \frac{\text{selected events with the true cathegory X}}{\text{total selected events}} \times 100 \tag{5.6}$$

Table 6.3 shows the efficiencies for each sample, including the efficiency for the CC inclusive. The efficiency is defined as the number of events in a given sample, where the true category matches the selected category, over the number of events generated in the FGD1 FV with the true category corresponding to the category of the selected sample. The efficiency of a cathegory type X is defined as:

$$Efficiency_X(\%) = \frac{\text{selected events with true cathegory X}}{\text{total true generated events for cathegory X in the FGD1 FV}} \times 100 \tag{5.7}$$

Table 5.5 shows the composition of the CC sample for each cut step [7]. We can see how at each cut step we gain in the CC inclusive signal. The biggest improvements comes from the quality and fiducial cut, in this cut we reduce mainly external contamination from events from outside the FGD1. We achieve a purity on CC signal in FGD1 of $\sim 90.7\%$. It is also shown the corresponding number of events for data and MC (normalized to the PoT of the data).

True particle	Fraction (%)
μ^-	89.8
μ^+	0.36
e^-	0.44
e^+	0.08
π^-	7.5
π^+	1.3
p	0.44
other	0.1

TABLE 5.3: Composition for the CC-inclusive sample, according to the particle type selected as muon candidate.

Sample	Efficiency (%)
CC	53.3
CC-0-Pion	47.81
CC-1-Pion	28.37
CC-Other	29.71

TABLE 5.4: Efficiency per each sample. The efficiency is defined as the number of events in the given sample, where the true category matches the selected category, over the number of events generated in the upstream FGD FV with true category corresponding to the category of the selected sample.

Table 6.5 shows the topology composition of the CC sample selected by applying the cuts from Table 5.5 according to the true topology. We observe a dominant contribution of CC0π events of $\sim 50\%$. This is already expected since the T2K neutrino beam has its peak at energies where CCQE interactions are dominant.

[7] A possible improvement for the future can be to request the leading particle to be compatible with the muon PID before the momentum selection, this would increase the final selection efficiency. However, the purity of the muons will remain similar since for the TPC PID algorithm the pions and muons are similar. From a quick test, the purities of the highest momentum negative selected particles before the PID, but within the FV cut and after the CC selection, is is 95.3% muon, 2.5% π^-, 0.02% π^+ and 1.7% e^-. Thus, we expect a maximal variation of the selection efficiency of the muon to be 1.7%. A possible

Cut level	Composition (%)	Sample Reduction (%)	number Data events	number MC events
Total Multiplicity cut	2.27	100	1996217	108972.33
Quality and Fiducial cut	55.73	43.8	48731	47751.9
Backwards-going tracks and first TPC veto	68.7	34.7	35942	37786.1
Broken Track cut	70.2	33.8	34804	36833.2
Muon PID cut	90.72	24.8	25917	27082.1

TABLE 5.5: Composition with respect to the true inclusive CC, and sample reduction fraction achieved at each cut step. It is also shown the number of events at each cut step, for data and for Monte Carlo (normalized to the PoT of the total data) .

CC Inclusive	Topology Composition (%)
CC-0-pion	51.48
CC-1-pion	15.01
CC-Other	24.24
Background	4.03
Out of FGD 1 FV	5.23

TABLE 5.6: Composition of the inclusive CC sample respect to the true topology type. Background is defined as the anti–neutrino signal and neutral current events.

In Table 5.7 the composition of each one of the three samples, CC0π, CC1π^+ and CC-Other are shown, according to the *topology* definition. It is only shown the purity according to the topology type for which the sample is intended to select. In addition in the same table the fraction of events from the inclusive CC sample that are reconstructed as CC0π, CC1π^+ or CC-Other are added. Last two columns show the number of events selected in data and in MC (scaled to data) at each sample. As expected, the dominant channel is the CC0π and the samples CC1π^+ and CC-Other only represents 30% of the total inclusive CC sample. The sample with bigger purity respect to the signal is trying to select is also the CCOther sample with $\sim$ 73% of purity. The CC0π sample has also very good purity of $\sim$ 72% and the less clean sample corresponds to the CC1π^+. The complexity on select one and only one single pion is visible from this table. We have contamination mainly coming from the CCOther topology due to not reconstructed pions. This will be discussed later on this Chapter (see 5.4).

For details on the CC0π sample, the corresponding breakdown of the composition for each true *topology* category is shown in Table 5.8.

The composition for the CC0π sample according to the generator definition is shown in Table 5.9.

We observe the good purity for topology (in the true CC0π component) and for the reacion type which is indicated by the dominant CCQE contribution. In principle, any

reduction of the pion contamination instead may be obtained with additional PID information from the ECal and FGD2.

Sample	Composition (%)	fraction of events respect CC (%)	Number of entries MC (scaled to data)	Number of entries Data
CC-0-pion	72.43	68.4	19096.86	17438
CC-1-pion	49.24	16	4422.8	4085
CC-Other	73.6	15.5	4332.36	4297

TABLE 5.7: Composition according to its true topology type and *fraction of events* respect to the inclusive CC sample, of each sub–sample. Number of selected events in data and MC (normalized to the total PoT data) for each sample is also shown.

CC-0-pion Sample	Composition (%)
CC-0-pion	72.4
CC-1-pion	8.6
CC-Other	11.5
Background	2.3
External	5.2

TABLE 5.8: Composition for the CC0π sample, according to the *topology* types.

CC-0-pion Sample	Composition (%)
CCQE	63.3
Resonant	20.3
DIS	7.5
Coherent	1.4
NC	1.9
$\overline{\nu}_\mu$	0.19
ν_e	0.17
External	5.2
other	0.03

TABLE 5.9: Composition for the CC0π sample, according to the generator interaction types.

CCQE event will leave a CC0π signal if the proton does not interact either in the nuclear medium or the detector. Some resonant and coherent contribution will be included in the CC0π signal if the pion is absorved by the nucleus or the medium detector, and in a minor percentage also some DIS. But in general, CC0π events are a good indication of CCQE interactions. The main contamination in this sample comes from CCOther, from a topological point of view. From the interaction point of view, we cannot claim that the resonant is a contamination since due to FSI, any resonant can be a CC0π event. Certaintly, some of these resonant events may be with pion at the final state which we have not been identifiey, but from this table it is difficult to estimate. We always prefer to talk about topology in order to reject confusions.

For the CC1π^+ sample we show details of the selected sample in following Tables. Tables 5.10 and 5.11 show the purity of the CC1π^+ according to the topology definition or

the interaction type respectively. Most of the contamination comes from the CCOther contribution. This is mainly due to inefficiencies when reconstructed the total number of particles of the event. This is described in detail in the next Section 5.4.

CC-1-pion Sample	Composition (%)
CC-0-pion	6.4
CC-1-pion	49.2
CC-Other	31.0
Background	6.8
External	6.6

TABLE 5.10: Composition for the CC1π^+ sample, according to the *topology* types.

CC-1-pion Sample	Composition (%)
CCQE	5.3
Resonant	39.4
DIS	31.3
Coherent	10.6
NC	4.7
$\overline{\nu}_\mu$	1.7
ν_e	0.4
External	6.6
other	0.04

TABLE 5.11: Composition for the CC1π^+ sample, according to the generator interaction types.

The CC1π^+ sample composition according to the *topology* types was also checked (Table 6.7) in the case that the reconstructed positive pion is found by using the TPC PID, the Michel electron tagging or the FGD PID when there are no Michel electrons in the event:

1. Positive pion TPC. CC1π^+ events where the positive pion is reconstructed using the TPC PID (no Michel electron or FGD–Only pion tracks).
2. ME. CC1π^+ events where the positive pion is reconstructed using the Michel electron tagging (no TPC pions, it allows to be FGD–Only pion tracks).
3. FGD-only. CC1π^+ events where the positive pion is reconstructed using the FGD PID (no TPC pions either Michel electrons).

This simple exercise will help to understand better how the reconstruction performs in order to isolate the CC1π^+ sample.

Table 6.8 shows the number of entries (for data and Monte Carlo scaled to data) in each case.

CC-1-pion Sample	Composition TPC pion sample(%)	Composition ME sample(%)	FGD PID (%)
CC-0-pion	4.1	4.8	26.3
CC-1-pion	50.3	51.4	34.4
CC-Other	34.1	26.6	27.6
Background	8.8	4.0	4.7
External	2.7	13.1	7.0

TABLE 5.12: Composition for the CC1π^+ sample, with the positive pion identified with the TPC criteria (second column), Michel electron criteria (third column) or the FGD PID (fourth column), according to the *topology* types.

Pion criteria	Number of entries MC (normalized to data) (normalized to data)	Number of entries Data
positive pion TPC	2532.1	2316
ME	1491.6	1420
FGD-only	399.1	349

TABLE 5.13: Number of entries according to the tagging of the pions for the CC1π^+ sample, for data and Monte Carlo scaled to data.

These three sub–samples of the CC1π^+ sample are used for the total CC1π^+ sample. We can see that purity on CC1π^+ is higher for the TPC and ME criteria. In both cases the purity is $\sim$ 50%, while for the FGD–Only pions purity on CC1π^+ is $\sim$ 34%. As already observed from the pull distributions in the FGD, we have some difficulties to select pions in the FGD and we have a high contamination of protons.

Tables 5.14 and 5.15 show the break down of the composition according to the *topology* types and the generator definitions, respectively for the CCOther sample.

CC-Other Sample	Composition (%)
CC-0-pion	5.8
CC-1-pion	7.8
CC-Other	73.6
Background	8.7
External	4.1

TABLE 5.14: Composition for the CC-Other sample, according to the *topology* types.

As already seen from Table 5.7, the CCOther has a high purity. The main contamination comes from background events and CC1π^+. The background contamination is mainly NC (6.8%, from 5.15). This is due to muon miss–identification with a negative pion. Pion and muon have a very similar behavior in the TPC and it makes them indistinguishable. Only the charge requirement helps to distinguish muons respect to positive pions or the request of highest momentum negative track helps to distinguish

CC-Other Sample	Composition (%)
CCQE	3.9
Resonant	14.2
DIS	67.7
Coherent	1.4
NC	6.8
$\overline{\nu}_\mu$	0.9
ν_e	0.9
External	4.1
other	0.2

TABLE 5.15: Composition for the CC-Other sample, according to the generator interaction types.

with respect to the negative pions [8]. Then, this NC contamination may come from NC with at least one negative pion in the final state (it will be mainly DIS). According to the interaction type, since any non–DIS contribution (CC interaction), due to FSI, can gives us a CCOther signature it's difficult to say which, from the CC channels, can be considered contamination. For example, we cannot claim that the resonant contribution is contamination since these resonant pions can as well re–interact and produce more pions, charged or neutral. From the non charged current interaction we can neglect FSI effects to produce final CCOther. Both anti-neutrino or electron neutrino are contamination and the NC very few times will became CC due to FSI (muon absorption is negligible).

We also perform an analysis similar to what we do for the CC1π^+ sample. The following tables indicate that any criteria applied to select the "other" tracks has a high composition on CCOther. We check the composition for events tagged as CC-Other according to the method used to classify them as CC-Other (see Figure 5.7). Since the different requirements applied to tag an event as CCOther are not excluding between themselves we try just to perfom few simple checks. Thus, not all the CCOther events are considered in the following tables. We show on next tables CCOther events due to different reconstruction criteria or topology (multi–pion and neutral pion). In this way, we can have an idea on which tagging criteria is working better

We start by showing results when tagging CCOther events because we reconstruct more than one positive pion, and not excluding the possibility of negative or neutral pion identified. We show the composition of these events in the Table 5.16 taking into account in which way the pion identification is done:

1. Pion identified with the presence of a TPC pion and at least one Michel electron.

[8] To preserve energy conservation in the neutrino charged current interaction, the lepton uses to take the higher momentum values with respect all the emerging particles in the events.

2. Pion identified with the presence of a TPC pion and an FGD–Only pion.

3. Pion identified with the presence of more than one TPC pion.

CC-Other Sample	TPC+ME Composition (%)	TPC+FGD–Only Composition (%)	TPC Composition (%)
CC-0-pion	0.7	1.6	0.7
CC-1-pion	5.6	9.9	4.6
CC-Other	80.0	74.1	80.6
Background	11.1	11.5	12.1
External	2.6	2.9	1.9

TABLE 5.16: Composition for the CC-Other sample with more than one positive pion using the TPC and Michel electron criteria (second column), or in case there is more than one positive pion using the TPC and FGD–Only criteria (third column) or in case there is more than one positive pion using the TPC criteria (fourth column), according to the *topology* types.

We observe a very similar composition for the multiple positive pion sample inside the CCOthers in the three cases. We can consider to be the less effective cathegory the one that uses Michel electron information, but differences are minimal and we can say that in the CCOther sample the 3 ways to tag positive pions contribute in a very reasonable way.

Another helpful information to better understand the composition of the CCOther sample is the number of entries we have with one negative pion or with a neutral pion. This latter sample of events are the most difficult to isolate in the ND280 tracker region and for that reason it was combined with the CCOther sample. The difficulties on the selection of neutral pions is not only coming from reconstruction limitations, as can happen to the other particles as well. For electron and positrons at this analysis we only look for them in the TPC. Then, no short tracks of electron/positrons in the FGD can be identified. We have also to consider that some electron/positrons are produced by secondary interactions of the primary particles in the events, like the pion with the detector, then when trying to identify these electron/positrons they not come from a neutral pion but from a secondary interaction. For the high angle electron/positron tracks we have the same limitation than in the other particles, since at this analysis we don't add ECal information and then we cannot identify high angle tracks.

Table 5.17 shows the composition for the case where at least one negative pion is reconstructed using the TPC criteria and no positive pion or electron/positron has been identified, for the CC-Other sample.

We observe a very good purity of the CCOther sample when identifying negative pions. Since the muon has a reasonable good purity in the identification in the sample, we

CC-Other Sample	Composition (%)
CC-0-pion	4
CC-1-pion	3.5
CC-Other	82.9
Background	7.1
External	2.5

TABLE 5.17: Composition for the CC-Other sample when having at least one negative pion using the TPC criteria, according to the *topology* types.

expect a good purity for the negative pion (their main contamination, due to the charge and MIP properties, is the muon). However, main contamination comes from neutral current events. In this later case the mis–identification of the muon with a pion is the origin of this contamination.

Finally, Table 5.18 shows the composition for the case where at least one electron or positron is reconstructed using the TPC criteria and in case when no positive pion is reconstructed either any negative pion, for the CC-Other sample.

CC-Other Sample	Composition (%)
CC-0-pion	7.2
CC-1-pion	8.6
CC-Other	70.1
Background	9
External	5

TABLE 5.18: Composition for the CC-Other sample when having at least one electron/positron using the TPC criteria, according to the *topology* types.

In this last case, also if purity is quite good, $\sim 70\%$, is the lower purity of the different sub–samples of CCOther detailed here. As already discussed, main contamination may come from different reasons. One reason is the limited reconstruction, on which we can have some pion and proton contamination for the electron/positron selection in the TPC. Another reason can be the secondary interaction that can produce electron/positrons in the events, and probably very close to the vertex.

Table 5.19 shows the number of entries (data and Monte Carlo scaled to data) for each pion-tagging criteria for the CC-Other sample (the sum of these events are not the total number of events in CC-Others since they are not excluding each other, i.e. it can be a neutral pion tagged as well as negative pion in the same event).

From this table we can get an idea of the contribution of each particle tagging to the final CCOther sample. We see that events with identified neutral pions are the dominant contribution. Events with negative pions or the events with identified positive pions

Pion criteria	Number of entries MC (scaled to data)	Data
TPC + FGD-only	101.4	58
TPC + ME	1111.4	1140
Positive TPC	642	762
Negative pion TPC	1490.5	1538
electron/positron TPC	2622.2	2774

TABLE 5.19: Number of entries according to some specific cases of tagging of the pions for the CC-Other sample, for data and MC scaled to data.

(taking into account the three positive pion tagging method) are also giving an important contribution.

From the tables presented at this Section we observe a good performance of the different identification methods used. The CC0π and CCOther topologies are the samples with higher purity, and then, particle identification seems to do a good work. For the single pion topology, as it will be discused later in this Chapter, is the more complicated to isolate. We see that this new ν_μ CC inclusive sample selection can be used for the neutrino event rate estimation at ND280 since it accomplish the requirements needed by the T2K oscillation analysis:

- A good selection, according to purity and efficiency, of the ν_μ CC events.
- A good separation of CCQE–like events, CC0π topological definition.
- An estimation of the single pion contribution.

5.3.2 Sample Kinematical Distributions

Here we present the results of the selected data-MC comparisons and self-consistency checks of the data. Event displays on each topology type for real data reconstructed events are shown in Appendix C.

Figure 6.8 shows the muon momentum distributions of the selected inclusive CC ν_μ events and the corresponding three sub–samples: CC0π, CC1π and CC-Other, according to the *topology* definition.

We observe a general good agreement for data/MC in the different samples. The biggest disagreements come from the CCOther sample at muon momentum from 500 MeV to 1500 MeV. The reasons of this disagreement can have different explanations related to the model prediction but it's difficult to identify which is the correct answer. Figure 5.15 shows the comparison with the Monte Carlo generator definition of the interactions.

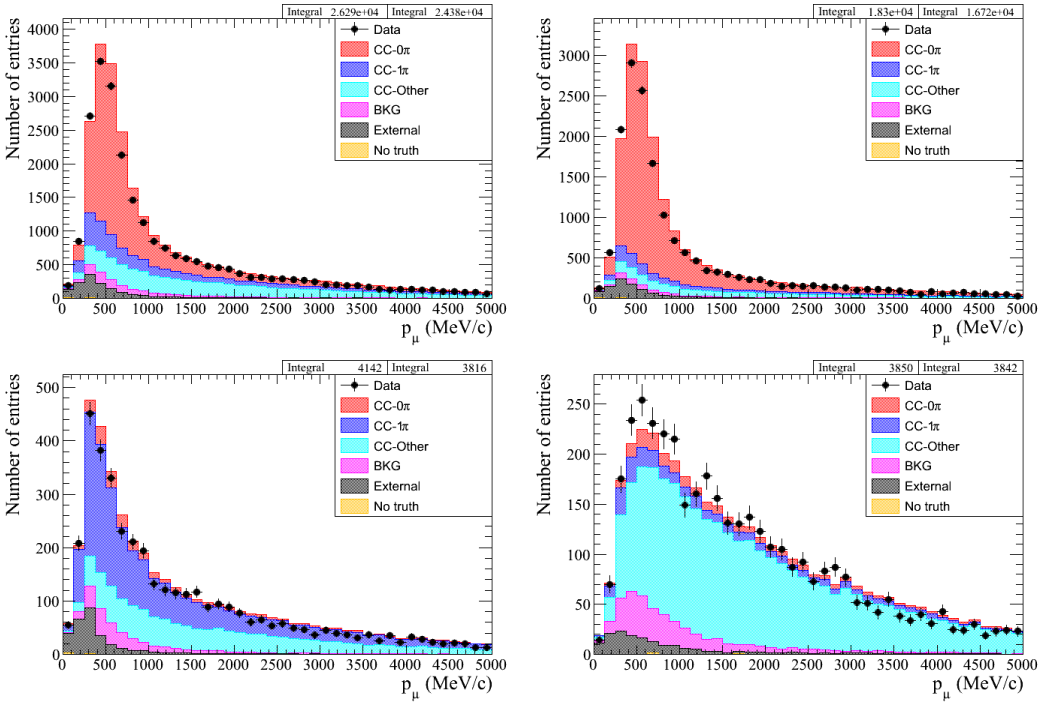

FIGURE 5.14: Muon momentum distribution for the CC (left) and CC0π samples (right) in the top row, and for the CC1π (left) and CC-Other samples (right) in the bottom row. The different samples at the *topology* level are indicated.

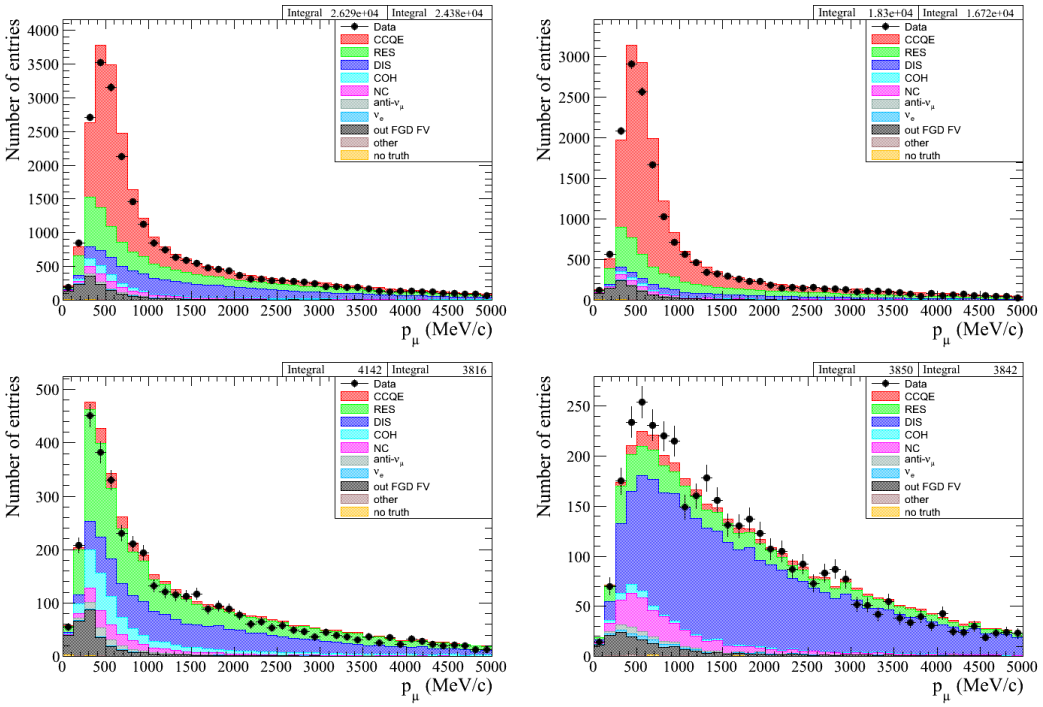

FIGURE 5.15: Muon momentum distribution for the CC (left) and CC0π samples (right) in the top row, and for the CC1π (left) and CC-Other samples (right) in the bottom row. The different interactions at the generator level are indicated.

In Figure 6.9 the distribution of the muon angle, respect to the z–axis of ND280, for the selected inclusive CC ν_μ sample and the three sub-samples CC0π, CC1π and CC-Other are shown, according to the *topology* definition.

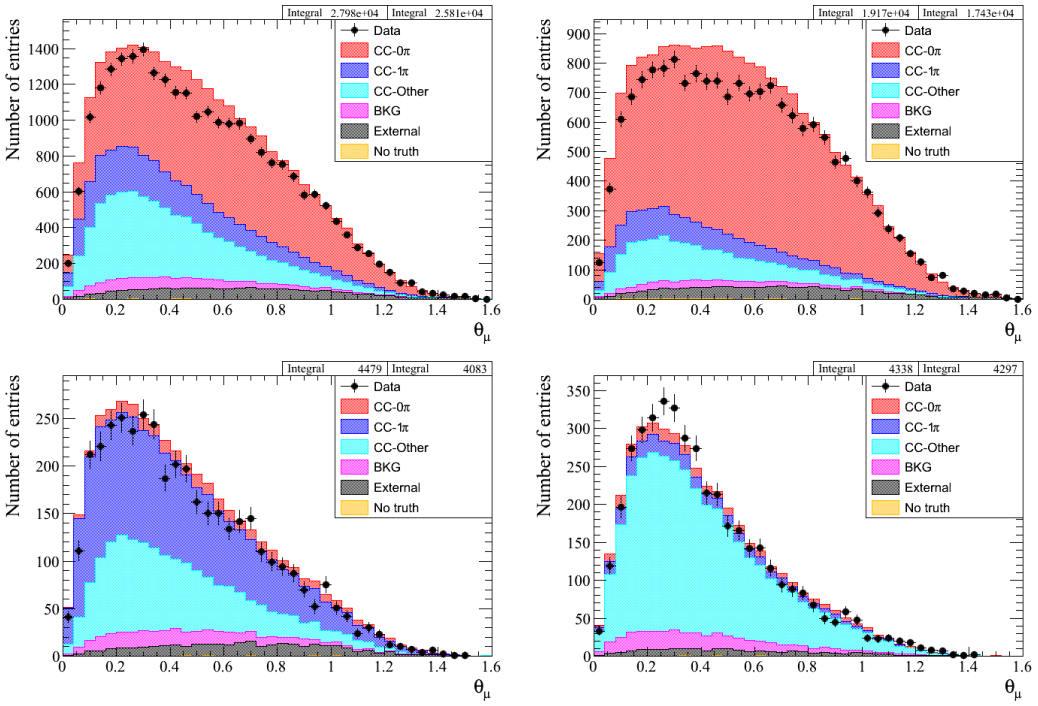

FIGURE 5.16: Muon angle, respect to the z–axis of ND280, distribution for the CC (left) and CC0π samples (right) in the top row, and for the CC1π (left) and CC-Other samples (right) in the bottom row. Using the *topology* definition.

From the muon angle distributions we can see two important disagreements for the data/MC comparisons. The first one is in the CC0π sample on which the MC over-predicts the data. This overprediction is done at values from 0–0.8 radians. The same behaviour for the muon angle, at the moment on which the analysis was taking place and then using the same model, was also observed by P0D-TPC-based analysis in the same topology channel. We think that this disagreement can be related to the not considered MEC contributions [9]. These possible MEC events have to be included in the CC0π sample if any of the emerging nucleons does not interact with the nucleus before to emerge from it. Since these events are present in data but not in MC, the MEC effect can explain this disagreement. In any case, we have to highlight that this is just a possible explanation. Recent version of NEUT already includes the prediction of one type of these MEC events and current analysis in ND280 should check if the inclusion of this effect can correct this disagreement. This is also visible in the CC inclusive sample since bigger the contribution comes from the CC0π sample.

[9] Meson Ex-Change effect: events on which the W boson interacts with more than one nucleon in the nucleus.

The other disagreement observed is in the CCOther sample. In this case the effect is the opposite than the CC0π sample, the data is under–estimated. Since this behavior has been already observed in the muon momentum distribution we expect that explanations will be similar and studies need to be done in order to know which is the origin of this mis–modelling at the CCOther topology.

We show in Figure 5.17 the same angular distributions but using the generator definition.

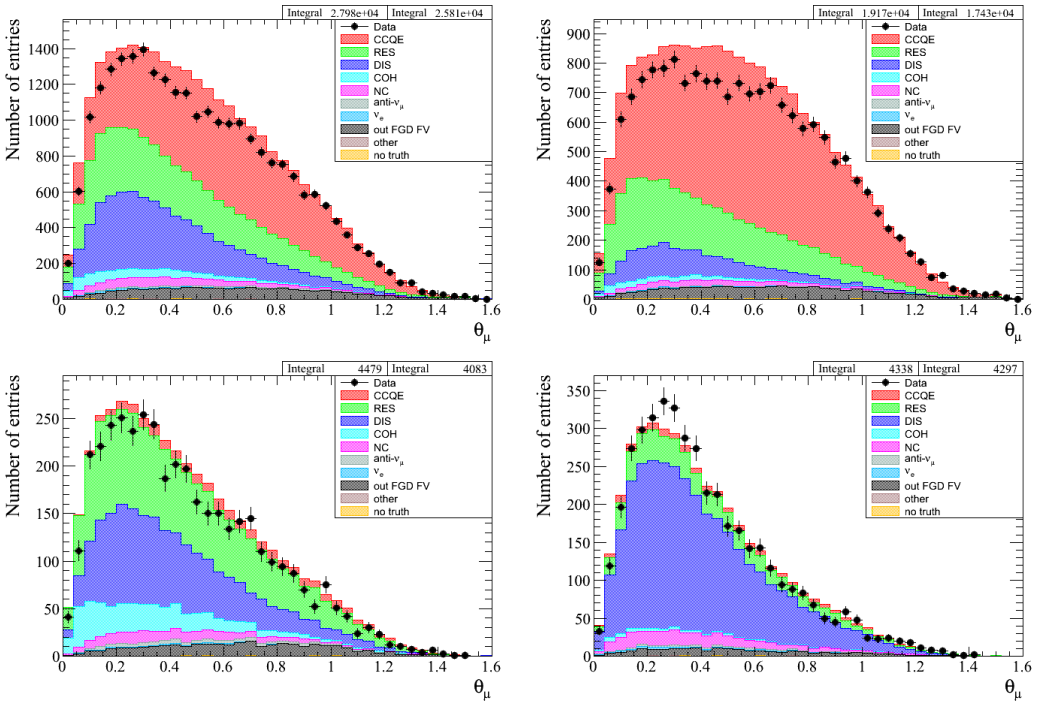

FIGURE 5.17: Muon angle distribution for the CC (left) and CC0π samples (right) in the top row, and for the CC1π (left) and CC-Other samples (right) in the bottom row. Using the generator definition of the interactions.

In general, we observe a general good agreement between data and the Monte Carlo prediction on the shape distributions. The agreement is especially good for the CC0π (muon momentum) and CC1π^+ sample. The CCOthers is the sample in which the model still have small discrepancies with the data, in momentum and angle. Some discrepancies are found in the muon angular distributions for the CC0π, but the general agreement in the momentum is very good.

5.4 Event Migration

Events may be assigned to the wrong sub-sample because of different reasons. A detailed study of such event migration is presented in the following.

5.4.1 True CC0π Events classified as CC1π^+

There is a set of CC0π events that get mis–categorized as CC1π^+, 6.4% of the selected CC1π^+ sample. This happens for the following reasons:

- 45% of the time because protons in the TPC are mis–identified as pions. This can happen because of reconstruction failures but also because the dE/dx separation between pions and protons becomes poor above 1 $\sim GeV/c$. See Figures 5.53.20.
- 45% of the time there are spurious short tracks in the FGD1 that look pion-like. This can be either from mis–reconstructed protons or muons.
- 10% of the time because of spurious Michel electrons from other magnet interactions.

5.4.2 Events classified as $CC0\pi$ because pion was missed

Overall we correctly tag approximately 57% of the π^+s in the true CC-1π category.

Studies were done for the reasons why the π^+ track failed to be reconstructed and hence classified a true CC1π^+ event as $CC0\pi$ (8.6% of the selected $CC0\pi$ sample). We found that there were four main reasons why the pion was not tagged:

- 30% of the missed π^+ are π^+ that undergo a secondary interaction in the FGD; this makes the π^+ harder to reconstruct, partly because the tracking is harder, but also because the PID cut doesn't work correctly [10].
- 10% of the missed π^+ emit a Michel electron in FGD1, but the Michel electron is not detected. Two main reasons have been identified: either because it is in a subsequent bunch or because it is below the 200PE cutoff.
- 30% of the missed π^+ enter the TPC, but are not identified as π^+; ie, there is a TPC PID failure. This is ussually for pion with momentum from 500MeV to 1500Mev (see 3.20).
- 30% of the missed π^+ go directly from the FGD1 into the ECal. Our current cuts are not designed to be able to tag this π^+ topology.

[10] The resulting particles of the interactions we refer are with very short lenght and then difficult to reconstruct.

5.4.3 True CC-Other Events classified as $CC1\pi^+$

The same set of problems with tagging π^+ also causes migration of true CC-Other events into the CC1π^+ category (7.8% of the CCOther sample).

Another reason for true CC-Other events into the CC1π^+ category is because π^0 from CC-Other are missed. Our electron tagging only tag a small fraction of π^0, for now the ECal and FGD are not used to tag neutral pions. Then, no short tracks contained in the FGD1 or high angle tracks are used to identify these neutral pions. Approximately half of the true CC-Other events in the CC1π^0 category have π^0 in their final state.

5.5 Effect of the Detector Uncertainties in the Sample

We apply the detector error propagation event by event in the sample selected, as explained in Chapter 4. In this Section we show the effect of this propagation. The muon momentum and angle for data and expected MC events with the total detector systematical uncertainty are shown in Figure 5.18 for the three samples (CC0π, CC1π and CCOther). Both the statistical and detector systematical errors are show in the plots.

We observe bigger contribution of the errors on the CCOther sample. For the CC0π sample we see that at very low momentum uncertainties are bigger. This is due that for some detector errors they became bigger at low momentum values (for example the charge mis–identification), which can be due that we don't obtain ebough statistics in the control sample used or the systematic itself is bigger at low momentum due to reconstruction. For the angular observable we observe similar contribution of the errors in all three samples and at intermediate angular range contributions are bigger. There are very few bins on which these errors doesn't cover the data/MC disagreement, actually only visible for angular variables. The biggest discrepancy comes from angular distributions for the CC0π sample. A proper treatment, as a cross section analysis, should be done in order to understand if also cross section parameter unceratinties in the model, or flux uncertainties can cover such differences.

The dominant contributions to the overall error are due to the pion re–interaction, see Figure 5.19 and out–of–fiducial–volume, see Figure 5.20, systematic errors, but some others can be dominant in certain regions of the phase–space. The total error is shown in Figure 5.21 in this Section.

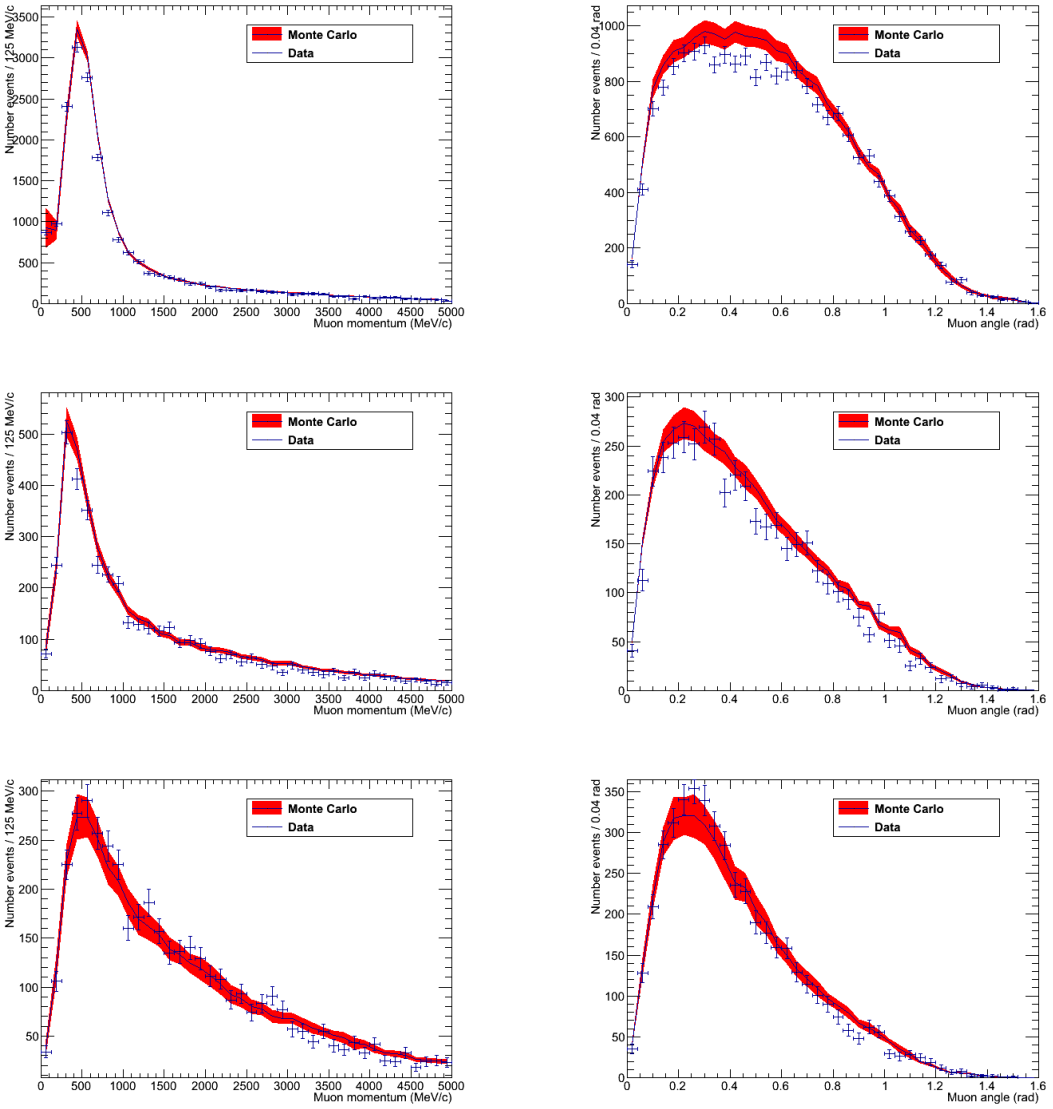

FIGURE 5.18: Muon momentum (left) and angle (right) data (dots) with their statistical error and expected MC events (histogram) with the red band indicating the total systematic uncertainty. The first row is CC0π, the second CC1π and finally the third is CCOther events.

Note that those plots are just for illustration, as the final fit to obtain the expected neutrino event rates at Super-K uses the probability density function of the number of entries [11]

The covariance matrix, normalized to the number of events per bin, used by the final fit, and output from ND280 to oscillation analysis in Super-K, is shown in Figure 5.22.

[11] A covariance matrix was computed and used for the propagation of the errors.

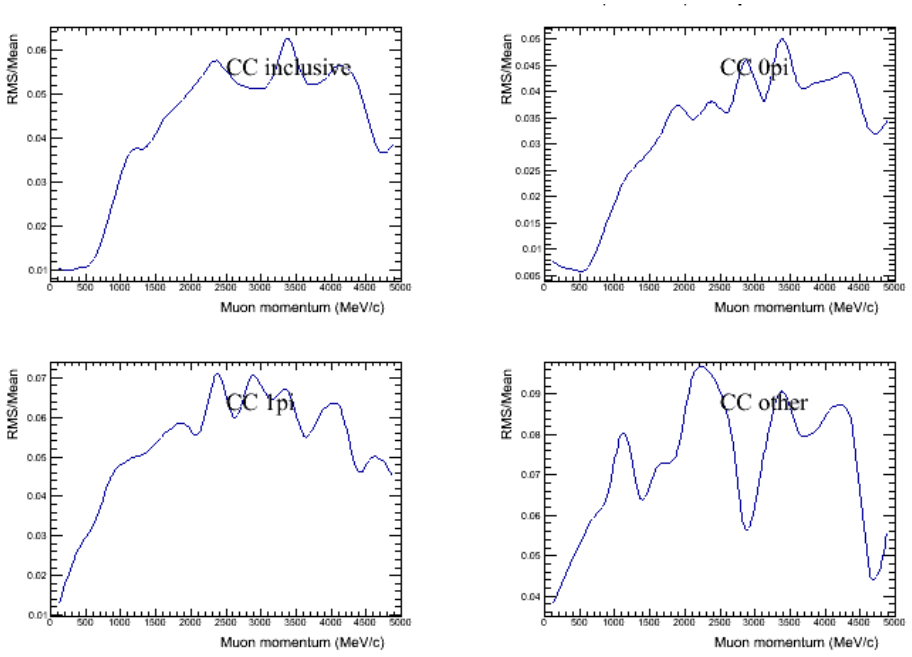

FIGURE 5.19: Relative systematic error induced by the pion cross section interaction uncertainty. Upper left: CC inclusive, upper right: CC0π, lower Left: CC1π, lower right: CCOther.

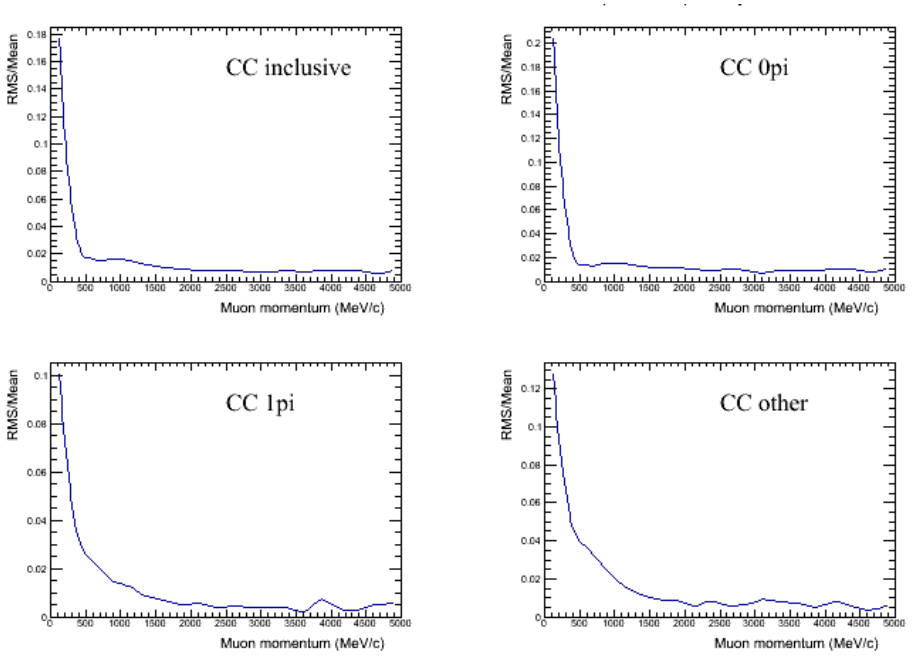

FIGURE 5.20: Relative systematic error induced by the OOFV background uncertainty. Upper left: CC inclusive, upper right: CC0π, lower Left: CC1π, lower right: CC-Other.

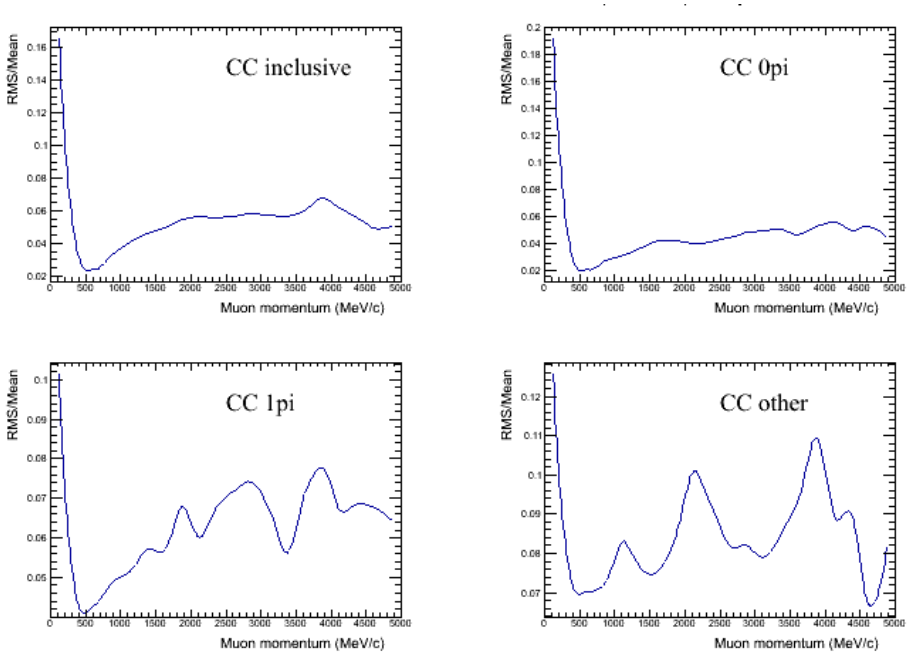

FIGURE 5.21: Relative systematic error induced by the all the uncertainties. Upper left: CC inclusive, upper right: CC0π, lower Left: CC1π, lower right: CC-Other.

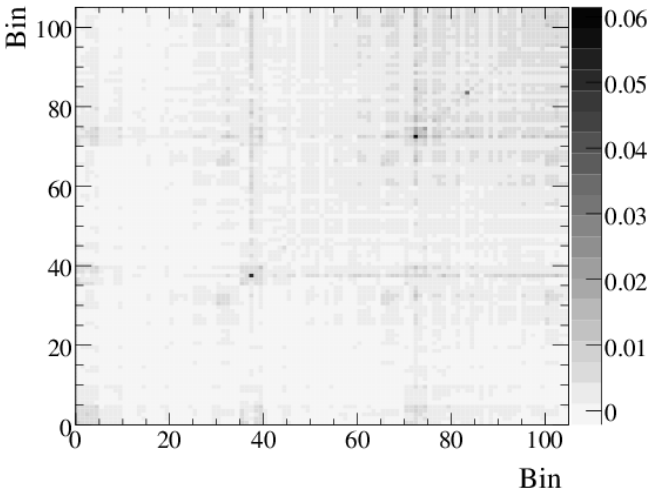

FIGURE 5.22: Covariance matrix normalized to number of events used by the final fit for the ND280 output. Bins are defined according to the vectors: 0.00, 300.00, 500.00, 600.00, 700.00, 1000.00, 2000.00, 30000.00 MeV/c in momentum and -1.00, 0.85, 0.90, 0.94, 0.98, 1.00 in angle.

5.6 Results obtained with the new ν_μ CC inclusive approach

The results from this analysis was used by the BANFF group (*Beam And Nd280 Flux measurement task Force*) using the BANFFv2 analysis framework. BANFFv2 provides and estimation of the rate of neutrino events at SK [12]. The new fitted beam and cross section parameters are input to the Super-K oscillation analysis. In this Section we summarize the results obtained.

Figure 5.23 shows the reduced uncertainties on the cross section and flux parameter errors in SK before and after the ND280 constraint, i.e. the results of the analysis presented in this Chapter. It is shown for the ν_μ flux (left plot) and ν_e flux (right plot). We can observe how the error values have been reduced when adding the ND280 constraint.

The Super-K prediction for the number of ν_e candidates with the ND280 constraint is summarized in Table 5.20 with the related errors. It shows a large error reduction due to the ND280 constraint, further diminished using the new analysis approach and data in 2013.

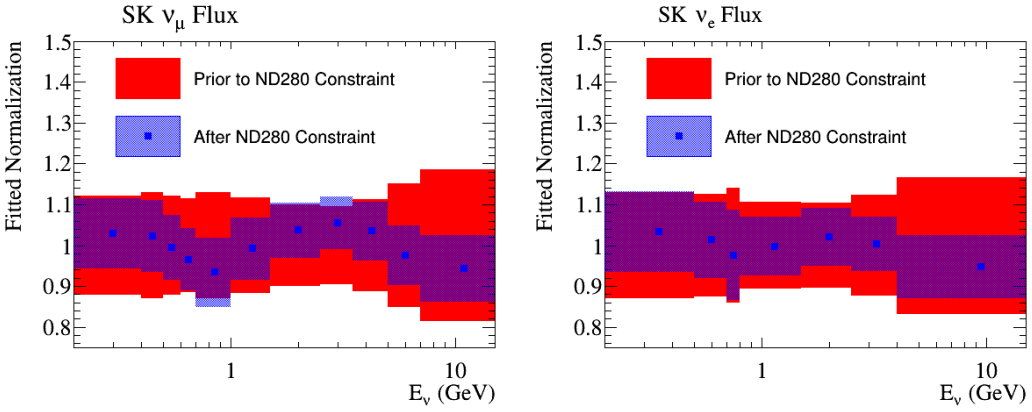

FIGURE 5.23: Reduced uncertainties on the cross section and flux parameter errors in SK before and after the ND280 constraint. For the ν_μ flux (plot) and ν_e flux (plot)

	$\sin^2 2\theta_{13} = 0.1$		$\sin^2 2\theta_{13} = 0.0$	
	ν_e Prediction	Error	ν_e Prediction	Error
NEUT Nominal	21.6	-	4.9	-
No ND280 Constraint	22.6	26.5%	5.3	22.0%
2012 ND280 Constraint (using old ν_μ CC approach)	21.8	4.9%	5.1	6.5%
2013 ND280 Constraint (using new ν_μ CC approach)	20.4	3.0%	4.6	4.9%

TABLE 5.20: The Super-K prediction for the number of ν_e candidates with the ND280 constraint.

[12] BANFFv2 uses a likelihood fit method.

From results provided by the BANFF group we observe that the new analysis strategy applied in the ν_μ selection improved systematical constraint for oscillation analysis.

Final oscillation results were publish for both ν_μ disappearance and ν_e appearance channels on 2013 [65] [66] [67].

T2K is the first experiment that observed direct evidence of $\nu_\mu \rightarrow \nu_e$ by the appearance channel [68], and excluded $\theta_{13} = 0$ at a 7.3σ significance. This result, combined with public results from reactor experiments allows for regions of δ where is excluded at the 90% confident level. T2K's ν_μ disappearance results provided independent measurements of $sin^2\theta_{23}$ and Δm^2_{23} [69].

Nowadays, the NuMu group in ND280 follows the same analysis strategy and is hardly working to include the same event selections from different targets by using the different ND280 sub–detectors. The addition of different targets is important mainly for the water target. By using water target it can be reduced uncertainties related to the differences on cross section values from CH to water, since in SK the target is also water (see Table XX in [67]).

As well, the analysis presented here allowed to study in depth the different neutrino interactions occurred on CH (FGD1) and to provide cross section measurements in the different samples presented. In next chapter one of them is presented: the ν_μ CC1π^+ cross section analysis on CH.

Chapter 6

ν_μ Charged Current Single Pion Measurement on CH

We have discussed the importance of the cross section estimation for neutrino–nucleus interactions at any neutrino oscillation experiment in Chapters 2 and 5. From the results presented on Section 5.6 we see that one of the biggest cross section parameter errors to oscillation analysis in T2K are the ones related to the CC1π^+ channel.

The main Monte Carlo used in T2K is NEUT, see Section , that uses external data to parametrize the different shapes and contributions of each interaction channel. For example, in the case of the neutrino single pion production it is represented by the Rein and Sehgal model [17] which already uses data from the ANL [4] experiment. In addition to this, the T2K collaboration tune the model used in NEUT according to additional external data. T2K uses mainly data from MiniBooNE [29] but also from SciBooNE [71] and K2K [39] to tune model parameters.

Published data from the mentioned experiments show discrepancies with the most common theoretical models [3], including the ones used by NEUT, for the different interaction channels. These discrepancies became bigger at the intermediate energy region, from $\sim$ 0.1 eV to $\sim$ 10 GeV. Figure 6.1, from [3], shows the neutrino cross section as a funtion of the neutrino energy predicted by models and compared with experimental results. This makes momentous for T2K to compare the T2K data with the current models and check if their are consistent.

In order to understand if a model describe accurately the interaction under study, it is strongly recommended to use measurements which are done in a *model independent* approach. This allows us to perform a non biased comparison of our result to external data and to the theoretical models. Furthermore it would be also important to provide

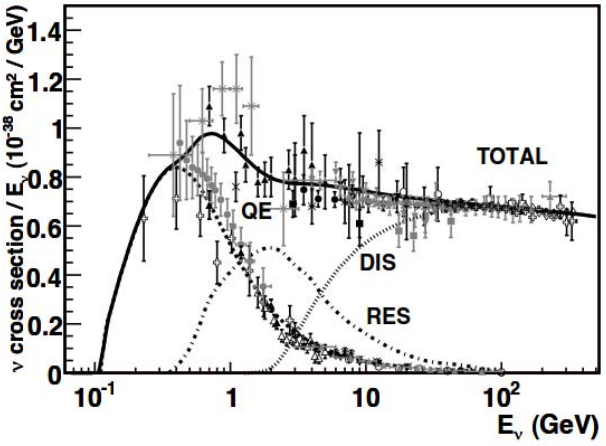

FIGURE 6.1: Neutrino cross section from prediction (lines) and experimental data (dots with error bars) respect to the neutrino energy. The different neutrino interaction channels at intermediate energies are represented. From [3].

information about the possible nuclear effects on the interactions. In fact, as already seen in Chapters 2 and 5, nuclear effects play a notable role on the interaction description and their estimation.

We have to highlight that not only neutrino cross sections are dependent to the neutrino energy, also the neutrino flux and the nuclear effects depends on the neutrino energy. Thus, to perform a reliable cross section measurement it is important to understand as well the correlations between the flux, the nuclear effects and the cross sections [**?**].

The analysis presented in this Chapter is the ν_μ Charged Current Single π^+ cross section measurement on hydrocarbon (CH). The measurement is performed using the ND280 tracker with addition of the ECal detector and considering the Run 2 + Run 3 + Run 4 data period. Run 1 has been excluded since the ECal was not ready at the time of that run period and this detector is used to improve the event selection.

The event selection in based on the CC1π^+-like enriched sample, presented in Chapter 5. Two modifications have been apported to the presented selection:

1. the pion identification for the FGD–only tracks,
2. a new ECal π^0 veto in order to reduce the presence of neutral pions in the selected sample.

In order to control the different background sources in our enriched CC1π^+ sample, we use three control samples. These samples are selected to represent with reasonable accuracy our signal contamination. We use them to subtract all the different backgrounds

except for those coming from out of our defined fiducial volume. In this last case we trust on the MC prediction. The background subtraction is presented in Section 6.6.

The cross section is performed using a Bayesian unfolding method 6.8. This method has been implemented in a new multi-purpose software framework, the `xsTool`, recently developed and used by the ND280 analyzers. The `xsTool` is intended to provide a set of common tools useful for cross section analysis. The analysis presented here is one of the first analysis using this software.

The Monte Carlo neutrino interaction generator is NEUT, but GENIE [72] Monte Carlo has been also used to produce fake data for testing the method (see ApppendixD).

The analysis is performed within a model independent approach and it measures the cross section with respect to several kinematic observables. The list of observables developed for the analysis have been chosen in order to be able to compare with results from other experiments (MiniBooNE, MINERνVA, ANL and BEBC). These observable also are of special interest to cross check with the Rein and Sehgal model. We present the differential, double differential and energy dependent cross section results in the different forms:

1. The cross section as function of the energy energy [1] is performed using two assumptions on the energy reconstruction:
   - $\sigma(E_{RecoMB})$. This method assumes that there is only one proton missing in the emerging particles (using MiniBooNE's formula [29]). The unfolding is done using the true neutrino energy provided by the Monte Carlo.
   - $\sigma(E_{Reco})$. This method assumes that there is only one proton missing in the emerging particles. The assumption is the same used by MiniBooNE but adding some missing terms. The unfolding is done using the true neutrino energy provided by the Monte Carlo.
2. $d\sigma/dp_\mu$, where p_μ is the momentum of the muon.
3. $d\sigma/dp_\mu dcos\theta_\mu$, where θ_μ is the angle between the muon and the neutrino directions.
4. $d\sigma/dp_\pi$, where p_π is the momentum of the pion.
5. $d\sigma/d\theta_\pi$, where θ_π is the angle between the pion and the neutrino direction.

[1] The energy dependent results are presented as model dependent results and we will present separately. The unfolding is done using the true neutrino energy predicted by the Monte Carlo. They are model dependent but necessary for energy dependence results due to the flux estimation at each energy bin, needed in the cross section energy dependent measurements but not in the differential results where each bin is divided by the total flux.

6. $d\sigma/dQ^2$, where Q^2 is the 4–momentum transfer of the interaction. This result is presented using E_{RecoMB} for the energy reconstruction formula used, since in this case we can add the Michel electrons events. This measurement is a nice method to do a cross section measurement with respect an observable directly related to the neutrino energy in a model independent strategy. Q^2 can provide as well information about the Δ production.

7. $d\sigma/d|Q_3|$, where $|Q_3|$ is the absolute value of the 3–momentum transfer. This result is presented using E_{RecoMB} for the energy reconstruction formula, since in this case we can add the Michel electrons events. $|Q_3|$ can provide information about the Δ production.

8. $d\sigma/d\theta_{\pi\mu}$, where $\theta_{\mu\pi}$ is the angle between the muon and the pion directions. We consider that any angular observable is much sensitive to the Final State Interaction (FSI) effect. Particles can modify their energy and direction when emerging from the nucleus due to the nuclear medium. This effect can alter the observed angle and we want to see if it is well reproduced by the model.

9. $d\sigma/dW$, where W is the invariant mass of the interaction. This result is presented using E_{RecoMB} for the energy reconstruction formula used, since in this case we can add the Michel electrons events. W can provide information about the Δ production. This observable is also interesting by itself since some measurements on CC1π^+ performed by other experiments use to add a cut on W to restrict to regions where the $\Delta(1232)$ is dominant and the Rein and Sehgal model is considered to be a good description of this channel.

10. $d\sigma/dCos\theta_{planar}$, where $Cos\theta_{planar}$ is defined as the polar angle in the *Adler's system* as described later in this Chapter. This result is presented using E_{Reco} for the energy reconstruction formula used, since Michel electrons cannot be included for the measurement [2] and this energy reconstruction approach supposes a better estimation of the neutrino energy for the interaction studied. This measurement supposes an approach to the FSI effect and it is the first time it is measured since the ANL and BEBC experiments.

11. $d\sigma/d\psi_{planar}$ where ψ_{planar} is defined as the azimuthal angle in the Adler's system. This result is presented using E_{Reco} for the energy reconstruction formula used, for the same reasons as the $d\sigma/dCos\theta_{planar}$ measurement. This measurement is expected not to be so affected by FSI effects as the $d\sigma/dCos\theta_{planar}$ measurement and it can provide information related to the pion angular estimation done by the Rein and Sehgal model.

[2] We need to have access to the pion angle and Michel electrons doesn't provide this information.

Sample	Data PoT	NEUT MC PoT	GENIE MC PoT
Total	$5.734 \cdot 10^{20}$	$6.41 \cdot 10^{21}$	$6.78941 \cdot 10^{21}$

TABLE 6.1: Number of PoT for each data set. The PoT in data corresponds to the collected data after good spill and data quality criteria are applied. The PoT in MC corresponds to the used MC sample, for NEUT and GENIE.

Results are presented in two different sections in order to separate model dependent results (energy dependent cross section measurements) from the results that are perform in a model independent measurement, the differential results [3].

6.1 The Monte Carlo and Data Sets

The two T2K official Monte Carlo productions are used in this analysis. We have used the two Monte Carlo in three different ways:

1. using NEUT as an unfolding reference for the Data,
2. using GENIE as fake data and NEUT as reference Monte Carlo to check the unfolding performance,
3. NEUT as fake data with NEUT as reference Monte Carlo to check the unfolding performance.

We summarize the total Monte Carlo and data proton on target (PoT) in Table 6.1.

6.2 Signal Definition

The signal is defined using the CC1π^+ topology described in Chapter 5: events with a true negative muon and one positive pion at the Final State of the Interaction (FSI), any number of nucleons and no more particles in the event.

For the cross section measurement we need to take into account that a fraction of the phase–space is invisible to the detector. To avoid model dependent extrapolations we measure the cross section only in the phase–space covered by the detector. On Section 6.9 we present the analysis preformed to obtain the valid phase–space considered in the analysis.

[3] For the differential cross section measurements the unfolding process is done using the same formula as the reconstructed one with true kinematical variables.

Note that we distinguish two samples, the one using the Michel electron sample and the one that reconstructs the pion using the TPC. The principle is that when we reconstruct the pion using the TPC we can reconstruct momentum and angle of the track but when using the Michel electron sample we only can parametrize the momentum of the pion and we do not have access to his angle. Thus, for the results we use the sample composed by the TPC and Michel electron together or only the TPC sample.

6.3 The Charged Current Single Pion Selection

In Chapter 5 it is described the procedure for the event selection used in the analysis. In order to improve the purity of the selection without decrease the efficiency in a notable sense two modifications has been apported to the previous selection. The changes affect the FGD particle identification and add a new ECal π^0 veto. Any cut step not described here has been already described in Chapter 5.

The set of $CC1\pi^+$ selection cuts are:

1. *Data quality flag.*
2. *Bunching.*
3. *Total Multiplicity cut.*
4. *Quality and Fiducial cut.*
5. *Backwards–going tracks and TPC1 veto.*
6. *Broken Track cut.*
7. *Muon PID cut.*
8. *One π^+ cut.* The ν_μ CC1π^+ exclusive sample selection is done by the identification of one, and only one, π^+ and rejecting events with π^0 or π^-.

   The π^+ candidate is tagged using the TPC 5.2.3.1 and the Michel electron 5.2.3.2 identification. Identification and rejection of events with π^- is done using the TPC PID, and for the π^0 is done by using TPC and ECal (Section 6.3.1).

   In this enriched sample we don't use the FGD–Only pions and we have added the ECal for π^0 rejection.

We keep the other two samples described in Chapter 5 (the CC0π and CCOther) as a way of controlling and understanding the migrations between the samples. Note that the

π^+ topology is highly dominated by secondary interactions (SI) because of the hadronic nature of the pion. Effects like pion absorption or re–interaction inside the detector make difficult to get a high purity of the sample. For this reason, a detailed study about the migrations from our signal to other samples is required. Details about these studies are discussed in Section 6.5.

We count the number of π^+ in the event as the number of TPC and FGD (only the Michel electron criteria) π^+ that are identified. In events where we don't identify Michel electrons we check if there are at least one FGD–Only track identified as π^+ and we move these events to the CCOthers sample [4]. Some of these events are CC1π^+ signal although its purity is low, $\sim$ 33%. Due to the impossibility from the current reconstruction to determine the momentum for these pions and thanks to the relatively low purity of these events we decided to move these events to the CCOther sample. These events, also if moved to CCOther sample, are not used in any of our control samples used for the background subtraction.

The scheme in Figure 6.2 shows the sample selection.

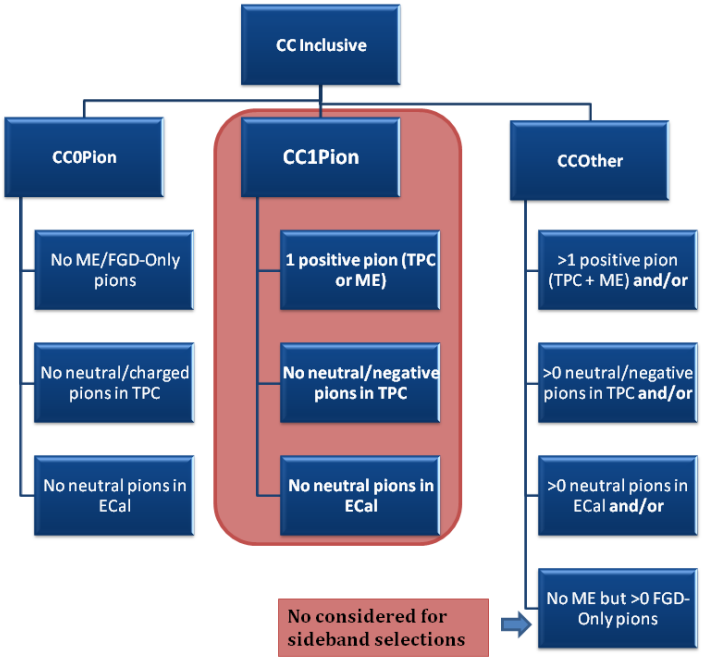

FIGURE 6.2: Scheme of the selection for the $CC1\pi^+$ sample. Starting from the CC Inclusive, then splitting into the three sub–samples. Finally, the $CC1\pi^+$ is selected.

In this Chapter we explain the new ECal π^0 veto and the FGD–Only track criteria. Since the FGD–Only identification has been improved from previous Chapter.

[4] The FGD–Only pion events in th CC1π^+ sample corresponds to less than the 10% of the total.

6.3.1 ECal PID

The ECal PID is used to identify neutral pions, and these events are moved to the CCOther sample. This neutral pion tagging using the ECal detector (Barrel or Downstream) is done as follows:

1. *Isolated object in ECal*: look for reconstructed objects with segments in the ECal detector and no segment in other sub–detector. By object it means: any track or cluster detected.

2. *Time Bunch:* the object is reconstructed in the same time bunch as the muon candidate.

3. *Most energetic*: from all possible ECal objects that pass these cuts we select the most energetic one. The reason for that is that we need to identify only one neutral pion to move the event into the CCOther sample and the reconstruction efficiency is better for high energy clusters.

4. *Shower–like*: the object must be identified as a shower–like object using the MIP–EM observable measured by the ECal (see 3.2.4).

5. *Closer object*: The ECal object must have hits in the first 5 layers of the ECal. This neutral pion comes from the initial interaction and goes to ECal where produces a shower.

6. *Distance to muon*: the distance between the muon candidate (its end position) and the isolated ECal object (its start position) must be bigger than 700 mm. This cut is applied in order to exclude mis–identification of the electron or positron (which represent the neutral pion signature) with the muon candidate from the TPC when reaching the ECal detector.

7. *Distance to positive*: the distance between any positive TPC track (end position) and the isolated ECal object (start position) must be bigger than 700 mm. This cut is applied in order to exclude mis–identification of the electron or positron with any pion or proton in the event. It checks also the distance to positrons tracks, this does not affect since these positrons are already identified as π^0 events and moved to CCOthers.

In Figure 6.3 we show the number of events where there are reconstructed ECal π^0, for the CC inclusive sample, separated by true topology type (on the X–axis) and according to the true particle type associated to the ECal object tagged. In order to understand better how this tagging is working we split the CCOther sample into two: events with

true π^0 and events with no true π^0. Note that the true particle type in the plots corresponds to the true particle tagged in ECal and not to the primary particle (for primary particle we refer to the one comming from the neutrino interaction and not due to any secondary interaction), this explains why we don't see explicitly π^0 but electrons/positrons/gammas. We can see that the neutral pion tagging is working quite well since the main contribuion are electrons and positrons.

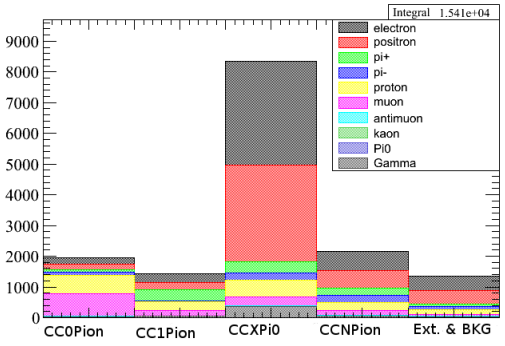

FIGURE 6.3: Distribution of the number of ECal π^0 events respect to the topology type according the true particle type of the ECal object tagged.

6.3.2 FGD PID

Events with no TPC pions neither Michel electrons but FGD–Only reconstructed pions are moved to CCOther but not used in the control samples for background subtraction.

From the selection based on the FGD PID we do not obtain a high purity sample. Furthermore those events are characterised by serious problems. Several attempts to reconstruct the momentum of these FGD–Only tracks have been tested unfruitfully. The intrinsic problem comes from the fact that these particles have a high probability to re-interact in the detector and make very difficult to establish this relation. Short tracks with relative large momentum, re-interacting in the detector and producing secondary π^0 are a good example of the kind of complications we faced. Also, broken tracks reconstructed as an unique FGD–Only track supposes a problem for the momentum reconstruction.

In previous Chapter has been already shown the pull distributions of these tracks before any selection is applied except the inclusive CC selection, see Figure 5.6. It also has been explained the selection procedure. Then, here we just summarize the steps in the selection and describe the ones that differs from the ones in Chapter 5.

To identify positive pions in the event the following requirements on the tracks were applied:

1. To be in the same time bunch than the muon candidate.
2. No segments in any TPC.
3. The track must start and end inside the FGD1 volume, no fiducial volume is applied. This is the main difference respect to Chapter 5. Using this volume condition we gain in efficiency and no significant change on purity has been observed.
4. The cosine of the angle must be > 0.3 (or $<$ -0.3 in case of backward going).
5. The pion pull must be $>$ -5. and $<$ 1.5. The low boundary of this cut helps on reduce the electron/positron contamination and the higher boundary helps on rejecting protons.

Figure 6.4 shows the pull pion distribution for the selected FGD–Only tracks identified as pions, in the CC inclusive sample. Figure 6.5 shows the distribution of the number of selected positive pions using the FGD–only tracks also for the CC inclusive sample.

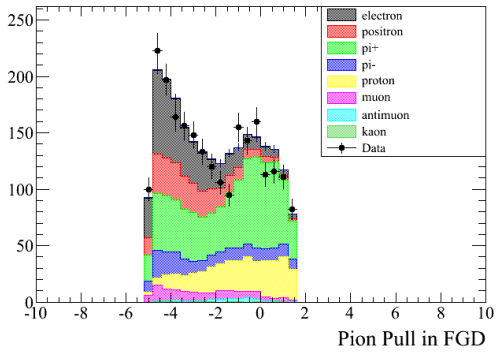

FIGURE 6.4: Pion pull distribution of the selected positive pions in the FGD–only tracks for the CC sample.

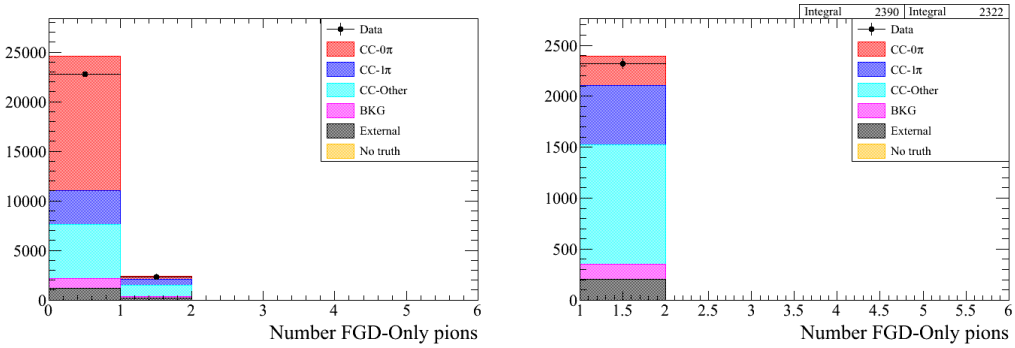

FIGURE 6.5: Distribution of the number of positive pions reconstructed using the FGD PID criteria for FGD–only tracks, according to the true topology type, left. On the right, same distribution but excluding the zero bin to observe better the brakdown topology composition of the identified pions.

6.4 Selection composition and efficiencies

This section describes the composition and efficiency of the selected exclusive CC1π^+ sample. NEUT is used as the default MC. Just for matter of comparison we show some values using GENIE [5].

Table 6.2 shows the composition of the CC1π^+ sample depending on the true particle type of the muon candidate. The muon purity is ∼90% and the main background is due to the indistinguishable π^- contamination.

Table 6.3 shows the efficiency of the sample. The efficiency is defined according to equation 5.7.

Table 6.4 shows the purity of the CC1π^+ sample at each cut step, it is also shown the corresponding number of events.

True particle	Fraction (%)
μ^-	87.54
μ^+	0.96
e^-	0.24
e^+	0.02
π^-	8.61
π^+	2.4
p	0.21
other	0.06

TABLE 6.2: Composition for the CC1π^+ sample, according to the particle type selected as muon candidate.

Sample	Efficiency in NEUT (%)	Efficiency in GENIE (%)
CC1π^+	24.7	23.6

TABLE 6.3: Efficiency for the CC1π^+ exclusive sample.

Cut level	Purity CC1π^+ (%)	Sample Reduction (%)	number Data events	number MC events
Quality and Fiducial cut	9.3	100	47090	35550.24
Backwards-going tracks and TPC1 veto	11.3	80.29	34762	28545.15
Broken Track cut	11.5	78.27	33660	27827.29
Muon PID cut	14.8	58.31	24378	20012.32
One Pion cut	61.5	6.6	2739	2278.97

TABLE 6.4: Composition of true CC1π^+, sample reduction fraction, number of events, for data and for NEUT Monte Carlo (scaled to total data PoT), at each cut step.

[5] When using GENIE it is specified.

Table 6.5 shows the purities of the CC1π^+ sample selected by applying the full set of cuts from Table 6.4 according to the true topology. In Table 6.6 purity is shown according to the generator definition. In both tables is shown purities according to NEUT (second column) and to GENIE (third column).

CC1π^+ Sample	Topology Composition (%) NEUT	Topology Composition (%) GENIE
CC-0-pion	4.96	3.66
CC1π^+	61.45	68.69
CC-Other	21.99	15.32
Background	6.17	5.71
Out of FGD 1 FV	5.42	6.62

TABLE 6.5: Composition of the sample respect to the true topology type using NEUT (second column) and GENIE (third column). Background is defined as the anti-neutrino, electron neutrino and neutral current events.

CC1π^+ Sample	Composition (%) NEUT	Composition (%) GENIE
CCQE	4.65	2.91
Resonant	45.96	62.20
DIS	23.85	18.43
Coherent	13.95	4.12
NC	3.86	3.55
$\overline{\nu}_\mu$	1.94	1.86
ν_e	0.33	0.27
External	5.42	6.62
other	0.04	0.02

TABLE 6.6: Composition for the sample, according to the generator interaction types using NEUT.

We see differences on purity depending on the used Monte Carlo but in general they are not large. For example, it seems that NEUT over predicts the coherent signal as we see from Table 6.6. The higher contribution of the coherent signal in NEUT seems to be due to an over prediction as recently shown by the MINERνA measurements [30]. It seems that GENIE predicts larger purity of true CC1π^+ topology component in our selected sample. We suspect that these differences are due to the pion production parameters. In GENIE we can see a lower composition of the DIS component that can explain a relative increment of resonant interaction, for CCQE and the other channels we don't observe size-able differences.

From the tables showed in this Section we can see that adding the new ECal π^0 veto and removing events selected with the FGD–Only tagging, the purity of the CC1π^+ sample have been increased respect to the previous selection presented in Chapter 5. Now the

purity is $\sim 61\%$ and previously it was $\sim 49\%$. From a general point of view, it is always recommended to follow a background subtraction strategy with control samples than only trust on the MC prediction and apply a purity correction for the cross section measurement. But the background subtraction becomes more important as lower is the purity of the selected events. For this reason, in this analysis it have been done a hard effort to understand and control the background in a data driven approach, see Section 6.6.

The composition of the sample (according to the *topology* types) when the pion is reconstructed by using the TPC PID (second column) or the Michel electron criteria (third column) is shown in Table 6.7. Table 6.8 shows the number of entries (for data and Monte Carlo scaled to the total PoT of data) in the two case: positive pion TPC and pions identified with the Michel Electron.

CC1π^+ Sample	Composition (%) TPC pion	Composition (%) ME pions
CC-0-pion	4.1	6.3
CC1π^+	61.1	62.04
CC-Other	24.71	17.5
Background	7.9	3.31
External	2.16	10.82

TABLE 6.7: Composition for the sample, with the positive pion identified with the TPC criteria (second column) and identified with the Michel electron criteria (third column), according to the *topology* types.

Pion criteria	Number of entries MC (scaled to data)	Number of entries Data
positive pion TPC	1503.91	1563
ME	1084.20	1176

TABLE 6.8: Number of entries according to the tagging of the pions in the sample.

We see that both pion tagging methods have similar purities, where the TPC method has more CCOther contamination and the Michel electron tagging give us more out of fiducial volume contamination. Events selected with TPC criteria are dominant respect to the ME one in the sample.

6.4.1 Sample Details

In this Section we present the observables defined for the selected CC1π^+ sample. Distributions of all variables that are used for the cross section measurements are showed in this section before to do the cross section extraction. In all cases we show these distributions using NEUT compared to data.

6.4.1.1 Expected Average Neutrino Direction

In order to provide differential results that can be compared with other experiments and also to provide results for all the variables defined in this Chapter (i.e. planar angles, neutrino energy or momentum transfer variables) we need to use the neutrino direction. As already seen, ND280 is an off–axis detector respect to the neutrino beam direction. The expected average neutrino direction provided by the MC is used to compute the different angles. This direction is performed using the mean value of the neutrino in his x, y and z components according to the true neutrino direction.

The expected average value for the true neutrino direction, using x, y and z coordinates (ND280 is oriented in the Z direction) is [6]:

$$\nu_{direction} = (-0.013, -0.025, 0.999) \tag{6.1}$$

To appreciate the effect Figure 6.6 shows the difference between:

- the true muon angle respect to the true neutrino direction and the reconstructed muon angle using the expected average neutrino direction (blue line),
- the true muon angle respect to the true neutrino direction and the reconstructed muon angle computed respect the z–axis (violet line).

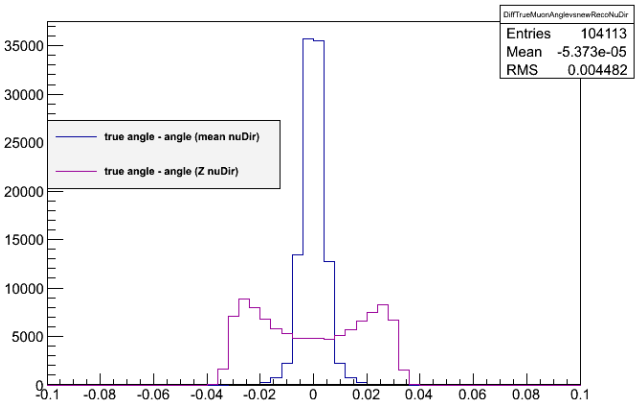

FIGURE 6.6: Difference of the true muon angle respect: i) reconstructed muon angle using the expected average neutrino direction, ii) reconstructed muon angle computed vs the z–axis, in radians.

In Figure 6.7 we show the expected average neutrino angles, i.e. azimutal and polar (in radians) from left to right.

[6] Units are in mm

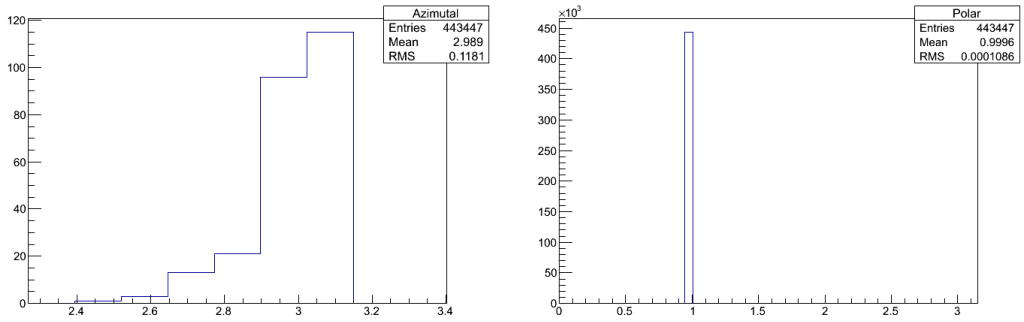

FIGURE 6.7: Azimutal (left) and polar (right) expected neutrino angles, using NEUT MC, for all the true CC inclusive events generated in the FGD1 FV.

From now, the muon(pion) angle is performed using the muon(pion) and neutrino reconstructed directions.

6.4.1.2 Muon Kinematics

Figures 6.8 and 6.9 show respsectively the muon momentum and the muon angle distributions for the selected exclusive CC1π^+ events according to the *topology* (left) and generator definition (right).

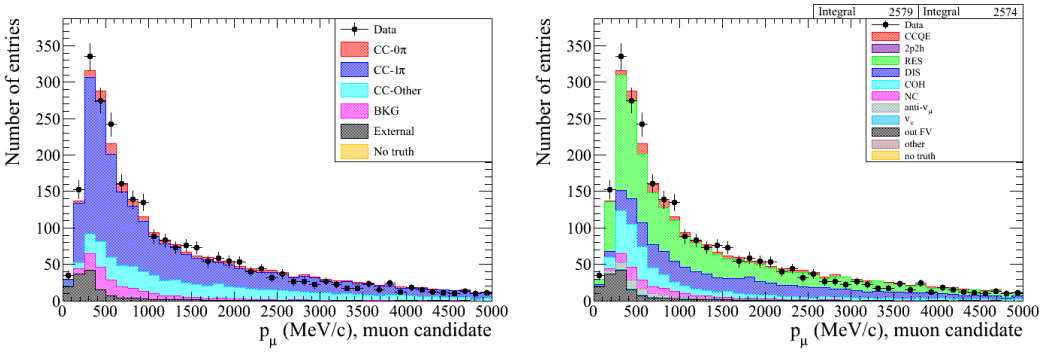

FIGURE 6.8: Muon momentum distribution for the CC1π^+ according *topology* (left) and generator (right) level.

In Figure 6.10 we show the 2–D distribution of the reconstructed muon momentum with respect to reconstructed muon angle (left) and the true muon momentum with respect to true muon angle (right), for the true CC1π^+ signal.

In Figure 6.11 we show the 2–D distribution of the reconstructed minus the true muon momentum respect the true muon momentum (left) and the reconstructed minus the true muon angle with respect to the true muon angle (right), for the true CC1π^+ signal. It is also shown the difference of reconstructed minus the true for the muon momentum and angle.

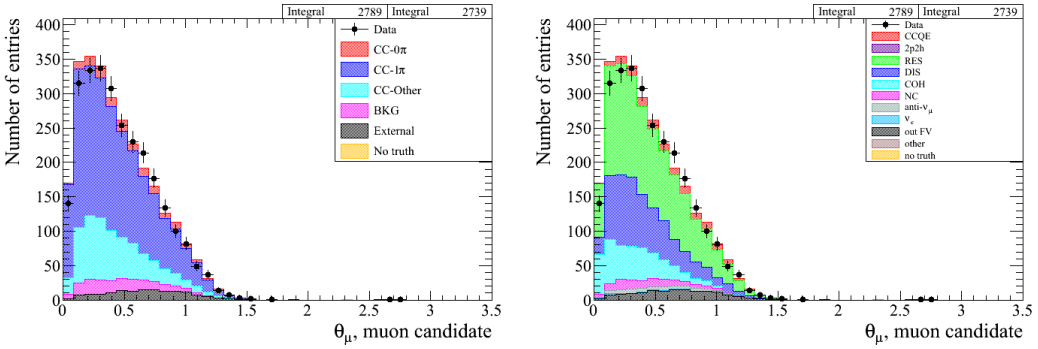

FIGURE 6.9: Muon angle distribution for the CC1π^+ according *topology* (left) and generator (right) level.

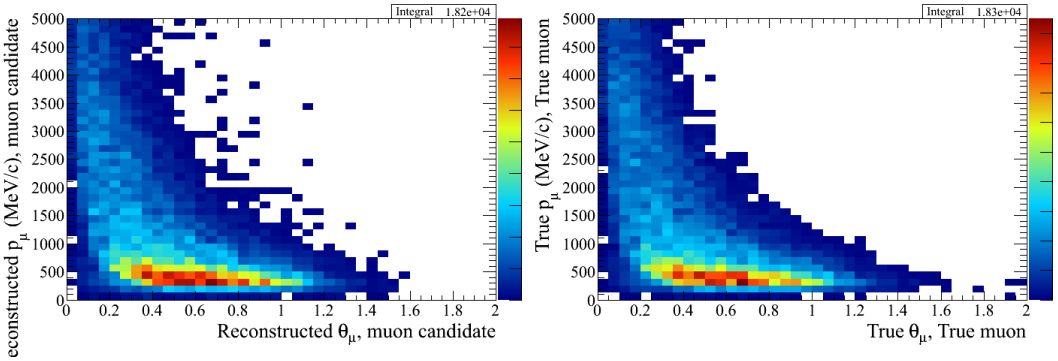

FIGURE 6.10: Momentum of the muon vs angle of muon, for reconstructed variables (left) and true variables (right). For true CC1π^+ signal.

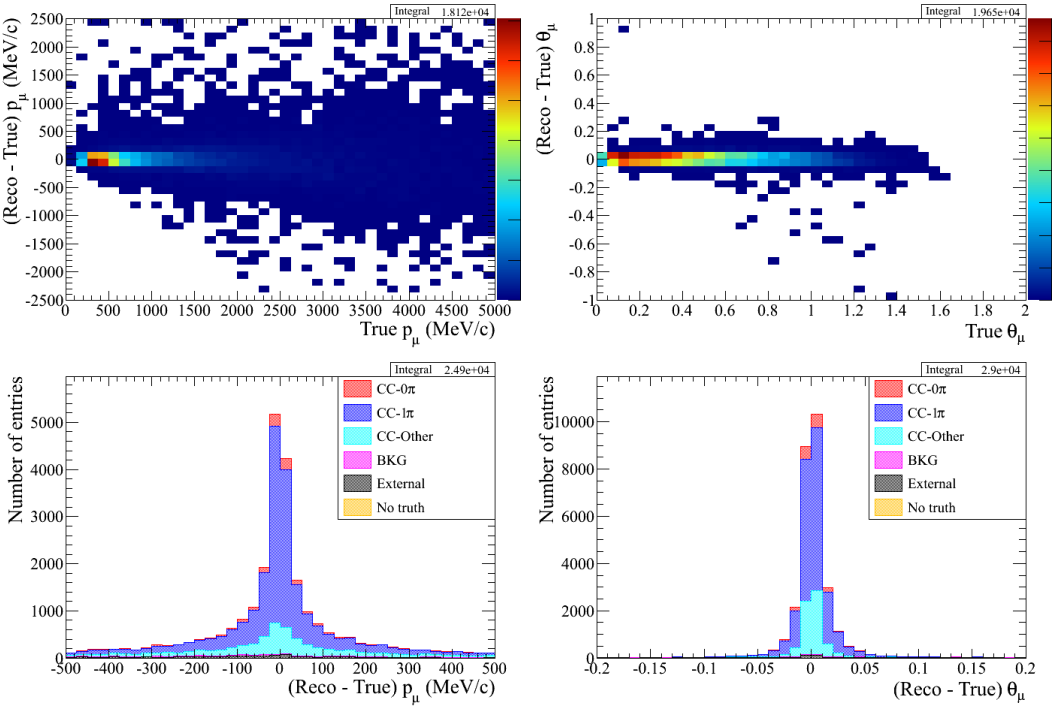

FIGURE 6.11: The reconstructed minus the true momentum muon vs the true momentum of the muon (left). The reconstructed minus the true angle of the muon vs the true muon angle (right). For true CC1π^+ signal. Bottom plots are the difference of the reconstructed minus the the truth of the muon momentum and the muon angle.

In general we observe a fair qualitative agreement between the reconstructed and the true values for the muon variables. This is due to the good performance of the TPC.

6.4.1.3 Pion Kinematics

We show results for both pion identification criteria presented previously.

The momentum of the pion identified with a Michel Electron can be reconstructed by looking at the distance between the Michel electron cluster and the vertex of the event and then using a momentum–by–range technique [7]. This is rather complex and it drives to wrong results[8]To perform a momentum–by–range for the Michel electrons we need to measure the distance of the vertex to the energetic center. A Michel electron uses to be detected as a cluster or a single hit in the detector or a very short track. Then, to reconstruct the distance in the case of a cluster, the most abundant in the Michel electron tagging, it is needed to look for the most energetic hit in the cluster and then check the distance. These distances uses to be very short, then the resolution on the measured distance and angle tends to be very bad.. So, we have decided to apply a different technique: a simple parametrization. The distribution of the true momentum of the true pions in the sample when identified by the Michel electron tagging and it is a true CC1π^+ event, is shown in Figure 6.12. As we observe, the momentum of these true pions have a peak at the value around 130 MeV. The spread of the momentum is not so large, so we can associate a momentum of the pion of 130 MeV. When measuring the differential cross section with respect to the pion momentum, we will use a bin size that takes into account this spread.

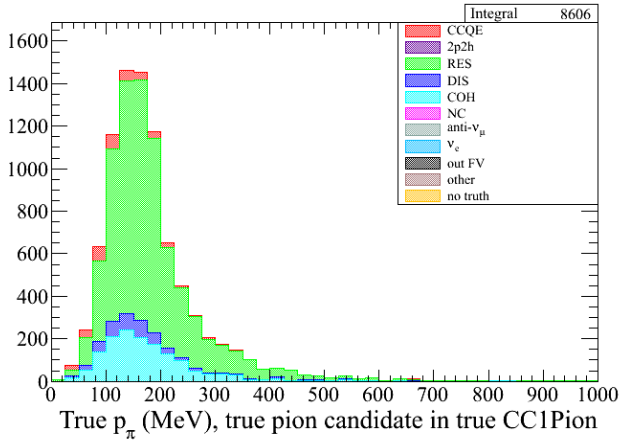

FIGURE 6.12: Distribution of the momentum of the true pion in the true CC1π^+ topology in the sample when the pion is reconstructed by Michel electron tagging.

[7]Establish a relation between the momentum and the lenght of the track.

The angle of these pions is not expected to have a preference value (see Section 6.9). For this reason, when the pion angle is explicitly used for the computation of the cross section we exclude events identified using Michel electrons.

Figure 6.13 shows the pion momentum distribution according to the *topology* (left) and generator (right) definition. Top and bottom plots showe events considering all $CC1\pi^+$ sample (top plots) and events considering sub-sample when the pion is reconstructed only using the TPC pion identification (bottom plots).

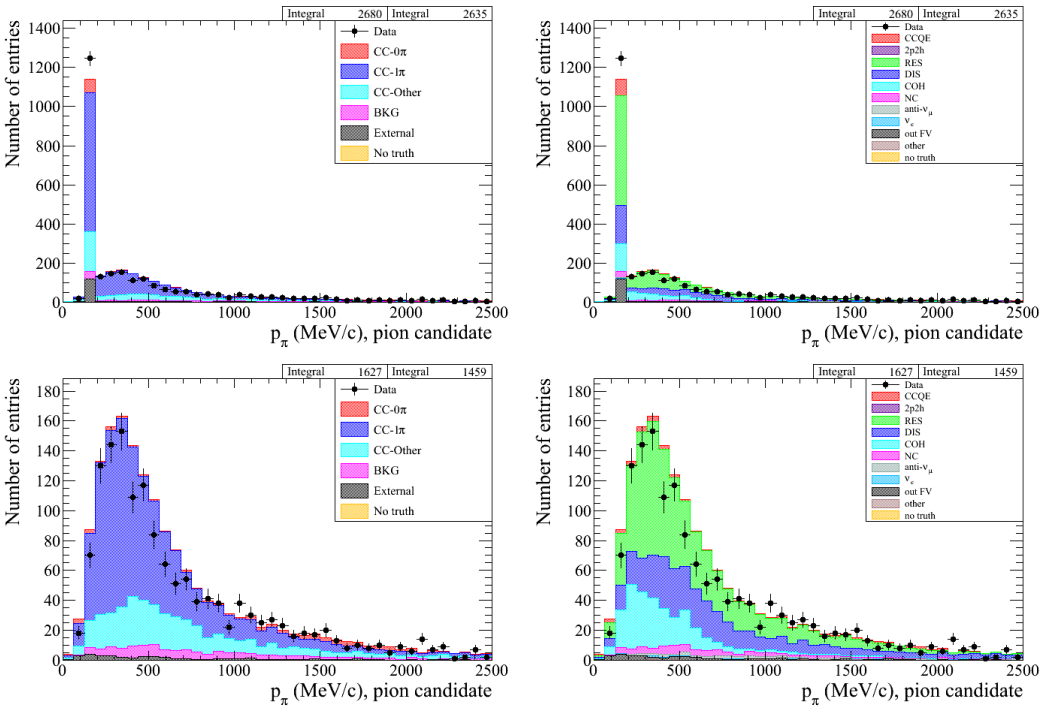

FIGURE 6.13: Pion momentum distribution for the CC1π^+ according *topology* (left) and generator (right) level. Top plots are for the total $CC1\pi^+$ events and bottom plots are only showing event with a pion selected in the TPC.

In Figure 6.14 the distribution of the pion angle is shown, according to the *topology* (left) and generator (right) definition. Only for pions reconstructed with the TPC criteria.

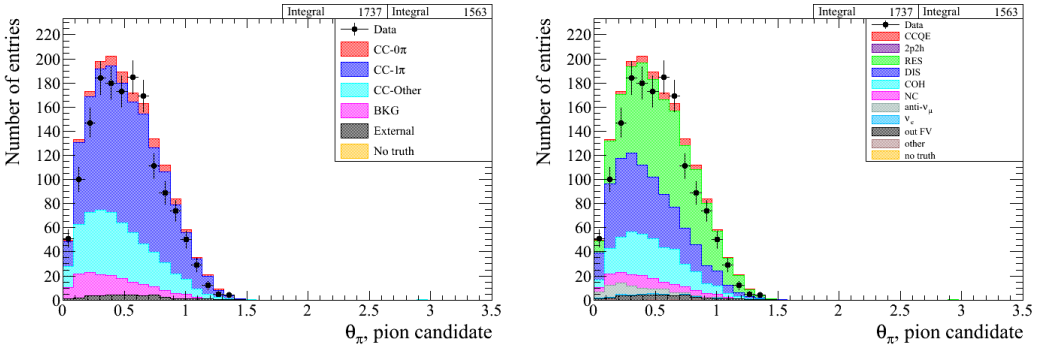

FIGURE 6.14: Pion angle distribution for the CC1π^+ according *topology* (left) and generator (right) level. Only TPC pions.

Figure 6.15 shows the 2–D distribution of the difference between the reconstructed and the true pion momentum respect to the true pion momentum (left). On the right, the figure shows the difference between the reconstructed and the true pion angle with respect to the true pion angle, for the true CC1π^+ signal. It is also shown the difference between the reconstructed and the true for the pion momentum and angle.

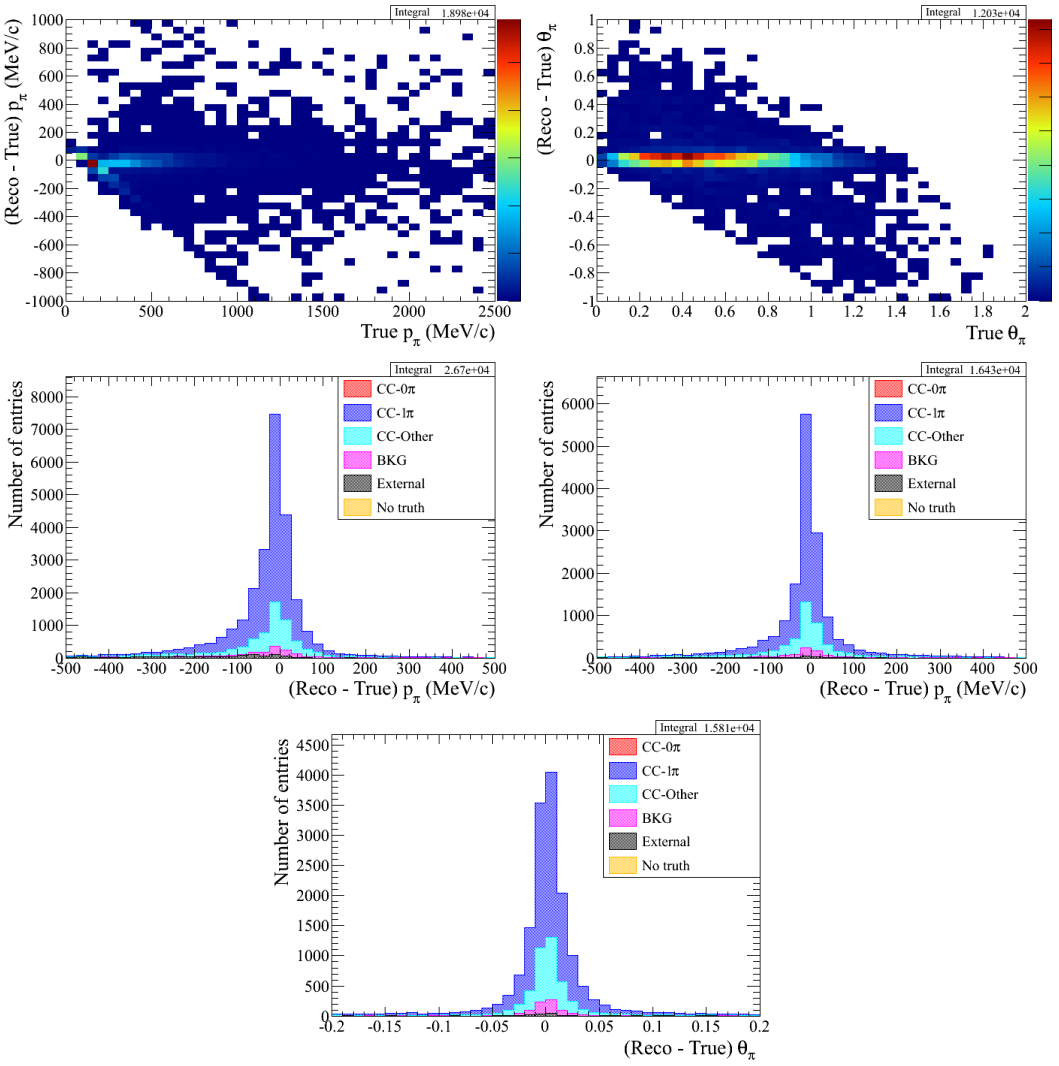

FIGURE 6.15: Reconstructed minus the true momentum pion vs the true momentum of the pion (left). Difference between the reconstructed and the true angle of the pion vs the true pion angle (right), only for TPC pions in this case. For the true CC1π^+ signal in the CC1π^+ sample. Bottom plots are the difference between the reconstructed and the truth of the pion momentum for all the $CC1\pi^+$ sample (left) and for the sub-sample of $CC1\pi^+$ when the pion is reconstructed with TPC (right). Bottom plot is the difference of reconstructed minus the truth for pion angle, for the $CC1\pi^+$ sample, only TPC pions.

We can conclude that we have a fair agreement between reconstructed and true variables for the pion considering that the purity on selecting pions is lower than for the muon case.

6.4.1.4 Neutrino Energy

The neutrino energy reconstruction for the CC1π^+ sample is done using two different formulas.

The first formula used is the so–called "MiniBooNE's Formula"[29], E_{RecoMB}, and it is defined as:

$$E_{RecoMB} = \frac{m_\mu^2 + m_\pi^2 - 2m_N(E_\mu + E_\pi) + 2p_\mu \cdot p_\pi}{2(E_\mu + E_\pi - |\mathbf{p}_\mu| cos\Theta_{\nu,\mu} - |\mathbf{p}_\pi| cos\Theta_{\nu,\pi} - m_N)} \tag{6.2}$$

This formula assumes that the final state includes a proton that has not been reconstructed and applies energy and momentum conservation under the assumption that the target proton is at rest inside the nucleus.

For events where the pion is selected using the Michel electron tagging, and consequently no angle is reconstructed, we use an approximation that consist on neglect the term with the pion angle, equation below.

$$E_{RecoMBapproach} = \frac{m_\mu^2 + m_\pi^2 - 2m_N(E_\mu + E_\pi) + 2p_\mu \cdot p_\pi}{2(E_\mu + E_\pi - |\mathbf{p}_\mu| cos\Theta_{\nu,\mu} - m_N)} \tag{6.3}$$

We can justify the decision due to the small difference on neutrino energy in cases where we have Michel electron and we use the $E_{RecoMBapproach}$ formula. The pion momentum is low in this case ($\sim 130 MeV$) and its impact on the total energy is small. Figure 6.16 shows the neutrino energy reconstruction for Michel electron events.

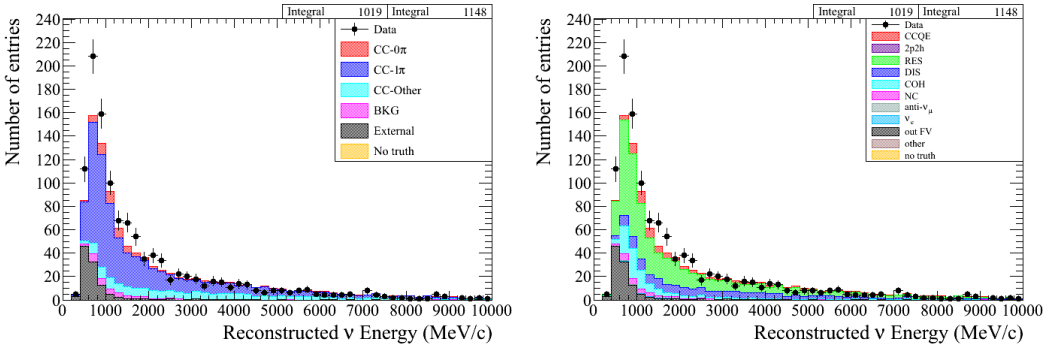

FIGURE 6.16: Neutrino energy reconstruction for Michel electron events for the CC1π^+ sample according *topology* (left) and generator (right) level.

Figure 6.17 shows the neutrino energy distribution for all the selected exclusive CC1π^+ events (using ME and TPC pions) according to the *topology* (left) and generator (right) definition.

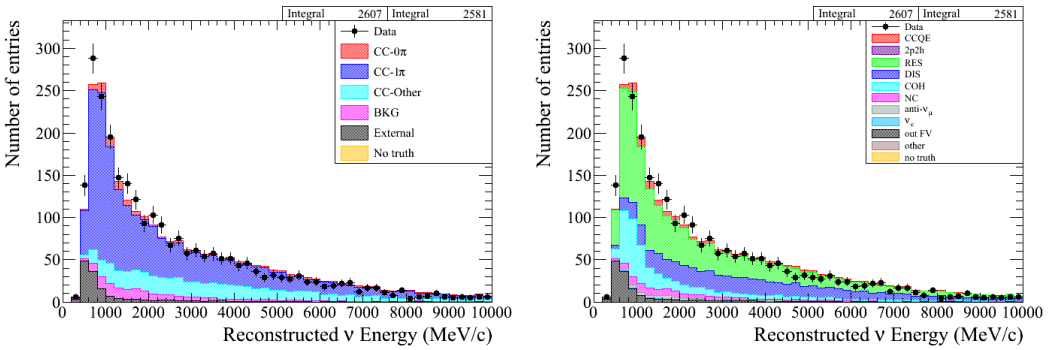

FIGURE 6.17: Neutrino energy distribution for the CC1π^+ according *topology* (left) and generator (right) level.

The true neutrino energy calculated using the "MiniBooNE's Formula" is compared to the true neutrino energy predicted by the MC generator in Figure 6.18, using TPC and ME pions. Left plot shows the difference between the true neutrino energy calculated using true values with the "MiniBooNE's Formula" and the predicted true neutrino energy by the MC generator. The plot on the right shows the same difference between the two true neutrino energies approaches respect to the true neutrino energy predicted by the MC generator, for the true CC1π^+ signal.

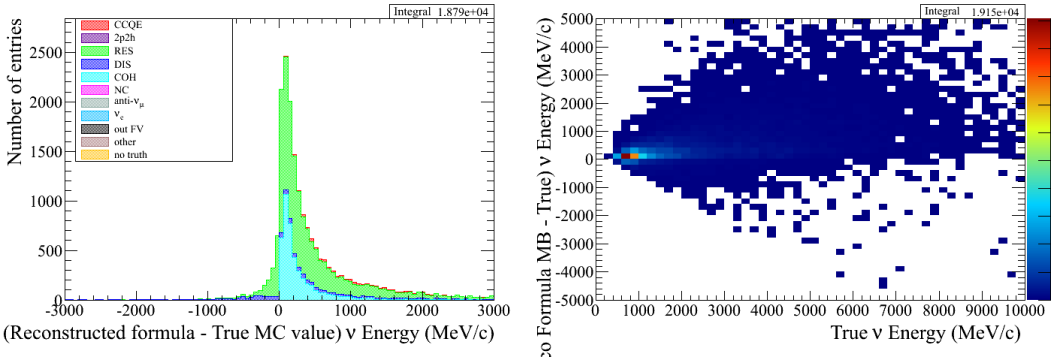

FIGURE 6.18: Difference between the true neutrino energy using the MiniBooNE's formula and the true neutrino energy predicted by MC, left. Same difference but plotted with respect to the true neutrino energy predicted by the MC, right. For true CC1π^+ signal.

In Figure 6.19 it is compared the true neutrino energy predcited by the MC to the reconstructed values we obtain with the "MiniBooNE's Formula".

We perform another development for the neutrino energy. We use the same approach used in the "MiniBooNE's Formula" but adding some terms that were not included in the final expression of the previous E_{RecoMB} formula. We will refer to this formula as E_{Reco} and it is defined as:

$$E_{Reco} = \frac{m_p^2 - (m_p - E_{bind} - E_\mu - E_\pi)^2 + |\overrightarrow{p}_\mu + \overrightarrow{p}_\pi|^2}{2(m_p - E_{bind} - E_\mu - E_\pi + \frac{\overrightarrow{p}_\nu(\overrightarrow{p}_\mu + \overrightarrow{p}_\pi)}{E_\nu})} \tag{6.4}$$

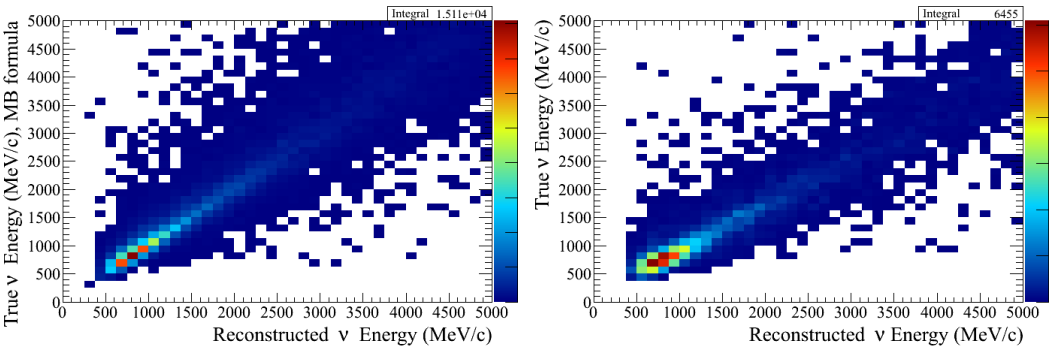

FIGURE 6.19: True neutrino energy predicted by the MC respect to the reconstructed neutrino energy using the "MiniBooNE's Formula". Left plot is for the true CC1π^+ signal, right plot is excluding the Michel electron events.

with E_{bind} defined as the binding energy for the nucleons at the nucleus estimated to be 25 MeV.

For this reconstruction method we don't use Michel electron events since the pion reconstructed direction is required. This is the formula we use for the computation of the planar angles which are defined later in this Section. To compute these angles we already need the pion direction then no Michel electron sample can be included.

Figure 6.20 shows the E_{Reco} distribution for the selected exclusive CC1π^+ events according to the *topology* (left) and generator (right) definition, with no Michel electron events.

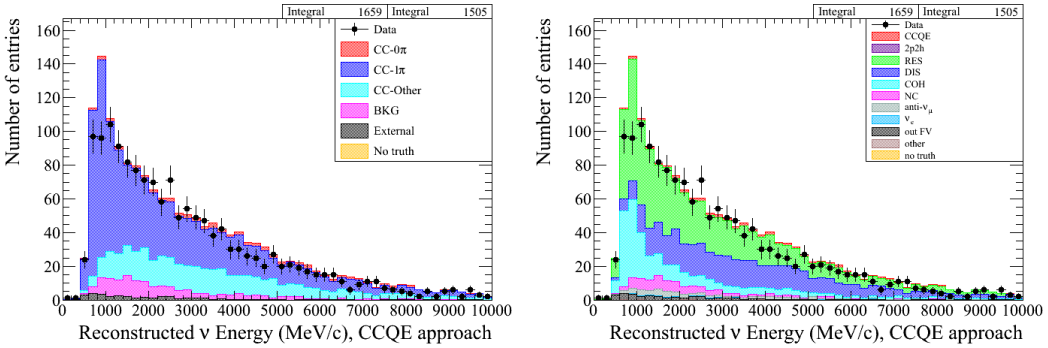

FIGURE 6.20: Neutrino energy distribution for the CC1π^+ according *topology* (left) and generator (right) level, using E_{Reco}.

6.4.1.5 Momentum transfer

The 4–momentum transfer (Q^2) is defined as:

$$Q^2 = -q^2 = (p_\mu - p_\nu)^2 \tag{6.5}$$

Where p_μ and p_ν are the 4–momentum vectors of the muon momentum and neutrino momentum respectively. The neutrino 4–momentum transfer reconstruction is done using the E_{RecoMB} energy formula. Then, we can use the Michel electron sample [9].

Figure 6.21 shows the Q^2 for the selected CC1π^+ events according to their *topology* (left) and generator interaction code (right) definitions.

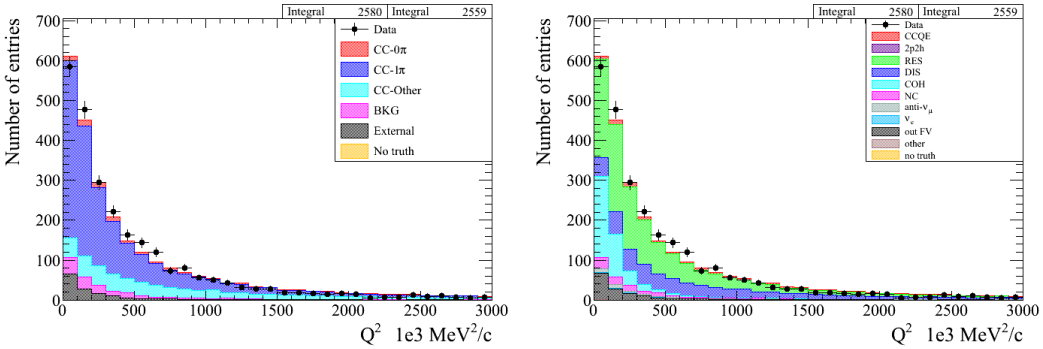

FIGURE 6.21: Square value of the momentum transfer of the interaction for the CC1π^+ according *topology* (left) and generator (right) level.

Figure 6.22 shows the 2–D distribution of the difference between the reconstructed and the true Q^2 with respect to true Q^2 (left plot), for the true CC1π^+ signal. It is also shown (right plot) the difference between the reconstructed and the true for the Q^2 in the sample to show differences between signal and background. We observe that the background is shifted to negative values of this difference which means that for non–signal events the true momentum transfer is bigger. This is expected for CCOther events, main bakground, since the momentum transfer of these events should be bigger. We see that in case of CC0π the difference is shifter at positive values, in this case the momentum transfer is smaller than in the single pion event.

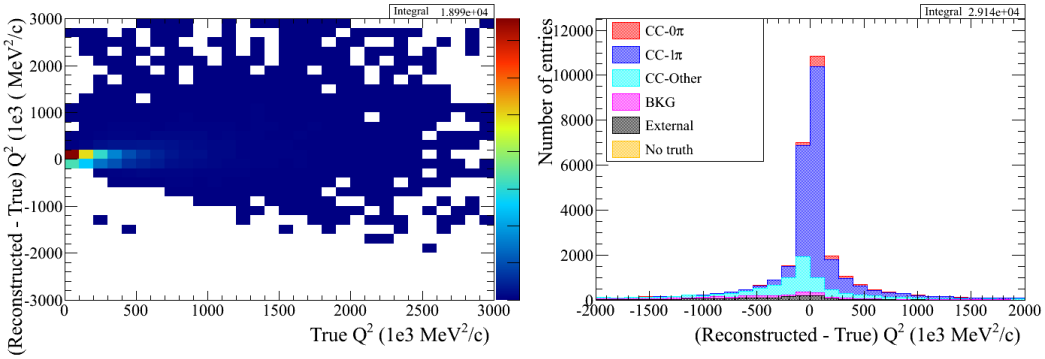

FIGURE 6.22: Difference between therReconstructed and the true square value of the momentum transfer vs true, top plot, for true CC1π^+ signal in the CC1π^+ sample. Bottom plot, difference of reconstructed minus the true Q^2 value in the sample.

[9] In the Michel electron case we just use the $E_{RecoMBapproach}$ instead E_{RecoMB}.

In order to provide a more accurate information about the interaction, similar studies are done by using the absolute value of the 3–momentum transfer vector,$|Q_3|$. This value is defined as:

$$|Q_3| = |\overrightarrow{p}_\nu - \overrightarrow{p}_\mu| \tag{6.6}$$

This is expected to be the Δ^{++} momentum. In this case we also use the E_{RecoMB} to reconstruct the neutrino energy in order to add the Michel electrons events. Figure 6.23 and shows $|Q_3|$ for the selected CC1π^+ events according to their *topology* (left) and generator interaction code (right) definitions.

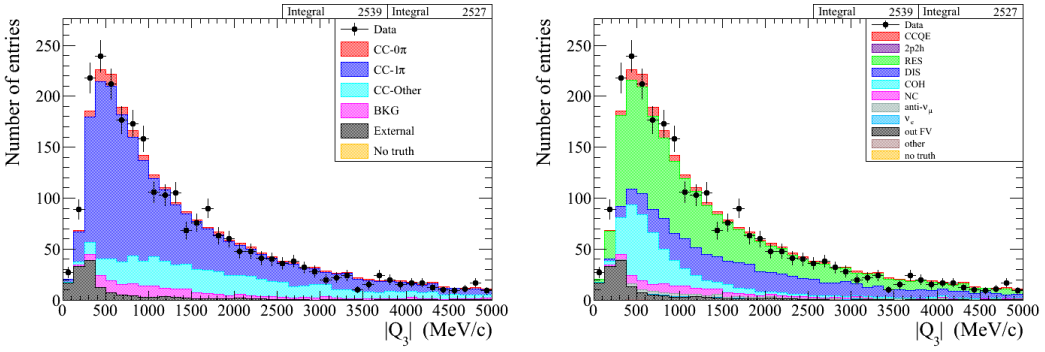

FIGURE 6.23: Absolute value of the 3–momentum transfer of the interaction for the CC1π^+ according *topology* (left) and generator (right) level.

Figure 6.24 displays the 2–D distribution of the difference between the reconstructed and the true $|Q_3|$ with respect to true $|Q_3|$, for the true CC1π^+ signal (left plot). It is also shown the difference between the reconstructed and the true for the $|Q_3|$ in sample in order to show differences between signal and background (right plot). We can appreciate that all CC0π contamination is shifted at very high and positive values. This is expected since the momentum transfered in the interaction should be lower for CC0π that in CC1π^+ events.

6.4.1.6 Special Angular Variables

To have a better understanding of the CC1π^+ sample we studied also some angular distributions which are related to the decay properties of the Δ^{++}. The angular variables can be only measured in cases where the pion has been reconstructed using the TPC.

The distribution of the relative angle between the muon and pion directions in the laboratory frame, $\theta_{\mu\pi}$, is shown in Figure 6.25. It is shown according to the *topology* (left) and generator (right) definition.

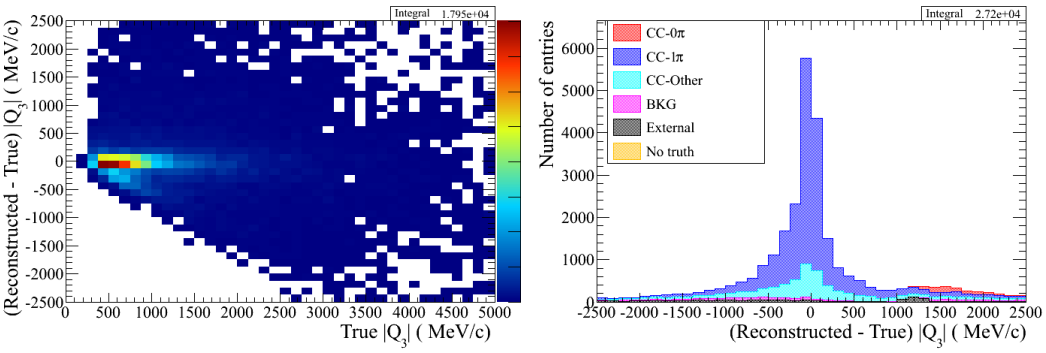

FIGURE 6.24: Distribution of the difference between the reconstructed and true absolute value of the 3–momentum transfer vs the true, top plot, for the true CC1π^+ signal. On the bottom plot, it is shown the difference between the reconstructed and the true Q_3 in the sample.

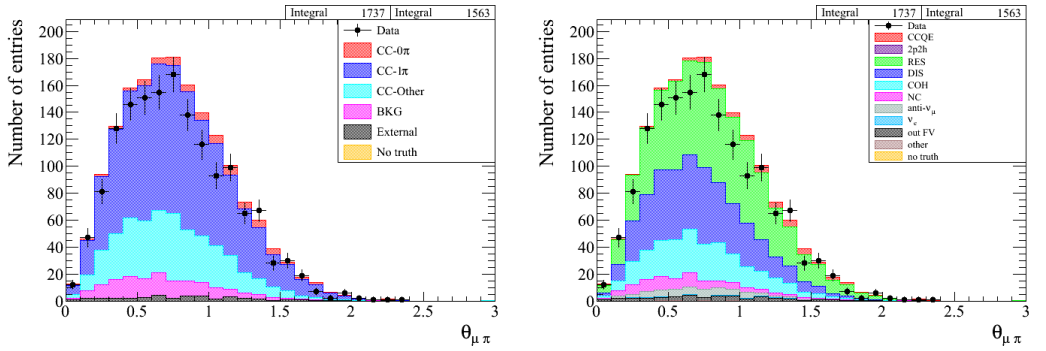

FIGURE 6.25: $\theta_{\mu\pi}$ distribution for the CC1π^+ according *topology* (left) and generator (right) level.

In Figure 6.26 difference between the reconstructed and the true $\theta_{\mu\pi}$ is shown. It is also shown the 2–D distribution of the difference between the reconstructed and the true $\theta_{\mu\pi}$ respect to the true $\theta_{\mu\pi}$, for the true CC1π^+ signal.

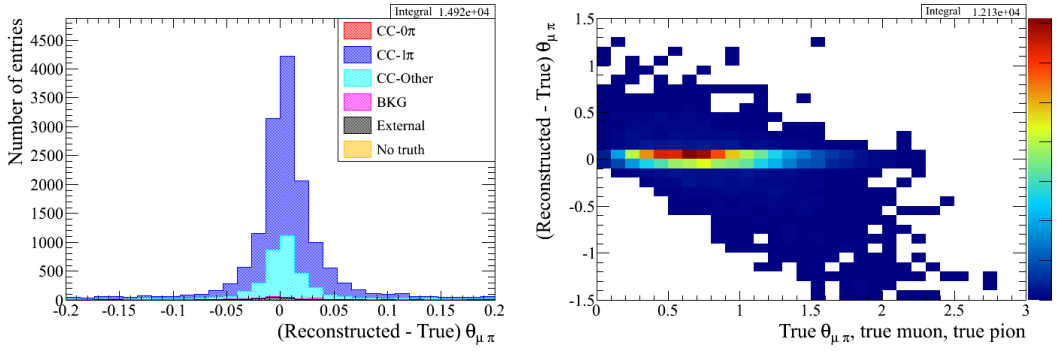

FIGURE 6.26: Difference between the reconstructed angle between the muon and pion and the true angle predicted by MC, left. Same difference but plotted respect to the true angle predicted by the MC (right) for true CC1π^+ signal.

Interesting angles to study are the θ_{planar} and the ψ_{planar} angles, defined in the Adler's system which corresponds to the Δ rest frame, Figure 6.27.

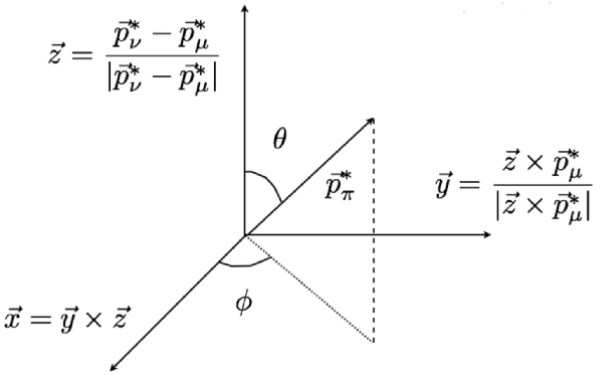

FIGURE 6.27: Azimutal and polar angles defined in the Adler's system, the Δ rest frame.

Since we do not know the target nucleon Fermi momentum we approximate the Δ 4–momentum by:

$$p^\mu_{\Delta^{++}} \approx (E_\nu + (m_p - E_{bind}) - E_\mu, \overrightarrow{p_\nu} - \overrightarrow{p_\mu}) \tag{6.7}$$

The 3 axis are as follows

$$\begin{aligned} \overrightarrow{X} &= \overrightarrow{Y} \times \overrightarrow{Z} \\ \overrightarrow{Y} &= \frac{\overrightarrow{Z} \times \overrightarrow{p^*_\mu}}{|\overrightarrow{Z} \times \overrightarrow{p^*_\mu}|} \\ \overrightarrow{Y} &= \frac{\overrightarrow{p^*_\nu} \times \overrightarrow{p^*_\mu}}{|\overrightarrow{p^*_\nu} \times \overrightarrow{p^*_\mu}|} \end{aligned} \tag{6.8}$$

with p^*_ν and p^*_μ are the neutrino and muon momentum in the Δ rest frame. The pion momentum is also computed in the Δ rest frame. The Adler angles computed with particles leaving the nucleus keep the information about the interaction at the nucleon level. This is shown by Figure 6.28, the two angular distributions are shown comparing the reconstructed angles when the pion leaves the nucleus with the angles at the nucleon level, for true resonant interaction with proton as target nucleon, only Monte Carlo.

These two variables can provide hints of parity violation (P–violation) as it was already seen in ANL [4]. The P–violation was observed due to the lack of preference in the Δ direction in both variables, this indicates no polarization of the Δ particle. For the ANL experiment, the distributions are a bit different with respect to the distributions we obtain with ND280. In Figure 6.29 we show the results presented by ANL.

The difference with respect to our data is probably due to the full phase–space covered by ANL and that the target used was deuterium which minimize any FSI effect. The

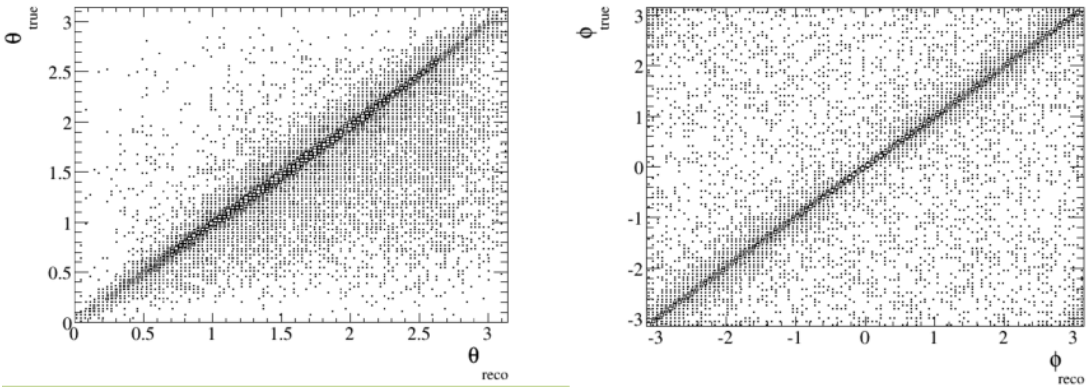

FIGURE 6.28: Scatter plot of the polar angles showing the true angle (observable at the nucleus level), as a function of the reconstructed angle (observable at the nucleus level). Left plot is for the θ angle and right plot for the ψ angle. For true resonant interaction with proton as target nucleon.

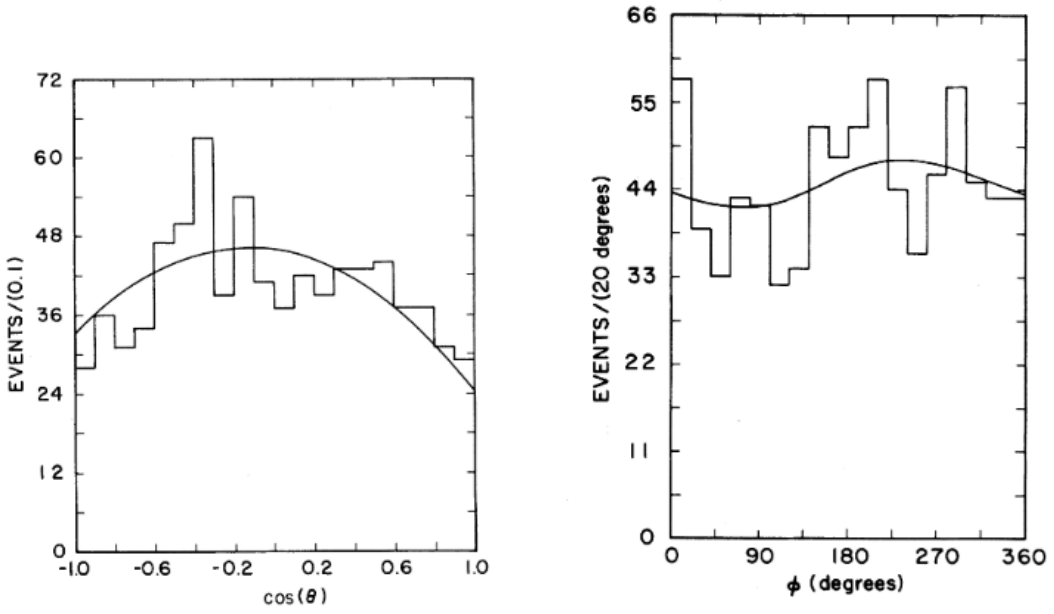

FIGURE 6.29: Results presented by ANL in [4]. Left plot shows the $\cos\theta_{planar}$ and right plot shows the ϕ_{planar} angle.

Rein and Sehgal model assumes that these angular distributions must be close to flat [10] (similar to ANL distributions), if no considering that the direction of the resulting particles and their momentum should be affected by the nuclear medium. This lead to think that distortions with respect to ANL distributions are due to the non full space covered in our analysis and the heavier target used.

Figure 6.30 shows the distribution of the $\cos\theta_{planar}$ of the selected exclusive CC1π^+ events according to their *topology* (left) and at generator level (right) definitions.

[10] The $\cos\theta_{planar}$ is not flat, it has some decreases at the borders for ANL, but there are not any prefered direction.

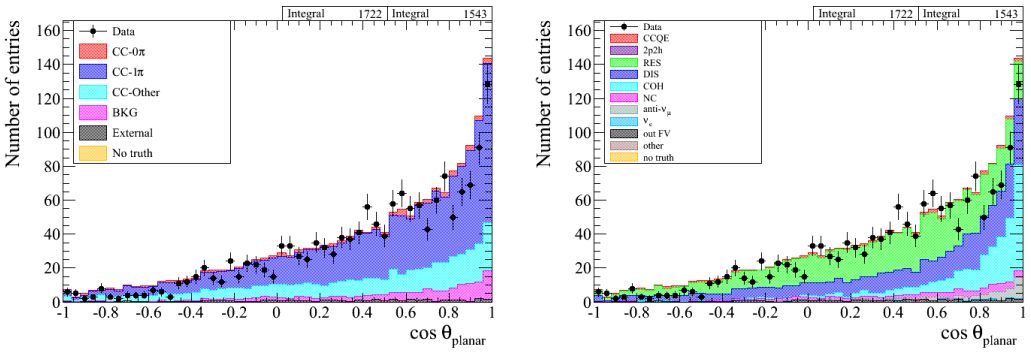

FIGURE 6.30: $\cos\theta_{planar}$ distribution for the CC1π^+ according *topology* (left) and generator (right) level.

If we compare distributions in Figure 6.30 with ANL 6.29, left plot, we see that the shape of the distribution from $[-1, 1]$ in the $\cos\theta_{planar}$ observed by ANL is not preserved. We perfom some studies in order to understand the origin of the differences. For these studies we just use run 4 since available statistics is enough and we perform the studies using only Monte Carlo. In Figure 6.31 a set of plots of $\cos\theta_{planar}$ for:

1. all true generated CC1π^+ signal in FGD1 FV,
2. all true CC1π^+ signal in the CC inclusive sample and
3. all true CC1π^+ signal in the CC1π^+ selected sample.

The reconstructed CC1π^+ events have been already shown in Figure 6.30.

We also show the angular value instead of the cosine of the angles for the same distributions in Figure 6.32.

From Figure 6.31, $\cos\theta_{planar}$ distribution, we can see more in detail why our reconstructed sample differs so strongly from ANL results. In plot *(i)* for all the true generated events we see that the distribution is not similar to ANL results, we don't see any decrease at the borders of the distribution. This can be explained by nuclear effects: angles are computed respect the pion direction and the pion direction is always computed after leaving the nucleus. Pion direction can be affected by the nuclear medium and it can loss enegy when leaving the nucleus. Plot *(ii)* show all true CC1π^+ signal in the CC inclusive sample where the selection implying a forward going muon is already applied. For CC inclusive events we don't do any attempt to identify pions, then the backward–going tracks (for pions) are not rejected. However, there is a decrease on negative values. Plot *(iii)* shows finally all true CC1π^+ when the CC1π^+ sample is selected where the condition of forward–going pions is applied. Here we see a bigger decrease

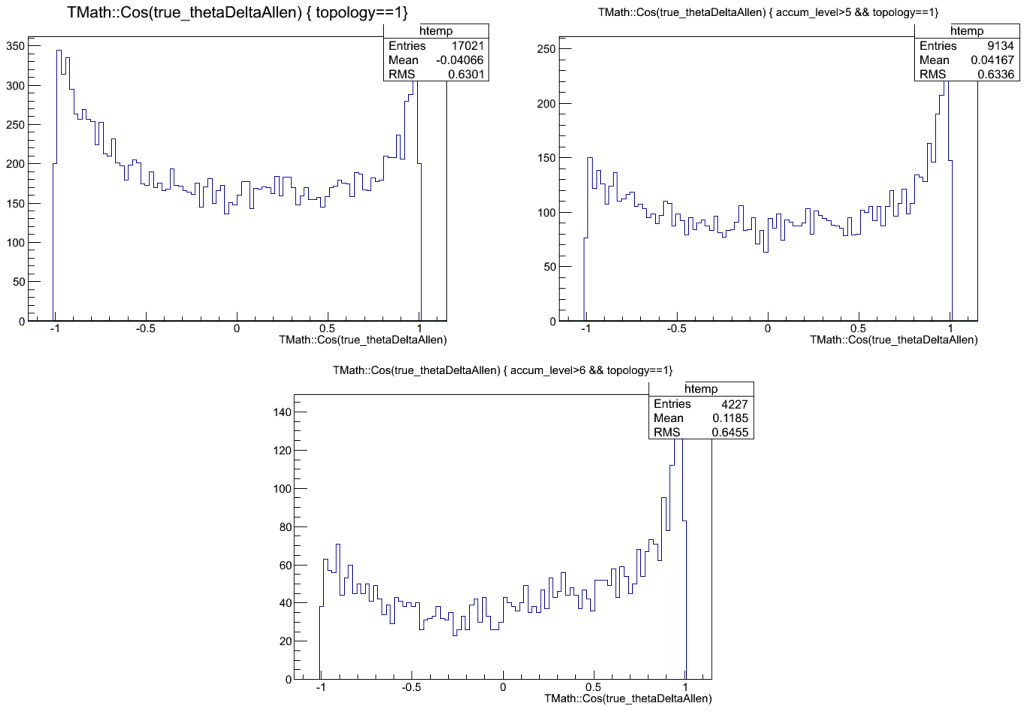

FIGURE 6.31: $\cos\theta_{planar}$ distribution for: i) all true generated CC1π^+ signal in FGD1 FV, top left, ii) all true CC1π^+ signal in the CC inclusive sample, top right and iii) all true CC1π^+ signal in the CC1π^+ selected sample, bottom.

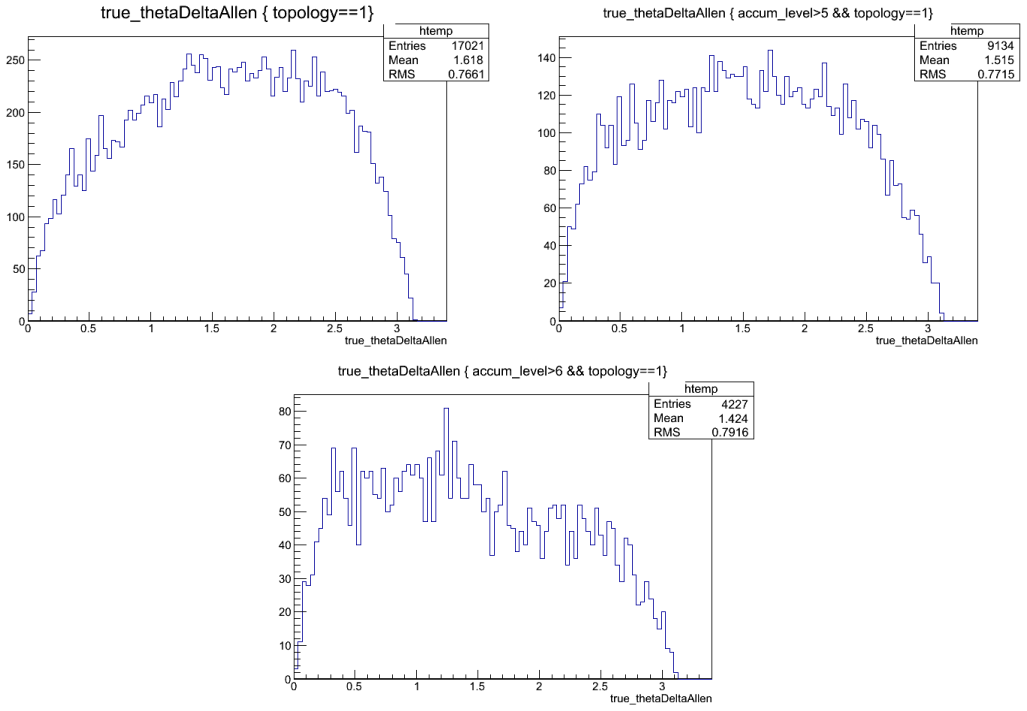

FIGURE 6.32: θ_{planar} distribution for: i) all true generated CC1π^+ signal in FGD1 FV, top left, ii) all true CC1π^+ signal in the CC inclusive sample, top right and iii) all true CC1π^+ signal in the CC1π^+ selected sample, bottom left. Units are in radians.

of the negative values. To understand why the distribution is not similar to ANL either when looking all the true generated events it is worth to check the distribution of these angles when computing them inside the nucleus which give the information of the muon and pion directions from the interaction point and not when leaving the nucleus. In this case the distribution is similar to the ANL result, as shown in Figure 6.33 for the $\cos\theta_{planar}$. Only the most negative part does not show the small decrease showed by ANL. In Figure 6.33 it is also shown the relations between the $\cos\theta_{planar}$ and the true neutrino energy, the $\cos\theta_{planar}$ and the true proton momentum, the $\cos\theta_{planar}$ and the and pion momentum, all before leaving the nucleus. We observe no dependence on neutrino energy. The most significant dependence comes from the pion momentum. We see that at low momentum pions $\cos\theta_{planar}$ tends to -1. This can explain the high suppression we have at $\cos\theta_{planar} \sim -1$ since only TPC pions are used in this measurement and pions below 200 MeV have a low efficiency in our selected sample (see Figure 6.56).

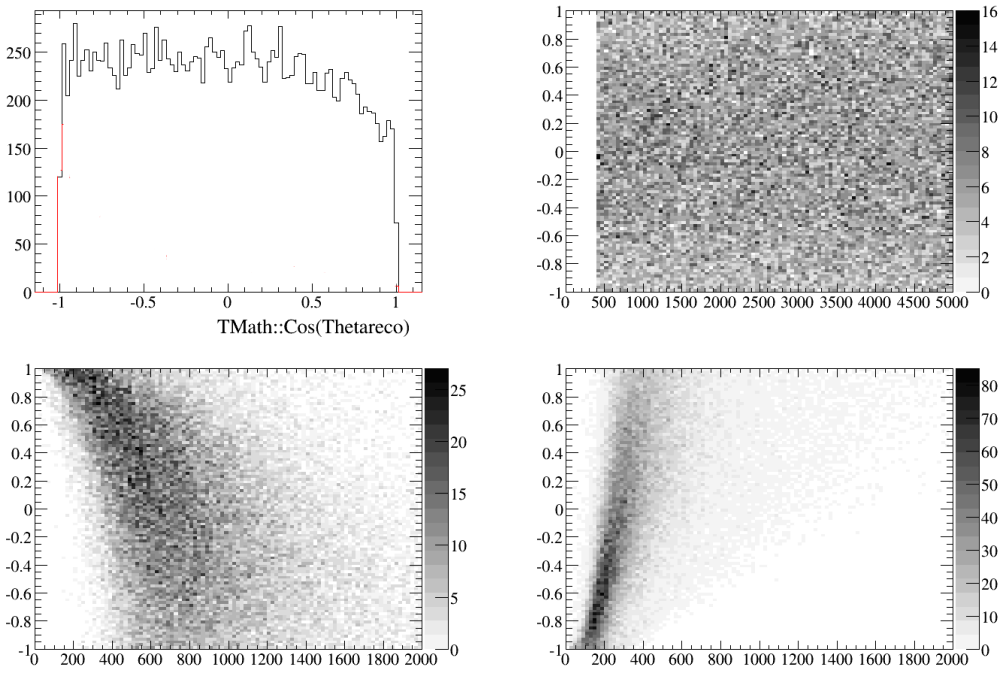

FIGURE 6.33: NEUT $\cos\theta_{planar}$ distribution before FSI, when particles are inside the nucleus (left–top). $\cos\theta_{planar}$ distribution respect to: i) true neutrino energy, top right, ii) true proton momentum, bottom left and iii) true pions momentum, bottom right. Units are in MeV.

For that reason, we consider that the observed differences respect to ANL when looking into the observables when the particles leave the nucleus are mainly due to nuclear effects, affecting to the direction of the leaving particles.

As described in [17], in the resonant pion production, the Rein and Sehgal model assumes θ_π to be isotropic in the Adler's frame. From the study of the sample presented in Table 6.6 we know that the resonant pion production is dominant in the sample.

Figure 6.34 shows the difference between the reconstructed and the true distributions of the $\cos\theta_{planar}$ in the CC1π^+ sample. It is also shown the 2–D distribution of the difference between the reconstructed and the true $\cos\theta_{planar}$ respect to the true $\cos\theta_{planar}$, for the true CC1π^+ signal in the sample.

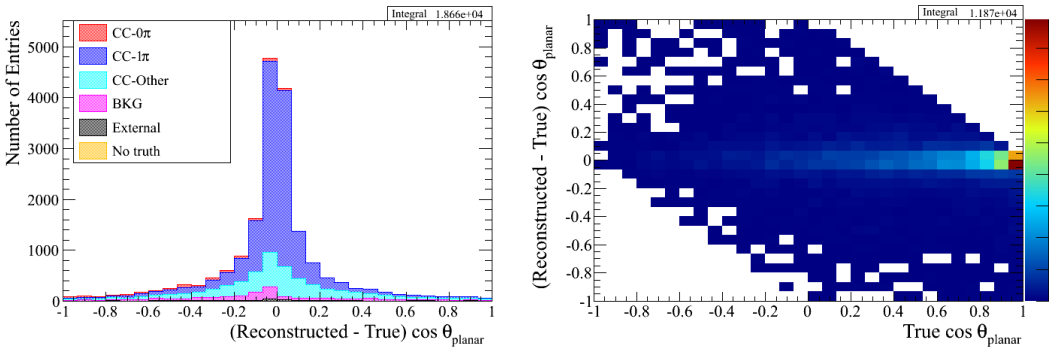

FIGURE 6.34: Difference between the reconstructed and the true $\cos\theta_{planar}$ values, left. Same distribution respect to the true $\cos\theta_{planar}$, for true CC1π^+ signal, right plot.

Figure 6.35 shows the distribution of the ϕ_{planar}, defined in Figure 6.27, of the selected exclusive CC1π^+ events according to their *topology* (left) and generator interaction code (right) definitions.

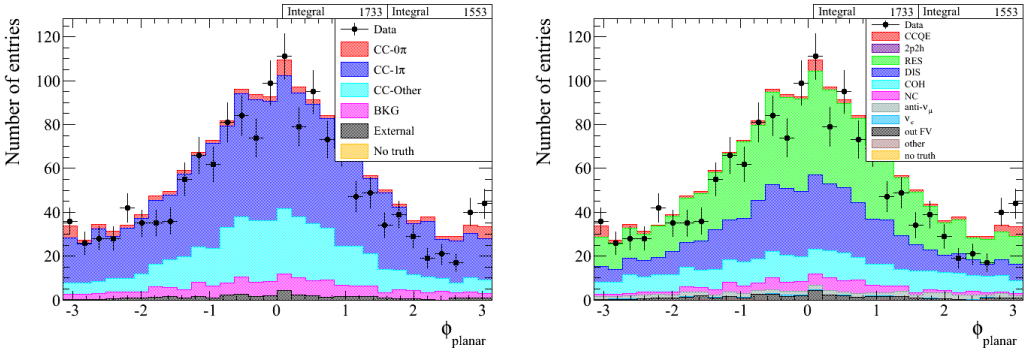

FIGURE 6.35: ϕ_{planar} distribution for the CC1π^+ according *topology* (left) and generator (right) level.

If we compare distributions on Figure 6.35 with ANL 6.29, right plot, we see that the shape of the distribution observed by ANL is not preserved, as it happen previously. In this case, ANL was observing an almost flat distribution. To understand if differences can arise from different phase–space covered or nuclear effects we did similar check as the previously presented for $\cos\theta_{planar}$.

In Figure 6.36 we can see more in detail why our reconstructed sample differs from ANL results. In plot *(i)* for all the true generated events we see that the distribution is flat, similar to ANL. Figure 6.36 *(ii)* shows all true CC1π^+ signal in the CC inclusive sample and for this angle we still have an almost flat distribution. In Figure 6.36 *(ii)* when

applying the further criteria to select the pions the distribution start to be peacked around zero. It is clear that in this case the non–flat distribution is due to the pion phase–space in this analysis.

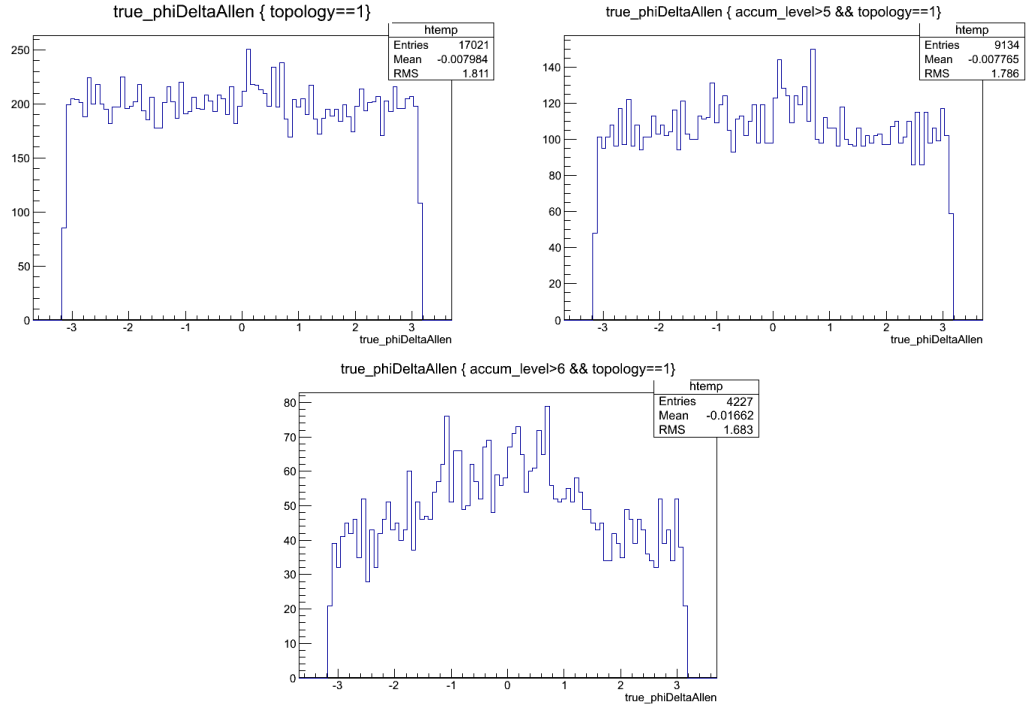

FIGURE 6.36: ϕ_{planar} distribution for: i) all true generated CC1π^+ signal in FGD1 FV, top left, ii) all true CC1π^+ signal in the CC inclusive sample, top right and iii) all true CC1π^+ signal in the CC1π^+ selected sample, bottom.

Figure 6.37, on right plot, shows the difference between reconstructed respect to the true distributions of the ϕ_{planar} in the sample. It is also shown the 2–D distribution of the difference between the reconstructed and the true ϕ_{planar} respect to the true ϕ_{planar}, left plot, for the true CC1π^+ signal.

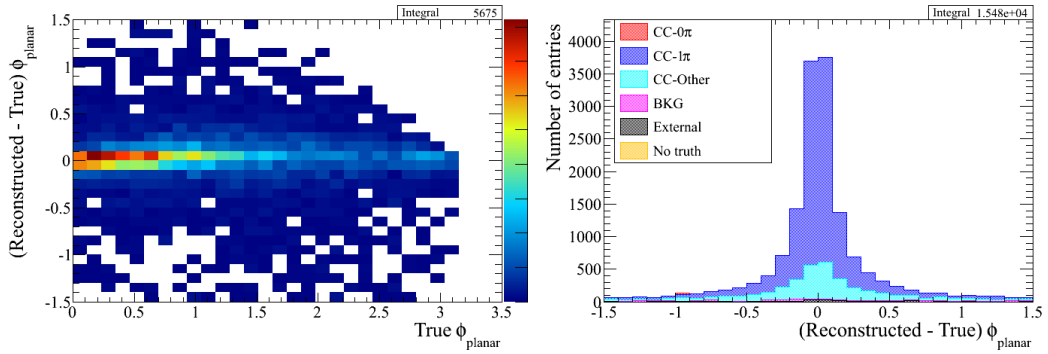

FIGURE 6.37: Difference between the reconstructed and the true ϕ_{planar} values, left. Same distribution respect to the true ϕ_{planar}, for true CC1π^+ signal, right plot.

6.4.1.7 Invariant Mass

The invariant mass, W, is a variable that plays an important role in CC1π^+ interactions. W also provides indication of the relative population of the dominant Δ^{++} resonant production versus competing channels with larger masses of the Δ or non–resonant production. The Reigh and Sehgal model is considered to be better understood for W values below 2.0 GeV, reason why MiniBooNE or MINERνA in their CC1π^+ published analysis added a cut on the reconstructed W value (usually at 1.4 GeV). The transition region around the 2 GeV in the W is unclear. Thus, a cut on W can be useful when we want to perform neutrino flavor oscillations by using a CC1π^+ channel, since in this region the model is better understood.

The invariant mass, W, is defined as:

$$W^2 = ((E_\nu + m_p) - E_\mu)^2 - (|p_\nu| - |p_\mu|)^2;$$

where E_ν is computed using the E_{RecoMB}. In this way, we can include pions identified by Michel electrons.

Figure 6.38 shows the distribution of W of the selected exclusive CC1π^+ events according to their *topology* (left) and generator level (right).

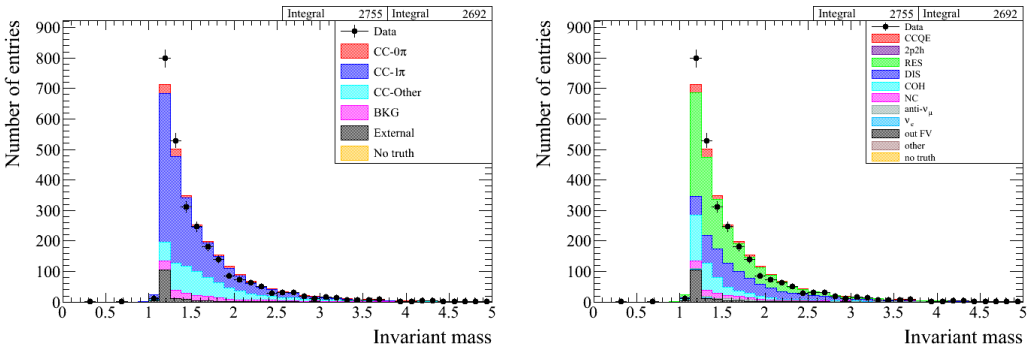

FIGURE 6.38: W distribution for the CC1π^+ according *topology* (left) and generator (right) level. Using NEUT.

Figure 6.39 shows the 2–D distribution of the difference between the reconstructed and the true W with respect to the true W, for the true CC1π^+ signal.

6.5 Event Migration

In this Section we analyze the reasons that can cause a lost of the signal and the background contamination in the sample.

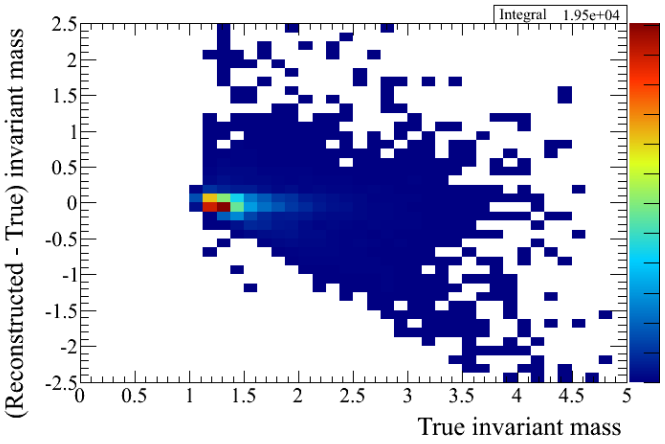

FIGURE 6.39: Difference between the reconstructed and the true W value with respect to the true W. For true CC1π^+ signal.

The main part of the lost true CC1π^+ signal into the CC0π sample have been already covered in previous Chapter 5. We can summarize these studies as follows:

1. Around a 30% of the times, the migration is due to the impossibility to reconstruct the primary pion because of secondary interactions.
2. Another important percentage of missing pions are explained by problems on reconstruction of the Michel electron tagging ($\sim$ 10%).
3. Another reason is the fact that the pion goes to the ECal detector that is still not used to identify π^+ ($\sim$ 30%).
4. Finally, there are some misidentification of the pion in the TPC ($\sim$ 30%).

6.5.1 Background events

The main background in the CC1π^+ sample is due to the CCOthers contamination. This can be caused by different reasons.

Some CCOthers events can be identified as CC1π^+ events since we can only reconstruct one of the possible pions. Some other CCOthers events are due to neutral pions that are not identified.

In Tables 6.9 and 6.10 the true composition of the background broken by topology and interaction type respectively is shown. The CCOthers topology have been splitted into CCXπ^0, for cases when there is at least one true neutral pion in the event, and CCNπ, for cases where we have more than one positive pion or at least one negative pion.

BKG type	Topology Composition (%)
CC-0-pion	15.5
CCXπ^0	28.7
CCNπ	26.2
Background	14.9
Out of FGD 1 FV	14.6

TABLE 6.9: Background composition of the exclusive CC1π^+ sample respect to the true topology type. Background is defined as the anti–neutrino, electron neutrino and neutral current events.

BKG type	Composition (%)
CCQE	9.2
Resonant	13.5
DIS	47.7
Coherent	0
NC	9.5
$\overline{\nu}_\mu$	4.5
ν_e	0.85
External	14.6
other	0.1

TABLE 6.10: Background composition of the exclusive CC1π^+ sample, according to the generator interaction types.

The ECal and TPC π^0 tagging rejects some events with π^0 but some of these π^0 are contained in the FGD volume and any kind of identification for π^0 in FGD is done so far.

DIS events clearly are the main background in the sample, according to the interaction type. We also can see that a non–negligible component of our background comes from original resonant interactions and most probably the resulting pion re–interacts or is absorbed.

Additional contamination is coming from CC0π events mainly due to proton mis–identification as π^+, in TPC.

Another check for this background is shown Table 6.11 where the true particle type of the muon candidate when is not a true CC1π^+ is shown. There is a non–negligible contribution of misidentified π^- in the sample. The total background has a 47.7% component of DIS, so, the 21.3% of muon mis–identification with π^- can explain about 50% of the DIS contamination without requiring pion re–interaction or charge ex–change (negative pions are a clear proof of DIS). We can explain part of our background, a non–negligible one, by mis–identification of the primary muon ($\sim$ 31%). The reduction of

this background requires additional reconstruction tools allowing the separation of pions and muons in ECAL or FGD and the reconstruction of high angle tracks as muons.

True particle	Fraction (%)
μ^-	68.7
μ^+	2.4
e^-	0.6
e^+	0.03
π^-	21.3
π^+	6.6
p	0.24
other	0.13

TABLE 6.11: Composition for muon candidate in the background of the CC1π^+ sample, according to the particle type of the muon candidate.

In conclusion, our main background is CCOthers. This CCOthers contamination comes from un–identified π^0, SI effects (pion re–interaction, absorption and charge ex–change) and muon miss–identification. While first and last contamination sources can be rejected by improvements on the reconstruction and particle identification, background contaminations due to SI are instead difficult to handle.

As we have shown, there are several different contributions to the background in the CC1π^+ sample. The biggest one comes from CCOther ($\sim 24\%$) events, due to multiple–pion or CCXπ^0. CC0π ($\sim 5\%$) and NC interactions and some anti–neutrino contributions ($\sim 6\%$) are also playing a role in the background. External contamination ($\sim 6\%$) is composed by interaction types occurring out of the FGD1 FV.

6.6 Background Control Samples

In order to constraint the background, we use data–based control samples that reproduce the physics of our contamination. In total we define three control samples used independently for the different types of contamination according to the topology type. The control samples contains CC events that are selected with no overlapping with our CC1π^+ sample and also not overlapping between the different control samples themselves. For this reason, those kind of control samples are usually called "side–bands".

Side–band samples are used to extract normalisation constant (α_k) that will be used later in the background subtraction for our $CC1\pi^+$ sample. The α_k parameters are defined as:

$$\alpha_k = \frac{S_{data,k}}{S_{MC,k}} \tag{6.9}$$

with $S_{data,k}$ being the total number of events in side–band k for data and $S_{MC,k}$ the total number of events in side–band k for MC [11]. In this way we re–normalize the corresponding number of background events.

One property we want to keep in our side–bands is a good agreement between the shape of the side–band and the contamination. We need to constrain the same energy regions and similar kinematical conditions.

It's important to emphasize that not all CC *non–selected* events for CC1π^+ are good candidates as side–bands, i.e. the total CC10π or the total CCOther. We need to understand that the contamination comes from events that are not CC1π^+ but there are several reasons to mis–identify them as CC1π^+.

Each contamination source has its their own physical origin, but the resulting topology comes out similar to the CC1π^+ signal. For example, we have some probability to miss one pion in one event, but this probability is lower to miss more than 1 pion in one event. Following the discussion on previous section, the main assumptions for the different contaminations are:

- the CC0π contamination comes from protons mis–identified as pion.
- CCOther contamination comes from non–reconstructed pions (neutral or charged).
- NC contamination comes from a negative pion mis–identified as muon.

Thus, three control samples describing those main contaminations have been defined. This is the working principle we use to define control samples. Comparisons of muon momentum and angle distributions between the side–band and the contamination in our sample are presented.

Normalization of plots in this section is done as follows: for data–MC comparisons the normalization is done per PoT, for MC–MC comparison instead (true component in control sample vs true contamination type in $CC1\pi^+$ sample) the normalization is done by area. The three control samples are defined as follow:

1. CC0π1P. This control sample is used to constraint contamination due to CC0π, CCOther events where pions are not reconstructed at all and part of non-ν_μ–CC

[11] The total number of events in the MC is normalized to the total data PoT.

(i.e. NCE, Anti–ν_μ). The control sample starts from the CC0π sub-sample and we add the conditions:

- The event has one additional TPC track different from that of the muon. Is not needed any requirement, by exclusion, the track should be a proton.

-Momentum of this track (proton candidate) must be $600MeV < p_{proton} < 1800MeV$. This intermediate energy region is where we found more problems to identify pions respect to protons in the TPC due to the crossing of the pion and proton expected dE/dX vs momentum distributions (see Figure 3.20).

-the angle between the muon and the proton candidates may be $0.5 < \theta_{\mu-proton} < 1.5$.

Figure 6.40 shows the muon candidate momentum and angle for CC0π1P control sample for data and MC. We observe a good agreement between data and MC. Table 6.12 shows the topological composition of the $CC0\pi1P$ side–band selected.

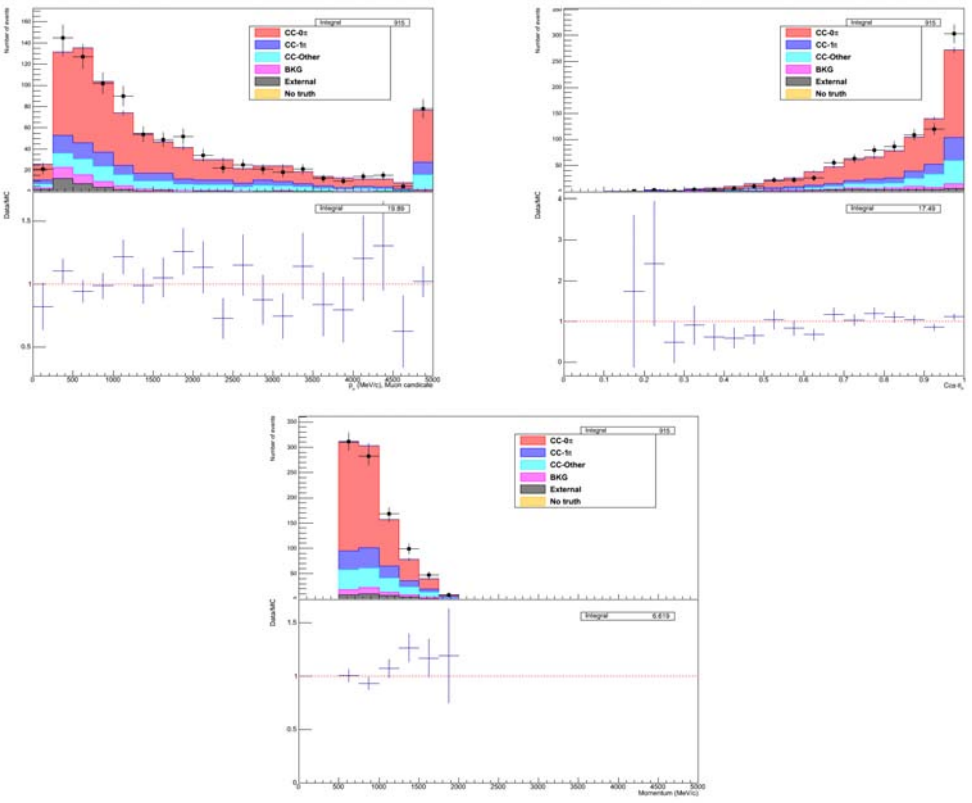

FIGURE 6.40: Muon momentum (top left) and cosine of the angle (top rigth) distribution for the CC0π1P control sample, ratios between data and MC are also shown. Proton candidate momentum in the CC0π1P control sample distribution on bottom plot.

Figures 6.41, 6.42 and 6.43 show the agreement between shapes of the true component of the different topologies we want to constraint with respect to the CC0π1P sample. The agreement is shown for muon momentum and angle. We see that

$CC0Pi1P$ sample	Topology Composition (%)
CC-0-pion	64.17
CC-1-pion	13.73
CCXπ^0	9.50
CCNπ	5.05
Non-$\nu_\mu CC$	4.12
Out FGD1 FV	3.44

TABLE 6.12: Composition of the CC0π1P side–band respect to the true topology type.

shapes for the different components between the control sample and the contamination in CC1π^+ sample have a good agreement for muon angle and for the momentum at low values we have small discrepancies. Althought, the agreement between this MC–MC are enough to consider there is no a bias in the control sample respect to the contamination. We can conclude that this sample can be used to constraint the background contributions since shapes are well preserved and no bias is observed.

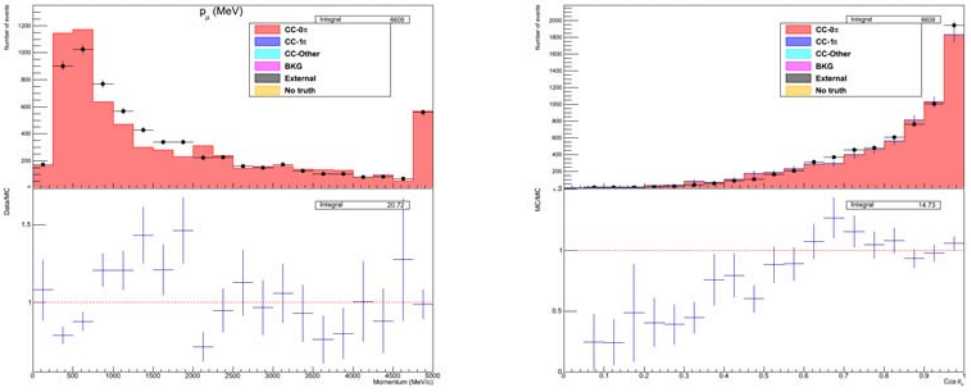

FIGURE 6.41: Muon momentum (left) and cosine angular distribution (right) for the true CC0π component in the CC0π1P control sample with respect to the CC0π contamination. Contamination is shown in histogram and control sample is using dots.

2. *Control A*. This control sample is used to constraint the event contamination from CCOther (mainly multiple pion events) and Non–ν_μ–CC (i.e. NC–Xπ^+, Anti–ν_μ). The control sample starts from the CCOther sub-sample and we add the conditions:

   -At least one TPC track tagged as π^+.

   -The number of TPC tracks must be less than 3, not counting the muon track.

   On Figure 6.44 we can see muon candidate momentum and angle for *Control A* sample for data and MC. We observe a reasonable agreement between data and MC. Table 6.13 lists the topological composition of the selected *Control A* side–band.

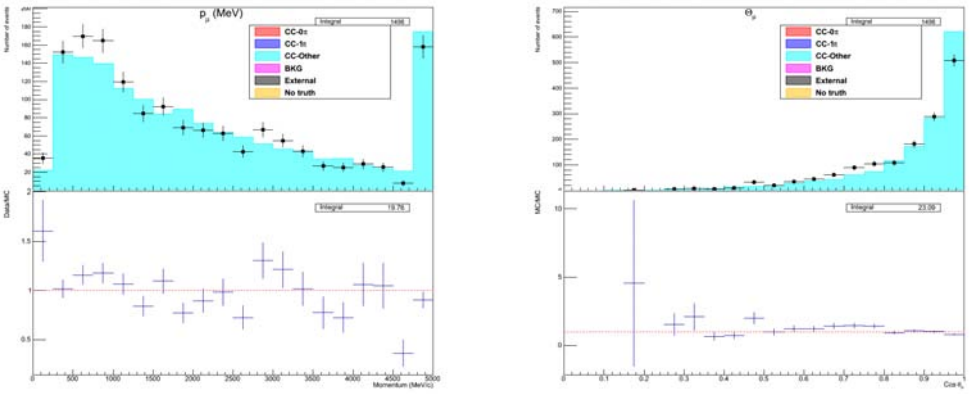

FIGURE 6.42: Muon momentum (left)and angular distribution (right) for the true CCOther component in the CC0π1P control sample with respect to the CCOther contamination, Contamination is shown in histogram and control sample is using dots.

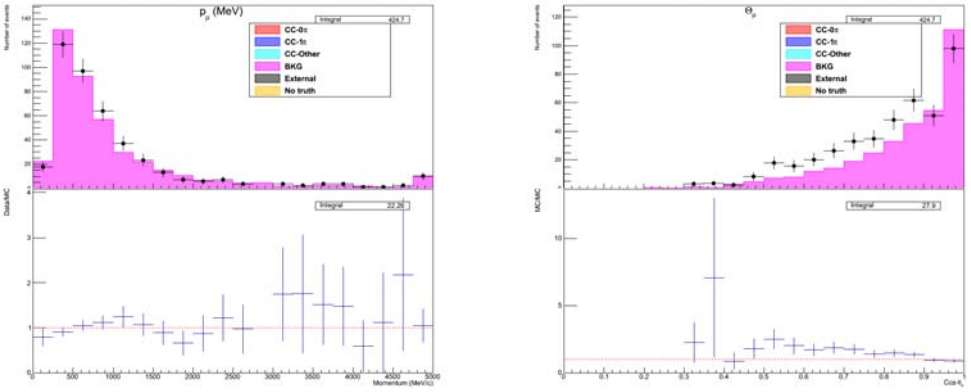

FIGURE 6.43: Muon momentum (left) and angular distribution (right) for the true non–ν_μ (NC, anti–ν and ν_e) component in the CC0π1P control sample with respect to the non–ν_μ contamination, contamination is shown in histogram and control sample is using dots.

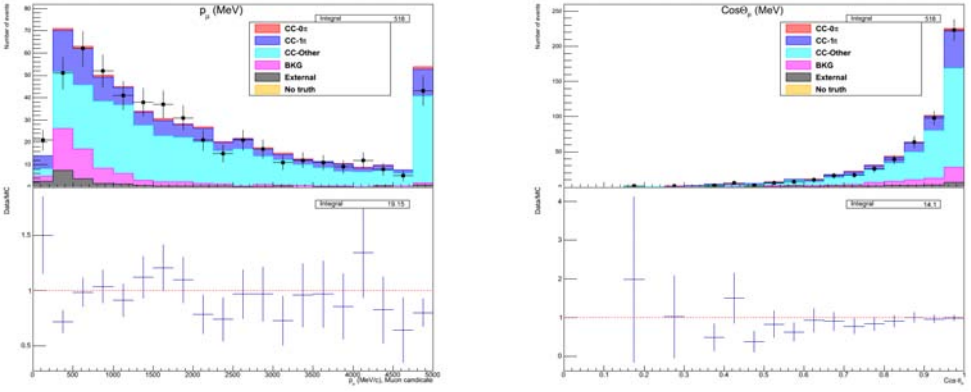

FIGURE 6.44: Muon momentum (left) and angle distribution (right) for the *Control A* sample.

Control A sample	Topology Composition (%)
CC-0-pion	1.9
CC-1-pion	21.95
CCXπ^0	39.96
CCNπ	21.69
Non-$\nu_\mu CC$	10.74
Out FGD1 FV	3.76

TABLE 6.13: Composition of the *Control A* side–band respect to the true topology type.

Figures 6.45 and 6.46 show the agreement between shapes of the true component of the different topologies we want to constraint with *Control A* sample. We see that shapes for the different components between the control sample and the contamination have a good agreement and no bias have been found. We can conclude that we can use this sample to constraint the topologies showed here.

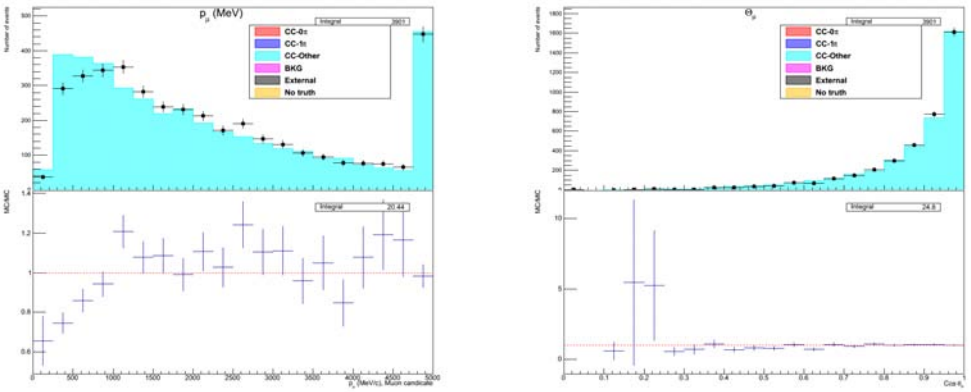

FIGURE 6.45: Muon momentum (left) and cosine angular distribution (right) for the true CCOther component in the Control A sample with respect to the CCOther contamination, contamination is shown in histogram and control sample is using dots.

3. *Control B.* This control sample is used to constraint contamination due to CCOther (mainly because of neutral pions) and Non–ν_μ–CC (i.e. NC–Xπ^0, Anti–ν_μ). The control sample starts from the CCOther sub-sample and we add the following conditions:

   - No selected π^+ in the TPC. In this way we reject overlapping with Control A.

   - At least one e^- or e^+ tagged in TPC. In the case of a e^+ candidate, we add the requirement to have momentum below 400 MeV/c, in order to reject some mis–identified protons.

   -Number of TPC tracks, without counting the muon, must be exactly 2.

   Figure 6.47 shows the comparison of Data vs MC for the muon candidate momentum and angle for *Control B* sample. We see good agreement between data

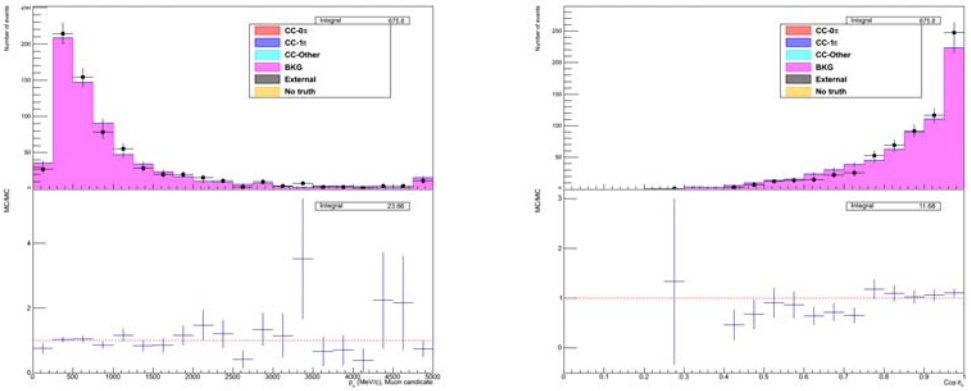

FIGURE 6.46: Muon momentum (left) and angular distribution (right) for the true non–ν_μ (NC, anti–ν and ν_e) component in the Control A sample with respect to the non–ν_μ contamination, contamination is shown in histogram and control sample is using dots.

and MC. On Table 6.14 we can see the topological composition of the *Control B* side–band selected.

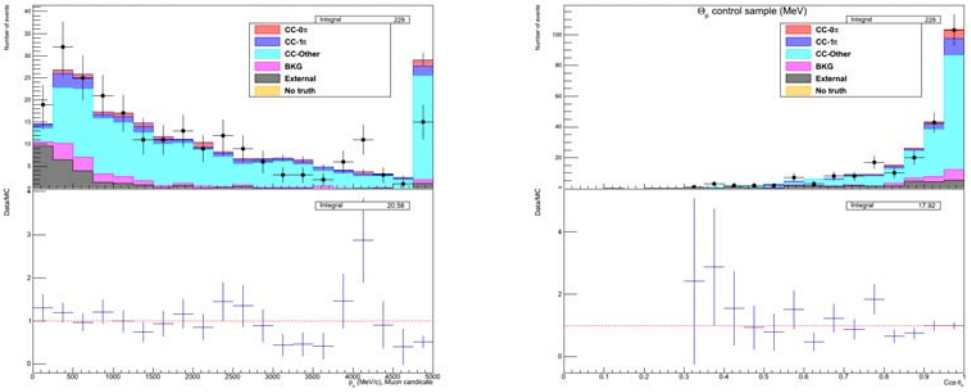

FIGURE 6.47: Muon momentum (left) and angle distribution (right) for the Control B sample.

Control B sample	Topology Composition (%)
CC-0-pion	4.57
CC-1-pion	8.38
CCXπ^0	56.19
CCNπ	12.18
Non-$\nu_\mu CC$	6.87
Out FGD1 FV	11.82

TABLE 6.14: Composition of the *Control B* side–band respect to the true topology type. Using NEUT.

Figures 6.48 and 6.49 show the comparison between shapes of the true component of the different topologies we aim to constraint with the *Control B* sample. Muon

momentum and angle are superimposed to the shape of the same observable obtained from the true contamination of each topology type in the CC1π^+ sample. The shapes for the different components between the control sample and the contamination in CC1π^+ sample show a good agreement and we conclude that we can use this sample to constrain these topologies showed here.

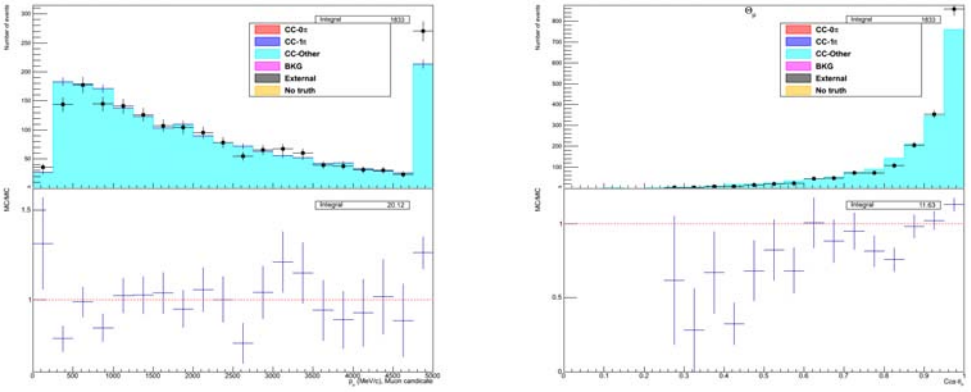

FIGURE 6.48: Muon momentum (left) and angular distribution (right) for the true CCOther component in the Control B sample with respect to the CCOther contamination, contamination is shown in histogram and control sample is using dots.

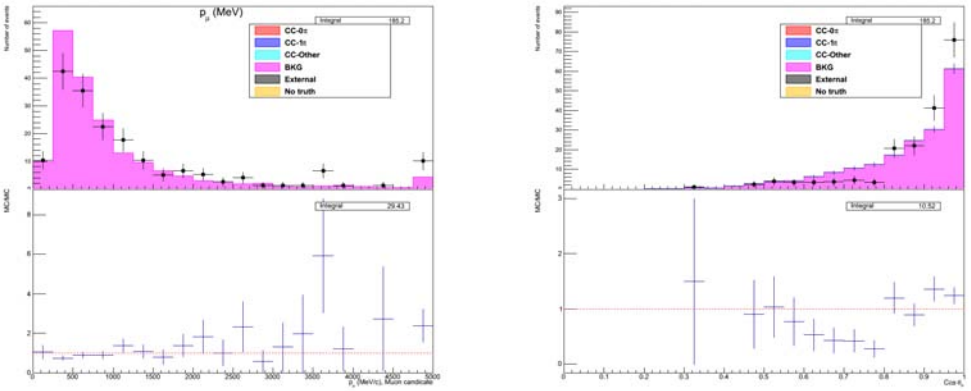

FIGURE 6.49: Muon momentum (left) and angular distribution (right) for the true non–ν_{mu} (NC, anti–ν and ν_e) component in the Control B sample with respect to the non–ν_{mu} contamination, contamination is shown in histogram and control sample is using dots

The three control samples considered show no bias on energy or direction for the contamination we want to constraint. Also if some small disagreements have been found, generally talking, these control samples represents quite well the contamination.

We would like to stress that no control sample have been performed to constraint the out of FV contamination. We explored few selections and none of these control samples could reproduce the kinematic properties of the contamination observed in the sample. Any special treatment has thus been considered for this contamination.

The $CC0Pi1P$ has no Michel electron so we did not make any effort to identify potential side–bands with this signature. But *Control A* and *Control B* samples have potentially Michel electrons. Table 6.15 show the purity of *Control A*, second column, when there are no Michel electrons explicitly identified in the event and when they are Michel electrons, third column.

Control A	Topology Composition (%) no ME	Topology Composition (%) with ME
CC-0-pion	2.36	0.37
CC-1-pion	24.63	12.95
CCXπ^0	42.71	30.70
CCNπ	15.71	41.77
Non-$\nu_\mu CC$	10.77	10.66
Out FGD1 FV	3.83	3.55

TABLE 6.15: Composition of the Control A side–band respect to the true topology type when no Michel electrons in the event (second column) and when there are Michel electrons (third column).

Both cases are taking into account in Control A but we observe that a biggest contribution of our signal is present in the control samples. This signal contribution is bigger in the cases when we don't have Michel electrons. The effect to have this signal contribution in the control samples is minimized in the unfolding process.

In Table 6.16 we show purity of *Control B* when they have no Michel electrons identified in the event (second column) and when they are Michel electrons (third column).

Control B	Topology Composition (%) no ME	Topology Composition (%) with ME
CC-0-pion	5.06	0.75
CC-1-pion	8.89	4.4
CCXπ^0	55.34	62.82
CCNπ	12.09	12.83
Non-$\nu_\mu CC$	6.74	7.87
Out FGD1 FV	11.88	11.32

TABLE 6.16: Composition of the *Control B* side–band respect to the true topology type when no Michel electrons in the event (second column) and when there are Michel electrons in the events (third column).

We prefer to keep side–bands without split them according the number of Michel electrons since these control constrain different contamination topologies and there are no obvious indication on how to split or reject events on side–bands according the number of Michel electrons. We also do not see large differences between Michel electron and non–Michel electron events to justify additional selections. On the other hand, the

number of events, on data, with only Michel electrons and no other TPC track than the muon is negligible.

6.7 Systematical Errors

This Section discuss the relevant systematics for this analysis. For each systematic source a fractional covariance matrix has been computed. The computation of the systematic errors is shared inside the collaboration. The systematics related to the ECal reconstruction efficiency has been computed explicitly for this analysis.

6.7.1 ND280 Detector Systematics

These systematics have been presented in Chapter 4. We summarize the list of detector systematics on Table 4.1.

6.7.2 Beam Flux Uncertainties Systematics

We just summarize the different contributions in the flux parametrisation error:

1. Kaon production multiplicity uncertainty.
2. Pion production multiplicity uncertainty.
3. Proton beam uncertainty.
4. Off–axis angle uncertainty.
5. Horn angular alignment uncertainty.
6. Horn field asymmetry uncertainty.
7. Production cross sections.
8. Horn absolute current uncertainty.
9. Target alignment uncertainty.
10. Secondary nucleon production uncertainty.
11. Near Detector phase–space uncertainty.
12. Proton beam intensity uncertainty.

Detailed description of the measurement of these uncertainties can be found in [36]. The total flux fractional covariance matrix is calculated by the quadratic sum of each contributions listed above.

To estimate the flux uncertainty, pseudo–experiments are made using an specific software framework, `T2KReWeight`. This framework uses the covariance matrix provided by the Beam group of T2K and then the throws are generated and weights calculated.

6.7.3 Cross Section Parametrization Systematics

The cross section parametrization uncertainties are constrained by fits to external neutrino interaction and pion scattering data (mainly MiniBooNE).

Cross section modeling errors are shown in Table 6.17, Table 6.18 and Table 6.19. We separate the parameter that are turned off/on (Table 6.18) from the other parameters that already exist in the default MC simulation (Table 6.17).

Parameter	Nominal Value	Error
M_A^{CCQE}	1.21 GeV	37.2%
M_A^{RES}	1.16 GeV	9.5%
CC-oth shape	0	40%
p_F	217 MeV/c	13.8%
W_{shape}	87.7	51.7%
pionless Δ decay	0.2	20%

TABLE 6.17: Cross section parametrization, with nominal value and errors assigned.

Parameter	Nominal Value	Error
Spectral Function	Off	100%
$1\pi E_\nu$ shape	Off	50%

TABLE 6.18: Parameters that are not included in the default MC simulation, with nominal value and errors assigned.

An additional source of cross section uncertainties is coming from the Final State Interaction (FSI) parameters. This source of error is due to uncertainties on the pion's final state before it leaves the nuclear medium after the neutrino interaction. We consider this systematic errors independently to the other cross section parameters.

Similarly to the flux uncertainty, the propagation of the cross section and FSI uncertainties in this analysis was done using the `T2KReWeight` framework.

Parameter	Energy range (GeV)	Nominal value	Error
CCQE	$0.0 < E_\nu < 1.5$	1	11%
CCQE	$1.5 < E_\nu < 3.5$	1	30%
CCQE	$3.5 < E_\nu$	1	30%
CC1π	$0.0 < E_\nu < 2.5$	1.63	43%
CC1π	$2.5 < E_\nu$	1	40%
CC-COH	$0.0 < E_\nu$	1	100%
NC-oth	$0.0 < E_\nu$	1	30%
NC-1π^0	$0.0 < E_\nu$	1	43%

TABLE 6.19: Cross section normalizations with range of neutrino energy, nominal value and errors assigned.

6.8 The Unfolding Method

We use the so–called *Bayesian Unfolding* method. Unfolding methods are widely used to extract cross section values since they represent the best way to eliminate detector effects and results can be directly compared from experiment to experiment.

This method was already used in previous T2K cross section analysis [33]. It consist in an iterative method on which the calculated distribution has a slight bias on the previous distribution, it is described in [73].

The general idea for the differential cross section measurement is as follows. We can define the flux integrated cross section value at each bin k for a given variable X as:

$$\langle \frac{\partial \sigma}{\partial X} \rangle_k = \frac{N_k^{unfolded}}{\epsilon_k N_{targets} \Phi \Delta X_k} \tag{6.10}$$

being $N_k^{unfolded}$ the estimated number of true events in bin k, ϵ_k is the efficiency of reconstructing events in bin k, $N_{targets}$ is the number of target nucleons, Φ is the integrated flux value and ΔX_k is the bin width of bin k.

The number of nucleons in the FGD1 FV has been estimated to be $5.5 \cdot 10^{29}$[74]. We calculate $N_k^{unfolded}$ using the Bayesian method and the subtraction of the background using the 3 side–bands. The Bayesian unfolding method is based on extract a distribution from a reconstructed data sample using as a reference the true distribution predicted by the MC, with the unfolding accounting for the detector systematics.

From the MC, the *smearing matrix* gives the probability of an event in the true bin j of being reconstructed in the reconstructed bin i and it is calculated as:

$$R_{ij} = P(r_i|t_j) \tag{6.11}$$

The efficiency for a true bin j is given by:

$$\epsilon = \sum_{\alpha}^{\text{reco bins}} P(r_\alpha|t_j) \tag{6.12}$$

The probability to find an event in a given reconstructed bin can be estimated using the MC following the equation:

$$P(r_i) = \sum_{\alpha}^{\text{true bins}} P(r_i|t_\alpha)P(t_\alpha) \tag{6.13}$$

with:

$$P(t_j) = \frac{N_{t_j}}{\sum_{\alpha}^{\text{true bins}} N_{t_\alpha}} \tag{6.14}$$

being N_{t_j} the number of true events in bin j. With the Bayes' theorem the *unsmearing matrix* can be calculated as:

$$P(t_j|r_i) = \frac{P(r_i|t_j)P(t_j)}{P(r_i)} \tag{6.15}$$

The true distribution is computed by applying the *smearing matrix* and the background subtraction to the data:

$$\hat{N}_{t_j} = \frac{1}{\epsilon_j}\sum_i P(t_j|r_i)(N_{r_i} - \sum_{k}^{\text{all bkg}} \alpha_k B_{ri,k}) \tag{6.16}$$

with N_{ri} the number of reconstructed events in bin i, $B_{ri,k}$ the number of predicted events in bin i of background type k, α_k the normalization constant coming from the control samples and ϵ_j the true efficiency in bin j. $\alpha_k = 1$ for those backgrounds with no associated control sample. The α_k coefficients have been defined in Section 6.6 as the ratio between data and MC events for the corresponding side–band selected sample.

Iteratively, $\hat{N}_{t_j}$ can be used as the new value of N_{t_j} to find the new *unsmearing matrix* and re–evaluate $\hat{N}_{t_j}$. However, while increasing the number of iterations the statistical errors may also increase in size adding correlations between bins since each iteration takes the same information from the data. For this reason the number of iterations chosen for the calculation is one. On Appendix D we present the study performed to test which is the proper number of iterations. It has been estimated using NEUT as

fake data and some other fake data samples (NEUT modified from the nominal values and GENIE). In favour of an small number of iteration the shape of the original data and Monte Carlo distributions are very close to each other.

6.8.1 Propagating Uncertainties in the Cross Section

The propagation of uncertainties is done using pseudo–experiments to build a covariance matrix. For each source of uncertainty, s, we perform N pseudo–experiments. Each pseudo–experiment gives a new differential cross section, σ^{s_n} , which is compared to the nominal differential cross section, σ^{nom} to calculate the covariance matrix:

$$V_{ij}^{s} = \frac{1}{N}\sum_{s_n=1}^{N}(\sigma_i^{s_n} - \sigma_i^{nom})(\sigma_j^{s_n} - \sigma_j^{nom}), \tag{6.17}$$

where $\sigma_i^{s_n}$ is the differential cross section in bin i evaluated with throw n of the systematic uncertainty s, and σ_i^{nom} is the nominal differential cross section in bin i.

The error on the total cross section is then obtained to be:

$$\sigma_\sigma = \sqrt{\sum_{i=1}^{N_{bins}}\sum_{j=1}^{N_{bins}}(V_{ij}\Delta_i)}, \tag{6.18}$$

where Δ_i is the width of bin i. Statistical uncertainties are evaluated using 2000 pseudo–experiments for both MC and data. The content of each histogram that is an input to the unfolding are varied according to a discrete Poisson statistics smeared with a Gaussian around the nominal value. The Gaussian allows negative values.

Since these throws are correlated we cannot re-generate a pseudo–experiment when a throw is negative. We decided to set to 0 all throws with negative value. The difference between allowing the uncertainty to have negative values (non truncated Gaussian) and setting all negative throws to 0 (truncated Gaussian) is small and compatible with the statistical uncertainties.

The number of pseudo–experiments used for the measurements presented in this analysis is 2000 in each error source.

6.9 Definition of the Phase-Space Considered

Due to the impossibility to reconstruct backward–going tracks using the TPC and the possible inefficiency on the reconstruction at high angles and low momentum tracks, we needed to understand the phase–space on which we can perform the cross section analysis without model dependency due to the absence of data. We perform a set of phase–space studies to establish which is the region for the measurement performed.

We do the studies, muon and pion, independently. Momentum efficiency is studied for pions when using or not Michel electrons. The resulting phase–space available is then applied to the reconstructed variables and to the true phase–space measured in the cross section.

We show in Figure 6.50 the efficiency for the CC1π^+ respect to the true muon momentum for the different space covered for the muon (showing results respect to different muon cosinus restrictions, this was perform in order to check if any clear relation can be seen). Efficiency is defined as usual:

$$Efficiency = \frac{\text{total true } CC1\pi^+ \text{ selected}}{\text{total } CC1\pi^+ \text{ events generated}} \tag{6.19}$$

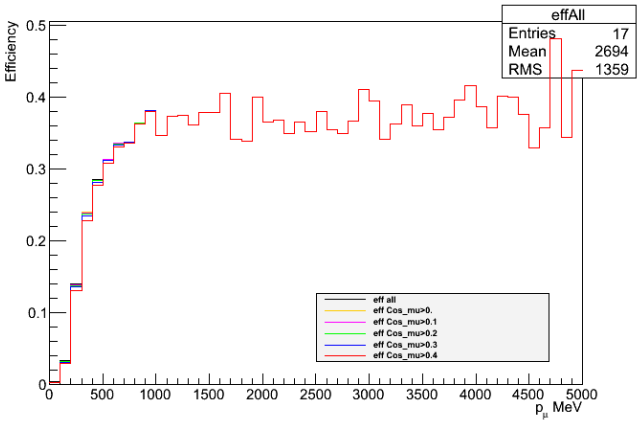

FIGURE 6.50: Efficiency of the $CC1\pi^+$ signal as a function of the true muon momentum. Each line represents distribution for a different space covered for the muon.

Figure 6.51 shows a zoom of previous distributions at the low momentum region of the muon, where some differences are visible.

On Figure 6.52 we observe the distribution of the efficiency of CC1π^+ as a function of the true muon cosine.

We can conclude that for the muons, high angles and low momentum has a low efficiency and we have to consider it into the phase–space of our measurements.

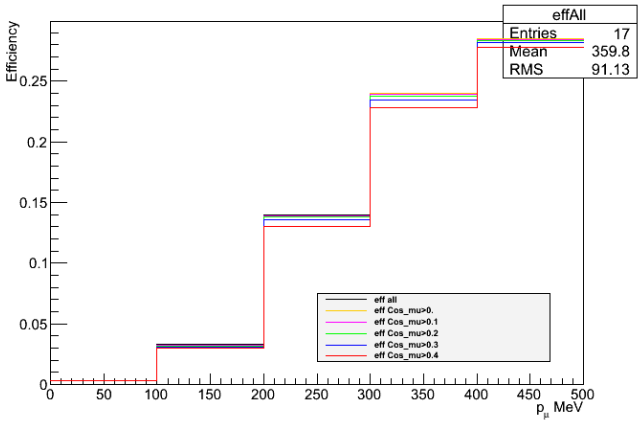

FIGURE 6.51: Distribution of the CC1π^+ efficiency for true muon momentum up to 500 MeV and for different space reductions.

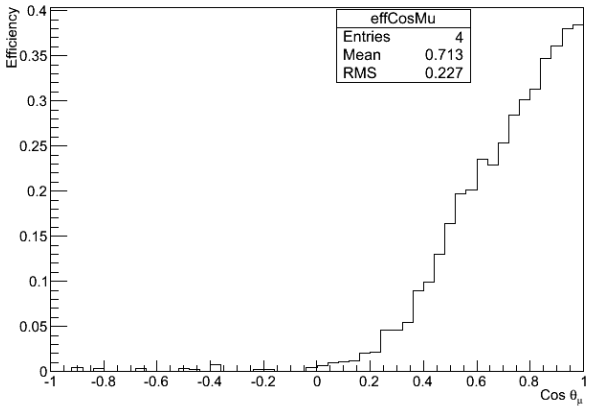

FIGURE 6.52: Efficiency of the $CC1\pi^+$ signal as a function of the true muon cosine.

For Michel electron pion identification the situation is different. Pions identified with the ME presence can be in any direction, and efficiency does not depend *a priori* on the direction. To understand this better and establish a phase–space condition we look at Figure 6.53. The true momentum vs true angle for the true pion in the true $CC1\pi^+$ events inside the $CC1\pi^+$ sample is shown. We can see that a large amount of events are backward going.

Figure 6.54, left plot, show the reconstructed cosine with respect to the momentum of the pion candidate in the TPC for the true $CC1\pi^+$ events. As expected, no backward–going pion are reconstructed. As well we can see that contribution of high angles is small. For Michel electrons we don't have a true particle associated, then we cannot have a look directly on the true momentum and true angle of the true track associted. On the contrary, we can show the true pion phase–space when we select tru $CC1\pi^+$ using Michel electrons. This true information is shown in Figure 6.54, right plot. We see from this plot that when we use ME tagging we don't need to apply phase–space reduction.

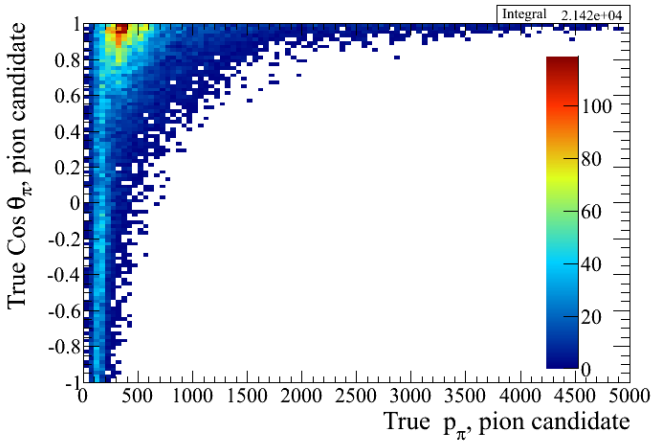

FIGURE 6.53: True pion momentum with respect to the cosine of the angle for true $CC1\pi^+$ events in the $CC1\pi^+$ sample.

Backward going pions, that are usually with low momentum are properly covered by the sample using Michel electrons. In addition, Figure 6.55 show the distribution of the efficiency of CC1π^+ as a function of the true pion momentum. Contrary to the muon case, we don't see a big decrease on efficiency for low momentum pions, but this is the case we use both TPC and Michel eletrons to reconstruct the pions.

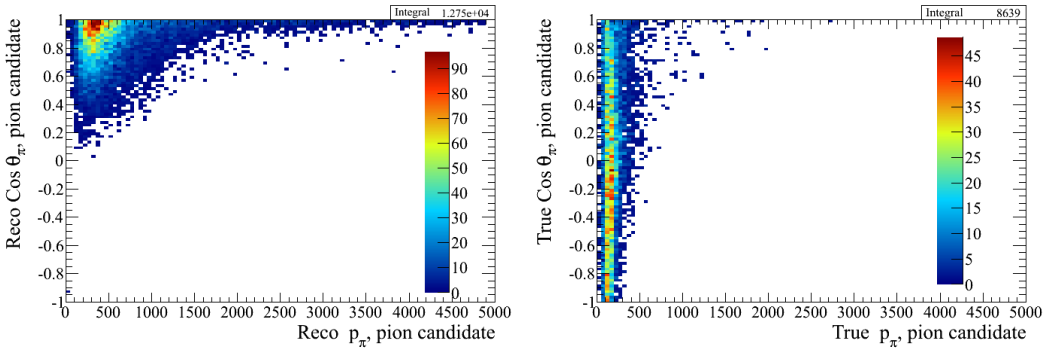

FIGURE 6.54: Reconstructed pion momentum with respect to cosine of the angle for the pion candidate when reconstructed in the TPC in true $CC1\pi^+$, left plot. True pion momentum with respect to cosine of the angle true variables true $CC1\pi^+$ events when a Michel electron is reconstructed, right plot.

Thus, no momentum or angular re–definitions need to be applied for the pion phase–space when we use Michel electrons. However, we need to identify the allowed phase–space for the TPC pions.

An analogous check to the one for the muons has been performed by studying the efficiency when selecting TPC pions. Efficiency respect to the pion momentum in for TPC pions is shown in Figure 6.56. In this case we see a similar behaviour than in the muon case. We observe a very low efficiency below 200MeV and above this value the efficiency obtained is enough to perfom the analysis without model dependency.

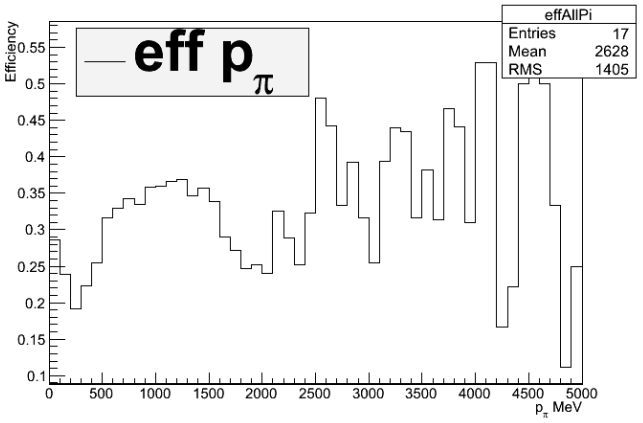

FIGURE 6.55: Efficiency of the $CC1\pi^+$ signal as a function of the true pion momentum.

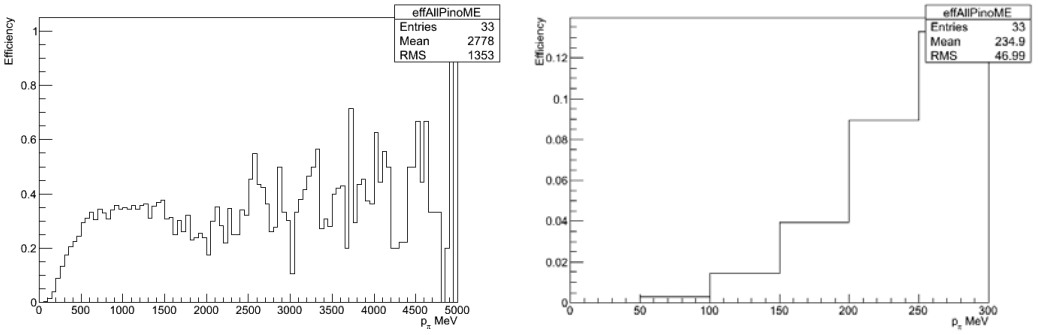

FIGURE 6.56: Efficiency of the $CC1\pi^+$ signal as a function of the true pion momentum, left plot. Right plot shows same distribution with a zoom from 0 to 300 MeV.

Following the information presented above we decide to apply a re-definition on the phase–space for the muon observables as follows:

1. We require $\cos\theta_\mu > 0.2$.
2. We require $p_\mu > 200.$ MeV.

We decide that we apply a re-definition on the phase–space of the pion variables as follows:

1. If Michel electrons are included in sample (when not needed explicitly pion angular variables) we don't apply reduction on the pion phase–space.
2. When we don't use Michel electrons sample in the measurement we apply a reduction of phase–space similar to the muon case: $\cos\theta_\pi > 0.2$ and $p_\pi > 200MeV$.

Only in cases where the explicit variable is used for the unfolding, we cover the low efficiency by using a bigger bin to reject the model dependency, but non-visible variables will follow the phase-space requirement.

For an easier way to understand the phase–space used in the measurement, we tag it as:

- A: full phase–space.
- B: $\cos\theta_\mu > 0.2, \cos\theta_\pi > 0.2, p_\mu > 200MeV, p_\pi > 200MeV$. Not using the ME sample.
- C: $\cos\theta_\mu > 0.2, p_\mu > 200MeV$. If using the ME sample.
- D: $\cos\theta_\mu > 0., \cos\theta_\pi > 0.2, p_\mu > 0MeV, p_\pi > 200MeV$. For the double differential measurement on muon kinematical variables, then, low efficiency is covered by bin sizes.
- E: $\cos\theta_\mu > 0.2, \cos\theta_\pi > 0., p_\mu > 200MeV, p_\pi > 200MeV$. For the pion angle differential result, then, low efficiency is covered by bin sizes.
- F: $\cos\theta_\mu > 0.2, p_\mu > 200MeV, p_\pi > 0MeV$. For the pion momentum differential result, then, low efficiency is covered by bin sizes.
- G: $\cos\theta_\mu > 0.2, \cos\theta_\pi > 0.2, p_\mu > 200MeV, p_\pi > 0MeV$. For the pion momentum differential result if no ME sample is used, then, low efficiency is covered by bin sizes.
- H: $\cos\theta_\mu > 0.2, \cos\theta_\pi > 0.2, p_\mu > 0MeV, p_\pi > 200MeV$. For the muon momentum differential result, then, low efficiency is covered by bin sizes.

6.10 Results

The CC1π^+ differential cross section results are computed in this analysis in different ways to be able to offer all available information from the ND280 detector interesting for the modelling of the CC1π^+ cross section. Differential cross section and double differential cross section have been measured. These results aim to be as model independent as possible. However, as presented in the next Section, we performed energy dependent measurements.

For each cross section result we provide the corresponding values of statistical and systematical uncertainties. The flux averaged cross section result is also provided, just for completition.

The binning in each measurement has been chosen taking into account the available statistics for the sample used and the resolution of the reconstructed variables respect to the true predicted variables from MC. This have been decided by looking into fake data (using NEUT normalized to the total PoT data and used as data) before to use real data and before the unfolding process takes place. The unfolding process is done using the same formula, when needed, as the reconstructed one and using the true kinematical distributions.

The biggest errors comes from the flux uncertainties ($\sim$ 15%). The biggest detector error is the modelling of the secondary pion interactions in the detector. While at low momentum ($p < 300$ MeV) the dominant detector error is the charge mis–identification for the TPC tracks.

Several tests on the unfolding process using fake data are showed in Appendix D.

The result of the flux–averaged cross section value is:

$$< \sigma >= (0.117613 \pm 0.00435(stat) \pm 0.02394(syst)) \times 10^{-38} cm^2 / \text{ Nucleon},$$

while the predicted value by NEUT is $0.12249810^{-38} cm^2/Nucleon$, which is compatible with our data. To obtain this value the full phase–space has been considered and the full sample, including Michel electrons. We provide this measurement just for matter of comparison but it is delicate to interpret since it has many assumptions. One example is the use of the full phase–space. A better estimation would derive if we assume only the phase–space available but for other experiments the flux averaged cross section is usually provided for the full phase–space. consequently, it would be difficult to compare such results from different experiments if each consider a different phase–space.

Before to present each differential result, we show in Tables 6.20 6.21 6.22 6.23 the absolute value of the error of each source for each measurement. It is included the phase–space considered and the number of bins used is provided.

6.10.1 Differential Cross Section on P_μ and Double Differential Cross Section on $(P_\mu, \cos\theta_\mu)$

Figure 6.57 shows the result for the differential cross section on P_μ. For this measurement we have used a phase–space where the muon is defined in $\cos\theta_\mu > 0.2$ and its momentum is between $0 < P_\mu < 50 GeV$. Last bin in the plots accounts for all the reamining bins not showed, normalized by the bin size of the bin used for the measurement. The binnning used in the measurement is:

$$\{0.0, 0.3, 0.4, 0.5, 0.6, 0.7, 0.8, 0.9, 1., 1.1, 1.2, 1.4, 1.6, 1.8, 2., 3., 5., 50.0\} GeV$$

	$\frac{d\sigma}{dp_\mu}$	$\frac{d\sigma}{dp_\mu d\cos\theta_\mu}$
Total Bins	17	20
Phase-Space	H	D
Data Stat.	0.00386	0.00398
MC Stat.	0.00127	0.00127
Cross Section Err.	0.00894	0.00923
FSI	0.00144	0.00158
Flux	0.0157	0.01634
Detector	0.00912	0.00867

TABLE 6.20: Number of bins, phase–space and absolute error values splitted by source from each measurement. For the results on the muon kinematics, $\frac{d\sigma}{dp_\mu}$, $\frac{d\sigma}{dp_\mu d\cos\theta_\mu}$

	$\frac{d\sigma}{dp_\pi}$	$\frac{d\sigma}{dp_\pi}$ no ME	$\frac{d\sigma}{d\theta_\pi}$
Total Bins	15	17	16
Phase-Space	F	G	E
Data Stat.	0.00288	0.00259	0.00239
MC Stat.	0.000965	0.00078	0.00072
Cross Section Err.	0.00714	0.00545	0.00472
FSI	0.00138	0.00198	0.00102
Flux	0.01386	0.00843	0.00766
Detector	0.00678	0.00739	0.00549

TABLE 6.21: Number of bins, phase–space used, absolute error values splitted by source from each measurement. For the results on the pion kinematics, $\frac{d\sigma}{dp_\pi}$, $\frac{d\sigma}{dp_\pi}$ (not including ME) and $\frac{d\sigma}{d\theta_\pi}$)

	$\frac{d\sigma}{d\theta_{\mu\pi}}$	$\frac{d\sigma}{d\phi_{planar}}$	$\frac{d\sigma}{d\cos\theta_{planar}}$
Total Bins	27	16	20
Phase-Space	B	B	B
Data Stat.	0.00239	0.00219	0.00222
MC Stat.	0.00074	0.00069	0.00068
Cross Section Err.	0.00447	0.00487	0.00509
FSI	0.00098	0.00086	0.00112
Flux	0.00732	0.00722	0.00699
Detector	0.00522	0.00515	0.00397

TABLE 6.22: Number of bins, phase–space used and absolute error values splitted by source from each measurement. for the results on angular combined variables, $\frac{d\sigma}{d\theta_{\mu\pi}}$, $\frac{d\sigma}{d\phi_{planar}}$ and $\frac{d\sigma}{d\cos\theta_{planar}}$

	$\frac{d\sigma}{dQ^2}$	$\frac{d\sigma}{d\lvert Q_3\rvert}$	$\frac{d\sigma}{dW}$
Total Bins	16	13	28
Phase-Space	C	C	C
Data Stat.	0.00317	0.00303	0.00542
MC Stat.	0.00106	0.00103	0.0019
Cross Section Err.	0.00815	0.00823	0.00728
FSI	0.00114	0.00114	0.00121
Flux	0.1276	0.01266	0.01360
Detector	0.00595	0.00605	0.00778

TABLE 6.23: Number of bins, phase–space used and absolute error values splitted by source from each measurement. For the results on momentum transfer and invariant mass, $\frac{d\sigma}{dQ^2}$, $\frac{d\sigma}{d|Q_3|}$ and $\frac{d\sigma}{dW}$

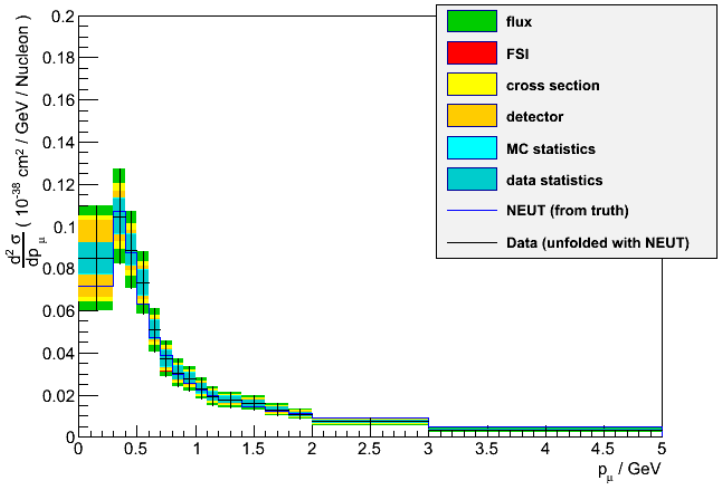

FIGURE 6.57: $d\sigma/dP_\mu$ result using unfolding Bayesian method with NEUT for the CC1π^+ sample.

For low energy muons we don't have enough statistics to do a finner binning, the efficiency is low. For that reason we decided to have an unique and coarse bin covering this region. In this way we can also avoid model dependency when unfolding with the MC for low efficiency regions. From Figure 6.57 we can appreciate that low momentum muons are dominated by statistical and detector uncertainties. We observe that data is well described by NEUT.

For the double differential cross section, $(P_\mu, \cos\theta_\mu)$, the result is shown in Figure 6.58. For this measurement we consider the phase–space: muon is defined as forward–going, i.e. $\cos\theta_\mu > 0$, and no restriction in muon momentum is applied. High angle muon tracks have a low efficiency on reconstruction, for this reason, the first bin used in the cosine of the muon is the range $0 < \cos\theta_\mu < 0.8$. Muon momentum range in the cross section measurement is performed from $0 < P_\mu < 50GeV$. The last bin in the plot

includes all entries in the bin range and above, normalised to the bin size used for the measurement. The binnning used in the measurement, for the P_μ is:

$\{0.0, 0.4, 1.2, 1.6, 2., 50.0\}$ GeV

And for the $\cos\theta_\mu$ is:

$\{0.0, 0.8, 0.85, 0.9, 1.0\}$

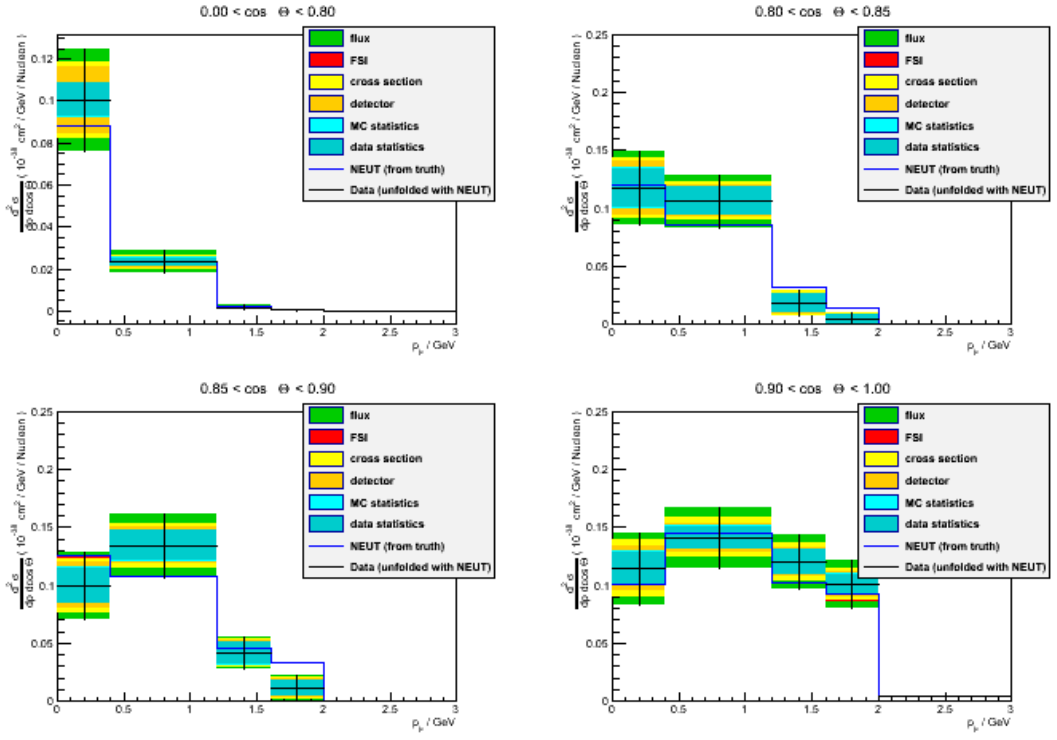

FIGURE 6.58: $d\sigma/dP_\mu d\cos\theta_\mu$ result using unfolding Bayesian method with NEUT for the CC1π^+ sample.

In this measurement we are dominated by statistical uncertainties and this is more evident when looking into higher angles. This is due to the acceptance of our detector and the fact that double differential measurements needs bigger statistics than the simple differential. We see than in general for muon-only variables, as presented in this sub–section the model represents quite well the data. We can notice some model over–prediction in some bins at higher angles for momentum from 1200 to 2000 MeV. This is probably due to the fact that the single pion model is less understood at higher energies.

6.10.2 Differential Cross Section on P_π and on θ_π

Here we present results for the differential cross section on p_π and on θ_π. For p_π, we show the result in two different ways: one for the full sample and the other one for the CC1π^+ sub-sample when the pion is reconstructed using only the TPC. This second result is

provided for a comparison in particular to see if the model performs good description in both samples.

Figure 6.59 shows the result for the differential cross section on p_π where the full CC1π^+ sample is considered. For this measurement, we apply phase–space where the muon is defined in $\cos\theta_\mu > 0.2$ and $p_\mu > 200.$ MeV. Pion momentum range in the cross section measurement is performed from $0 < P_\pi < 50.$ GeV. The last bin showed in the plot contains all entries above the bin limit and it has been normalized to the real bin size. We use a bigger bin size at low momentum to take into account possible model dependency due to the pion momentum parametrization for pions tagged using Michel electrons. The first bin size is estimated to contain $\sim$ 90% of the pions when they are identified using the Michel electron tagging (according to the MC prediction). The binnning used in the measurement when using the full sample is:

$\{0.0, 0.4, 0.5, 0.6, 0.7, 0.8, 0.9, 1., 1.1, 1.2, 1.3, 1.4, 1.6, 2., 3., 50.0\}$ GeV

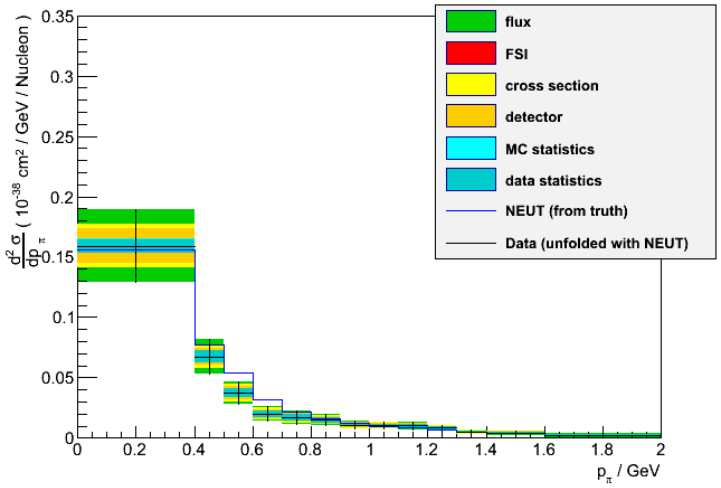

FIGURE 6.59: $d\sigma/dp_\pi$ result using unfolding Bayesian method with NEUT for the CC1π^+ sample. For the full sample, using TPC pions and Michel electrons sample.

We observe that NEUT provides a general good description of the data in $d\sigma/dp_\pi$. Only one region, $0.5 - 0.7$ GeV presents an overprediction by the model. We can see that the model is providing a good description of our data when we use all pion momentum spectrum available, i.e. when adding Michel electrons.

If the Michel electron sample is not included, the measurement requires a phase–space where the muon and pion have $\cos\theta_\mu > 0.2$, $\cos\theta_\pi > 0.2$, and $p_\mu > 200.$ MeV. Pion momentum range in the cross section measurement is performed from $0 < p_\pi < 50GeV$. The last bin showed in the plot contains all entries above the bin limit and it has been normalized to the real bin size. The binnning used in the measurement is:

$\{0.0, 0.2, 0.3, 0.4, 0.5, 0.6, 0.7, 0.8, 0.9, 1., 1.1, 1.2, 1.3, 1.4, 1.6, 2., 3., 50.0\}$ GeV

The differential cross section on p_π considering the just mentioned condition is presented in Figure 6.60.

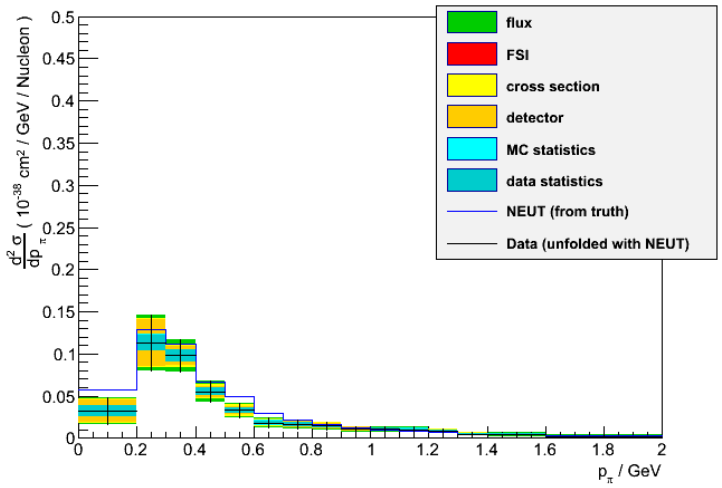

FIGURE 6.60: $d\sigma/dp_\pi$ result using unfolding Bayesian method with NEUT for the CC1π^+ sample when no using the Michel electrons sample.

In this case, when not using the Michel electrons sub-sample, we observe that the model overpredicts the data at low momentum and at smaller discrepancy at intermediate energies aroung 0.5GeV. This seems reasonable since we are not using Michel electrons which in general cover the low momentum region. This overprediction of the model to the data at low momentum pions has been observed in other experiments like MiniBooNE and MINERνA, which are experiments that work at higher energies than T2K.

Figure 6.61 shows the result for the differential cross section on θ_π. For the measurement we have use a phase–space where the muon and pion has a $\cos\theta_\mu > 0.2$ and $\cos\theta_\pi > 0$, since Michel electron sample is not included, and $p_\mu > 200.$ MeV and $p_\pi > 200$ MeV. For the single differential cross section on θ_π the binnning used is:

$\{0.0, 0.1, 0.2, 0.3, 0.4, 0.5, 0.6, 0.7, 0.8, 0.9, 1., 1.2, 1.4, 1.6, 1.8, 2., 3.1416\}$

For this measurement we observe a disagreement between the data and the prediction, NEUT tends to overstimate the data. We observe this overprediction at both low and high angle pions. the disagreement can be due to different reason. For a clear understanding of the situation, the study of the angles in the Adler's frame is needed.

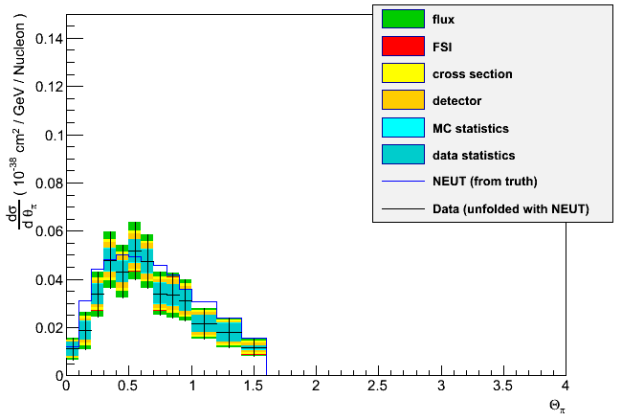

FIGURE 6.61: $d\sigma/d\theta_\pi$ result using unfolding Bayesian method with NEUT for the CC1π^+ sample.

6.10.3 Differential Cross Section on ϕ_{planar}

Figure 6.62 shows the result for the differential cross section on ϕ_{planar}. For this measurement we have used a phase–space where the muon and pion has a $\cos\theta_\mu > 0.2$ $\cos\theta_\pi > 0.2$, and $p_\mu > 200.$ MeV, $p_\pi > 200.$ MeV, since Michel electron sample is not included. The binnning used in the measurement is:

$$\{-\pi, -2.8, -2.4, -2., -1.6, -1.2, -0.8, -0.4, 0., 0.4, 0.8, 1.2, 1.6, 2., 2.4, 2.8, \pi\}$$

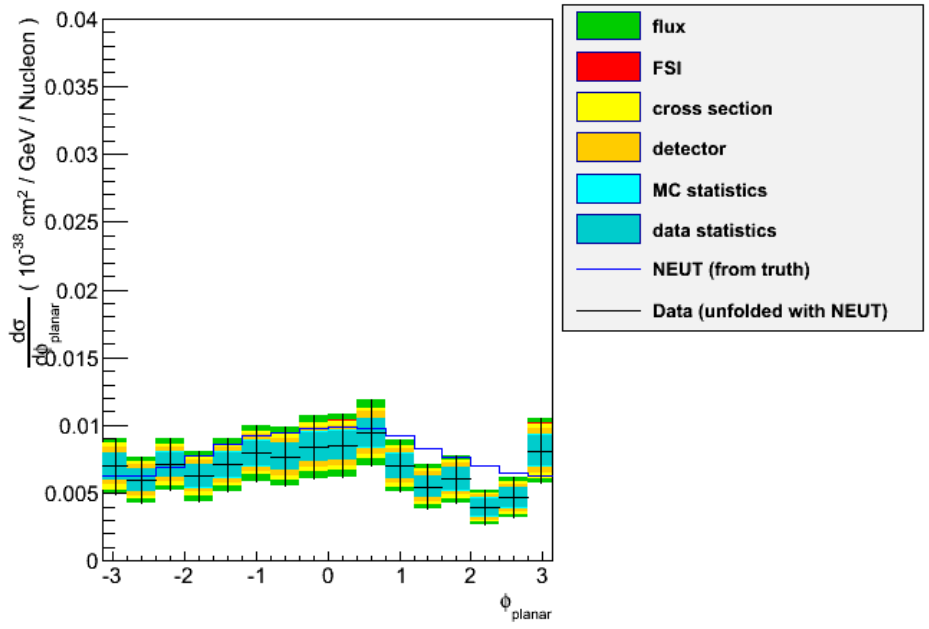

FIGURE 6.62: $d\sigma/d\phi_{planar}$ result using unfolding Bayesian method with NEUT for the CC1π^+ sample.

In this result we can see that the distribution is not totally flat and the decrease between $\pi \sim 2.5$ is not well described the prediction. In Section 6.4.1 similar plots but where the distribution is studied before the deconvolution, were shown. The flat shape, as discused in Section 6.4.1, presented is lost when we select the muon and the pion to be forward. It is interesting to see that applying an extra cut on the invariant mass for the sample selection ($W > 1.4GeV$), as showed on Appendix E, the model is still overpredicting the data in this region (actually with the cut on W the disagrement is bigger). It has to be noticed that the W cut is usefull when we want to see the signal in the region when the Δ^{++} has been produced but such cut reduces the CC1π^+ signal in the region where the interaction mode is dominated by other channel. The region with $W < 1.4GeV$ is also efective if we want to reject non–resonant events. But this is something we cannot recommend since, as discussed in the event selection, nuclear effects play an important role and the interaction ocurred in the nucleon doesn't has to correspond to the final state. Then, to apply such a cut on W can bias our sample and is not clear that the selection is covering the single pion topology. We observe that adding this W cut in our analysis, we don't get a better explanation of the data by the model and we are adding more statistical uncertainty due to the removed events. To conclude, we prefer to reject this cut on W for the mentioned reasons.

6.10.4 Differential Cross Section on $\cos\theta_{planar}$

Figure 6.63 shows the result for the differential cross section on $\cos\theta_{planar}$. For this measurement we have used a phase–space where the reconstructed muon and pion has a $cos\theta_\mu > 0.2$, $cos\theta_\pi > 0.2$, since Michel electron sample is not included, and $p_\mu > 200$ MeV, $p_\pi > 200$ MeV. The binnning used in the measurement is:

$\{-1., -0.9, -0.8, -0.7, -0.6, -0.5, -0.4, -0.3, -0.2, -0.1, 0., 0.1, 0.2, 0.3,$
$0.4, 0.5, 0.6, 0.7, 0.8, 0.9, 1.\}$

According to the cross section differential result, we see a very different behaviour respect to ANL distributions. This has been already discussed in Section 6.4.1 and can be explained by nuclear effects. We also observe big discrepancies between the data and the prediction at the very low values. This discrepancy is expected to be due to low momentum pions (see Section 6.4.1). In this sample we are not using Michel electrons, which are suposed to cover the low momentum region and the pions below 200 MeV are already not considered in the phase–space. This can explain why the prediction also has an small contribution at low values. Direction and momentum of the pions can be modified with respect the original values inside the nucleus and low momentum pions will be more affected by these changes. The pions affected doesn't need to be only

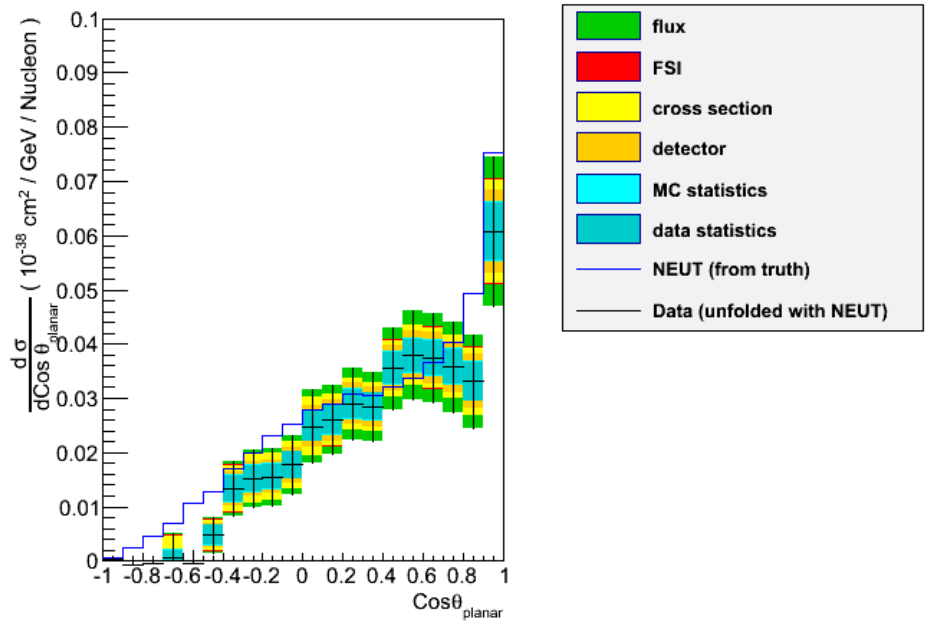

FIGURE 6.63: $d\sigma/d\cos\theta_{planar}$ result using unfolding Bayesian method with NEUT for the CC1π^+ sample.

the ones below 200 MeV. And then, this disagreement on data–prediction at the low region can be explained by a poor understanding of the FSI effects. We can see, as well, some discrepancies at higher values of this angle. For higher cosine values we don't have any strong argument which can explain the behaviour since at higher momentum values (associated to this cosine values) should be less affected by FSI effects.

6.10.5 Differential Cross Section on the angle between muon and pion

Figure 6.64 shows the result for the differential cross section on $\theta_{\mu\pi}$. For this measurement we have used a phase–space where the muon and pion has a $cos\theta_\mu > 0.2$, $cos\theta_\pi > 0.2$, and $p_\mu > 200.$ MeV, $p_\pi > 200.$ MeV. The binnning used in the measurement is:

$\{0.0, 0.1, 0.2, 0.3, 0.4, 0.5, 0.6, 0.7, 0.8, 0.9, 1., 1.2, 1.4, 1.6, 1.8, 2., 3.141516\}$

In this result we observe a quite good description of the data provided by NEUT. Statistical uncertainties are dominant since the Michel electrons sample is not included.

6.10.6 Differential Cross Section on Momentum transfer

In this section results for the differential cross section depending on Q^2 and on $|Q_3|$, 4–momentum and 3–momentum transfer, are shown.

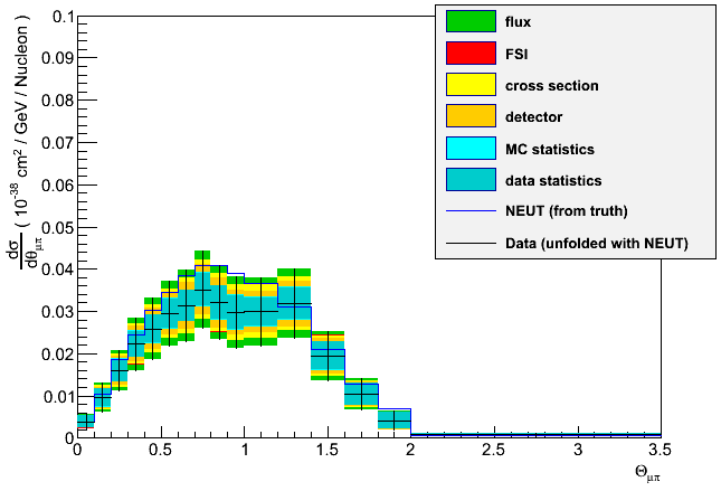

FIGURE 6.64: $d\sigma/d\theta_{\mu\pi}$ result using unfolding Bayesian method with NEUT for the CC1π^+ sample.

6.10.6.1 Differential Cross Section on the 4–Momentum Transfer

Figure 6.65 shows the result for the differential cross section on Q^2. This measurement requires a phase–space re–definition where the muon has a $\cos\theta_\mu > 0.2$ and $p_\mu > 200.$ MeV. The binnning used in the measurement is:

$$\{0.0, 0.1, 0.2, 0.3, 0.4, 0.5, 0.6, 0.7, 0.8, 0.9, 1., 1.2, 1.4, 1.6, 1.8, 2., 50.0\} GeV^2$$

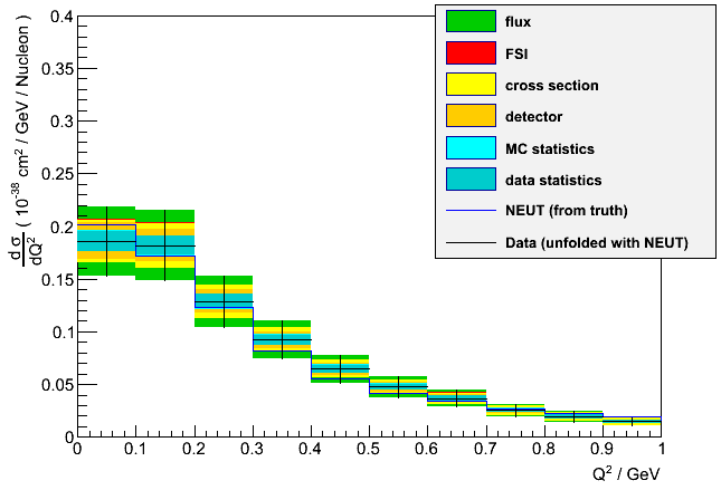

FIGURE 6.65: $d\sigma/dQ^2$ result using unfolding Bayesian method with NEUT for the CC1π^+ sample.

We observe that all errors are bigger for low Q^2 values. We can expect that FSI errors can be bigger at low momentum transfer, where a higher probability of pion absorption can be expected in the low Q^2 region. For detector errors this can be understood. At low Q^2 values we expect pions and/or muons caractherized by low momentum and thus

suffering of higher systematics (like charge mis–identification and momentum resolution). However, we observe a good agreement between the MC prediction and the data.

6.10.6.2 Differential Cross Section on 3–Momentum Transfer

Figure 6.66 shows the result for the differential cross section on $|Q_3|$. This measurement requires a phase–space where the muon has a $\cos\theta_\mu > 0.2$ and $p_\mu > 200.$ MeV. The binnning used in the measurement of the differential cross section $\frac{d\sigma}{d|Q_3|}$ is:

$\{0.0, 0.2, 0.4, 0.6, 0.8, 1., 1.2, 1.4, 1.6, 1.8, 2., 3., 6., 50.0\} GeV$

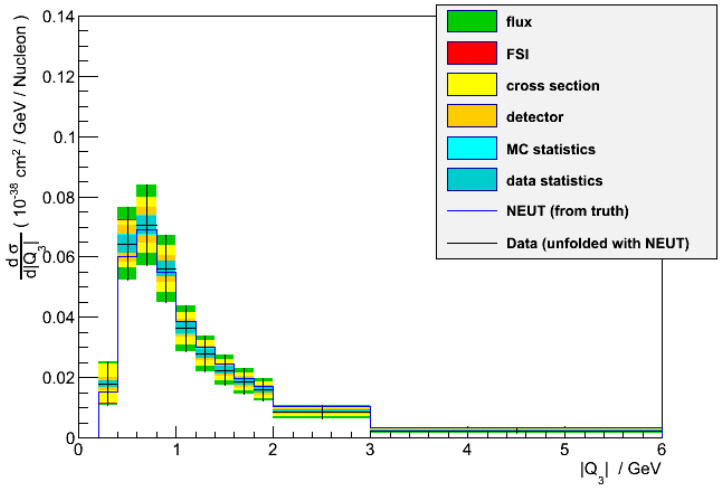

FIGURE 6.66: $d\sigma/d|Q_3|$ result using unfolding Bayesian method with NEUT for the CC1π^+ sample.

As it happens in the case of Q^2 values, errors increases at low values of $|Q_3|$. We observe values are picked at ~ 0.8 GeV and NEUT provides a good description of the data.

Taking into account all the results provided when unfolded with momentum transfer variables, which are the variables dependending on the reconstructed energy in the most model independent way, we see the model describes reasonably well the data. We don't see discrepancies along the momentum transfered in the interaction.

6.10.7 Differential Cross Section on Invariant Mass

Figure 6.67 shows the result for the differential cross section on W. For this measurement we have use a phase–space where the muon has a $\cos\theta_\mu > 0.2$ and $p_\mu > 200.$ MeV. The binnning used in the measurement is:

$\{0.0, 1., 1.1, 1.2, 1.3, 1.4, 1.5, 1.6, 1.7, 1.8, 1.9, 2., 2.1, 2.2, 2.3, 2.4, 2.5,$
$2.6, 2.7, 2.8, 2.9, 3., 3.2, 3.4, 3.6, 3.8, 4., 50.0\}$

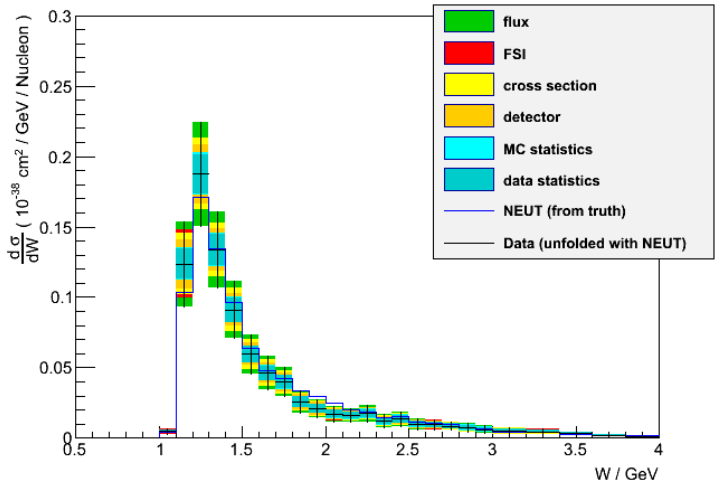

FIGURE 6.67: $d\sigma/dW$ result using unfolding Bayesian method with NEUT for the CC1π^+ sample.

As already observed in the momentum tranfer results, the data is well described by the model used in NEUT. This good agreement is also seen at high W values. According to the information showed in this results the model is providing a good estimation of the signal at any value of the W.

6.11 Model dependent results: $\sigma(E)$

In this section we show model dependent results for the energy dependent cross section. They are model dependent since we unfold the reconstructed energy formula using the true neutrino value predicted by NEUT. We avoid to unfold using the energy reconstructed formula with true kinematical variables because we need to use the proper flux value at each energy bin and we have the relation between the true energy predicted by the MC to the flux. Any other solution like make a migration matrix to relate the true kinematical variables to the flux and then to the true energy using the reconstructed formula can be quite complicated. This issue is avoided for the differential measurements where we divide by the total flux value at each bin.

We perform the measurement using the two different neutrino energy reconstructed formula. We show these results for completeness of the analysis also if we think that model dependent results are not of main relevance for neutrino cross section measurements when model independent measurements are available. The binnning used in both measurement is the same:

$\{0.0, 0.2, 0.4, 0.5, 0.6, 0.7, 0.8, 1., 1.2, 1.4, 1.6, 1.8, 2., 2.3, 2.6, 3., 1000.0\} GeV$

Before to present each result, we show in Table 6.24 the absolute value of the uncertainty of each source for both measurements. It is included the phase–space considered and the number of bins used is provided.

	$\sigma(E_{RecoMB})$	$\sigma(E_{Reco})$
Total Bins	16	16
Phase-Space	C	B
Data Stat.	24.39	19.97
MC Stat.	8.405	6.97
Cross Section Err.	109.84	61.56
FSI	21.98	13.02
Flux	92.09	63.6
Detector	49.77	48.94

TABLE 6.24: Number of bins, phase–space used and absolute error values splitted by source. For the measurements $\sigma(E_{RecoMB})$ and $\sigma(E_{Reco})$.

6.11.1 Energy dependent Cross Section using the MiniBooNE Formula

Figure 6.68 shows the result for the energy dependent cross section result. For this measurement we have used a phase–space where the muon has a $cos\theta_\mu > 0.2$ and $p_\mu >$ 200 MeV, since Michel electrons are used.

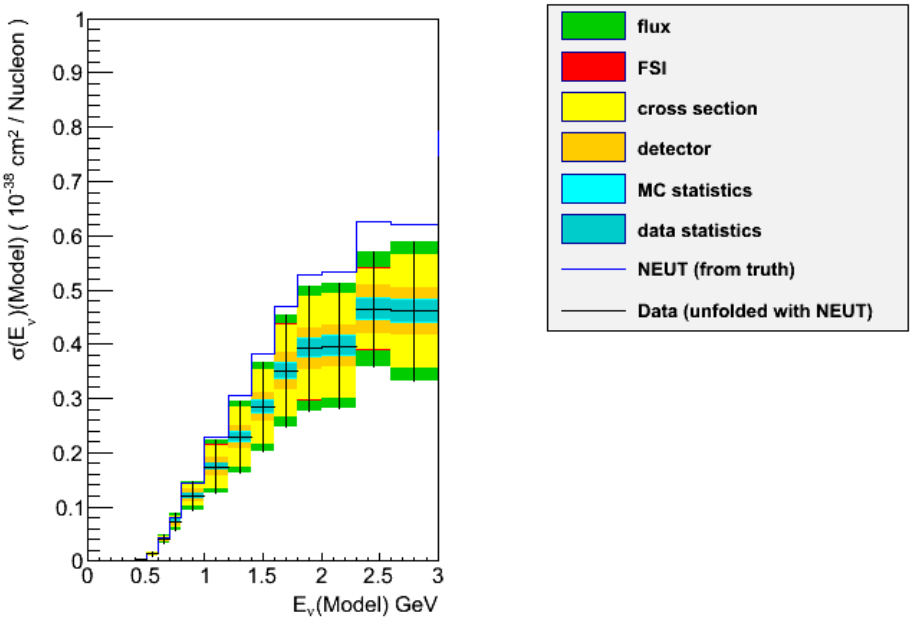

FIGURE 6.68: $\sigma(E_{RecoMB})$ result using unfolding Bayesian method with NEUT for the CC1π^+ sample.

When looking into the results it's difficult to interpret discrepancies respect to prediction since the formula used for the reconstructed value and the prediction is not the same, then, intrinsic discrepancies due to the formula are also present. These results are not meant to provide a direct and clean relation between the data and the model. They are shown for completeness and also to allow comparisons of the predicted energy and the different reconstructed neutrino formula that we are using.

6.11.2 Energy dependent Cross Section using the E_{Reco} Formula

Figure 6.69 shows the results for the energy dependent cross section using the formula developed for the analysis, $\sigma(E_{Reco})$. For this measurement we have used a phase–space where the muon and pion has a $cos\theta_\mu > 0.2$, $cos\theta_\pi > 0.2$, since Michel electron sample is not included, and $p_\mu > 200$ MeV, $p_\pi > 200$ MeV.

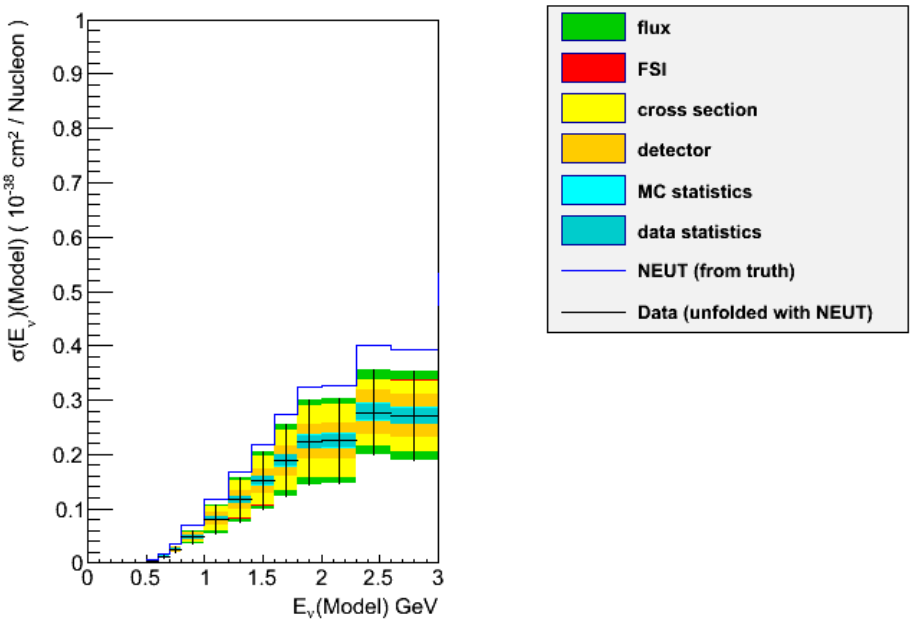

FIGURE 6.69: $\sigma(E_{Reco})$ result using unfolding Bayesian method with NEUT for the CC1π^+ sample.

Differences on the results with respect to truth NEUT prediction as mentioned is difficult to disantangle. But from the results presented at the energy dependent measurements we see that the agreements between the prediction energy and the reconstructed neutrino energies are very similar. At the low neutrino energy values the agreement is better when using the MiniBooNE's aproach.

6.12 Conclusions and Discusion of the Analisys

The analysis presented in this Chapter describes the CC1π^+ cross section measurement in CH realised in the off–axis near detector of the T2K experiment, the ND280.

The sample selection, composition and background contamination have been studied. Using NEUT as the default MC generator we observe a purity of the CC1π^+ signal of $\sim 60\%$. The main contamination source in the sample is due to un–identified CCOther events and mainly due to limitations on the current reconstruction. Three control samples have been performed in order to subtract the background using data instead of appying the purity correction with the aim to reject the model dependency.

We have presented a wide set of observables that have been used for the different differential cross section measurements presented. All of these observables are shown with the aim to provide information which can be crucial to understand our current neutrino interaction models. The MC used for the comparisons and the unfolding method uses the Rein and Sehgal model to describe the single pion production. We have added to the observables, the planar angles, that we consider can be crucial in the model for the pion angular parametrization. All the observables, before the unfolding process, have been presented and described the behaviour with respect to the predicted one.

We listed the uncertainties that plays a role in the measurement. The error propagation has been briefly discussed and the unfolding Bayesian method used for the calculation has been explained. The biggest contribution from the errors source is the uncertainty on the flux while the biggest contribution from detector systematics is the one related to the secondary interactions of the pion. At low energies it is the charge mis–identification to become the dominant detector systematic. Cross section parameter error are the second biggest contribution to the uncertainties, from which we strees again the importance on provide cross section measurements to test the models and then try any improvement on them.

Several preliminary tests on the unfolding procedure, using fake data, has been performed in order to prevent any pathology intrinsinc to the method. We checked the number of iterations in the unfolding method and we concluded that one iteration is the optimal number for this analysis, mainly because of the possibility to introduce fluctuations related to the limited statistics available. An study on the accessible phase-space in which we are senitive to our signal have been developed in order to reject model dependencies in the regions where the efficiency is low. When possible, we construct coarse bins to merge low statistics and poor efficiency.

From all these studies, we can conclude that the selection is solid and consistent and the kinematical variables are well reconstructed.

In the Appendix E, a new set of results are presented where an additional cut is applied to reject events with invariant mass higher than 1.4GeV. Since this cut reduces the available statistics, and we wanted to keep the same binning as the ones in the main results shown in this Chapter, we only show the results with the W cut when the errors are not so fluctuated due to low statistics. The study on the W cut has been done to study if the description of the data improves when selecting the region where the Δ^{++} is produced. However, by comparing to the main results, we conclude that this cut on the invariant mass reduces the statistics in our sample but any obvious improvement in the model prediction is observed. We consider that the sample presented in this Chapter, without any restriction on the invariant mass, provides more interesting results since we consider all the interactions that can produce a CC1π^+ event.

All the work presented here has been done with the aim to provide results as model independent as possible to make their interpretation to other experiments easier. This model independency of the analysis pretends to be useful to improve current models. From the different differential cross section measuremets presented we want to highlight that:

1. We observe a quite good description of the data for the CC1π^+ topological channel in all *muon-only* observables (only depending on muon kinematics). Muon-only variable results use Michel electron events, then we can think that the fact that we cover low energy pions makes our result to converge better with the model. Or it can be that the leptonic part of the interaction is better understood by the model.

2. We observe in general an overprediction from the model to the angular pion observables. This is clearly seen in the pion angle differential cross section but also in the planar angles. Thanks to the deep study of the planar angles we understood the problem is mainly concentrated on the low momentum pion region, in the case of $\cos\theta_{planar}$. We can extract that:

    - For pion angular variables the low momentum pions, which are mainly reconstructed using Michel electrons, are not represented in the data sample. In addition to this, low energy pions (also if $p > 200MeV$) are more sensitive to nuclear effects and the possible loss of energy and change of direction of the track is not well predicted by the model.
    - ϕ_{planar} angle still shows discrepancies with respect to the model, also if we think this variable is less sensitive to FSI effects than $\cos\theta_{planar}$. We expect

that the differential measurement on ϕ_{planar} can provide a valuable information to be taked into account by theorists because of its lower dependency with respect to FSI.

- Any improvement on the analysis should start by the addition of low momentum pions in the analysis. Due to reconstruction limitation it was not possible to add low momentum pions for angular distributions. In general, the inclusion of low momentum tracks with good efficiency will help for a better description in neutrino physics.

3. Pion momentum differential result is in good agreement when we use the Michel electrons sample. Otherwise, the model overpredicts the data at low momentum values.

4. All distributions related to the neutrino energy (differential measurements on the momentum transfer and on the invariant mass), seems to be in general in a good agreement with the prediction.

All the results are presented in this Chapter, are showed by bin including the error values, on tables in Appendix F.

We would like to conclude this analysis streesing the needed for new measurements on neutrino cross section sensitive to low momentum particles. Since the cross section estimation is still one of the dominant uncertainties in any neutrino oscillation experiment, it becames crucial to improve the interaction models.

This analysis explores observables from which some of them haven't been looked at since the ANL and BEBC experiments. With the addition of a well defined sample and the rejection of the use of sophisticated cuts and just the particle recognition. We think that the analysis have been made an important effort to provide important nuclear information.

Chapter 7

Conclusions

In the T2K experiment, an almost pure ν_μ beam is used to measure the neutrino oscillation parameters. The main goal of the T2K experiment is the measurement of the oscillation of muon neutrinos. The oscillation program requires an accurate prediction of the rate of interactions in the far detector. T2K predicts this rate by measuring interaction of neutrinos at the near detector.

The first analysis presented, the ν_μ CC inclusive analysis in Chapter 5, improved the event selection in ND280 with respect to previous analysis. In the ν_μ CC inclusive analysis we distinghish three different samples according to the number of pions in the final state of the interaction. In this way, a better constraint of the CCQE–like events and the one of the main backgrounds, the $CC1\pi^+$, is achieved.

In order to do the event selection, we fully exploit the TPC detector to identify charged and neutral pions. In addition, we add positive pion identification in the FGD1 in order to improve the different sub–samples by adding low energy pions stopping in the scintillator target.

Thanks to this new strategy on the event selection, systematics related to the neutrino cross sections parameters were reduced. In 2013 T2K presented the most precise measurement of the θ_{23} oscillation parameter and provide the first evidence of ν_e appearance from a ν_μ beam. The measurement of the CC inclusive rate at the near detector was a basic ingredient in this achievement.

From the experience of the analysis presented in this work, we identified a list of improvements in the ND280 detector and data selection that should help improving future analysis:

- Include short track reconstruction for muon and electron/positron contained in the FGD (FGD–Only). This wil help on improve purities at each sample.
- Cover the full phase–space by adding high angle and backward–going tracks. This will imply to add ECal particle identification for muons and pions, both charged and neutral.
- Identify the $CC\pi^0$ sample within the CCOther sample and treat it separately. This will help to reduce reduce cross section parameter errors since the neutral pion is one of the biggest uncertainties.
- Include selections from water target analysis. P0D or FGD2 can be used as water target and this selection will reduce oscillation analysis uncertainties since the far detector is a water–based detector.

The list of improvements are just an indication for future ND280 selection analysis. However, a parallel activity to reduce neutrino cross section uncertainties is to improve the current neutrino interaction models.

A way to help on the improvement of such models is to compare with our data and check their mutual consistency. Data published by other experiments show discrepancies with the theoretical models for almost all interaction channels and energy ranges. It is of the greatest importance to study cross section on all possible interaction channels that are in tension with the model. $CC1\pi^+$ is one of the main channels to study. For this reason, we have developed the $CC1\pi^+$ cross section measurement in FGD1 (CH target). This measurement is performed with the aim of a model independent measurement and to challenge the Rein and Sehgal model that is the base of the T2K Monte Carlo generator (NEUT).

With the idea of a model independent measurement we perform the analysis with a roadmap as follows

- The selection of $CC1\pi^+$ events is based on pure topological arguments, avoiding as much as possible using kinematical properties of the event that may bias the selected sample.
- Perform differential cross section measurements with respect to observables of physical interest. These observables are chosen in order to be able to compare with results from other experiments and to provide data for model comparison and validation. The observables that have been considered of major interest for a cross check of the model are the so–called “Adler’s angles”. These angles are

a clean proof of nuclear effects or a good estimation of the goodness of the pion angle estimation. We also add measurements with respect to momentum transfer or invariant mass obsevables which are of interest to compare with the model prediction.

- The cross section measurement is done using a Bayesian unfolding method in order to take into account detector dependencies.
- We have considered in each result the phase–space to which we can be sensitive in order to avoid model dependency during the unfolding process.
- The background of the sample is extracted during the unfolding process using control samples not passing the selection criteria. The control sample selection is performed in such a way that it represents consistently the shape and origin of the background in the main $CC1\pi^+$ selected sample.
- All the differential measurements are unfolded using the same reconstructed formula in the Monte Carlo with the predicted kinematics.
- We have chosen the size of the different bins by taking into account the observable resolution.
- We have improved the neutrino energy estimator for $CC1\pi^+$ events, in addition to the one performed by the MiniBooNE experiment.

The results of this analysis showed that:

1. There is a general good agreement on data with the prediction when we use the full sample that includes low momentum pions. While when not including the low mometum pions we see an overestimation at low momentum by the Monte Carlo.
2. The observables showing larger discrepancies with respect to the prediction are the angular variables on which we could not include the low momentum pions [1]. These discrepancies can be explained partly by the absence of the low momentum pions. The result on the ϕ_{planar} show an overestimation at high values by the Monte Carlo with respect to the data, in this case it is not clear that the discrepancy is explained by the absence of low momentum pions. While for the $\cos\theta_{planar}$ are more visible and are bigger at low values. The low values on $cos\theta_{planar}$ is expected to correspond to the low momentum pions contribution, mainly.

[1] Low momentum pions are not included for angular variables due to reconstruction limitations.

We have repeated the results with a cut in the invariant mass following the procedure of previous experiments. This cuts reduces the non–resonant background and enhances the $\Delta(1232)$ contributions that are supposed to be better described by the Rein and Sehgal model. Adding this cut the differential cross sections agreements with the model does not improve.

During this analysis we learn that it is crucial to include low momentum particles (muons, pions, electrons, ...). This will increase our phase–space availabe and will help for a more complete comparison with the different models. The inclusion of the low momentum particles (both momentum and angle) requires the reconstruction of very short tracks in the FGD1, i.e. tracks < 30 cm lenght. A larger improvement can be achieved with new detection technologies that allow short track reconstruction and full 3D reconstruction capabilities like the one achieved with gas or liquid time projection chambers.

Appendix A

Neutrino Oscillations Theory

In the 1968 the Homestake experiment gave the first experimental evidence that neutrino oscillation might occur. However, only in 1998 and 2002 with Super-KamiokaNDE and SNO results, the oscillation phenomenon was confirmed. For his work directing the Kamioka experiments, and in particular for the first-ever detection of astrophysical neutrinos Masatoshi Koshiba was awarded the Nobel Prize in Physics in 2002. Raymond Davis Jr. and Riccardo Giacconi were co-winners of the prize.

There are at least three neutrinos flavors: electronic (ν_e), muonic (ν_μ) and tauonic (ν_τ). From a theoretical point of view, neutrino oscillations can be described by a neutrino mixing matrix with four free parameters: three mixing angles and a CP violating phase, δ [1]. The hypothesis of neutrino mixing is based on the assumption that the total Lagrangian contains a neutrino mass term, which does not conserve flavor lepton numbers. If neutrinos have non-zero mass and the mass eigenstates do not correspond to the flavor eigenstates, then neutrinos can mix. The process is similar to the mixing in the quark sector.

In this case the flavor states, $|\nu_\alpha\rangle$, are super-impositions of the mass states, $|\nu_i\rangle$:

$$|\nu_\alpha\rangle = \sum_i U^*_{\alpha i} |\nu_i\rangle \tag{A.1}$$

being $\alpha = e,\ \mu,\ \tau$ and $i = 1, 2, 3$, "U" the unitary mixing matrix and $|\nu_i\rangle$ the mass eigenstates with m_i mass eigenvalues.

For an initial ν_α neutrino, the neutrino state at distance L is given by

[1] This is assuming the Dirac framework, if neutrinos are Majorama particles then there are another two phases.

$$|\nu(L)\rangle = \sum_i U^*_{\alpha i} |\nu_i(L)\rangle = \sum_i U^*_{\alpha i} e^{\frac{-im_i^2 L}{2E})} |\nu_i\rangle \tag{A.2}$$

with E being the neutrino energy. This means that a neutrino flavor is a superimposition of different mass eigenstates. Furthermore, when traveling, the contribution at each mass eigenstate may change, giving a different superimposition of mass states. Thus, when a neutrino is detected the probability of observing this neutrino that initially ($t = 0$) was of flavor α as a neutrino of flavor β at $t = L$ is give by:

$$P(\nu_\alpha \to \nu_\beta) = |\langle \nu_\beta | \nu_\alpha(L) \rangle|^2 = |\delta_{\alpha\beta} + \sum_{i \geq 2} U_{\beta i}(e^{\frac{-i\Delta m_{i1}^2 L}{2E}} - 1) U^*_{\alpha i}|^2 \tag{A.3}$$

where the neutrino masses are labeled following the usual convention $m_1 < m_2 < m_3$, and $\Delta m^2_{i1} = m^2_i - m^2_1$. For better explain the neutrino oscillation phenomenon let's assume for the moment we have only two neutrino flavors: ν_α and ν_β. In this case the matrix U can be written as a rotation

$$U = \begin{pmatrix} cos\theta & sin\theta \\ -sin\theta & cos\theta \end{pmatrix} \tag{A.4}$$

the neutrino oscillation is thus parametrized using only one parameter, θ, usually called the mixing angle. Then the probability to change the flavor is given by:

$$P(\nu_\alpha \to \nu_\beta) = sin^2(2\theta) sin^2\left(\frac{\Delta m^2 L}{4E}\right) \tag{A.5}$$

with $\Delta m^2 = m^2_2 - m^2_1$ and defining an oscillation length as

$$L_0 = 4\pi \frac{E}{\Delta m^2}. \tag{A.6}$$

Taking E in MeV, Δm^2 in eV^2 and L in m we have

$$L_0 \simeq 2.48 \frac{E}{\Delta m^2} \tag{A.7}$$

and we get the transition probability written in the usual way

$$P(\nu_\alpha \to \nu_\beta) = sin^2(2\theta) sin^2\left(\pi \frac{L}{L_0}\right) = sin^2(2\theta) sin^2\left(\frac{1.27 \Delta m^2(eV^2) L(Km)}{E(GeV)}\right) \tag{A.8}$$

Last equation means that if we assume only two families ($\alpha = \mu$ and $\beta = e$), if we produce a pure ν_μ beam, at distance L it will be composed by a mixture of ν_μ and ν_e.

The amplitude of the oscillation is determined by the mixing angle θ and the L/E dependence of the probability of this oscillation is characterized by Δm^2.

There are some variations on the oscillation parameters when we take into account that the neutrino is propagating in a medium [75], [76]. Neutrinos in matter have a different effective mass than neutrinos in vacuum, and since neutrino oscillations depend upon the squared mass difference of the neutrinos, neutrino oscillations may be different in matter than they are in vacuum.

If we take in account all the three neutrino families, the U matrix becomes a 3x3 unitary matrix.

$$U = \begin{pmatrix} c_{12}c_{13} & s_{12}c_{13} & s_{13}e^{-i\delta} \\ -s_{12}c_{23} - c_{12}s_{23}s_{13}e^{i\delta} & c_{12}c_{23} - s_{12}s_{23}s_{13}e^{i\delta} & s_{23}c_{13} \\ s_{12}s_{23} - c_{12}c_{23}s_{13}e^{i\delta} & -c_{12}s_{23} - s_{12}c_{23}s_{13}e^{i\delta} & c_{23}c_{13} \end{pmatrix} \tag{A.9}$$

where $c_{ij} = cos\theta_{ij}$ and $s_{ij} = sin\theta_{ij}$. This U matrix is called Pontecorvo-Maki-Nakagawa-Sakata matrix (or PMNS matrix or lepton mixing matrix) and is the analogue for the CKM matrix, describing the quark mixing. There are four parameters that describes the mixing: three mixing angles, θ_{12}, θ_{23} and θ_{13}, and the CP violating phase δ.

Appendix B

The ECal Shower Reconstruction Efficiency Systematic

The shower reconstruction efficiency has been performed for the Barrel and Dowstream ECal detectors and it has been evaluated to estimate the unceratinty on the reconstruction of shower–like objects in such detectors. This systematic is needed for analysis looking for neutral pions reaching the ECal.

The systematic has been computed in order to provide the shower–like uncertainty for analysis looking for events that occurs in the FGD1 or FGD2 detectors and want to identify a possible track going to the Barrel or the Dowstream ECal where it produces a shower. This is specially important for the neutral pion identification. If the neutral pion lifetime is very short and it mainly decay to photons which easily convert to electron/positron. If any photon or electron/positron reach the ECal detector it will probably produce an electromagnetic shower taht can be identified.

We use a control sample to estimate the systematic, in both data and Monte Carlo. Then, we correct the value obtained by the control sample using the real efficiency in our selection, according to the Monte Carlo. This procedure has been also applied in the other detector systematics which have been propagated as *efficiency–like* (see 4.1).

B.1 Data Control Sample

The estimation of the systematic as a Monte Carlo to data comparison is done using a control sample. The control sample tries to find events where showers are created in the ECal. The suitable sample may be the one selecting only isolated objects in the ECal (events with reconstructed objects in the ECal detectors and no segments at any other

detector). Due to the difficulties to find a proper reference in data for events with only isolated objects in the ECal, we follow a different approach. In this approach, we get the efficiency of reconstruct an ECal object.

The control sample is then defined as:

- We require in the sample at least one TPC track. This TPC track must satisfied the *Quality and Fiducial cut* as defined in Section 5.2.4. It must start in any FGD detector, if it starts in FGD2 the same fiducial volume as in the FGD1 is defined.
- The TPC track must be going to the Barrel or Downstream ECal detectors.
  - the track end position in the TPC is in the last layers of the TPC3 and their direction is pointing to the Downstream ECal, or
  - the track end position is in the TPC edges (top–bottom–left–right) and pointing to the Barrel ECal.
- The selected TPC track which is already selected to be pointing to the ECal cannot be the highest momentum negative track in the event. This requirement reduces the probability of the track to be a muon and increases the probability to be a pion, proton, electron or positron. These particles, not the muon, are suitable to create a shower–like in the ECal. This is because electrons/positrons/hadrons can easily interact with the ECal material producing multiple new particles with less energy, each of these particles can continue interacting creating lower energy particles till these particles stop in the ECal and are absorved by the material. While the muon can easily exit the ECal without interacting.

Once these conditions are satisfied, we check if there is an ECal object with conditions as follows:

- this object must be with a maximum of 70 cm away from the end position in in TPC of the TPC selected track. This is requested to avoid ECal objects that also have segments in TPC. We expect to identify ECal showers that are product of a TPC track.
- the Ecal object has to be reconstructed as shower–like, i.e. the MIP–EM reconstructed variable in ECal must be positive.

With these conditions we obtain a sample with a composition according to the particle type of the TPC track which indicates they are mainly protons, as we can see from

Table B.1. Showing the particle composition according to MC. This is done for the TPC track selected in case this TPC track is pointing to Barrel or Downstream ECal. The sample is dominated by particles other than muons $\sim 85\%$ in Barrel and $\sim 95\%$ in Downstream ECal.

True particle	Fraction for Barrel (%)	Fraction for Downstream (%)
μ^-	14.2	5.1
π^-	4	2.6
π^+	16.1	17.1
p	45.3	57.4
e^-	7	3.2
e^+	11.5	8.3
μ^+	1.7	5.5
other	0.2	0.7

TABLE B.1: Composition of the particle selected in TPC that ends close to the Barrel or Dowstream ECal detectors.

The efficiency in the control sample is calculated for the data and for the Monte Carlo, in case of Barrel or Downstream detector, according to:

$$Eff_{\text{Control Sample}} = \frac{\text{number of events with selected TPC track and selected ECal object}}{\text{number of events with selected TPC track}} \tag{B.1}$$

In Figure B.1 we show the efficieny respect to the momentum of the TPC track, for the Barrel and Dowstream ECal. We observe a good efficiency in general except for the momentum tracks around 400MeV. The behaviour is similar for data and Monte Carlo.

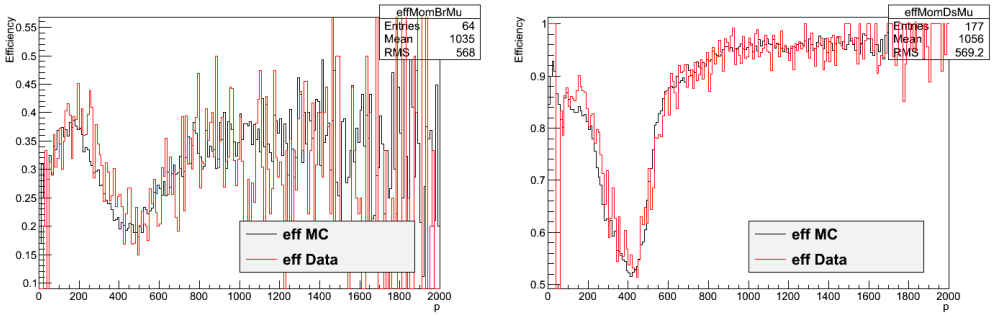

FIGURE B.1: Efficieny respect to the momentum of the TPC track, for the Barrel (left) and Dowstream ECal (right).

The low efficeincy at $\sim$ 400 MeV can be explained by pion interactions with the TPC material. We can see the relation between the the azimuthal angle and the momentum of the TPC track in Figure B.2. The information is shown for Barrel and Downstream ECal for all the selected TPC track events and the ones with the selected ECal object.

We observe that at certain values of the azimuthal angle we don't have too many TPC tracks selected for the Barrel ECal. but in general we observe that events seems to be concentrated at some angular regions (from -2 to -1 and from 1 to 2) in both sub–detectors.

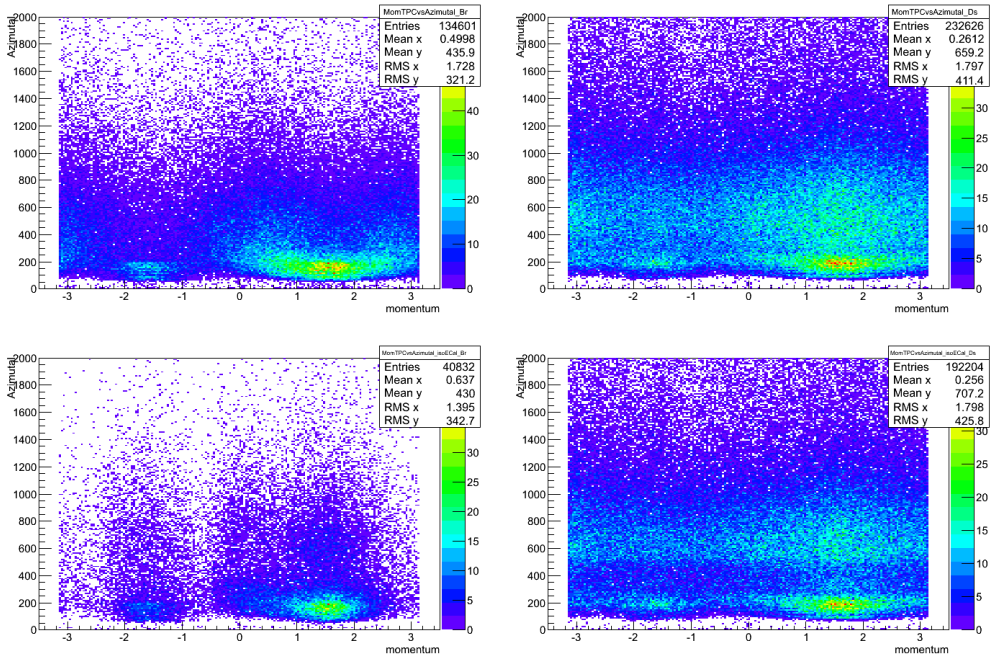

FIGURE B.2: Relation between the the azimuthal angle (x–axis) and the momentum of the TPC track (y–axis). Left plots correcpond to the Barrel ECal and right plots to the Downstream ECal. Top plots show the relation in all TPC track events selected, bottom plots show the same infomration when it is also selected the ECal object.

The efficiencies from the control sample are shown in Table B.2, with the statistical uncertainties, which are also considered.

	MC (%)	Data (%)	MC statistical (%)	Data statistical (%)
Barrel	0.303	0.315	0.0027	0.0085
Downstream	0.826	0.839	0.0021	0.0065

TABLE B.2: Total efficiencies obtained from the controls samples and statistical uncertainties. For Barrel and Dowstream ECal and for data and Monte Carlo events.

We observe a better efficiency for the Downstream than for the Barrel ECal. This can be explained by the fact that the Dowstream ECal bars are all double ended, whereas the barrel has a mixture of single and double ended bars. Double ended bars will allow to a better reconstruction. Efficiency in data is slightly better than in Monte Carlo. This can be explained by the plots shown in B.1 on which at low momentum, for both Barrel and Downstream, we observe higher efficiency for data and from Figure B.2 we see that we have more abundance of ECal showers created when the TPC particle is below $\sim$ 700 MeV.

B.2 Correction Factor

For the propagation of the systematic we need the "real" efficiency of our sample in Monte Carlo, for our purposes we use the ν_μ CC Inclusive sample selected in the FGD1, since it is enough for this estimation.

We check the true isolated ECal objects, in Barrel and Dowstream, and how many times they are reconstructed with an ECal object as a shower–like.

We need to establish in which conditions the true objects are suitable to be considered. It means that not all true ECal ojects can be consireded since not all of them may have a minimun efficiency on their reconstruction as an object in the ECal. For example, very low energetic objects should not be consireded.

For this reason we perform a very simple study to to establish the threshold required to the true ECal objects to be considered for the systematic efficiency correction.

Once we define these thresholds, we just calculate the value of the correction as follow:

$$Eff_{\text{MC in current analysis}} = \frac{\text{number of reconstructed isolated ECal objects shower–like}}{\text{number of true isolated ECal objects}} \tag{B.2}$$

This is calculated in the sample on which we want to propagate the error and it is calculated one time.

B.2.1 ECal Thresholds

To establish the minimum requirements to the true ECal objects we look into two different variables in both Barrel and Downstream ECal:

- the true momentum of the ECal object,
- the true lenght of the ECal object.

This is checked for any ECal object, independently of the presence of other segments in any sub-detector (non–isolated object).

In Figure B.3 we show in the 2–D plots the distributions of the MIP–EM reconstructed variable with respect to the true lenght (top plots) and to the true momentum (bottom plots) of the objects in ECal. It is shown only for the Barrel ECal detector.

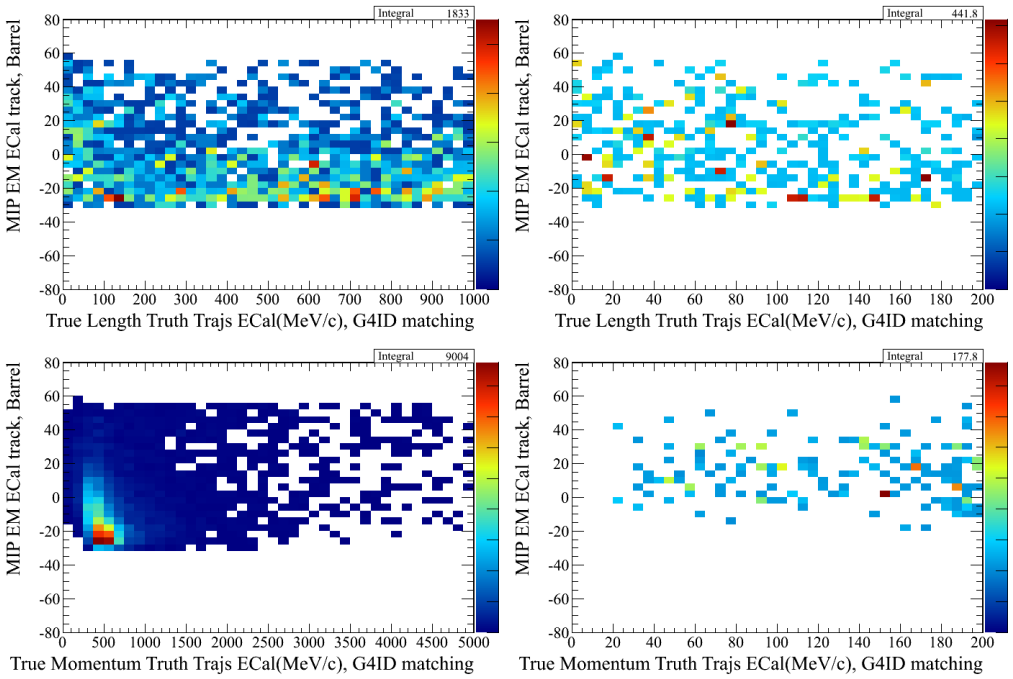

FIGURE B.3: MIP–EM reconstructed variable with respect to the true lenght (top plots) and to the true momentum (bottom plots) of the objects in ECal, plots at right correspond to a zoom at the lower values. It is shown only for the Barrel ECal detector.

In Figure B.4 we show in the 2–D plots the distributions of the MIP–EM reconstructed variable with respect to the true lenght (top plots) and to the true momentum (bottom plots) of the objects in ECal. It is shown only for the Downstream ECal detector.

From the Figures B.3 B.4 we can conclude from which values of the true observables we have a reconstructed object. And also, we can see that this dependence of threshold doesn't depend if the object of shower–like or not, looking into the MIP–EM. Now, in Figure B.5 we show the efficiency on reconstruct an ECal object with respect of these true variables, the true lenght (left plot) and momentum (right plot) of the ECal object. Top plots corresponds to the Barrel and the bottom ones corresponds to the Dowstream.

Finally we decide to apply the following cosiderations to our true ECal objects in order to compute the systematic correction factors:

- For Barrel ECal we consider only true objects when they have:
  1. True lenght $>$ 3 cm.
  2. True momentum $>$ 30 MeV.
- For Downstream ECal we consider only true objects when they have:
  1. True lenght $>$ 0 cm.
  2. True momentum $>$ 80 MeV.

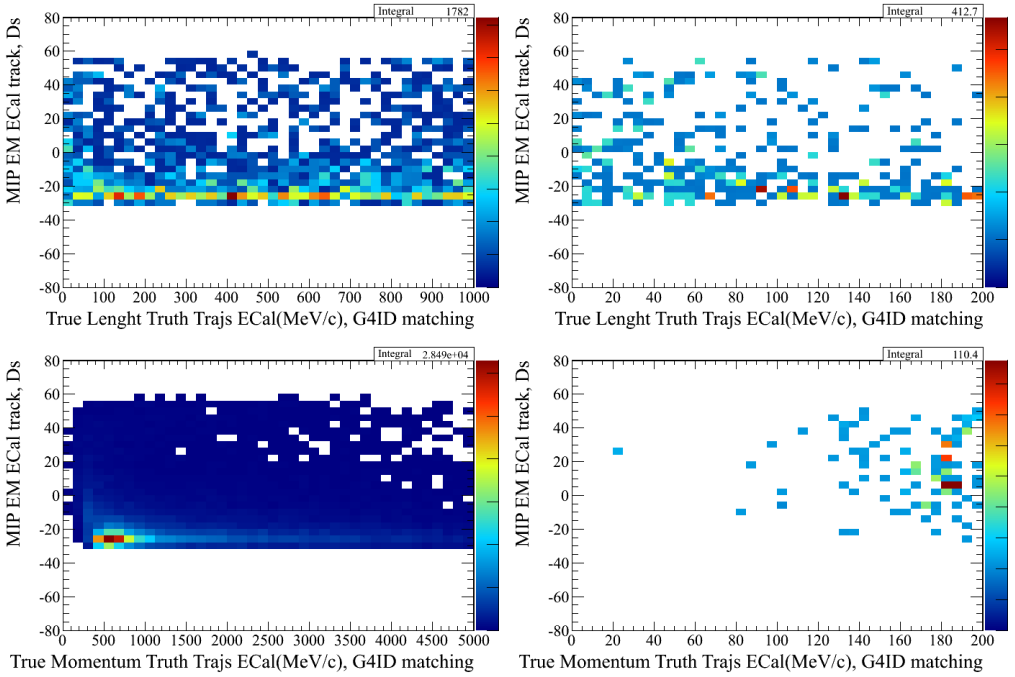

FIGURE B.4: MIP–EM reconstructed variable with respect to the true lenght (top plots) and to the true momentum (bottom plots) of the objects in ECal, plots at right correspond to a zoom at the lower values. It is shown only for the Downstream ECal detector.

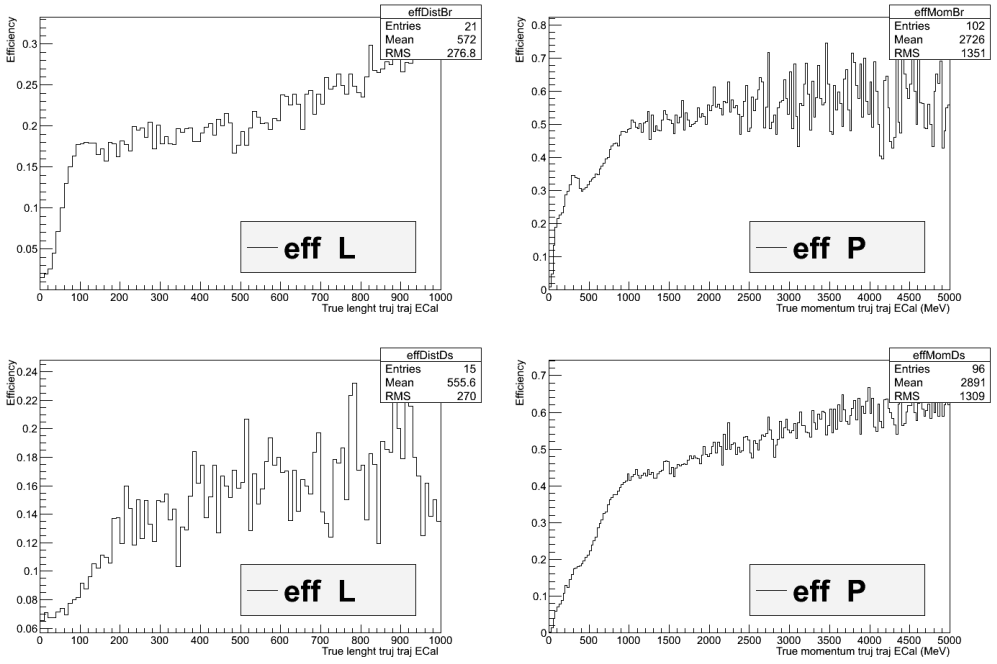

FIGURE B.5: Efficiency on reconstruct an ECal object with respect of the true lenght (left plot) and momentum (right plot) of the ECal object. Top plots corresponds to the Barrel and the bottom ones corresponds to the Dowstream.

Final results obtained for the correction factor that has to be applied for the systematic propagations are shown in Table B.3. It is shown the efficiency value in Monte Carlo using as sample on which to propagate the systematic a ν_μ CC inclusive selection in FGD1 [1].

	Efficiency correction factor
Barrel	1.1
Downstream	3.0

TABLE B.3: Correction factor (efficiency for MC in the ν_μ CC inclusive sample in FGD1) to be applied to the efficiencies obtained from control samples.

Finally we show in Figure B.6 the resulting ECal shower reconstruction systematic once it has been propagated into the ν_μ CC inclusive sample (see Chapter 5). It is show in the muon momentum distribution for the absolute and relative error (respect to the muon momentum) values.

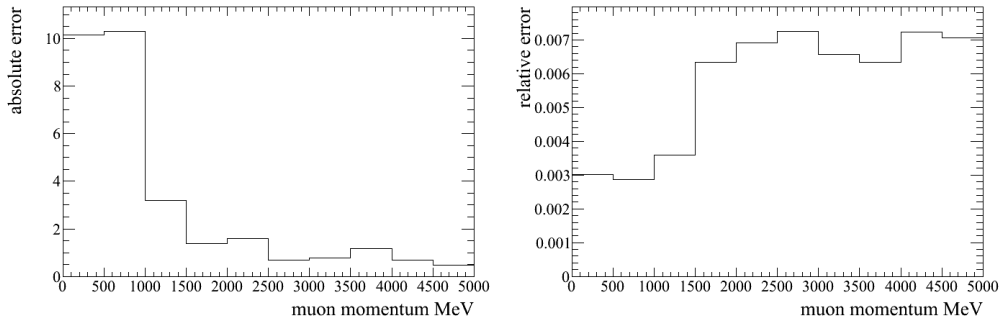

FIGURE B.6: Efficiency on reconstruct an ECal object with respect of the true lenght (left plot) and momentum (right plot) of the ECal object. Top plots corresponds to the Barrel and the bottom ones corresponds to the Downstream.

[1]The sample used for the estimation of these values for FGD1–based analysis are using the CC inclusive selection in FGD1 that is presented in 5. For FGD2–based analysis it is used a CC inclusive selection in FGD2 which is not presented in this thesis but the selection cuts are mostly the same except for the specific FGD2 cuts to select the interaction position in such detector.

Appendix C

ν_μ Charged current Event Displays

In this Appendix we show event displays for three events, one per each of the topologies studied in the ν_μ inclusive charged current analysis, in a few views. Following tables contain the most important kinematic and topological information relative to the different global reconstructed tracks of each events.

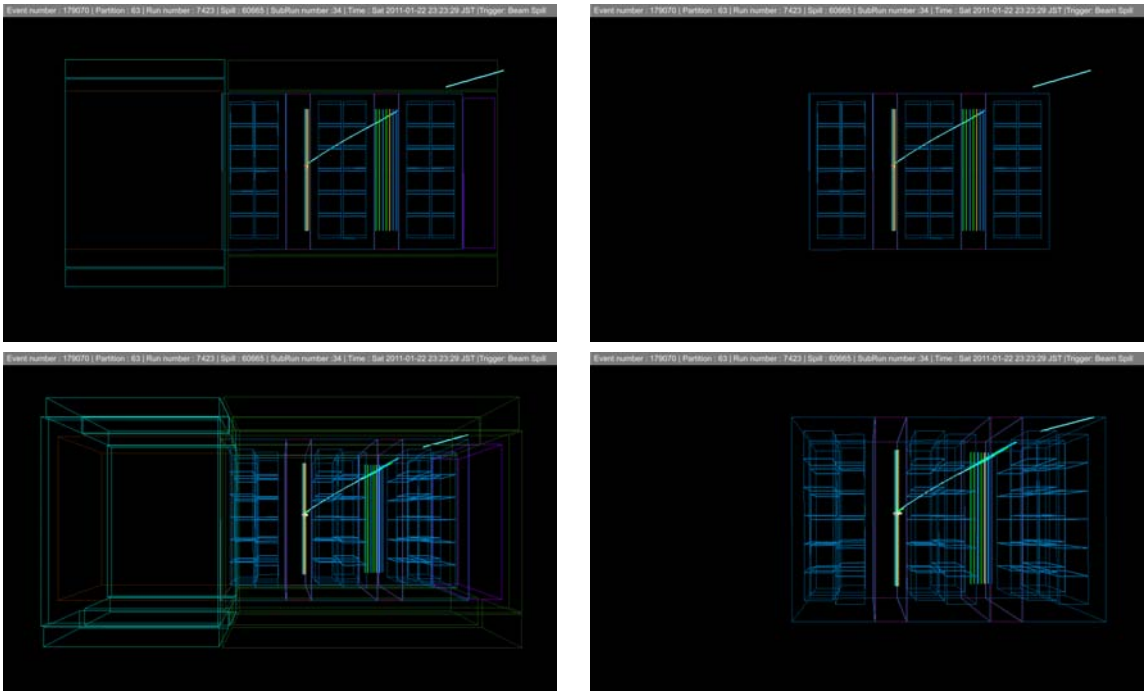

FIGURE C.1: Event display corresponding to a selected CC0π candidate with a single TPC track presented in several views: ZY (first row), XZ (second row), with all the ND280 detectors (left column) and with just the tracker (right column).

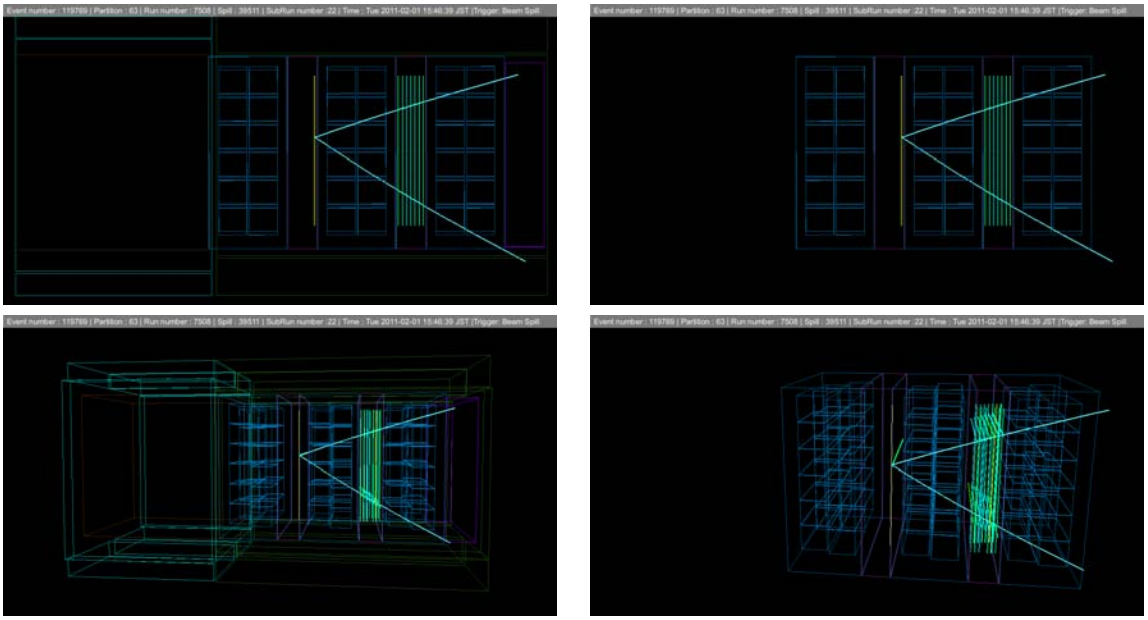

FIGURE C.2: Event display corresponding to a selected CC1π candidate with two TPC tracks, a muon and a pion candidate presented in several views: ZY (first row), XZ (second row), with all the ND280 detectors (left column) and with just the tracker (right column).

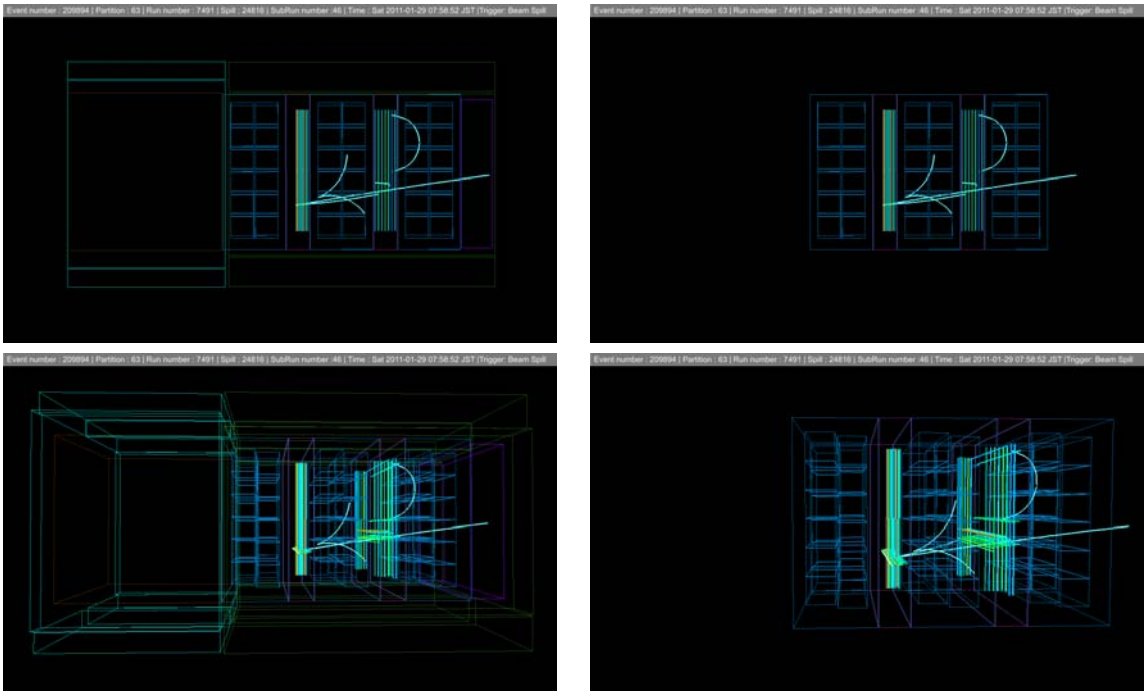

FIGURE C.3: Event display corresponding to a selected CC-Other candidate with several tracks in the event presented in several views: ZY (first row), XZ (second row), with all the ND280 detectors (left column) and with just the tracker (right column).

CC$O\pi$					
Tracks	PID	Charge	Momentum (MeV)	Position (mm) [x,y,z]	Direction [x,y,z]
track 0	Muon	-1	602.91	125.38, 115.31, 388.80	0.238, 0.565, 0.790

TABLE C.1: Kinematical and topological information on the global reconstructed track of CC0π event.

CC1π					
Tracks	PID	Charge	Momentum (MeV)	Position (mm) [x,y,z]	Direction [x,y,z]
track 0	Muon	-1	2790.09	-789.17, 213.83, 433.3	-0.06, 0.324, 0.944
track 1	Muon	1	2254.26	-789.1, 216.75, 433.3	0.187, -0.538, 0.822

TABLE C.2: Kinematic and topological information on the global reconstructed tracks of CC1π event.

CC-Other					
Tracks	PID	Charge	Momentum (MeV)	Position (mm) [x,y,z]	Direction [x,y,z]
track 0	Muon	1	767.81	-261.49, -478.22, 255.30	0.669, 0.042, 0.742
track 1	Electron	1	52.01	-422.44, -365.19, 597.83	-0.472, 0.354, 0.808
track 2	Electron	-1	43.94	-423.59, -362.21, 597.83	-0.358, 0.249, 0.900
track 4	Electron	1	30.47	-338.44, 43.65, 1803.24	-0.308, 0.204, 0.929
track 5	Electron	-1	47.17	-798.02, 902.14, 1741.19	0.559, -0.052, 0.827
track 6	Pion	1	1080.84	740.52, -134.81, 1479.94	0.615, -0.070, 0.785
track 7	Muon	-1	3055.5	-251.06, -484.25, 255.30	-0.165, 0.172, 0.971

TABLE C.3: Kinematic and topological information on the global reconstructed tracks of CC-0thers event.

Appendix D

Robustness and Consistency of the Unfolding Method

In this appendix we show the results on the different test performed on the unfolding method in order to proof the robustness and validity of the measurements. All these tests have been done with fake data, i.e. Monte Carlo scaled to the PoT data, with different samples. The fake data sets used are:

1. Nominal NEUT MC. Used as fake data to test pathological problems of the method. We use the $CC\pi^+$ selection and the sidebands in the NEUT nominal MC.
2. GENIE MC. Used as fake data. It is unfolded using NEUT and we try to recover the model.
3. NEUT MC with increased CCOther background by a 50%. We keep signal and other backgrounds as it was. With this sample we pretend to try effectiveness of sidebands controlling the CCOther background which is the dominating one.
4. NEUT MC with modified weigths on the interaction types. Events are re-weighted as a function of their interaction type ($w_{CCQE} = 2.$, $w_{RES} = 0.5$, $w_{COH} = 0.5$, $w_{DIS} = 2.$).

For simplicity we only do these studies using one of the measurements, $d\sigma/dp_\mu$.

The different studies performed are:

1. Studies done to obtain the proper number of iterations that we apply in the unfolding method.

2. The normalization constants calculated for the background subtraction and the residuals obtained.

3. The values of each systematical error spplited by shape and normatization factors.

4. Results of the differential cross section when using the background subtraction or the purity correction.

D.1 Number of Iterations

We check the number of iterations required using the fake data samples described previously. We check the different behaviour at each iteration of the following quantities:

1. the quadratic sum of the total data and MC statistical errors. This quantity does not take into account the bin to bin statistical and systematic correlation error.

2. the bias of the differential cross section value at each bin defined as:

$$Bias = \frac{x^i_{UNFOLD} - x^i_{TRUTH}}{x^i_{UNFOLD}} \tag{D.1}$$

   being x^i the differential cross section in bin i;

3. the χ^2 of the change between iterations as:

$$\chi^2 = \sum_i^{allbins} \frac{(x^i_N - x^i_{N-1})^2}{(\sigma^i_N)^2} \tag{D.2}$$

   x^i_N is the differential cross section in bin i eveluated with N iterations and σ^i_N is the statistical error associated. This quantity does not apply the bin to bin statistical and systematic correlation error.

In case of no iteration (i.e. we consider that true is equal to reco) we apply an efficiency correction to each bin.

D.1.1 Nominal NEUT MC

In case of the Nominal NEUT, Figures D.1 D.2 D.3 show the test quantities. We use all NEUT statistics to unfold (true values) and only MC NEUT Run 4 as fake data. This way, we minimize the statistical fluctuation contribution to the check. Figures show the total statistical error, the bias and χ^2 of the change between iterations.

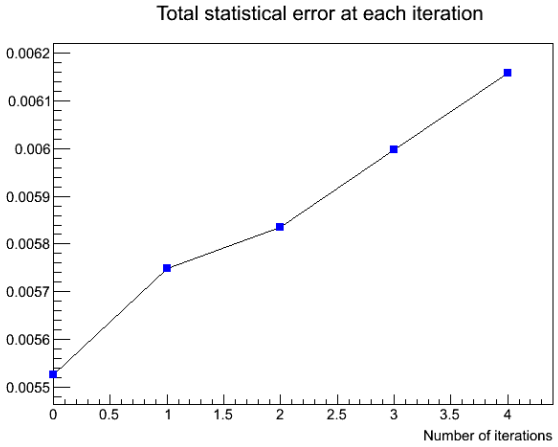

FIGURE D.1: Distribution by number of iterations on statistical errors of the diferential cross section.

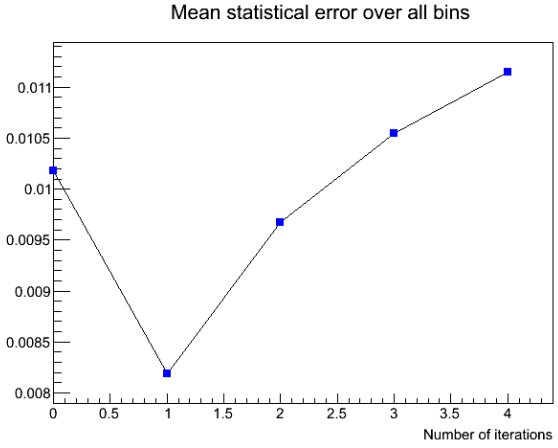

FIGURE D.2: Distribution by number of iterations on mean bias of the unfolded respect to the truth cross section.

Plots suggest that the optimal number of iterations is 1. As much iterations we apply, we get bigger statistics uncertainties. And with 1 iteration we already recover the model. The bin to bin error correlation increases with the number of iterations for its statistical part and the fake data is equal to the training sample.

We also perform exactly the same check but without applying background subtraction with sidebands. We want to see wich is the effect of the sidebands in our analysis. We see results of this check on Figures D.4 D.5 D.6. Using all NEUT statistics for training and only MC NEUT Run 4 as fake data. In the figures there are shown the total statistical error, the bias and χ^2 of the change between iterations.

From Figure D.4 we observe that not using sidebands to subtract the background reduces a bit statistical errors, as we see from the first iteration bin. On next iterations statitical

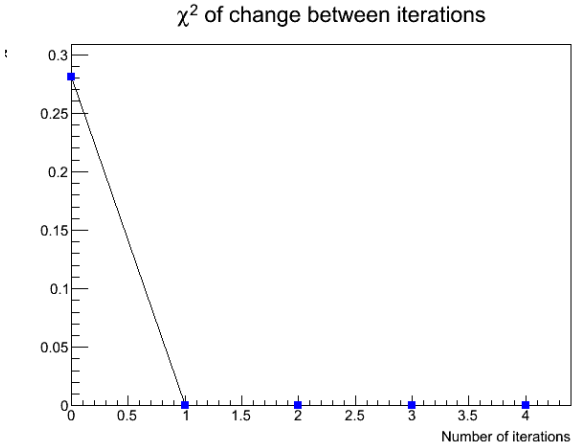

FIGURE D.3: Distribution by number of iterations on the χ^2 distribution of the different values of the cross section respect to previous iteration.

errors increases as the case of using sidebands. But the mean error value increases also a bit when no using sidebands. Seems that differences of true vs unfolding result prefers the use of sidebands, taking into account that statistical uncertainty will increase a bit.

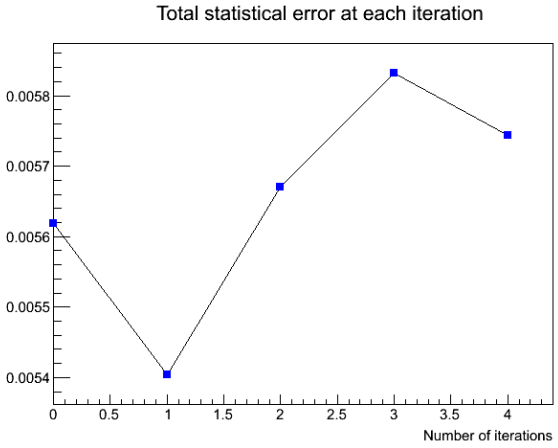

FIGURE D.4: Distribution by number of iterations on statistical errors of the diferential cross section.

In Figure D.7 we can see the differential cross section result on p_μ when using the nominal NEUT with run 4 as fake data and unfold using the all the run periods of the nominal NEUT and 1 iteration, with sidebands.

D.1.2 GENIE MC fake data

Figures D.8 D.9 D.10 show the checked quantities when using NEUT for unfold and GENIE as fake data. Figures show the total statistical error, the bias and χ^2 of the change between iterations.

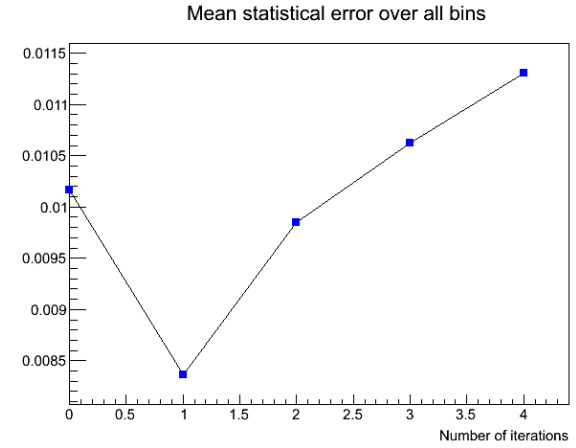

FIGURE D.5: Distribution by number of iterations on mean bias of the unfolded respect to the truth cross section.

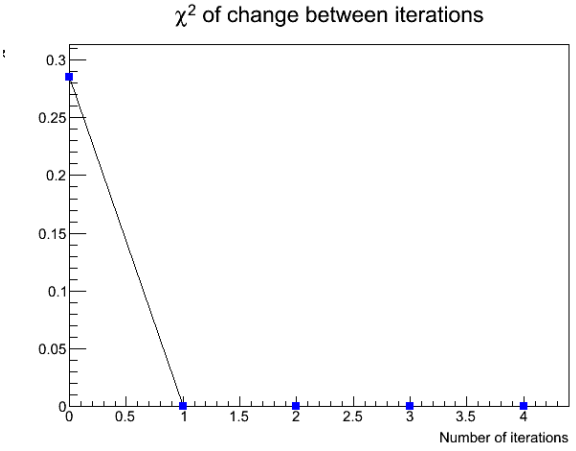

FIGURE D.6: Distribution by number of iterations on the χ^2 distribution of the different values of the cross section respect to previous iteration.

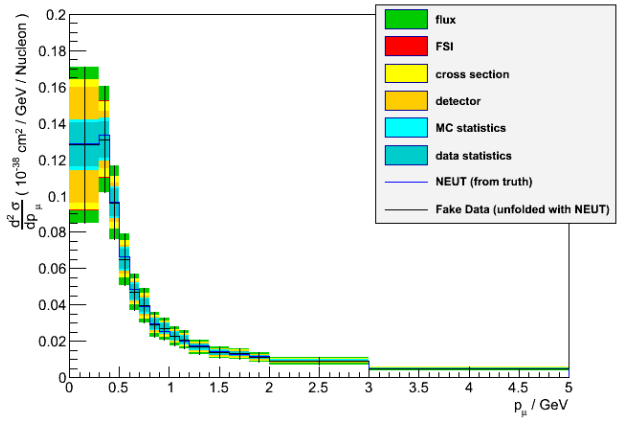

FIGURE D.7: Differential cross section results on p_μ when using the nominal NEUT with run 4 as fake data and unfold using all the run periods of the nominal NEUT, with sidebands. With 1 iteration

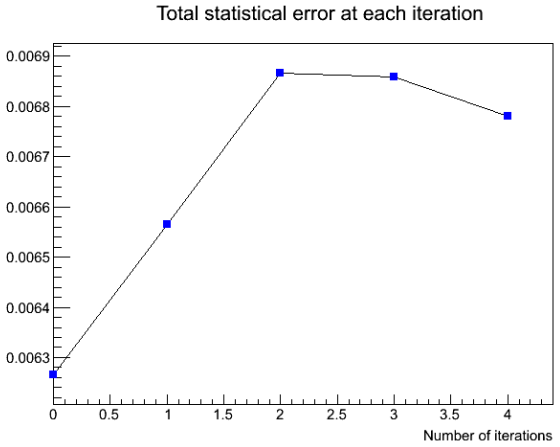

FIGURE D.8: Distribution by number of iterations on statistical errors of the diferential cross section.

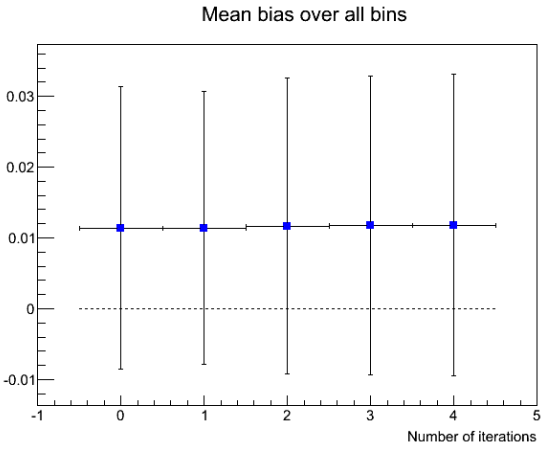

FIGURE D.9: Distribution by number of iterations on mean bias of the unfolded respect to the truth cross section.

Plots suggest that 1 iteration is again the optimal number. As much iterations we apply, we get bigger statistics uncertainties. And with 1 iteration we already recover the model. This is a bit more significant check since the GENIE fake data does not need to be equal to the NEUT prediction.

D.1.3 NEUT MC with increased CCOther fake data

The third case uses the NEUT MC with increasing a 50% the CCOther contamination. This test tries to check if the sidebands can recover the signal. Figures D.11 D.12 D.13 show the total statistical error, the bias and χ^2 of the change as function of the number of iterations.

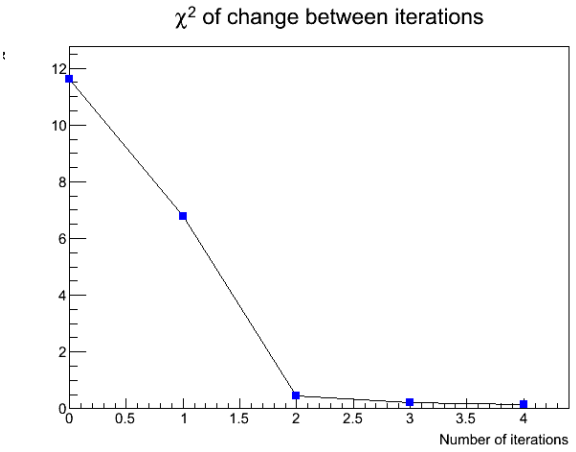

FIGURE D.10: Distribution by number of iterations on the χ^2 distribution of the different values of the cross section respect to previous iteration.

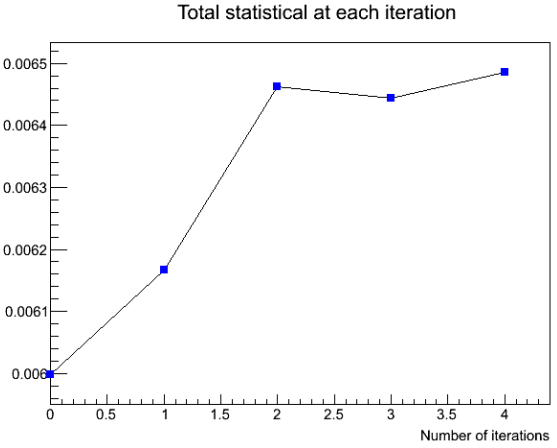

FIGURE D.11: Distribution by number of iterations on statistical errors of the differential cross section.

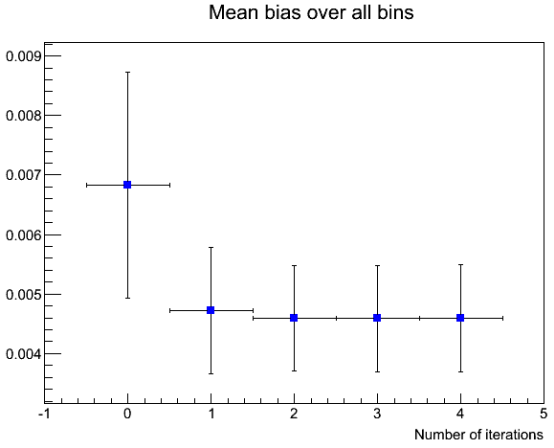

FIGURE D.12: Distribution by number of iterations on mean bias of the unfolded respect to the truth cross section.

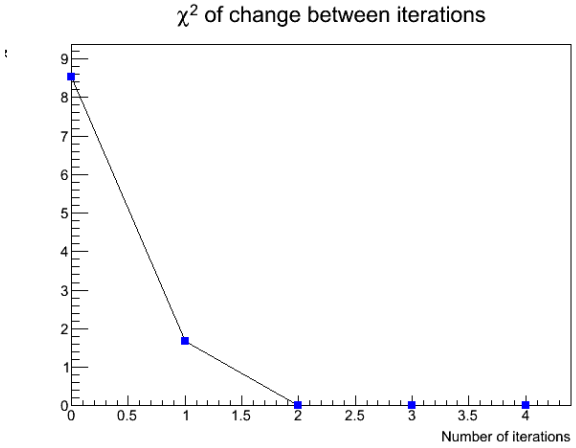

FIGURE D.13: Distribution by number of iterations on the χ^2 distribution of the different values of the cross section respect to previous iteration.

We see that 1 iteration is enough to recover the signal with small bias. In this case we see that the mean error value is a bit bigger than case of fake data with nominal NEUT.

As in the other cases, we see how statistical errors increase at each iterations.

In Figure D.14 we can see the differential cross section result on p_μ when using the NEUT sample with increased CCOther signal as fake data and unfold using the nominal NEUT and 1 iteration.

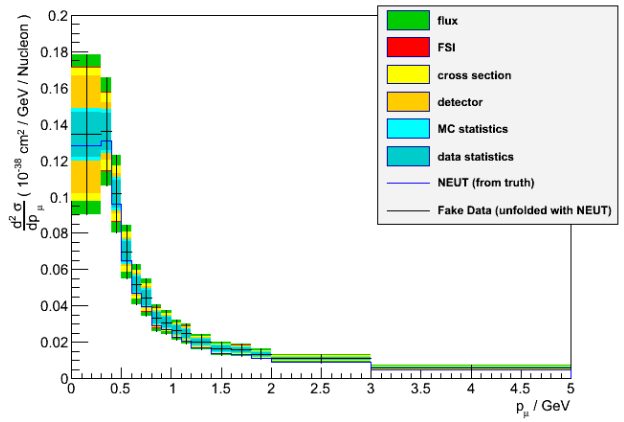

FIGURE D.14: Differential cross section results on p_μ when using the NEUT sample with increased CCOther signal as fake data and unfold using the nominal NEUT and 1 iteration.

D.1.4 NEUT MC with modified weigths on interaction types

The last case uses the NEUT MC with modifying the weigths on the interaction types is used as fake data. This test tries to check that the unfolding method can recover a very different signal form the one used for training (nominal MC). Figures D.15 D.16 D.17

show the total statistical error, the bias and χ^2 of the change as function of the number of iterations.

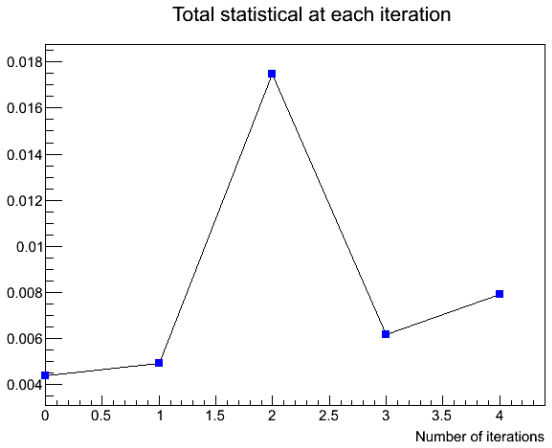

FIGURE D.15: Distribution by number of iterations on statistical errors of the differential cross section.

We see that with 2 iterations we recover the signal but the statistical error increses more than 4 times. One iteration gives us an small increase of statistical error and the recoveing of the signal is not bad at all.

In general we see a good recovering of the signal by appying one iteration for all the fake data studies. In the most difficult one, in this last case, we can recover quite well the signal at one iteration while we totally recover with 2 iterations. Nevertheless, statistical errors increases significantly for all cases when we increase the number of iterations. We can conclude with all these tests that the proper number of iterations is 1.

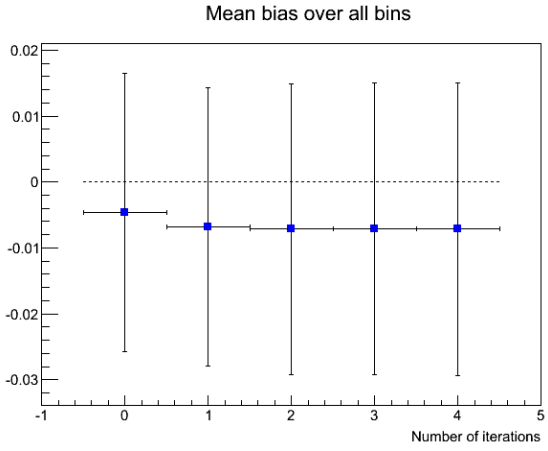

FIGURE D.16: Distribution by number of iterations on mean bias of the unfolded respect to the truth cross section.

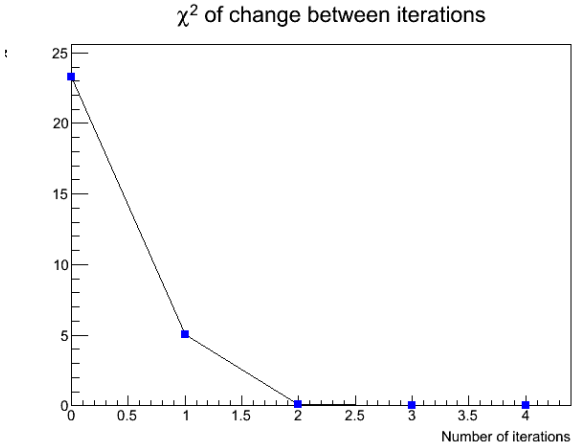

FIGURE D.17: Distribution by number of iterations on the χ^2 distribution of the different values of the cross section respect to previous iteration.

In Figure D.18 we can see the differential cross section result on p_μ when using the NEUT sample with modifying the weigths on the interaction types as fake data and unfold using the nominal NEUT and 1 iteration.

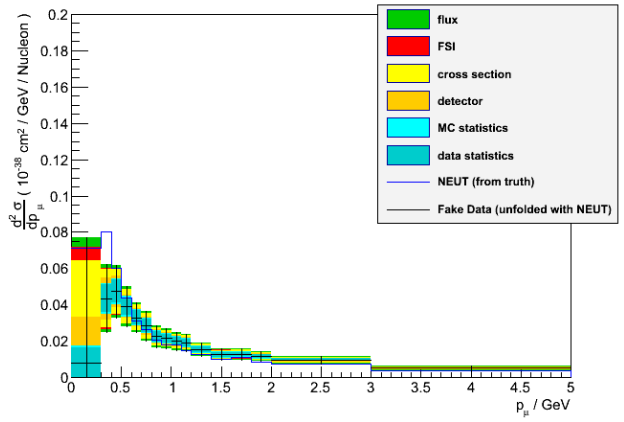

FIGURE D.18: Differential cross section results on p_μ when using the NEUT sample with modifying the weigths on the interaction types as fake data and unfold using the nominal NEUT and 1 iteration.

D.2 Control Sample Normalization Constant

The α_k coeficients that are used to subtract the background are evaluated before the unfolding is perform and they are computed for each sideband. Table D.1 shows the value of these coeficients for each sideband using the different fake data sets already described.

Sample	$\alpha_{CC0Pi1P}$
NEUT Nominal	1
GENIE	1.07388
Increased CCOther	1.07388
NEUT weigths interaction	1.12187
Sample	$\alpha_{ControlA}$
NEUT Nominal	1
GENIE	1.3093
Increased CCOther	1.3093
NEUT weigths interaction	1.32853
Sample	$\alpha_{ControlB}$
NEUT Nominal	1
GENIE	1.3093
Increased CCOther	1.34488
NEUT weigths interaction	1.7786

TABLE D.1: Value of the α coeficients for each sideband when using the different fake data tests.

D.2.1 Residuals distributions on the control sample normalization constant

We show the distribution of the residuals for each sideband at each fake data test. The residuals are defined as:

$$Residual = \frac{\alpha_k - \alpha_{norm}}{\alpha_{norm}} \tag{D.3}$$

with α_k as the value of the coeficient for the pseudo–experiment k and α_{norm} is the sideband coeficient for the nominal distributions. We have separe residuals for each uncertainty source. Each uncertainty uses 2000 pseudo-experiments.

Figures D.19, D.20, D.21 show the residuals distributions for the nominal NEUT sample for the 3 different sidebands.

Figures D.22, D.23, D.24 show the residuals distributions for the GENIE sample for the 3 different sidebands.

Figures D.25, D.26, D.27 show the residuals distributions for the increased CCOther sample for the 3 different sidebands.

Figures D.28, D.29, D.30 show the residuals distributions for the reweigthed interaction type values sample for the 3 different sidebands.

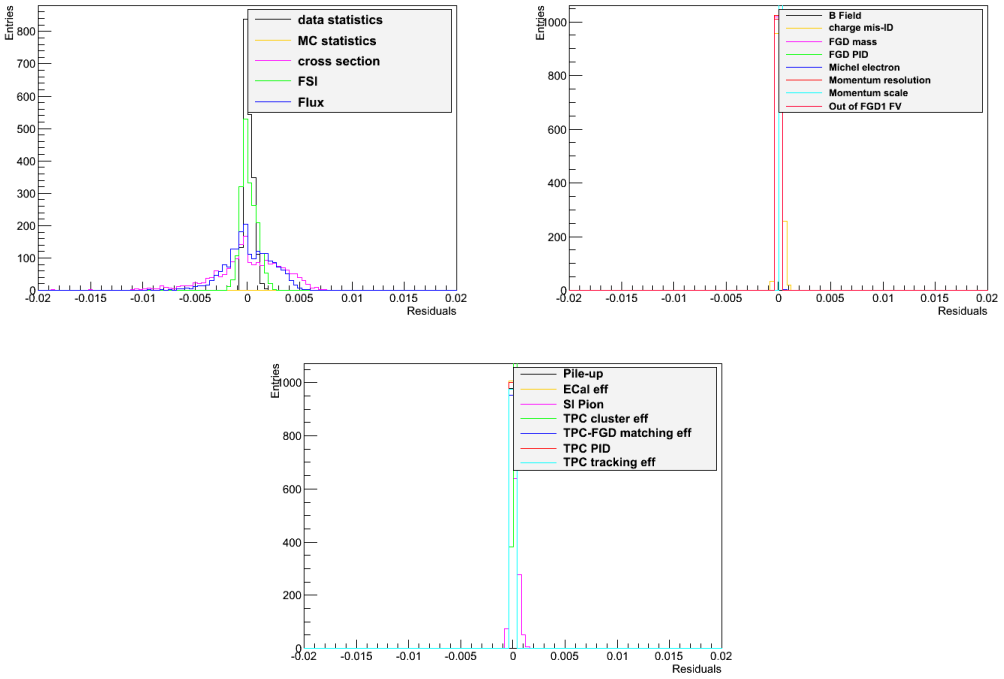

FIGURE D.19: Residuals for the nominal NEUT fake data sample separing by uncer-atinty type. For the CC0Pi1P sideband.

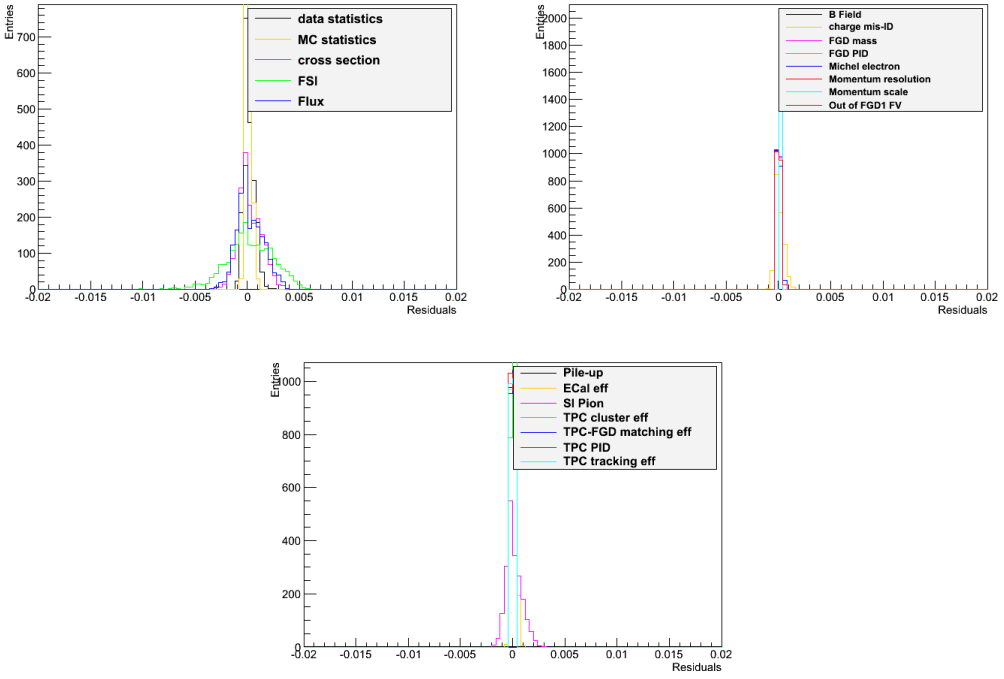

FIGURE D.20: Residuals for the nominal NEUT fake data sample separing by uncer-atinty type. For the Control A sideband.

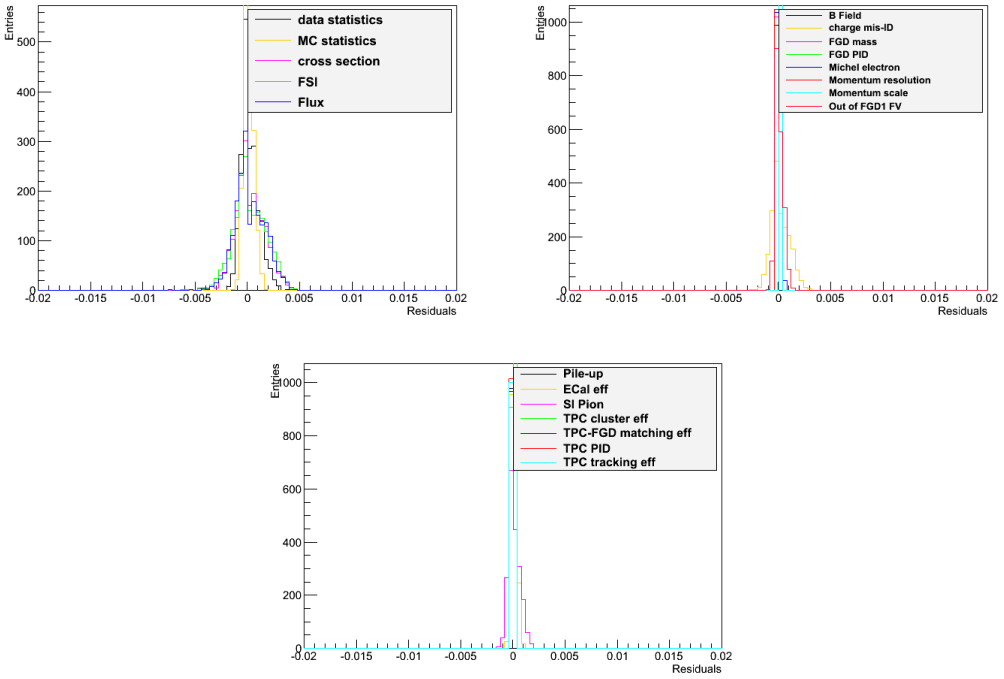

FIGURE D.21: Residuals for the nominal NEUT fake data sample separing by uncer-atinty type. For the Control B sideband.

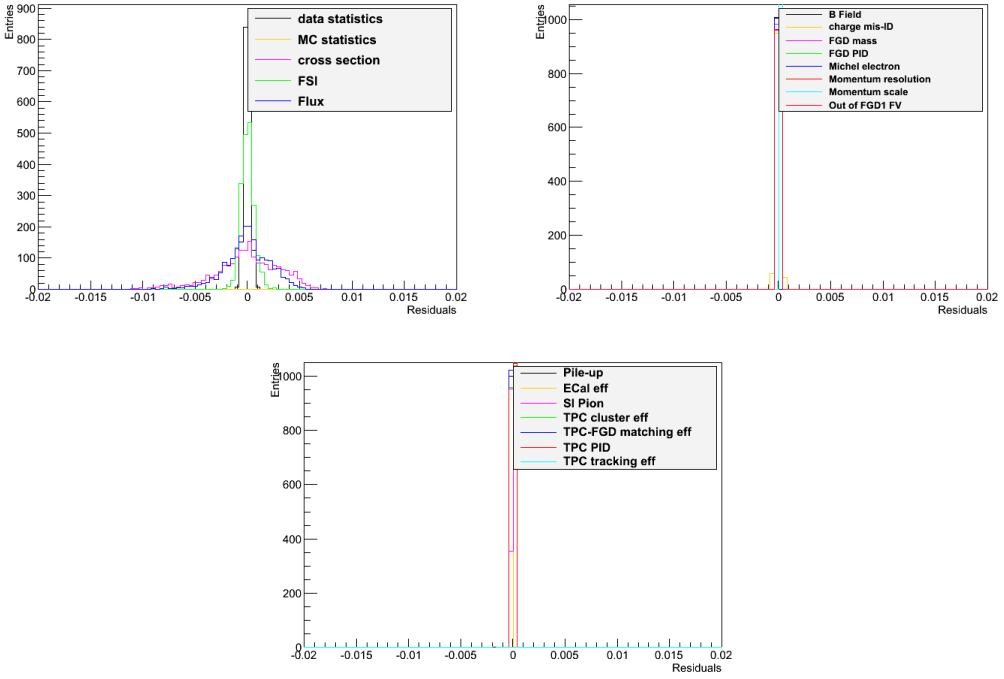

FIGURE D.22: Residuals for the GENIE fake data sample separing by unceratinty type. For the CC0Pi1P sideband.

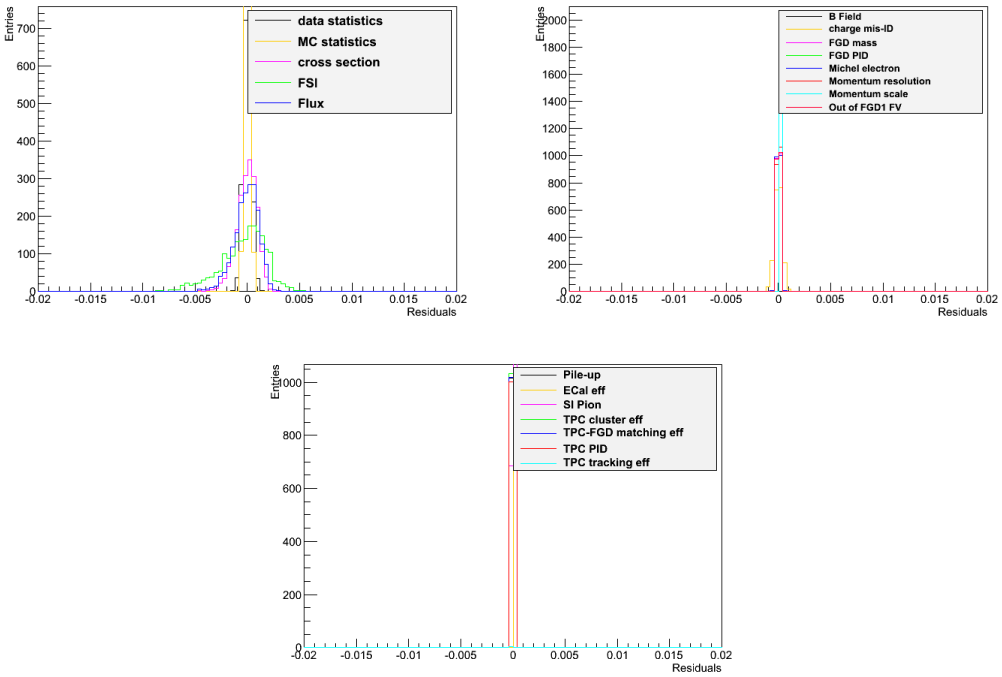

FIGURE D.23: Residuals for the nominal GENIE fake data sample separing by uncertainty type. For the Control A sideband.

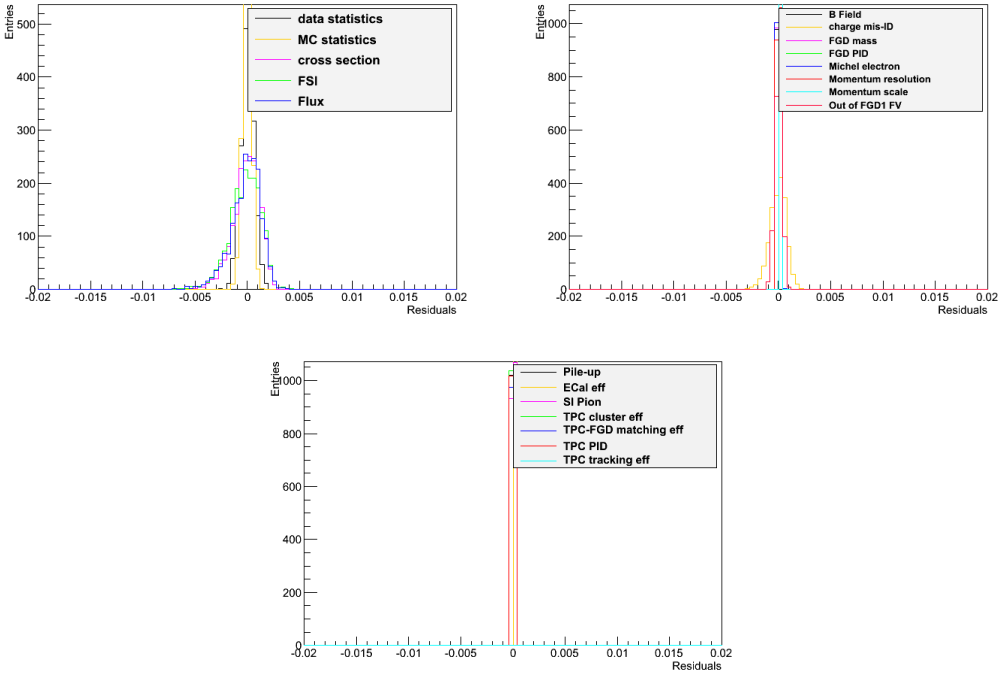

FIGURE D.24: Residuals for the nominal GENIE fake data sample separing by uncertainty type. For the Control B sideband.

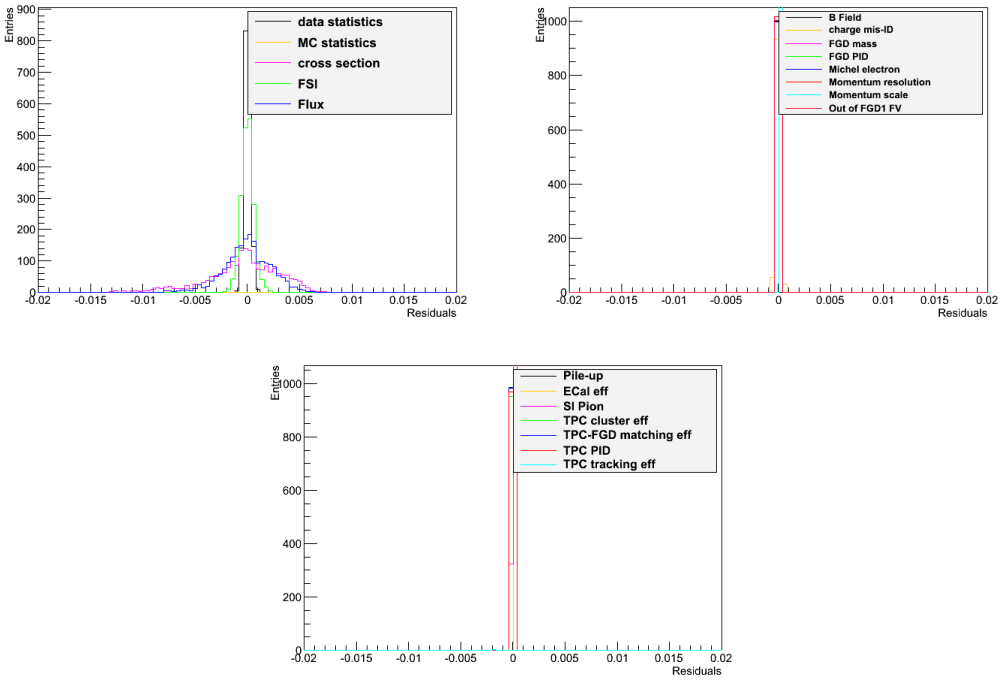

FIGURE D.25: Residuals for the increased CCOther fake data sample separing by unceratinty type. For the CC0Pi1P sideband.

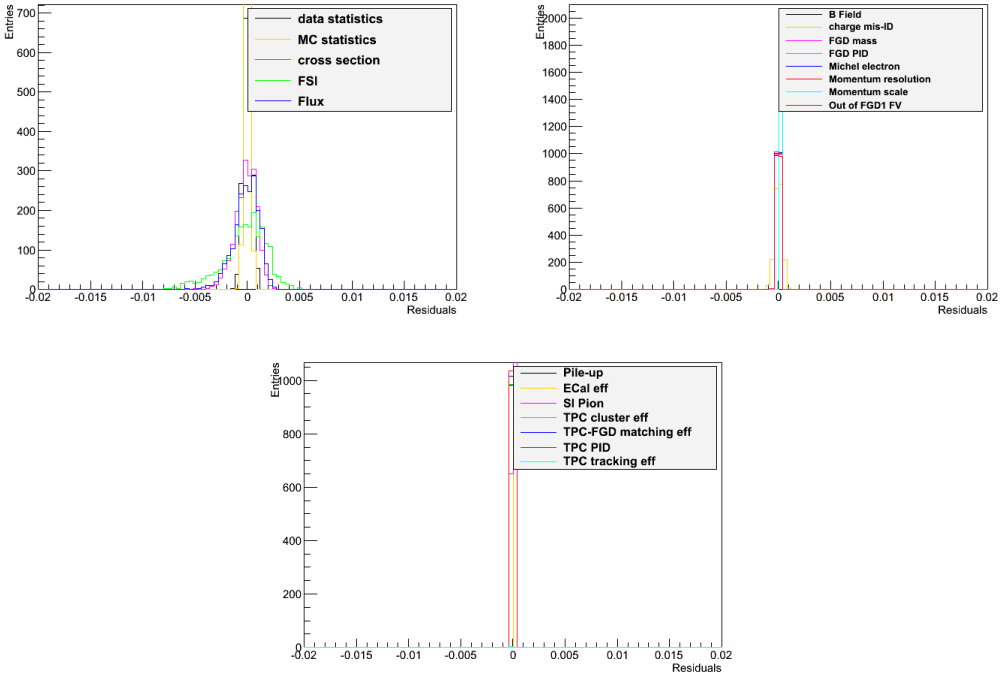

FIGURE D.26: Residuals for the increased CCOther fake data sample separing by unceratinty type. For the Control A sideband.

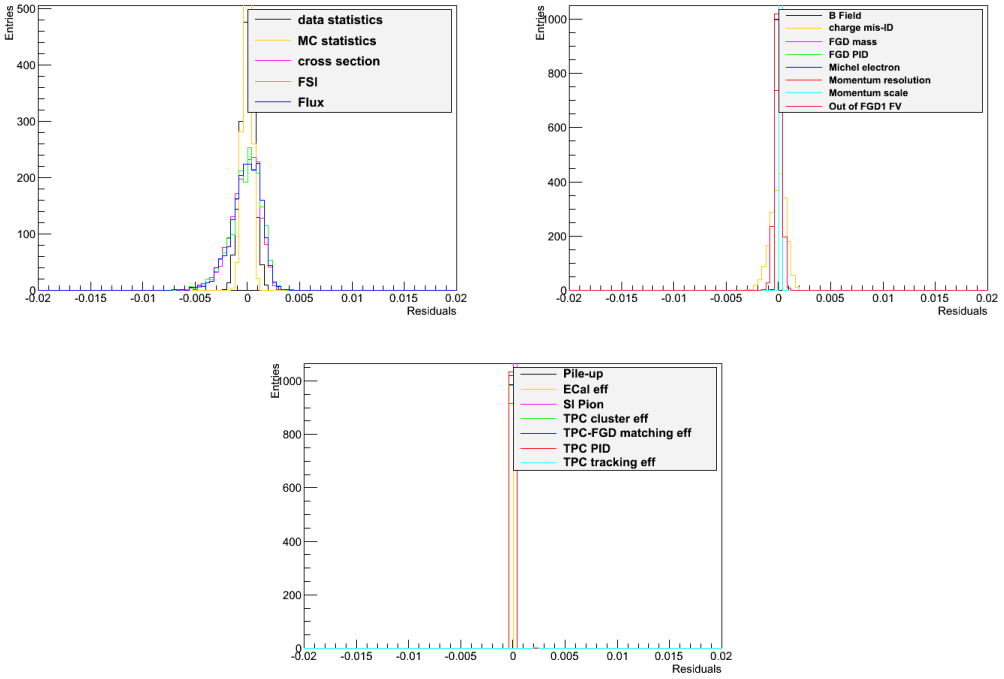

FIGURE D.27: Residuals for the increased CCOther fake data sample separing by unceratinty type. For the Control B sideband.

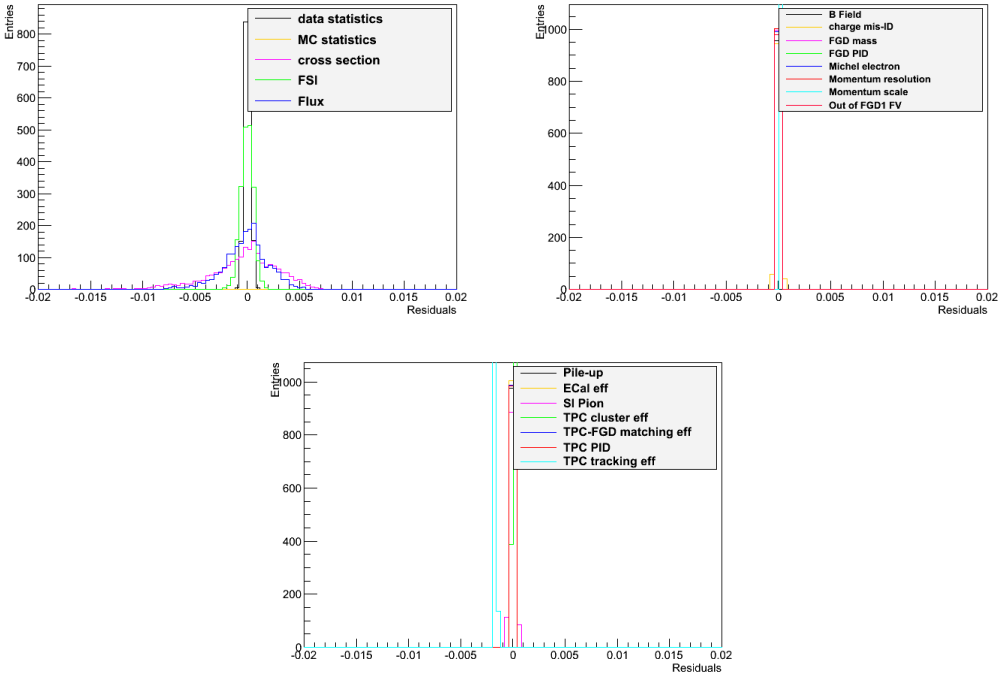

FIGURE D.28: Residuals for the reweigthed interaction type values fake data sample separing by unceratinty type. For the CC0Pi1P sideband.

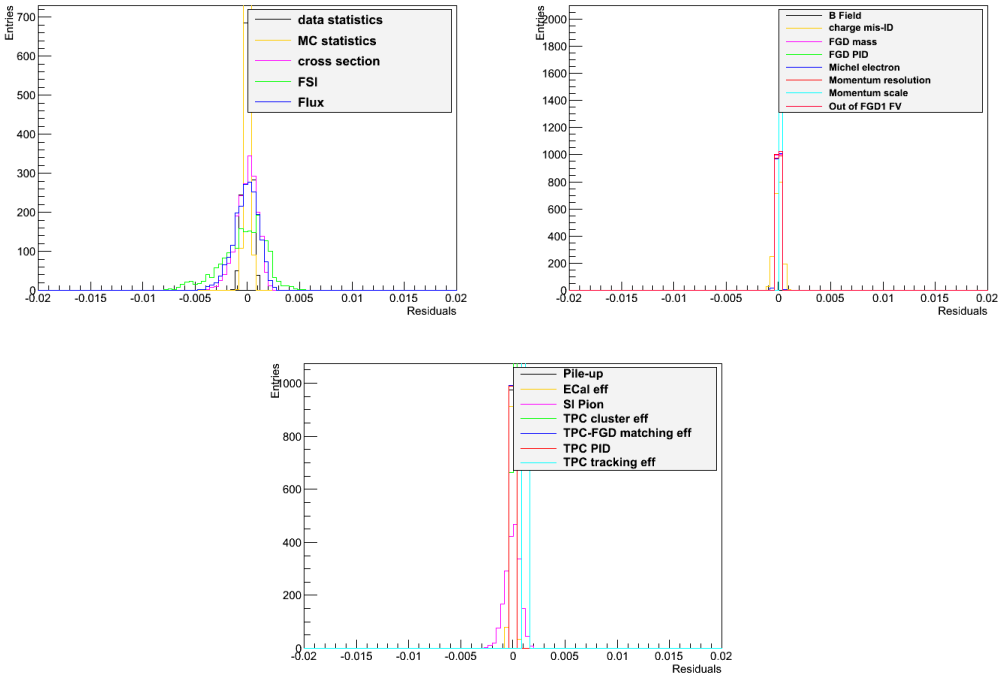

FIGURE D.29: Residuals for the reweigthed interaction type values fake data sample separing by unceratinty type. For the Control A sideband.

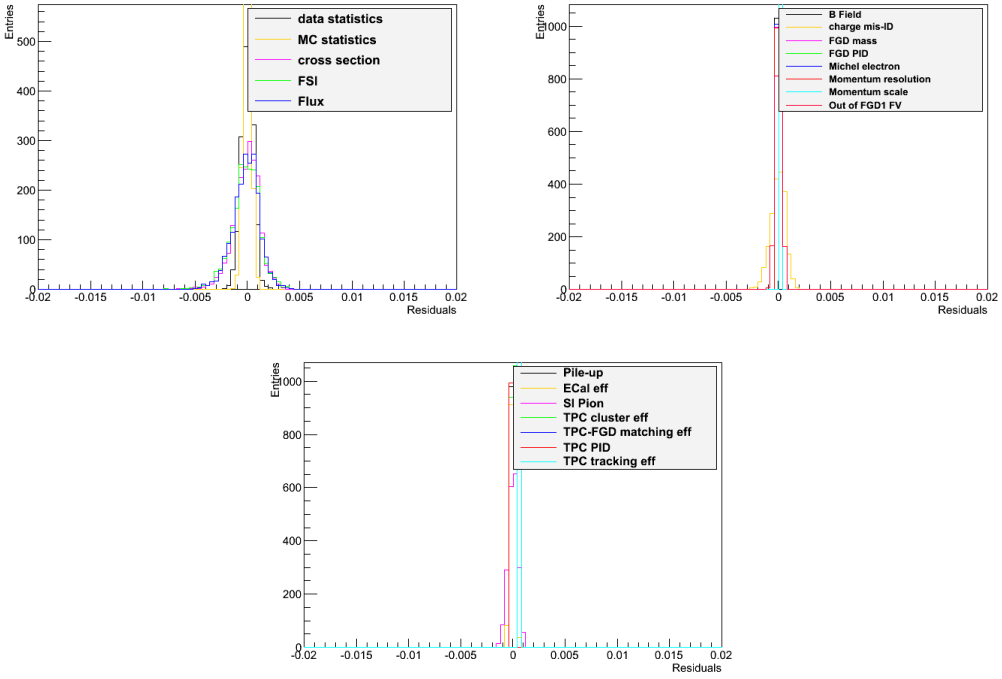

FIGURE D.30: Residuals for the reweigthed interaction type values fake data sample separing by unceratinty type. For the Control B sideband.

D.3 Shape and normalization errors with/without sidebands

Here we show the differences in the shape and normalization uncertainties when we use or not the sidebands to subtract the contamination.

In this test we use the nominal NEUT fake data. To evaluate the shape-only covariance matrix. The cross section distribution for each pseudo-experiment has been scaled to have the same integral as the nominal distribution:

$$V_{ij}^{shape} = \frac{1}{N}\sum_{s_n=1}^{N}\left(\frac{\sigma_{total}^{norm}}{\sigma_{total}^{s_n}}\sigma_i^{s_n} - \sigma_i^{norm}\right)\left(\frac{\sigma_{total}^{norm}}{\sigma_{total}^{s_n}}\sigma_j^{s_n} - \sigma_j^{norm}\right) \tag{D.4}$$

Normalization error is inferred from the total error by subtracting the shape-only value.

Table D.2 shows the relative error of the shape-only uncertainties when using or not sidebands. On Table D.3 only the normalization part is showed.

Source	with sidebands	without sidebands
XSection parameters	0.0013%	0.0016%
FSI	$3.5e-05$%	$3.2e-05$%
Flux	0.0024%	0.0026%
B-Field	$3e-06$%	$6.8e-06$%
Charge confusion	$1.6e-05$%	$1.5e-05$%
FGD mass	0.00017%	0.00018%
FGD PID	0.00011%	0.00011%
Michel syst.	0.00021%	0.00022%
Momentum resolution	0.0018%	0.0018%
Momentum scale	$6e-06$%	$7.2e-06$%
OOFV	0.0002%	0.00019%
Pile-up	$3.7e-12$%	$3.6e-12$%
ECal efficiency	0.00076%	0.0008%
SI Pion	$7.3e-06$%	$7.6e-06$%
TPC cluster efficiency	0.0005%	0.0005%
TPC-FGD matching efficiency	$8.1e-05$%	$8e-05$%
TPC PID	2.3%	2.419%
TPC tracker efficiency	0.13%	0.1076%

TABLE D.2: Fractional errors for the shape uncertainties in the total cross section when unfolding on $d\sigma/dp_{mu}$ and using nominal NEUT as fake data.

Source	with sidebands	without sidebands
XSection parameters	0.011%	0.013%
FSI	0.0023%	0.0025%
Flux	0.02%	0.022%
B-Field	0.00015%	0.00014%
Charge confusion	0.0084%	0.0095%
FGD mass	0.00092%	0.0012%
FGD PID	0.02%	0.02%
Michel syst.	0.00037%	0.00064%
Momentum resolution	0.28%	0.23.%
Momentum scale	0.00082%	0.00084%
OOFV	0.008%	0.0081%
Pile-up	0.0002%	0.00027%
ECal efficiency	0.52%	0.33%
SI Pion	0.0059%	0.0061%
TPC cluster efficiency	$negl.\%$	$negl.\%$
TPC-FGD matching efficiency	$6.1e-05\%$	$9.1e-05\%$
TPC PID	$negl.\%$	0.039%
TPC tracker efficiency	$negl.\%$	0.029%

TABLE D.3: Fractional errors for the normalization uncertainties in the total cross section when unfolding on $d\sigma/dp_{mu}$ and using nominal NEUT as fake data.

Appendix E

Additional cut on Invariant Mass

In this Appendix we show the cross section results with an additional cut applied on the selected sample: events must have $W < 1.4$ GeV.

This is presented as an additional check of the model since the Rein and Sehgal model has been traditionally understood to be valid up to $W < 1.4GeV$ (in the $\Delta(1232)$ production).

1. *Differential Cross Section on P_μ*

   Figure E.1 shows the result for the differential cross section on P_μ.

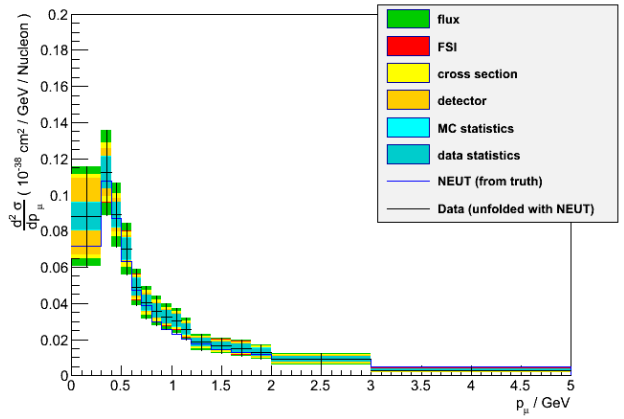

FIGURE E.1: $d\sigma/dP_\mu$ result using unfolding Bayesian method, 1 iteration.

2. *Double Differential Cross Section on $(P_\mu, cos\theta_\mu)$*

3. *Differential Cross Section on θ_π*

   Figure E.2 shows the result for the differential cross section on θ_π.

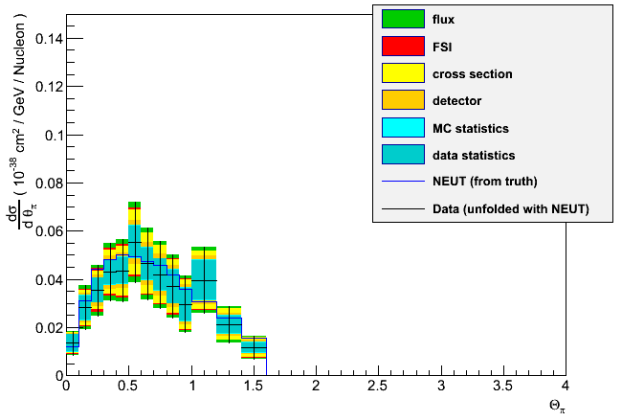

FIGURE E.2: $d\sigma/dCos\theta_\pi$ result using unfolding Bayesian method, 1 iteration.

4. *Differential Cross Section on* Q^2

   Figure E.3 shows the result for the differential cross section on Q^2.

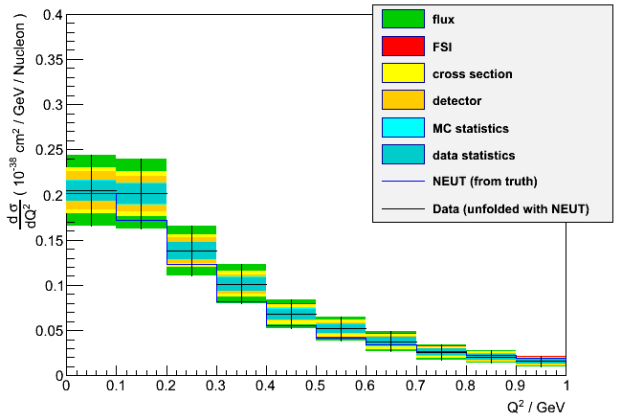

FIGURE E.3: $d\sigma/dQ^2$ result using unfolding Bayesian method, 1 iteration.

5. *Differential Cross Section on* $|Q_3|$

   Figure E.4 shows the result for the differential cross section on $|Q_3|$.

6. *Differential Cross Section on the angle between the muon and pion*

   Figure E.5 shows the result for the differential cross section on $\theta_{\mu\pi}$.

7. *Differential Cross Section on the angle* ψ_{planar}

   Figure E.6 shows the result for the differential cross section on ψ_{planar}.

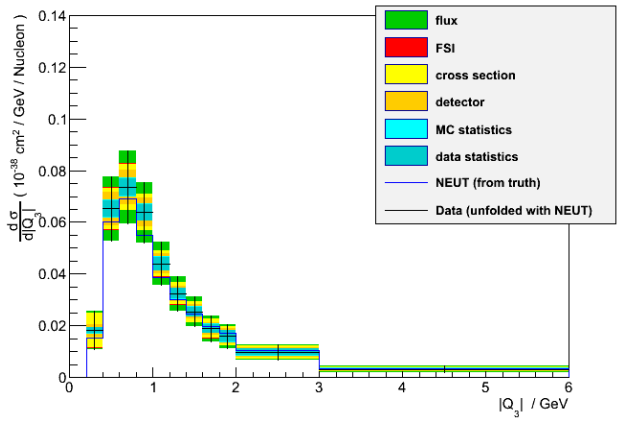

FIGURE E.4: $d\sigma/d|Q_3|$ result using unfolding Bayesian method, 1 iteration.

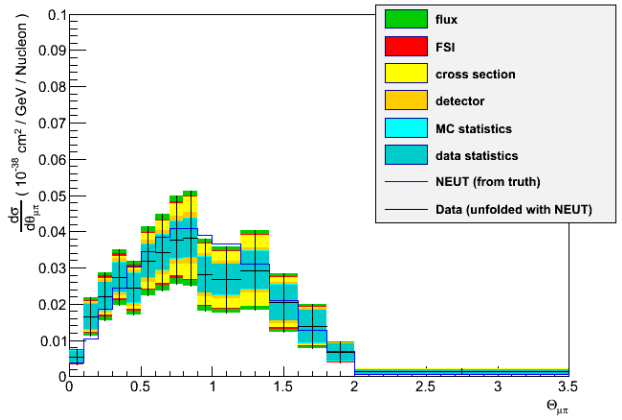

FIGURE E.5: $d\sigma/d\theta_{\mu\pi}$ result using unfolding Bayesian method, 1 iteration.

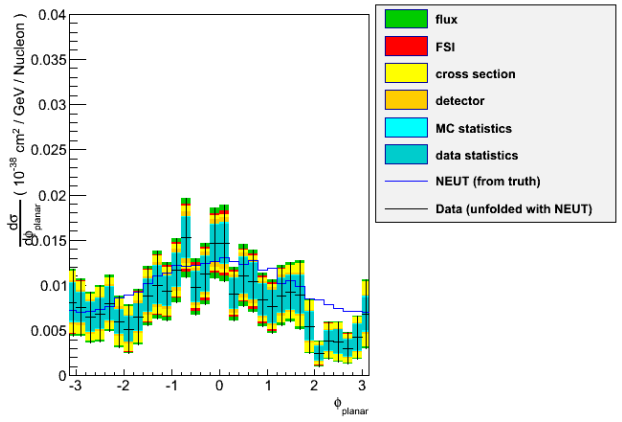

FIGURE E.6: $d\sigma/d\psi_{planar}$ result using unfolding Bayesian method, 1 iteration.

Appendix F

Cross Section Results by Bin

F.1 Differential Cross Section on P_μ and Double Differential Cross Section on $(P_\mu, Cos\theta_\mu)$

For the differential cross section on P_μ the binnning used in the measurement is:

$\{0.0, 0.3, 0.4, 0.5, 0.6, 0.7, 0.8, 0.9, 1., 1.1, 1.2, 1.4, 1.6, 1.8, 2., 3., 5., 50.0\}$

Table F.1 shows the bin order, the cross section value and error values splited by statistical, cross section parameters, FSI, flux and detector uncertainties at each bin.

bin Value	Data Stats.	Statistics Data	Statistics MC	Cross section param. error	FSI	Flux	Detector
1	0.0848	0.00735	0.0024	0.00886	0.00219	0.0144	0.0166
2	0.105	0.00842	0.0029	0.00978	0.00321	0.0161	0.00811
3	0.0889	0.00729	0.00249	0.00778	0.00096	0.0133	0.00562
4	0.0733	0.00603	0.00217	0.00622	0.000611	0.0109	0.00428
5	0.0509	0.00454	0.00161	0.0043	0.000753	0.00764	0.00282
6	0.0373	0.00379	0.00138	0.00399	0.000779	0.00572	0.0023
7	0.0305	0.00311	0.00122	0.00292	0.000633	0.00465	0.00172
8	0.0278	0.00268	0.00109	0.00247	0.000689	0.00421	0.0014
9	0.0231	0.00239	0.000976	0.00228	0.000571	0.00356	0.00117
10	0.0194	0.00215	0.000864	0.002	0.000497	0.00299	0.00106
11	0.0177	0.00171	0.000642	0.00168	0.000443	0.00271	0.000977
12	0.0162	0.00152	0.000618	0.0014	0.000445	0.00247	0.000957
13	0.013	0.00122	0.000516	0.00129	0.00042	0.00201	0.000768
14	0.0109	0.00104	0.000432	0.00111	0.000417	0.0017	0.000702
15	0.00734	0.000672	0.000212	0.000865	0.000219	0.00117	0.000515
16	0.00337	0.000314	0.000101	0.000435	0.000117	0.000562	0.000326
17	8.34e-05	1.11e-05	3.55e-06	1.17e-05	2.6e-06	1.37e-05	1.4e-05

TABLE F.1: Cross section value and error values splited by statistical, cross section parameters, FSI, flux and detector uncertainties at each bin. When unfolding on p_μ.

For the double differential cross section, the binnning used in the measurement, for the P_μ is:

$\{0.0, 0.4, 1.2, 1.6, 2., 50.0\}$

And for the $\cos\theta_\mu$ is:

$\{0.0, 0.8, 0.85, 0.9, 1.0\}$

Table F.2 shows the bin order, the cross section value and error values splited by statistical, cross section parameters, FSI, flux and detector uncertainties at each bin.

bin Value	Data Stats.	Statistics Data	Statistics MC	Cross section param. error	FSI	Flux	Detector
1	0.1	0.00803	0.00248	0.00847	0.00253	0.0162	0.0139
2	0.118	0.0171	0.00577	0.0101	0.00315	0.0187	0.0153
3	0.0998	0.0149	0.00504	0.0124	0.00287	0.0163	0.0127
4	0.115	0.0144	0.00485	0.0153	0.00234	0.0181	0.0126
5	0.0233	0.00205	0.000657	0.00233	0.00046	0.00376	0.00153
6	0.106	0.012	0.00429	0.00864	0.00196	0.0158	0.0051
7	0.134	0.0131	0.00492	0.0109	0.0026	0.0198	0.00694
8	0.141	0.00955	0.00329	0.0114	0.00227	0.0199	0.00739
9	0.00168	0.000655	0.000209	0.000472	0.00016	0.000306	0.000227
10	0.0179	0.00829	0.00274	0.0057	0.00137	0.00306	0.00274
11	0.0415	0.0097	0.00344	0.00558	0.0024	0.00641	0.00335
12	0.12	0.0105	0.00409	0.00935	0.00184	0.0172	0.00626
13	0.000379	0.000199	7.26e-05	0.000146	7.18e-05	7.14e-05	6.7e-05
14	0.00393	0.00438	0.00153	0.0026	0.0009	0.000799	0.00122
15	0.0111	0.00705	0.00245	0.00601	0.00249	0.00204	0.00266
16	0.101	0.00884	0.00323	0.00878	0.00227	0.0149	0.0058
17	5.29e-07	5.07e-07	2.34e-07	5.99e-09	2.61e-09	1.9e-09	1.72e-07
18	-3.91e-06	3.28e-05	1.09e-05	3.59e-06	5.36e-07	9.31e-07	9.17e-06
19	-7.3e-06	6.75e-05	2.16e-05	1.57e-05	5.12e-06	4.79e-06	2.54e-05
20	0.00379	0.000262	8.17e-05	0.000429	0.000106	0.000591	0.000358

TABLE F.2: Cross section value and error values splited by statistical, cross section parameters, FSI, flux and detector uncertainties at each bin. When unfolding on $d\sigma/dP_\mu d\cos\theta_\mu$.

F.2 Differential Cross Section on P_π and on θ_π

In the differential cross section on p_π the binnning used in the measurement when using the full sample (i.e. including Michel electrons) is:

$\{0.0, 0.4, 0.5, 0.6, 0.7, 0.8, 0.9, 1., 1.1, 1.2, 1.3, 1.4, 1.6, 2., 3., 50.0\}$

Table F.3 shows the bin order, the cross section value and error values splited by statistical, cross section parameters, FSI, flux and detector uncertainties at each bin.

bin Value	Data Stats.	Statistics Data	Statistics MC	Cross section param. error	FSI	Flux	Detector
1	0.159	0.00562	0.00191	0.0107	0.00257	0.0237	0.0132
2	0.0674	0.00503	0.00176	0.00642	0.00281	0.0102	0.00471
3	0.0375	0.00366	0.00125	0.00471	0.00118	0.00588	0.00385
4	0.02	0.00254	0.000855	0.00337	0.000535	0.00328	0.00264
5	0.0169	0.00234	0.00082	0.0027	0.000575	0.00295	0.00253
6	0.0148	0.00207	0.000768	0.00189	0.000449	0.00251	0.00231
7	0.0108	0.00145	0.000621	0.0016	0.000321	0.00196	0.00167
8	0.0104	0.00135	0.000603	0.00128	0.000331	0.00195	0.00145
9	0.0102	0.00134	0.000642	0.00131	0.000224	0.00194	0.00142
10	0.00816	0.00119	0.000566	0.00122	0.000207	0.00165	0.0012
11	0.00501	0.000827	0.000404	0.00103	0.000193	0.00114	0.000729
12	0.00432	0.000794	0.000305	0.00123	0.00015	0.00108	0.000657
13	0.00217	0.000471	0.000165	0.00112	0.000105	0.000707	0.00037
14	0.00135	0.000282	9.4e-05	0.000417	0.000112	0.000382	0.000177
15	2.19e-05	5.52e-06	1.89e-06	3.39e-06	1.05e-06	3.73e-06	2.82e-06

TABLE F.3: Cross section value and error values splited by statistical, cross section parameters, FSI, flux and detector uncertainties at each bin. When unfolding on p_{pi}.

Results without the Michel electron contribution, used a binning in the measurement is:

$\{0.0, 0.2, 0.3, 0.4, 0.5, 0.6, 0.7, 0.8, 0.9, 1., 1.1, 1.2, 1.3, 1.4, 1.6, 2., 3., 50.0\}$

Table F.4 shows the bin order, the cross section value and error values splited by statistical, cross section parameters, FSI, flux and detector uncertainties at each bin.

bin Value	Data Stats.	Statistics Data	Statistics MC	Cross section param. error	FSI	Flux	Detector
1	0.0322	0.00664	0.00184	0.00567	0.00528	0.00641	0.0107
2	0.113	0.00917	0.00282	0.0084	0.00376	0.016	0.0259
3	0.0979	0.00693	0.00222	0.00791	0.00255	0.0134	0.00901
4	0.0552	0.00479	0.00153	0.00545	0.00235	0.0081	0.00451
5	0.0329	0.00365	0.00112	0.00428	0.00116	0.00513	0.00358
6	0.0182	0.00255	0.00083	0.00321	0.000405	0.00304	0.00269
7	0.0164	0.00229	0.000804	0.00267	0.000574	0.00289	0.00295
8	0.0146	0.00213	0.00077	0.00191	0.000471	0.00251	0.00261
9	0.0107	0.00148	0.000621	0.00162	0.000344	0.00198	0.0019
10	0.0103	0.00139	0.000605	0.00135	0.000324	0.00197	0.00162
11	0.0102	0.00141	0.000631	0.00135	0.000236	0.00198	0.00159
12	0.00818	0.00124	0.000558	0.00128	0.000228	0.0017	0.00132
13	0.00498	0.000865	0.000403	0.00112	0.00023	0.00121	0.000812
14	0.00432	0.000858	0.000326	0.00144	0.000195	0.0012	0.00069
15	0.00211	0.000515	0.000179	0.00138	0.000158	0.000819	0.000374
16	0.00134	0.000278	9.38e-05	0.000459	0.000125	0.000408	0.000169
17	2.19e-05	5.57e-06	1.89e-06	3.56e-06	1.16e-06	3.88e-06	3.09e-06

TABLE F.4: Cross section value and error values splited by statistical, cross section parameters, FSI, flux and detector uncertainties at each bin. When unfolding on p_{π} without Michel electrons sub-sample.

For the single differential cross section on θ_{π} the binnning used is:

$\{0.0, 0.1, 0.2, 0.3, 0.4, 0.5, 0.6, 0.7, 0.8, 0.9, 1., 1.2, 1.4, 1.6, 1.8, 2., 3.1416\}$

Table F.5 shows the bin order, the cross section value and error values splited by statistical, cross section parameters, FSI, flux and detector uncertainties at each bin.

bin Value	Data Stats.	Statistics Data	Statistics MC	Cross section param. error	FSI	Flux	Detector
1	0.0111	0.0028	0.000915	0.00184	0.000856	0.00255	0.00129
2	0.0187	0.00372	0.00112	0.00363	0.0011	0.00449	0.00305
3	0.0338	0.00413	0.00131	0.00385	0.00163	0.00626	0.0036
4	0.048	0.00458	0.00159	0.00415	0.000541	0.0081	0.00557
5	0.0431	0.00438	0.00145	0.00432	0.00115	0.00735	0.00516
6	0.0517	0.00473	0.00166	0.00411	0.00149	0.00823	0.0054
7	0.0473	0.00479	0.00164	0.00368	0.000611	0.00741	0.00549
8	0.034	0.00424	0.00133	0.00382	0.000985	0.0056	0.00397
9	0.0333	0.0044	0.00138	0.00389	0.00122	0.00525	0.00438
10	0.0312	0.00443	0.0014	0.00349	0.000631	0.00479	0.00388
11	0.0216	0.00359	0.00101	0.00277	0.000676	0.00346	0.00295
12	0.0178	0.00381	0.00115	0.00266	0.0011	0.00296	0.00231
13	0.0116	0.000778	0.000661	0.00205	0.000764	0.002	0.00167
14	0	0	1.95e-08	0	0	0	0
15	0	0	1.94e-08	0	0	0	0
16	0	0	1.94e-09	0	0	0	0

TABLE F.5: Cross section value and error values splited by statistical, cross section parameters, FSI, flux and detector uncertainties at each bin. When unfolding on θ_π.

F.3 Differential Cross Section on Momentum Transfer

In this section results for the differential cross section depending on Q^2 and on $|Q_3|$, 4-momentum and 3-momentum transfer, are shown.

F.3.1 Differential Cross Section on Momentum Transfer

The binnning used in the measurement is:

$\{0.0, 0.1, 0.2, 0.3, 0.4, 0.5, 0.6, 0.7, 0.8, 0.9, 1., 1.2, 1.4, 1.6, 1.8, 2., 50.0\}$

Table F.6 shows the bin order, the cross section value and error values splited by statistical, cross section parameters, FSI, flux and detector uncertainties at each bin.

F.3.2 Differential Cross Section on 3-momentum Mransfer

The binnning used in the measurement in the differential cross section $\frac{d\sigma}{d|Q_3|}$ is:

bin Value	Data Stats.	Statistics Data	Statistics MC	Cross section param. error	FSI	Flux	Detector
1	0.186	0.00969	0.00322	0.01	0.00203	0.0257	0.0145
2	0.182	0.00881	0.00322	0.0147	0.00224	0.0252	0.0124
3	0.129	0.00688	0.00246	0.0113	0.00156	0.0184	0.00842
4	0.0921	0.00499	0.00207	0.00847	0.00147	0.0136	0.00572
5	0.0646	0.00372	0.00166	0.00643	0.000741	0.00976	0.00388
6	0.0476	0.00287	0.00135	0.00484	0.000872	0.00733	0.00303
7	0.0366	0.00254	0.00114	0.00406	0.000901	0.00576	0.0024
8	0.0252	0.0019	0.000902	0.00343	0.000895	0.00411	0.00186
9	0.0193	0.00164	0.000791	0.00293	0.0008	0.00321	0.00151
10	0.0146	0.00149	0.000656	0.00259	0.000638	0.00249	0.00129
11	0.0103	0.00116	0.000444	0.00219	0.000586	0.00181	0.000971
12	0.00609	0.00086	0.000339	0.00171	0.000513	0.00121	0.000702
13	0.00444	0.000713	0.000288	0.00143	0.000373	0.000919	0.000527
14	0.00314	0.00058	0.000231	0.00117	0.000315	0.00071	0.000442
15	0.00212	0.000488	0.0002	0.000999	0.000223	0.000535	0.000334
16	3.81e-05	9.44e-06	2.95e-06	1.72e-05	3.22e-06	9.34e-06	5.9e-06

TABLE F.6: Cross section value and error values splited by statistical, cross section parameters, FSI, flux and detector uncertainties at each bin. When unfolding on Q^2.

$\{0.0, 0.2, 0.4, 0.6, 0.8, 1., 1.2, 1.4, 1.6, 1.8, 2., 3., 6., 50.0\}$

Table F.7 shows the bin order, the cross section value and error values splited by statistical, cross section parameters, FSI, flux and detector uncertainties at each bin.

bin Value	Data Stats.	Statistics Data	Statistics MC	Cross section param. error	FSI	Flux	Detector
1	0	0	3.23e-08	0	0	0	0
2	0.018	0.00106	0.000539	0.00615	0.00132	0.00268	0.00189
3	0.0644	0.00295	0.0012	0.00486	0.00176	0.00907	0.00522
4	0.0705	0.00305	0.00114	0.00688	0.000802	0.00978	0.00505
5	0.056	0.0025	0.00101	0.00647	0.000661	0.00776	0.00357
6	0.0363	0.00182	0.000761	0.00456	0.000468	0.00518	0.00226
7	0.028	0.00146	0.000665	0.0036	0.000291	0.00411	0.00178
8	0.0225	0.0013	0.000566	0.00298	0.000293	0.0034	0.00152
9	0.0188	0.00113	0.00051	0.0024	0.00047	0.00291	0.00128
10	0.016	0.00106	0.000466	0.00223	0.000461	0.00253	0.00111
11	0.00876	0.000622	0.000214	0.00133	0.000373	0.00147	0.000694
12	0.00247	0.000226	7.49e-05	0.000416	0.000135	0.000451	0.00023
13	6.84e-05	9.71e-06	3.22e-06	1.28e-05	4.95e-06	1.32e-05	7.72e-06

TABLE F.7: Cross section value and error values splited by statistical, cross section parameters, FSI, flux and detector uncertainties at each bin. When unfolding on $|Q_3|$.

F.4 Differential Cross Section on Invariant Mass

The binnning used in the measurement is:

$\{0.0, 1., 1.1, 1.2, 1.3, 1.4, 1.5, 1.6, 1.7, 1.8, 1.9, 2., 2.1, 2.2, 2.3, 2.4, 2.5,$
$2.6, 2.7, 2.8, 2.9, 3., 3.2, 3.4, 3.6, 3.8, 4., 50.0\}$

Table F.8 shows the bin order, the cross section value and error values splited by statistical, cross section parameters, FSI, flux and detector uncertainties at each bin.

bin Value	Data Stats.	Statistics Data	Statistics MC	Cross section param. error	FSI	Flux	Detector
2	0	0	2.03e-08	0	0	0	0
3	0.00475	0.000695	0.000616	0.000794	0.00117	0.000728	0.000673
4	0.124	0.0108	0.00446	0.0133	0.0098	0.0182	0.013
5	0.188	0.0139	0.00555	0.0141	0.0025	0.0268	0.0147
6	0.134	0.0108	0.00422	0.0116	0.00178	0.0188	0.00968
7	0.0912	0.00872	0.00348	0.00995	0.00239	0.013	0.00707
8	0.0595	0.00567	0.00243	0.00752	0.00148	0.00893	0.005
9	0.0463	0.00521	0.00222	0.00624	0.00151	0.00726	0.0043
10	0.0397	0.00473	0.00208	0.00466	0.000932	0.0064	0.00405
11	0.0256	0.00376	0.00166	0.00377	0.000768	0.00428	0.00341
12	0.0209	0.00315	0.00143	0.00273	0.000972	0.00352	0.00273
13	0.0172	0.0029	0.00137	0.0025	0.000754	0.00306	0.00221
14	0.0159	0.00225	0.0013	0.0021	0.000782	0.00274	0.00199
15	0.0173	0.00298	0.0015	0.00216	0.00137	0.00318	0.00216
16	0.0121	0.00244	0.00138	0.00181	0.000848	0.00213	0.00179
17	0.0135	0.00273	0.00143	0.00207	0.000887	0.00248	0.00217
18	0.00991	0.00208	0.00132	0.00133	0.000458	0.00191	0.00169
19	0.00938	0.00178	0.00123	0.00132	0.00141	0.00174	0.00151
20	0.00856	0.00164	0.00109	0.00111	0.000324	0.00161	0.00123
21	0.0073	0.00183	0.00108	0.00126	0.000556	0.00142	0.00119
22	0.0061	0.00142	0.00106	0.000844	0.000374	0.00108	0.00109
23	0.00495	0.00133	0.000814	0.00101	0.000545	0.000969	0.00099
24	0.00452	0.00101	0.000705	0.000797	0.000313	0.000882	0.000758
25	0.00308	0.00091	0.000571	0.000547	0.000372	0.000529	0.000505
26	0.00177	0.000493	0.00036	0.000337	0.000142	0.000301	0.000323
27	0.00121	0.000556	0.000436	0.000277	0.000249	0.000221	0.000382
28	3.67e-05	1.03e-05	4.67e-06	6.79e-06	3.38e-06	6.73e-06	5.34e-06

TABLE F.8: Cross section value and error values splited by statistical, cross section parameters, FSI, flux and detector uncertainties at each bin. When unfolding on W.

F.5 Differential Cross Section on the angle between muon and pion

The binnning used in the measurement is:

$\{0.0, 0.1, 0.2, 0.3, 0.4, 0.5, 0.6, 0.7, 0.8, 0.9, 1., 1.2, 1.4, 1.6, 1.8, 2., 3.141516\}$

Table F.9 shows the bin order, the cross section value and error values splited by statistical, cross section parameters, FSI, flux and detector uncertainties at each bin.

bin Value	Data Stats.	Statistics Data	Statistics MC	Cross section param. error	FSI	Flux	Detector
1	0.00389	0.00137	0.000461	0.000345	0.000125	0.000724	0.000457
2	0.00957	0.00216	0.00072	0.0013	0.000369	0.00181	0.00109
3	0.016	0.00265	0.000882	0.0019	0.000531	0.00285	0.00196
4	0.0223	0.00306	0.00102	0.00223	0.000611	0.00379	0.00279
5	0.0259	0.00327	0.00108	0.00294	0.000794	0.0044	0.00335
6	0.0295	0.00343	0.00114	0.00305	0.000711	0.00488	0.00345
7	0.0313	0.00362	0.0012	0.0034	0.000806	0.00529	0.00411
8	0.0351	0.00384	0.00129	0.00352	0.000856	0.00578	0.00446
9	0.0321	0.00396	0.00123	0.0035	0.000953	0.00531	0.00431
10	0.0298	0.004	0.00129	0.00383	0.000756	0.00508	0.00338
11	0.0299	0.0034	0.00103	0.00397	0.000444	0.00511	0.00346
12	0.0318	0.00371	0.00123	0.00335	0.0007	0.00508	0.00373
13	0.0194	0.00331	0.001	0.00246	0.000754	0.00321	0.00231
14	0.0104	0.00261	0.000764	0.00111	0.000327	0.00173	0.00129
15	0.0041	0.00195	0.000578	0.00061	0.00013	0.000733	0.000471
16	0.000822	0.000387	0.000134	5.76e-05	6.42e-05	0.000105	7.59e-05

TABLE F.9: Cross section value and error values splited by statistical, cross section parameters, FSI, flux and detector uncertainties at each bin. When unfolding on $\theta_{\mu\pi}$.

F.6 Differential Cross Section on ϕ_{planar}

The binnning used in the measurement is:

$\{-\pi, -2.8, -2.4, -2., -1.6, -1.2, -0.8, -0.4, 0., 0.4, 0.8, 1.2, 1.6, 2., 2.4, 2.8, \pi\}$

Table F.10 shows the bin order, the cross section value and error values splited by statistical, cross section parameters, FSI, flux and detector uncertainties at each bin.

F.7 Differential Cross Section on $Cos\theta_{planar}$

The binnning used in the measurement is:

$\{-1., -0.9, -0.8, -0.7, -0.6, -0.5, -0.4, -0.3, -0.2, -0.1, 0., 0.1, 0.2, 0.3,$
$0.4, 0.5, 0.6, 0.7, 0.8, 0.9, 1.\}$

Table F.11 shows the bin order, the cross section value and error values splited by statistical, cross section parameters, FSI, flux and detector uncertainties at each bin.

bin Value	Data Stats.	Statistics Data	Statistics MC	Cross section param. error	FSI	Flux	Detector
1	0.00698	0.000967	0.000356	0.00102	0.000208	0.00112	0.000905
2	0.00596	0.000824	0.00034	0.000805	0.000158	0.000974	0.000733
3	0.0071	0.000885	0.000307	0.000842	0.00026	0.00112	0.000845
4	0.00626	0.000841	0.000339	0.000915	0.000101	0.00111	0.000712
5	0.00709	0.000922	0.0003	0.000846	0.000114	0.00117	0.000887
6	0.00795	0.000926	0.00032	0.000848	8.81e-05	0.00127	0.000946
7	0.0077	0.000983	0.000307	0.001	0.0002	0.00131	0.000905
8	0.00843	0.00105	0.000346	0.00104	0.000303	0.00144	0.000972
9	0.00852	0.00105	0.000358	0.00103	0.000321	0.00146	0.00101
10	0.00944	0.00106	0.000361	0.000944	0.000375	0.00153	0.0011
11	0.00699	0.000918	0.000291	0.000836	0.000155	0.00116	0.000809
12	0.00549	0.000783	0.000255	0.000814	9.29e-05	0.000923	0.000668
13	0.00604	0.00085	0.000277	0.000801	0.000182	0.000985	0.000725
14	0.00395	0.000679	0.000222	0.00057	0.000183	0.000726	0.00055
15	0.00465	0.000748	0.000254	0.000699	0.000201	0.000822	0.000611
16	0.00813	0.00116	0.000481	0.00123	0.000184	0.00133	0.000993

TABLE F.10: Cross section value and error values splited by statistical, cross section parameters, FSI, flux and detector uncertainties at each bin. When unfolding on ϕ_{planar}.

bin Value	Data Stats.	Statistics Data	Statistics MC	Cross section param. error	FSI	Flux	Detector
1	0.000308	3.46e-05	7.73e-05	0.000146	1.18e-05	6.05e-05	3.93e-05
2	-0.000806	0.000662	0.000402	0.000464	0.000208	0.000231	0.000345
3	-0.00042	0.000682	0.000537	0.000529	0.000221	0.000253	0.00053
4	0.000718	0.00127	0.000662	0.00363	0.00139	0.0016	0.000543
5	-0.000339	0.00141	0.000774	0.000927	0.000376	0.000367	0.000929
6	0.00481	0.00178	0.000844	0.00163	0.00117	0.00128	0.00109
7	0.0133	0.00239	0.000975	0.0031	0.000615	0.00261	0.00168
8	0.0152	0.00242	0.000931	0.00312	0.000658	0.00285	0.00185
9	0.0155	0.00233	0.00087	0.00311	0.000663	0.00288	0.00187
10	0.0177	0.00244	0.00093	0.00296	0.000486	0.00316	0.00203
11	0.0248	0.00269	0.00105	0.00367	0.00051	0.0041	0.00258
12	0.026	0.00269	0.00104	0.00294	0.000561	0.00413	0.00246
13	0.029	0.00269	0.00104	0.00294	0.000323	0.00454	0.00251
14	0.0284	0.00252	0.00101	0.00274	0.000639	0.00443	0.0024
15	0.0355	0.00291	0.00118	0.00282	0.00113	0.00545	0.0029
16	0.0379	0.00309	0.00129	0.00316	0.000928	0.00592	0.00311
17	0.0374	0.00317	0.00124	0.00311	0.000966	0.00593	0.00322
18	0.0358	0.00323	0.00117	0.00345	0.000704	0.00589	0.00315
19	0.0331	0.0036	0.00114	0.00369	0.00102	0.00585	0.00336
20	0.0607	0.00529	0.00175	0.00574	0.00152	0.00987	0.00532

TABLE F.11: Cross section value and error values splited by statistical, cross section parameters, FSI, flux and detector uncertainties at each bin. When unfolding on $Cos\theta_{planar}$.

F.8 Model dependent results: $\sigma(E)$

The binnning used in the two measurements is the same:

$\{0.0, 0.2, 0.4, 0.5, 0.6, 0.7, 0.8, 1., 1.2, 1.4, 1.6, 1.8, 2., 2.3, 2.6, 3., 1000.0\}$

F.8.1 Energy dependent Cross Section using MiniBooNE Formula

Table F.12 shows the bin order, the cross section value and error values splited by statistical, cross section parameters, FSI, flux and detector uncertainties at each bin.

bin Value	Data Stats.	Statistics Data	Statistics MC	Cross section param. error	FSI	Flux	Detector
1	0	0	0	0	0	0	0
2	3.55e-05	1.95e-06	2.49e-05	2.37e-05	2.59e-06	5.43e-06	3.89e-06
3	0.00286	0.000158	0.000171	0.00161	0.000191	0.000437	0.000313
4	0.0133	0.000729	0.000396	0.00339	0.000501	0.00203	0.00145
5	0.0395	0.00213	0.000895	0.00197	0.000633	0.00603	0.00427
6	0.0727	0.00373	0.0015	0.00566	0.00123	0.011	0.00765
7	0.121	0.00468	0.0019	0.0154	0.00251	0.018	0.011
8	0.174	0.00643	0.00322	0.0361	0.00679	0.0273	0.0145
9	0.229	0.00892	0.00463	0.0502	0.00768	0.0364	0.0192
10	0.284	0.0115	0.00637	0.0635	0.00677	0.0458	0.024
11	0.351	0.0142	0.00803	0.0787	0.00514	0.0564	0.0296
12	0.392	0.0161	0.00931	0.0876	0.00819	0.0633	0.0331
13	0.397	0.0164	0.00904	0.0875	0.00751	0.0641	0.0336
14	0.464	0.0192	0.0107	0.0596	0.013	0.075	0.0393
15	0.46	0.0191	0.0102	0.0939	0.0128	0.0745	0.039
16	0.588	0.0244	0.00842	0.11	0.022	0.0922	0.0499

TABLE F.12: Cross section value and error values splited by statistical, cross section parameters, FSI, flux and detector uncertainties at each bin. When unfolding on E_{RecoMB}, with *MiniBooNE's formula*.

F.8.2 Energy dependent Cross Section using the E_{Reco}

Table **??** shows the bin order, the cross section value and error values splited by statistical, cross section parameters, FSI, flux and detector uncertainties at each bin.

bin Value	Data Stats.	Statistics Data	Statistics MC	Cross section param. error	FSI	Flux	Detector
1	0	0	0	0	0	0	0
2	0	0	0	0	0	0	0
3	1.8e-05	6.84e-07	2.76e-05	1.18e-05	1.56e-06	2.68e-06	1.64e-06
4	0.00336	0.000328	0.000168	0.00107	0.000269	0.000474	0.000506
5	0.0123	0.00118	0.000431	0.000616	0.000454	0.00173	0.00184
6	0.0245	0.00234	0.000793	0.00164	0.000661	0.00345	0.00367
7	0.0479	0.00363	0.00123	0.00591	0.00109	0.00675	0.00671
8	0.0808	0.00403	0.00201	0.0191	0.00479	0.0138	0.0106
9	0.116	0.0061	0.00325	0.0299	0.00652	0.0205	0.0154
10	0.151	0.00813	0.00446	0.0397	0.00691	0.027	0.0201
11	0.189	0.0102	0.00583	0.0492	0.0057	0.0338	0.0251
12	0.223	0.0121	0.00705	0.0583	0.00541	0.04	0.0297
13	0.225	0.0122	0.0067	0.0579	0.00479	0.0404	0.03
14	0.277	0.015	0.00828	0.0445	0.00519	0.0497	0.0369
15	0.27	0.0147	0.00791	0.0519	0.00712	0.0486	0.0361
16	0.368	0.02	0.00699	0.0617	0.0131	0.0637	0.049

TABLE F.13: Cross section value and error values splited by statistical, cross section parameters, FSI, flux and detector uncertainties at each bin. When unfolding on E_{Reco}.

Bibliography

[1] N. Abgrall H. Aihara et al. T2K Collaboration, K. Abe. T2k neutrino flux prediction. *Phys. Rev. D*, 87(012001), Jannuary 2013. URL http://link.aps.org/doi/10.1103/PhysRevD.87.012001.

[2] K.A. Olive et al. Particle data group. *Chin. Phys. C*, 38(090001), 2014.

[3] G.P. Zeller J.A. Formaggio. From ev to eev: Neutrino cross sections across energy scales. *Rev. Mod. Phys.*, 84(1307), May 2012.

[4] Radecky et al. Study of single–pion production by weak charged currents in low–energy νd interactions. *Phys. Rev. D*, 25(5), March 1982.

[5] H. Aihara et al. K. Abe, N. Abgrall. The t2k experiment. *Nuclear Instruments and Methods in Physics Research Section A: Accelerators, Spectrometers, Detectors and Associated Equipment*, 659(1):106–135, 2011. URL http://www.sciencedirect.com/science/article/pii/S0168900211011910.

[6] Arnold Nordsieck. Neutron collisions and the beta-ray theory of fermi. *Phys.Rev.*, 234(46):234–235, August 1934. URL http://journals.aps.org/pr/abstract/10.1103/PhysRev.46.234.

[7] F. Reines F. B. Harrison H. W. Kruse Jr. Cowan, C. L. and A. D. McGuire. Detection of the free neutrino: a confirmation. *Science*, 124(3212):103–104, July 1956. URL http://www.sciencemag.org/content/124/3212/103.citation.

[8] G. Danby et al. Observation of high-energy neutrino reactions and the existence of two kinds of neutrinos. *Phys. Rev. Lett.*, 9(1):36–44, July 1962.

[9] Don S. Harmer Jr. Davis, Raymond and Kenneth C. Hoffman. Search for neutrinos from the sun. *Phys. Rev. Lett.*, 20(1205), May 1968.

[10] V. N. Gribov and B. Pontecorvo. Neutrino astronomy and lepton charge. *Phys. Lett. B*, 28(7):493–496, January 1969.

[11] The ALEPH Collaboration et al. Precision electroweak measurements on the z resonance. *Physics Reports*, 257(427), 2006.

[12] K. Kodama et al. Observation of tau neutrino interactions. *Phys. Lett. B*, 218(504), 2001.

[13] N.Abgrall et al. Maid analysis techniques. *arXiv:nucl-th/0603012v1*, March 2006.

[14] M. Ericson M. Martini, G. Chanfray and J. Marteau. *arXiv:0909.0642[nucl-th].*

[15] P. Lava C. Praet N. Jachowicz, P. Vancraeyveld and J. Ryckebusch. *Phys. Rev. C*, 76(055501), 2007.

[16] S. Chauhan M. S. Athar and S. K. Singh. *arXiv:0908.1443[nucl-th].*

[17] D. Rein and L. H. Sehgal. Neutrino-excitation of baryon resonances and single pion production. *Annals Physics*, 79(133), 1981.

[18] M. Kislinger R. P. Feynman and F. Ravndal. Current matrix elements from a relativistic quark model. *Phys. Rev. D*, 2706(3), 1971.

[19] F. Ravndal. Weak production of nuclear resonances in relativistic quark model. *Nuovo Cimento A*, 385(18), 1973.

[20] E. T. Osypowski M. G. Olsson and E. H. Monsay. Electroproduction of low hadronic masses. *Phys. Rew. D*, 2938(17), 1978.

[21] A. Kartavtsev E. A. Paschos and G. J. Gounaris. Coherent pion production by neutrino scattering off nuclei. *Phys. Rev. D*, 74(054007), 2006.

[22] L. S. Geng S. Hirenzaki L. Alvarez-Ruso and M. J. Vicente Vacas. Charged current neutrino-induced coherent pion production. *Phys. Rev. C*, 75(0555501), 2007.

[23] E. Hernandez J. Nieves J. E. Amaro and M. Valverde. Charged current neutrino-induced coherent pion production. *Phys. Rev. D*, 79(013002), 2009.

[24] K. Hiraide et al. Search for charged current coherent pion production on carbon in a few-gev neutrino beam. *Phys. Rev. D*, 78(112004), 2008.

[25] M. Hasegawa et al. Search for coherent charged pion production in neutrino-carbon interactions. *Phys. Rev. Lett.*, 95(252301), 2005.

[26] A. A. Aguilar-Arevalo et al. First observation of coherent π^0 production in neutrino-nucleus interactions with $e_\nu < 2$ gev. *Phys. Lett. B*, 664(41), 2008.

[27] A. Higuera et al. Measurement of coherent production of $\pi^\pm$ in neutrino and anti-neutrino beams on carbon from e_ν of 1.5 to 20 gev. *arXiv:1409.3835v2 [hep-ex]*, 2014.

[28] S. Boyd D. Scully. Measurement of charged current coherent production in fgd1. *T2K Technical Note TN-191*, 2015.

[29] A.A. Aguilar-Arevalo et al. Measurement of neutrino-induced charged-current charged pion production cross sections on mineral oil at $e_\nu \sim 1$ gev. *Phys. Rev. D*, 83(052007), 2011.

[30] B. Eberly et al. Charged pion production in ν_μ interactions on hydrocarbon at $< e_\nu >= 4.0$ gev. *arXiv:1406.6415v2 [hep-ex]*, 83, 2014.

[31] Y. Hayato. *Acta Phys.Polon. B*, (40):2477–2489, 2009.

[32] T2K Collaboration. Measurement of the inclusive numu charged current cross section on carbon in the near detector of the t2k experiment. *Phys. Review. D*, 092003 (87), September 2013.

[33] T2K Collaboration. Measurement of the inclusive electron neutrino charged current cross section on carbon with the t2k near detector. *Phys. Rev. L*, 113(241803), 2014.

[34] T2K Collaboration. Measurement of the ν_μ ccqe cross section on carbon with the nd280 detector at t2k. *arXiv:1411.6264 [hep-ex]*, 2014.

[35] T2K Collaboration. Measurement of the inclusive ν_μ charged current cross section on iron and hydrocarbon in the t2k on-axis neutrino beam. *Phys. Rev. D*, 90 (052010), September 2014.

[36] A. Ichikawa. Design concept of the magnetic horn system for the t2k neutrino beam. *Nuclear Instruments and Methods in Physics Research Section A: Accelerators, Spectrometers, Detectors and Associated Equipment.*, (690):27– 33, 2012. URL http://www.sciencedirect.com/science/article/pii/S0168900212007115.

[37] A. Carroll D. Beavis and I. Chiang. Long baseline neutrino oscillation experiment at the ags. *Tech. Rep.*, (52878), April 1995.

[38] T2K Collaboration. Evidence for an oscillatory signature in atmospheric neutrino oscillations. *Phys. Rev. L*, 93(101801), September 2004.

[39] K2K Collaboration. Measurement of neutrino oscillation by the k2k experiment. *Phys. Rev. D*, 74(072003), September 2006.

[40] A. Fasso A. Ferrari, P. R. Sala and J. Ranft. *CERN-2005-010. SLAC-R-773. INFN-TC-05-11*, 74, 2015.

[41] F. Carminati R. Brun and S. Giani. *CERN-W5013*, 1994.

[42] C. Zeitnitz and T. Gabriel. *Corpus Christi*, 1992.

[43] N. Abgrall et al. NA61/SHINE facility at the cern sps: beams and detector system. *CERN–PH–EP–2014–003*, 2014.

[44] The NA61/SHINE Collaboration. Pion emission from the t2k replica target: Method, results and application. *Nucl. Instr. Meth. A 701 99*, 2013.

[45] The NA61/SHINE Collaboration. Measurements of cross sections and charged pion spectra in proton-carbon interactions at 31 gev/c. *Phys.Rev. C*, 84(034604), 2011.

[46] The NA61/SHINE Collaboration. Measurement of production properties of positively charged kaons in proton-carbon interactions at 31 gev/c. *Phys.Rev. C*, 85 (035210), 2012.

[47] G. Arnison et al. Experimental observation of lepton pairs of invariant mass around 95 gev/c2 at the cern sps collider. *Phys. Lett. B*, 126:398–410, 1983.

[48] J. Altegoer et al. The nomad experiment at the cern sps. *Nucl. Instrum. Meth.*, A404:96–128, 1998.

[49] I. Giomataris et al. *Nucl. Instrum. Meth.*, 102(A560):405–408, 2006.

[50] N.Abgrall et al. Time projection chambers for the t2k near detectors. *Nuclear Instruments and Methos in Pnumuxsectionhysics Research Section A: Accelerators, Spectrometers, Detectors and Associated Equipment*, 637(46):234–235, May 2011.

[51] Y. Ashie et al. Measurement of atmospheric neutrino oscillation parameters by super- kamiokande i. *Phys.Rev. D*, 71(112005), 2005.

[52] S. Ahn et al. Detection of accelerator produced neutrinos at a distance of 250-km. *Phys. Lett. B*, 511:178–184, 2001.

[53] Super-KamiokaNDE Collaboration. Evidence for oscillation of atmospheric neutrinos. *Phys. Rev. Lett.*, 81(1562), 1998.

[54] Super-KamiokaNDE Collaboration. Measurement of the solar neutrino energy spectrum using neutrino electron scattering. *Phys. Rev. Lett.*, pages 2430–2434, 1999.

[55] M. Ahn et al. Measurement of neutrino oscillation by the k2k experiment. *Phys.Rev. D*, 74(072003), 2006.

[56] J. Hosaka et al. Three flavor neutrino oscillation analysis of atmospheric neutrinos in super-kamiokande. *Phys.Rev. D*, 74(032002), 2006.

[57] M. Shiozawa et al. Search for proton decay via $p \to e+\pi^0$ in a large water cherenkov detector. *Phys.Rev. Lett.*, 81:3319–3323, 2006.

[58] Y. Hayato et al. Search for proton decay through $p \to \bar{\nu}k^+$ in a large water cherenkov detector. *Phys.Rev. Lett.*, 83:1529–1533, 1999.

[59] H. Nishino et al. Search for proton decay via $p \to e + \pi^0$ and $p \to \mu^+\pi^0$ in a large water cherenkov detector. *Phys.Rev. Lett.*, 102(141801), 2009.

[60] J.V. Jelley. Cerenkov radiation and its applications. *British Journal of Applied Physics*, 6:227–232, 1955.

[61] The NuMu group of the T2K Collaboration. Cc–multiple–pion numu event selections in the nd280 tracker using run 1+2+3+4 data. *T2K Technical Note TN-152*, 2013.

[62] A. Hillairet. Nd280 tpc track–finding efficiency. *T2K Technical Note TN-163.*

[63] S. Oser. Elemental composition and masses of fgd xy modules. *T2K Technical Note TN-091.*

[64] B. Kirby J. Kim and M. Wilking. Michel electron tagging in fgd1. *T2K Technical Note TN-104.*

[65] The T2K Collaboration. Precise measurement of the neutrino mixing parameter θ_{23} from muon neutrino disappearance in an off-axis beam. *Phys. Rev. Lett.*, 112 (181801), May 2014.

[66] The T2K Collaboration. Observation of electron neutrino appearance in a muon neutrino beam. *Phys. Rev. Lett.*, 112(061802), 2014.

[67] The T2K Collaboration. Measurements of neutrino oscillation in appearance and disappearance channels by the t2k experiment with 6.6×10^{20} protons on target. *Phys. Rev. D*, 91(072010), April 2014.

[68] et al. K. Abe. Observation of electron neutrino appearance in a muon neutrino beam. *Phys. Rev. Lett.*, (112:061802), February 2014.

[69] et al. K. Abe. Measurement of neutrino oscillation parameters from muon neutrino disappearance with an off-axis beam. *Phys. Rev. Lett.*, (111:211803), February 2013.

[70] Allen et al. A study onf single– meson production in neutrino and antineutrino charged–current interactions on protons. *Nuclear Physics B*, (264), 1986.

[71] The SciBooNE Collaboration. Measurement on inclusive neutral current neutral pion production on carbon in a few-gew neutrino beam. *Phys. Rev. D*, 81(033004), October 2009.

[72] C.Andreopoulos et al. The genie neutrino monte carlo generator. physics and user manual. *Nucl. Instrum. Meth A*, (614), 2011. URL http://www.genie-mc.org/.

[73] G. D'Agostini. A multidimensional unfolding method based on bayes' theorem. *Nucl. Instrum. and Meth. in Physics Research A*, (362), 1995.

[74] Melody Ravonel Salzgeber. Measurement of the inclusive muon neutrino charged current cross section in the near detector of the t2k experiment. *Thesis. Universite de Geneve*, 637(4465), 2012.

[75] L. Wolfenstein. Neutrino oscillations in matter. *Phys. Review D*, 2369(17), May 1978.

[76] S.P. Mikheev and A. Yu. Smirnov. Neutrino oscillations in matter. *Sov. J. Nucl. Phys.*, 913(42), 1985.